



**CENTRO DE INVESTIGACIÓN Y DE ESTUDIOS AVANZADOS
DEL INSTITUTO POLITÉCNICO NACIONAL**

UNIDAD ZACATENCO

Programa de Nanociencias y Nanotecnología

**Influencia del óxido de grafeno (GO) en nanoestructuras
TiO₂-GO aplicadas al control de la contaminación del agua**

T E S I S

Que presenta:

FRANCISCO JAVIER GOMEZ CANO

Para obtener el grado de

DOCTOR EN CIENCIAS

En:

NANOCIENCIAS Y NANOTECNOLOGÍA

Directores de Tesis:

Dr. Iouri Koudriavtsev

Dr. Abdelhadi Kassiba

Ciudad de México

Septiembre 2024



**CENTER FOR RESEARCH AND ADVANCED STUDIES OF
THE NATIONAL POLYTECHNIC INSTITUTE**

ZACATENCO UNIT

Nanosciences and Nanotechnology Programme

**Influence of graphene oxide (GO) on TiO₂-GO nanostructures
applied to water pollution control**

T H E S I S

Presented by:

FRANCISCO JAVIER GOMEZ CANO

To obtain the degree of

DOCTORATE IN SCIENCE

In:

NANOSCIENCE AND NANOTECHNOLOGY

Thesis Directors:

Dr. Iouri Koudriavtsev

Dr. Abdelhadi Kassiba

Mexico City

September 2024



THESE DE DOCTORAT (COTUTELLE)

DE
LE MANS UNIVERSITE
SOUS LE SCEAU DE
LA COMUE ANGERS – LE MANS

ECOLE DOCTORALE N° 596
Matière, Molécules, Matériaux et Géosciences
Spécialité : « *Physique* »

Par

Francisco Javier GOMEZ CANO

**Influence of graphene oxide (GO) on TiO₂-GO nanostructures applied to
water pollution control**

Thèse présentée et soutenue à : *Centre de Recherche et d'Études Avancées de l'IPN-Mexique*

Et en vidéoconférence : *Institut des Molécules et des Matériaux du Mans, Le Mans Université*

Date : 06 Septembre 2024

Thèse N° : 2024LEMA1011

Rapporteurs avant soutenance :

Makowska-Janusik, Malgorzata, Professeur, *Faculté des Sciences et Technologies*, Université JD de Czesochowa, Pologne

Juan Carlos Durán-Álvarez, Professeur, *Institut des Sciences Appliquées et de la Technologie*, UNAM, Mexique

Composition du Jury :

Président : **Benoît Guiffard**, Professeur, *Institut d'électronique et des Technologies Numériques*, Université de Nantes, France.

Examineurs : **Makowska-Janusik, Malgorzata**, Professeur, *Faculté des Sciences et Technologies*, Université JD de Czesochowa, Pologne.

Juan Carlos Durán-Álvarez, Professeur, *Institut des Sciences Appliquées et de la Technologie*, UNAM, Mexique.

Miguel García Rocha, Professeur, *Département de physique*, Cinvestav, Mexique.

Benoît Guiffard, Professeur, *Institut d'électronique et des Technologies Numériques*, Université de Nantes, France.

Co-Encadrant : **Sandrine Coste**, Professeur associé, *Institut des Molécules et des Matériaux du Mans*, Le Mans Université, France.

Co-Encadrant : **Velumani Subramaniam**, Professeur, *J. Mike Walker '66 Department of Mechanical Engineering*, Texas A&M University. USA.

Co-dir. de thèse : **Iouri Koudriavtsev**, Professeur, *Section électronique des solides*, Cinvestav, Mexique.

Dir. de thèse : **Abdelhadi Kassiba**, Professeur, *Institut des Molécules et des Matériaux du Mans*, Le Mans Université, France.

TABLE OF CONTENTS

<i>Abstract</i>	i
<i>Resumen</i>	ii
<i>Résumé</i>	iii
<i>Introduction and motivation</i>	1
References.....	3
<i>CHAPTER I. Toward a comprehensive understanding of water pollution, remediation & naomaterials....</i>	5
1.1. Nanomaterials in water remediation	6
1.2. Adsorption.....	6
1.2.1. Nanomaterials as adsorbents.....	7
1.2.1.1. Carbon.....	8
1.2.1.2. Carbon-based nanomaterials (CBN)	9
1.2.1.3. Graphene-based materials (GBM)	10
1.2.1.3.1. Graphene-structure.....	11
1.2.1.3.2. Graphene oxide structure	12
1.2.1.3.3. Synthesis methods to fabricate GO	13
1.3. Advanced oxidation processes (AOP)	14
1.3.1. Photocatalysis	15
1.3.2. Nanostructured photocatalysts	16
1.3.3. Titanium dioxide (TiO ₂).....	16
1.3.3.1. Fundamentals and photocatalysis mechanism of TiO ₂	17
1.3.4. Heterojunction systems with TiO ₂	18
1.3.5. Hybrid nanostructures based on TiO ₂ -graphene	19
1.4. Conclusion	23
References.....	23
<i>CHAPTER II. Reagents, Methods, and Instrumentation</i>	29
2.1. Graphene oxide synthesis by Tour method	29
2.2. Hybrid nanostructures based on TiO ₂ and graphene oxide.....	30
2.2.1. Hybrid nanostructures by ball-milling.....	31
2.2.2. Hybrid nanostructures by photosonation	31
2.3. Characterization techniques	32
2.3.1. X-ray diffraction (XRD)	32
2.3.2. Raman spectroscopy	33
2.3.3. Fourier transform infrared spectroscopy (FTIR-ART)	35
2.3.4. X-ray photoelectron spectroscopy (XPS)	35
2.3.5. Brunauer-Emmett-Teller (BET).....	36

2.3.6.	Scanning electron microscopy (SEM)	36
2.3.7.	Transmission electron microscopy (TEM)	37
2.3.8.	Diffuse reflectance spectroscopy (DRS).....	37
2.3.9.	Electron paramagnetic resonance (EPR) spectroscopy.....	38
2.3.10.	Electrical conductivity measurements	39
2.4.	Experiment setup for MB removal	40
2.4.1.	MB stock solution and calibration curve	40
2.4.2.	Experimental set-ups for adsorption	41
2.4.3.	Experimental set-ups for photocatalysis	41
2.4.3.1.	Bandpass filter transmission	42
2.4.3.2.	Photocatalysis with ball-milling nanostructures	42
2.4.3.3.	Photocatalysis with photosonicated nanostructures.....	42
2.5.	Experiment setup for microalga photolysis and photocatalysis study	43
2.5.1.	Pulse-amplitude-modulation (PAM) fluorometry.....	43
2.5.2.	Sample preparation	44
2.5.3.	Diatoms solution used.....	44
2.5.4.	Experimental setup for microalgal degradation.....	45
	References.....	47
	CHAPTER III. Theoretical approach by DFT applied to GO and hybrid nanostructures TiO₂-GO	49
3.1.	Computational details	50
3.1.1.	Graphene oxide structures.....	50
3.1.2.	TiO ₂ -GO hybrid structures.....	50
3.2.	Graphene	51
3.2.1.	Optimized geometry.....	51
3.2.2.	Graphene band-structure	51
3.3.	Graphene oxide	52
3.3.1.	Optimized geometry.....	52
3.3.2.	Bandgap variation	55
3.3.3.	Electronic band structure	57
3.4.	Anatase TiO ₂ structure	58
3.4.1.	Optimized structure and band structure	58
3.5.	Hybrid structures based on TiO ₂ and Graphene/GO.....	60
3.5.1.	Optimized geometry of hybrid TiO ₂ -Graphene-based structures	60
3.5.2.	TiO ₂ -GO structure optimized geometry.....	61
3.5.3.	Electronic structures of hybrid nanostructures	62

3.4.	Conclusion	63
	References.....	63
CHAPTER IV: Tuning oxidation degree: A structural study of graphene oxides		67
4.1.	Removal of residual Mn ²⁺ ions	67
4.2.	Morphological and microstructural features	70
4.2.1.	X-ray diffraction	70
4.2.1.1.	Quantitative analysis	72
4.2.1.2.	Correlation between the size of nanocrystallites L _c and the oxidation degree	75
4.2.2.	Raman spectroscopy	75
4.2.2.1.	Quantitative analysis of the D/G ratio	77
4.2.2.2.	Identification of structural defects	79
4.2.2.3.	Graphitic domain size	81
4.2.3.	Morphology (SEM/TEM) and specific surface area (SSA).....	82
4.3.	Surface chemical composition features	84
4.3.1.	FT-IR characterization	84
4.3.1.1.	Chemical composition	85
4.3.2.	Quantitative determination of oxidation degree by XPS	87
4.4.	Mechanism of graphene oxide formation	89
4.5.	Electrical conductivity behavior	92
4.6.	Conclusion	93
	References.....	94
CHAPTER V: Mechano-synthesis: TiO₂-GO Hybrid nanostructures by ball-milling		99
5.1.	Microstructural analysis.....	100
5.1.1.	X-ray powder diffraction	100
5.1.2.	Raman spectroscopy analysis	102
5.1.2.1.	Effect of mechanical milling on graphitic domains	103
5.1.2.1.1.	D- and G-band positions	103
5.1.2.1.2.	A _D /A _G and graphite crystallite size	104
5.1.3.	Specific surface area (SSA)	105
5.2.	FT-IR component interactions	106
5.2.1.	Quantification of Ti-O-C bonds	107
5.3.	Morphology (SEM/TEM)	108
5.4.	Mechanism of formation of TiO ₂ -GO hybrid nanostructures	111
5.5.	Optical properties of hybrid nanostructures	112
5.5.1.	Absorbance	112

5.5.2.	Optical bandgap	113
5.6.	Electrical conductivity	114
5.7.	Conclusion	116
	References	117
	CHAPTER 6. Photosonication: Engineering of hybrid nanostructures based on TiO₂ & GO	121
6.1.	Structural and morphological analysis	122
6.1.1.	Morphology TiO ₂ -GO by TEM	122
6.1.2.	X-ray diffraction analysis	124
6.1.3.	Raman spectroscopy analysis	126
6.1.3.1.	Evolution of GO after incorporation into hybrid nanostructures	129
6.1.3.1.1.	D- and G-band positions	129
6.1.3.1.2.	A _D /A _G ratio and graphitic crystallite size	130
6.1.4.	Interface bonds analysis by FTIR-ART	131
6.2.	EPR study.....	132
6.2.1.	Ti ³⁺ defects on TiO ₂ by EPR.....	132
6.2.2.	Field splitting (W _{Δg}) and anisotropy after GO incorporation	134
6.2.3.	Paramagnetic behavior of GO as a function of the oxidation degree	135
6.2.4.	Paramagnetic behavior of GO as a function of temperature.....	137
6.3.	Relation between nanostructure formation by sonication and EPR active defects.....	139
6.4.	Optical features	141
6.5.	Electrical Conductivity	141
6.5.1.	Conductivity evolution with temperature changes	143
6.6.	Conclusion	145
	References.....	146
	CHAPTER 7. Mechanisms of dye removal on titanium oxide–graphene oxide nanostructures	150
7.1.	MB removal by adsorption	150
7.1.1.	Adsorption on TiO ₂	150
7.1.2.	Adsorption on TiO ₂ -GO mechano-synthesized nanostructures	152
7.1.2.1.	Effect of contact time and oxidation degree	152
7.1.2.2.	Kinetic Study	153
7.1.2.3.	A mechanistic model for dye diffusion.....	154
7.1.2.4.	Adsorption isotherms.....	157
7.1.3.	MB adsorption on TiO ₂ -GO photo-sonicated nanostructures evaluation	160
7.1.3.1.	Effect of the GO oxidation degree	160
7.1.3.2.	Kinetic study.....	162

7.1.3.3.	Mechanistic model for dye diffusion	163
7.1.3.4.	Adsorption isotherms	164
7.2.	Degradation by photocatalysis	167
7.2.1.	Degradation on TiO ₂	167
7.2.2.	Degradation of TiO ₂ -GO mechano-synthesized nanostructures	168
7.2.2.1.	Kinetic study	170
7.2.3.	Degradation on TiO ₂ -GO photosonicated nanostructures.....	171
7.2.3.1.	Kinetic study	173
7.2.3.2.	Degradation mechanisms	174
7.2.3.3.	Photocatalytic reactions and charge transfer mechanism	174
7.2.4.	MB molecular analysis after degradation by Raman spectroscopy	176
7.3.	Conclusion	178
	References.....	180
	CHAPTER 8. Study on microalgal photocatalytic destruction	183
8.1.	Measurements of <i>chlorophyll</i> fluorescence	184
8.2.	<i>Chlorophyll</i> fluorescence under visible light	185
8.3.	<i>Chlorophyll</i> fluorescence after overnight	186
8.4.	Microalgae absorption spectra	187
8.5.	Quantification of cell concentration.....	190
8.6.	Molecular analysis after degradation by Raman spectroscopy	190
8.7.	Conclusion	191
	References.....	192
	<i>General conclusions</i>	193
	<i>Future potential directions</i>	195
	<i>Supplementary information</i>	197
	<i>Contributions</i>	209
	<i>Copyright permissions</i>	211

Abstract

Growing environmental concerns have focused research efforts on the development of nanomaterials suitable for water pollution control applications. In this context, graphene oxides (GOs) and their hybrid nanostructures combining TiO₂ nanoparticles have been synthesized to exploit processes such as adsorption and photocatalysis for the removal of organic pollutants from water. The work carried out analyses the influence of the physicochemical properties of GOs, and in particular their oxidation degree, on the structural, electronic, and photoactivity properties of TiO₂-GO hybrid nanocomposites. Hybrid nanostructures based on TiO₂ and GO were prepared by high-energy milling and photosonation, and complementary characterization techniques such as X-ray diffraction, Raman spectrometry, SEM/TEM electron microscopy, FT-IR, XPS, and EPR electron paramagnetic resonance spectroscopy were applied. An in-depth analysis of the experimental results obtained on selective TiO₂-GO nanocomposites highlighted the evolution of the physicochemical and morphological properties of the nanostructures as a function of the controlled GO oxidation conditions. Furthermore, theoretical studies using DFT revealed the correlation between the variations of the electronic bandgap and the concentration of functional groups in the GO material. The adsorption and photocatalysis phenomena of the different TiO₂-GO compositions were investigated by degradation of methylene blue (MB) dyes with remarkable efficiency. The same experimental approach, which was then studied on biological organisms such as microalgae through the degradation of associated by-products, underlines the interdisciplinary nature of this work. Thus, by systematically studying the oxidation levels of GO and the techniques used to prepare nanocomposites, the work carried out contributes to a deeper understanding of the physicochemical characteristics of TiO₂-GO nanocomposites and optimizes their properties and characteristics for efficient photocatalytic activity applied to water purification.

Keywords: Titanium dioxide, graphene oxide, hybrid nanostructures, water remediation

Resumen

La creciente preocupación por el medio ambiente ha centrado los esfuerzos de investigación en el desarrollo de nanomateriales adecuados para aplicaciones de control de la contaminación del agua. En este contexto, se han sintetizado óxidos de grafeno (GOs) y sus nanoestructuras híbridas combinando nanopartículas de TiO_2 para explorar procesos como la adsorción y la fotocatalisis para la eliminación de contaminantes orgánicos del agua. El trabajo realizado analiza la influencia de las propiedades fisicoquímicas de los GOs, y en particular su grado de oxidación, sobre las propiedades estructurales, electrónicas y de fotoactividad de los nanocomposites híbridos TiO_2 -GO. Las nanoestructuras híbridas basadas en TiO_2 y GO se prepararon mediante molienda de alta energía y fotosonificación, y se aplicaron técnicas complementarias de caracterización como difracción de rayos X, espectrometría Raman, microscopía electrónica SEM/TEM, FT-IR, XPS y espectroscopia de resonancia paramagnética electrónica EPR. Un análisis en profundidad de los resultados experimentales obtenidos sobre nanocompuestos selectivos de TiO_2 -GO puso de manifiesto la evolución de las propiedades fisicoquímicas y morfológicas de las nanoestructuras en función de las condiciones de oxidación controlada del GO. Además, los estudios teóricos mediante DFT revelaron la correlación entre las variaciones del bandgap y la concentración de grupos funcionales en el GO. Los fenómenos de adsorción y fotocatalisis de las diferentes composiciones de TiO_2 -GO se investigaron mediante la degradación de colorantes azul de metileno (MB) con notable eficacia. El mismo enfoque experimental, que luego se estudió en organismos biológicos como las microalgas mediante la degradación de los subproductos asociados, subraya el carácter interdisciplinario de este trabajo. Así, mediante el estudio sistemático de los niveles de oxidación del GO y de las técnicas empleadas para la preparación de nanocomposites, el trabajo realizado contribuye a profundizar en el conocimiento de las características fisicoquímicas de los nanocomposites TiO_2 -GO y a optimizar sus propiedades y características para una eficiente actividad fotocatalítica aplicada a la depuración de aguas.

Palabras clave: Dióxido de titanio, óxido de grafeno, nanoestructuras híbridas, remediación del agua

Résumé

Les préoccupations croissantes en matière de préservation de l'environnement ont orienté les efforts de la recherche vers le développement de nanomatériaux adaptés aux applications à la dépollution de l'eau. Dans ce contexte, des oxydes de graphène (GO) et leurs nanostructures hybrides associant des nanoparticules de TiO_2 ont été synthétisés en vue d'exploiter des processus tels que l'adsorption et la photocatalyse pour l'élimination des polluants organiques dans l'eau. Les travaux menés ont permis d'étudier l'influence des propriétés physicochimiques des GO et en particulier leurs degrés d'oxydation sur les propriétés structurales, électronique et de photoactivité des nanocomposites hybrides TiO_2 -GO. La fabrication de nanostructures hybrides à base de TiO_2 et de GO par broyage à haute énergie et par photosonication a été mise en œuvre ainsi que des techniques de caractérisations complémentaires telles que la diffraction de RX, la spectrométrie Raman, la microscopie électronique SEM/TEM, la spectroscopie FT-IR, XPS et de résonance paramagnétique électronique RPE. L'analyse approfondie des résultats obtenus sur une variante de nanocomposites TiO_2 -GO a mis en évidence l'évolution des propriétés physico-chimiques et morphologiques des nanostructures en fonction des conditions d'oxydation contrôlées du GO. En complément, des études théoriques par DFT ont révélé la corrélation entre les variations de la bande électronique interdite et la concentration des groupes fonctionnels dans le matériau GO. Les phénomènes d'adsorption et de photocatalyse des différentes compositions TiO_2 -GO ont été étudiés à travers l'élimination du bleu de méthylène (MB) avec des efficacités remarquables. La même approche expérimentale qui a été ensuite explorée sur des organismes biologiques tels que des microalgues à travers la dégradation de sous-produits associés, souligne le caractère interdisciplinaire de ces travaux. Ainsi, en explorant systématiquement les degrés d'oxydation du GO et les techniques de fabrication des nanocomposites, les études effectuées contribuent à la compréhension et l'optimisation des propriétés et caractéristiques des nanostructures hybrides à base de TiO_2 et de GO pour une meilleure efficacité de leur utilisation pour la dépollution de l'eau.

Mots clés : Dioxyde de titane, oxyde de graphène, nanostructures hybrides, dépollution de l'eau

Introduction and motivation

Water is an essential resource for life on Earth, a fundamental element that sustains all living organisms and shapes our planet in countless ways. However, despite the importance of water for life, approximately 80% of the world's wastewater is discharged, mostly untreated, into rivers, lakes, and oceans [1]. In response, effective and economical technologies based on nanomaterials have been developed [2, 3] and show unique and often improved properties compared to their larger-scale counterparts [4]. In particular, these nanosized materials are characterized by exceptional properties such as large surface area, modulated optical properties, enhanced electrical and thermal conductivity, mechanical properties, and chemical reactivity. Moreover, nanomaterials may also exhibit tunable physical, chemical, and electronic properties not involved in bulk materials [5]. Thus, several classes of nanomaterials were exhaustively considered to eliminate or reduce the concentration of pollutants below a defined level to ensure human health and environmental safety without side effects [6]. In this context, the high specific surface of nanomaterials plays a key role in phenomena such as *adsorption* and *photocatalysis* which, contribute to the overall removal of pollutants [7, 8].

As an efficient material for water remediation, titanium dioxide (TiO_2) is worthy of interest and was extensively applied as a photocatalyst in addition to being non-toxic, corrosion-resistant, and biocompatible [9, 10]. When exposed to UV light, TiO_2 generates reactive oxygen species (ROS) that can break down chemical bonding in organic compounds leading to simpler and less harmful substances [11]. However, despite its advantages, TiO_2 faces several limitations as a photocatalyst in practical applications, as it requires (UV) light due to its broad bandgap (≈ 3.2 eV—anatase phase) [12]. On the other hand, its ability to adsorb pollutants in water is limited in its pristine form [13]. According to the review by Dong H. *et al.* 2015 [14], pristine TiO_2 has a low adsorption affinity for hydrophobic pollutants due to its inherent hydrophilic nature, which limits its ability to trap nonpolar organic pollutants. Other authors point out that it lacks specific surface modifications that could improve its adsorption capacity [15], and its porous structure is not optimized for efficient adsorption of hydrophobic pollutants [11]. In addition, pristine TiO_2 nanoparticles tend to agglomerate in aqueous media, reducing their effective surface area and thus their adsorption capacity [16].

To overcome these limitations, a relevant approach was developed based on the formation of hybrid TiO_2 nanostructures by using two-dimensional materials such as graphene oxide (GO). GO and carbon-based materials possess large surface areas, and their single-sheet structure facilitates the diffusion of contaminants to the adsorption sites, improving the efficiency of the process [17, 18]. In addition, GO can be chemically modified to selectively increase its affinity for specific contaminants, allowing more efficient and specific adsorption

[19, 20]. These combined properties make GO a highly effective component for improving the adsorption capacity of hybrid nanomaterials. The adsorption capacity of GO can influence the concentration and distribution of contaminants near TiO₂ particles, thus facilitating their degradation by photocatalysis when exposed to a light source [21, 22].

The limited study of the adsorption process in hybrid materials could be attributed to the fact that in several reported works, significantly lower adsorption removal efficiency is observed compared to the photocatalysis process [7, 23], which has led to disproportionate attention to the latter process. Moreover, these phenomena have been evaluated mainly as a function of the GO concentration added to the hybridized nanostructure. Therefore, this research stands out for its approach, focusing on the study of the intrinsic nature of GO and its influence on the engineering of the resulting morphologies, as well as on the physicochemical properties and their impact on the mechanisms related to the global removal of pollutants from water. To this end, GOs, with variable oxidation degrees, were synthesized by meticulously manipulating KMnO₄ concentrations, and subsequently incorporated into TiO₂ matrices using *ball-milling* and *photosonation* methods. These investigations revealed significant differences in the morphologies and characteristics of the resulting nanostructures, further highlighting the critical influence of fabrication methods on their properties.

The novelty of this Ph.D. thesis lies in the developed approaches to photoactive nanostructures based on TiO₂ and GO. Integrating theoretical knowledge, meticulous synthesis techniques, comprehensive characterization methods, and practical applications. By systematically exploring the interplay between GO oxidation degrees, TiO₂ modification methodologies, and fabrication techniques, this work contributes to better understanding and optimizing the properties of hybrid TiO₂-GO nanostructures. The ambition of this approach is to realize critical challenges in environmental remediation, paving the way for sustainable solutions to water pollution.

This work begins with a comprehensive literature review in Chapter 1, which covers fundamental concepts relevant to the materials and mechanisms considered in the performed studies. The second chapter reports the experimental details of the synthesis and fabrication methods of the investigated materials. It also describes the instrumentation of the characterization techniques used for the investigations of the relevant physical and chemical features of the functional nanomaterials. Chapter 3 develops a theoretical study using Density Functional Theory (DFT) to elucidate the relationship between the bandgap variations and the epoxide functional groups in GO. The theoretical insights highlighted the fundamental role of DFT simulations in understanding and optimizing atomic interactions in the developed experimental studies.

Chapter 4 reports the details of GO synthesis by the Tour method to obtain selective architectures of the functional nanostructures. Detailed investigations of their physicochemical properties were carried out by X-ray diffraction, Raman spectroscopy, and SEM-TEM observations. The chemical composition analysis revealed a nuanced evolution of the structural, morphological, and chemical characteristics as a function of the controlled oxidation

conditions. UV-VIS spectroscopy characterizes the modifications of the bandgap and electrical conductivity, providing a comprehensive understanding of the impact of GO oxidation on the optical and electronic properties. Further in Chapters 5 and 6, the investigations were devoted to the hybrid TiO₂-GO nanostructures obtained by *ball-milling* and *photosonation* methods. Microstructural analysis revealed a complex interplay between the phase composition and crystallinity, highlighting the impact of GO incorporation on the specific surface area, TiO₂ particle size, and electrical conductivity. While ball-milling proved an efficient modification of TiO₂ properties, photosonation emerged as a less aggressive alternative, showing clear advantages in the formation of core-shell structures, and facilitating the formation of Ti-O-C bonds at the interfaces.

In Chapter 7, the synthesized hybrid nanostructures were investigated in the process of degradation of methylene blue (MB) dyes. The incorporation of GO, either by *ball-milling* or *photosonation*, showed a synergistic effect, improving both adsorption and photocatalytic degradation ability. Finally, chapter 8 is an exploratory work toward practical applications of the hybrid nanostructures in ROS generation by photocatalytic processes and their effect on microalgae in solutions. By expanding research beyond traditional contaminant removal to encompass the complex interactions of aquatic ecosystems, this work lays the groundwork for specific solutions to mitigate the adverse effects of microalgal blooms. This interdisciplinary approach underscores the relevance and potential impact of the findings, opening an area to address environmental problems with innovative nanomaterials and methodologies.

References

1. UNESCO: The United Nations World Water Development Report 2021: Valuing water, (2021)
2. Alvarez, P.J.J., Chan, C.K., Elimelech, M., Halas, N.J., Villagrán, D.: Emerging opportunities for nanotechnology to enhance water security. *Nature Nanotechnology* 2018 13:8. 13, 634–641 (2018). <https://doi.org/10.1038/s41565-018-0203-2>
3. Gautam, R.K., Chattopadhyaya, M.C.: Nanomaterials for Wastewater Remediation. *Nanomaterials for Wastewater Remediation*. 1–347 (2016). <https://doi.org/10.1016/C2014-0-01159-8>
4. Zhao, W., Chen, I.W., Huang, F.: Toward large-scale water treatment using nanomaterials. *Nano Today*. 27, 11–27 (2019). <https://doi.org/10.1016/J.NANTOD.2019.05.003>
5. Zhang, W., Zhang, D., Liang, Y.: Nanotechnology in remediation of water contaminated by poly-and perfluoroalkyl substances: A review *. (2019). <https://doi.org/10.1016/j.envpol.2019.01.045>
6. WHO: A global overview of national regulations and standards for drinking-water quality. *Verordnung über die Qualität t von Wasser für den menschlichen Gebrauch (Trinkwasserverordnung -TrinkwV 2001)*. (2018)
7. Drisya, K.T., Edely, M., Solís-López, M., Jantrania, A., Auguste, S., Rousseau, A., Casteneda, H., Velumani, S., Kassiba, A.: Structural features and morphology of titanium dioxide–bismuth vanadate heterojunctions. *CrystEngComm*. 23, 7679–7690 (2021). <https://doi.org/10.1039/D1CE00982F>
8. Sánchez-Albores, R., Cano, F.J., Sebastian, P.J., Reyes-Vallejo, O.: Microwave-assisted biosynthesis of ZnO-GO particles using orange peel extract for photocatalytic degradation of methylene blue. *J Environ Chem Eng*. 10, 108924 (2022). <https://doi.org/10.1016/J.JECE.2022.108924>
9. Khudhair, D., Bhatti, A., Li, Y., Hamedani, H.A., Garmestani, H., Hodgson, P., Nahavandi, S.: Anodization parameters influencing the morphology and electrical properties of TiO₂ nanotubes for living cell interfacing and investigations. *Materials Science and Engineering C*. 59, 1125–1142 (2016). <https://doi.org/10.1016/J.MSEC.2015.10.042>
10. Zhang, H., Banfield, J.F.: Structural characteristics and mechanical and thermodynamic properties of nanocrystalline TiO₂. *Chem Rev*. 114, 9613–9644 (2014). <https://doi.org/10.1021/CR500072J>

11. Gopinath, K.P., Madhav, N.V., Krishnan, A., Malolan, R., Rangarajan, G.: Present applications of titanium dioxide for the photocatalytic removal of pollutants from water: A review. *J Environ Manage.* 270, 110906 (2020). <https://doi.org/10.1016/J.JENVMAN.2020.110906>
12. Cano, F.J., Romero-Nunez, A., Jantrania, A., Liu, H., Kassiba, A., Velumani, S.: Bandgap dependence on facet and size engineering of TiO₂: A DFT Study. *CCE 2021 - 2021 18th International Conference on Electrical Engineering, Computing Science and Automatic Control.* (2021). <https://doi.org/10.1109/CCE53527.2021.9632880>
13. Langhammer, D., Kullgren, J., Österlund, L.: Adsorption and Oxidation of NO₂ on Anatase TiO₂: Concerted Nitrate Interaction and Photon-Stimulated Reaction. *ACS Catal.* 12, (2022). <https://doi.org/10.1021/acscatal.2c03334>
14. Dong, H., Zeng, G., Tang, L., Fan, C., Zhang, C., He, X., He, Y.: An overview on limitations of TiO₂-based particles for photocatalytic degradation of organic pollutants and the corresponding countermeasures. *Water Res.* 79, 128–146 (2015). <https://doi.org/10.1016/j.watres.2015.04.038>
15. Safri, A., Fletcher, A.J.: Effective Carbon/TiO₂ Gel for Enhanced Adsorption and Demonstrable Visible Light Driven Photocatalytic Performance. *Gels.* 8, (2022). <https://doi.org/10.3390/gels8040215>
16. Li, R., Li, T., Zhou, Q.: Impact of Titanium Dioxide (TiO₂) Modification on Its Application to Pollution Treatment—A Review. *Catalysts* 2020, Vol. 10, Page 804. 10, 804 (2020). <https://doi.org/10.3390/CATAL10070804>
17. Yang, X., Wan, Y., Zheng, Y., He, F., Yu, Z., Huang, J., Wang, H., Ok, Y.S., Jiang, Y., Gao, B.: Surface functional groups of carbon-based adsorbents and their roles in the removal of heavy metals from aqueous solutions: A critical review. *Chem Eng J.* 366, 608 (2019). <https://doi.org/10.1016/J.CEJ.2019.02.119>
18. Jiang, M., Zhang, M., Wang, L., Fei, Y., Wang, S., Núñez-Delgado, A., Bokhari, A., Race, M., Khataee, A., Jaromír Klemeš, J., Xing, L., Han, N.: Photocatalytic degradation of xanthate in flotation plant tailings by TiO₂/graphene nanostructures. *Chemical Engineering Journal.* 431, (2022). <https://doi.org/10.1016/j.cej.2021.134104>
19. Anegebe, B., Ifijen, I.H., Maliki, M., Uwidia, I.E., Aigbodion, A.I.: Graphene oxide synthesis and applications in emerging contaminant removal: a comprehensive review. *Environmental Sciences Europe* 2023 36:1. 36, 1–34 (2024). <https://doi.org/10.1186/S12302-023-00814-4>
20. Sabzehmeidani, M.M., Mahnaee, S., Ghaedi, M., Heidari, H., Roy, V.A.L.: Carbon based materials: a review of adsorbents for inorganic and organic compounds. *Mater Adv.* 2, 598–627 (2021). <https://doi.org/10.1039/D0MA00087F>
21. Obulapuram, P.K., Arfin, T., Mohammad, F., Khiste, S.K., Chavali, M., Albalawi, A.N., Al-Lohedan, H.A.: Adsorption, Equilibrium Isotherm, and Thermodynamic Studies towards the Removal of Reactive Orange 16 Dye Using Cu(I)-Polyaniline Composite. *Polymers (Basel).* 13, (2021). <https://doi.org/10.3390/POLYM13203490>
22. Nguyen-Phan, T.D., Pham, V.H., Shin, E.W., Pham, H.D., Kim, S., Chung, J.S., Kim, E.J., Hur, S.H.: The role of graphene oxide content on the adsorption-enhanced photocatalysis of titanium dioxide/graphene oxide composites. *Chemical Engineering Journal.* 170, 226–232 (2011). <https://doi.org/10.1016/J.CEJ.2011.03.060>
23. Siddeeg, S.M.: A novel synthesis of TiO₂/GO nanocomposite for the uptake of Pb²⁺ and Cd²⁺ from wastewater. *Mater Res Express.* 7, (2020). <https://doi.org/10.1088/2053-1591/ab7407>

Chapter I:

Toward a comprehensive understanding of water pollution, remediation & nanomaterials

Water is an essential resource for life on Earth, a fundamental element that sustains all living organisms and shapes our planet in countless ways. From basic needs for human life to powering agriculture, industry, and energy generation, water plays a critical role in life, society, and the economy. In addition, its influence extends to biodiversity conservation and global climate regulation through the water cycle. However, despite the importance of water for life, approximately 80 percent of the world's wastewater is discharged, mostly untreated, into rivers, lakes, and oceans [1]. This proportion is higher in less developed countries where sanitation and wastewater treatment facilities are very poor [2].

Numerous anthropogenic and natural behaviors contribute significantly to water pollution. Although some industries treat their wastewater before releasing it into the environment, others simply discharge it untreated. This poses serious ecotoxicological threats because untreated wastewater contains a wide range of organic pollutants such as pesticides, petrochemicals, dyes, and others [3]. Some of these organic compounds are persistent and can cause health troubles as they are highly toxic and potentially carcinogenic. In addition, certain pollutants such as dyes, discharged into water, reduce light penetration, which impairs the performance of algae and growing aquatic plants, not to mention that many of them are ingested by fish and other living organisms and can be metabolized in their organisms to toxic intermediates [4]. To face such pollution issues, it is necessary to develop effective and economical technologies for water remediation that can eliminate the contaminants or reduce them below a certain established level to ensure human health and environmental safety without side effects [5].

In this context, various techniques have been developed for water treatment, such as ultrafiltration, sedimentation, gravity separation, flotation, precipitation, oxidation, adsorption, ion exchange, etc. [6]. However, standard wastewater treatment technologies reach their limits due to rapid population growth, large-scale industrialization, and urbanization. This has led to the demand for new technologies with higher efficiency and lower cost. The solutions based on nanomaterials are worthy of interest and attract great interest from the wide materials research community [7]. The present work is related to this research theme with the ambition to develop innovative materials and methodologies for the water remediation problem.

1.1. Nanomaterials in water remediation

Nanomaterials are known for their size-dependent properties at the nanometer scale in at least one of their dimensions [8]. These materials exhibit unique and often enhanced properties compared to their bulk counterparts [9]. Examples of nanomaterials include carbon nanotubes, metal nanoparticles, semiconducting nanocrystals, nanowires, and nanosheets, among others. Among the outstanding properties, it may be underlined the large surface area, modulated optical responses, enhanced electrical and thermal conductivity, original mechanical properties such as super-plasticity or characterized by higher Young modulus as well as important chemical reactivity. Several classes of nanomaterials can be designed to exhibit tunable physical, chemical, and electronic properties not involved in bulk materials [10].

Within the environmental context, key contributions are made by using nanomaterials which are used for the filtration, adsorption, and advanced oxidation processes. For example, carbonaceous nanomaterials have been successfully used in filtration and adsorption processes due to their large surface area correlating with the nanosized pore sizes [11]. On the other hand, various semiconducting oxides (TiO_2 , ZnO , Fe_3O_4 , WO_3 , etc.), as well as metal nanoparticles (Fe, Ag), are highly efficient for advanced oxidation processes such as photocatalysis. By using these nanomaterials, a significant reduction in the concentration of pollutants is achieved, highlighting the effectiveness of this approach for improving water quality. In this process, phenomena such as adsorption and photocatalysis take place, which, although different from each other, together contribute to the overall removal of pollutants [12].

1.2. Adsorption

Adsorption is considered a suitable and preferred approach due to its relatively low cost, simplicity of design, high removal efficiency, and easy recyclability [13]. Adsorption is a phenomenon when molecules of a substance in a gaseous or liquid state are attached to the surface of another material, known as an adsorbent [14]. On the other hand, the opposite process is named desorption corresponding to the release of the adsorbate from the adsorbent surface as schematically depicted in Fig. 1.1.

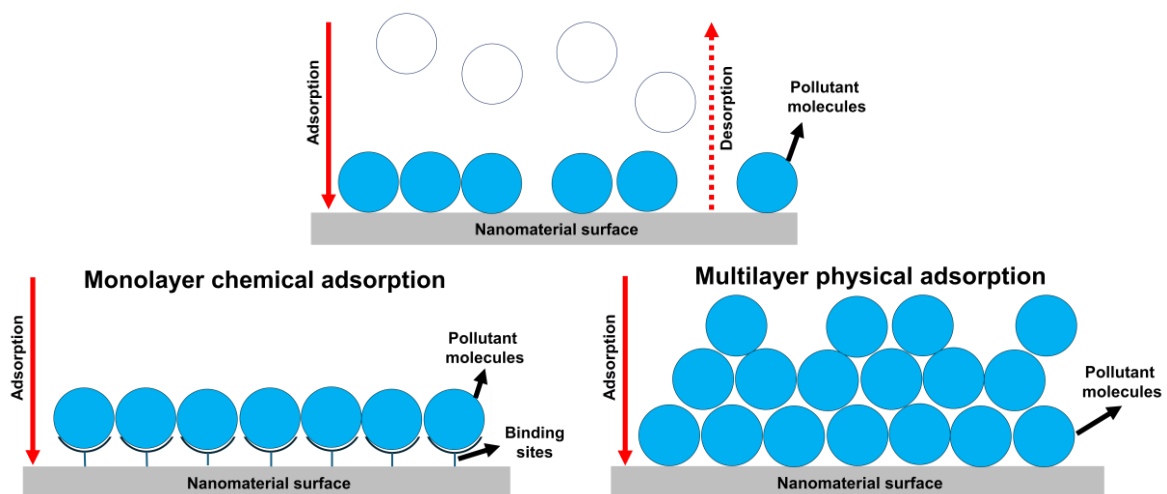


Fig. 1.1. Schematic representation of adsorption and desorption processes. Single-layer and multi-layer adsorption (*Adapted from [17] with copyright permission*)

Conceptually, adsorption is a phenomenon that occurs at the interface and can be categorized into two interaction mechanisms: (i) Physical adsorption occurs due to weak intermolecular forces such as Hydrogen bonding, Van der Waals forces, π - π interactions and electrostatic attraction. (ii) Chemical adsorption involves the formation of new chemical bonds between the surface of the nanomaterial (adsorbent) and the adsorbates (contaminants) [15]. Chemical adsorption is slower than physical adsorption and usually forms a monomolecular layer (monolayer) on the adsorbent surface, whereas physical adsorption usually involves the formation of a thick multilayer on the surface [16]. Fig. 1.1.b-c shows a schematic representation of monolayer and multilayer adsorption on the adsorbent surface. Table 1.1. shows the differences between physical and chemical adsorption.

Table 1.1. Physical and chemical adsorption comparison (*reprinted from [17] with copyright permission*)

Physical adsorption	Chemical adsorption
<i>Electrostatic interactions and Van der Waals forces are implicated</i>	<i>Covalent bonds are established between the surface and the molecules that have been adsorbed</i>
<i>Fast</i>	<i>Slow</i>
<i>Reversible</i>	<i>Irreversible</i>
<i>Not very specific</i>	<i>It is specific</i>
<i>Multilayers are formed</i>	<i>Monolayers are formed</i>
<i>Activation energy is unnecessary</i>	<i>Activation energy is necessary</i>
<i>It typically manifests at low temperatures and diminishes as the temperature rises.</i>	<i>Elevated temperature is required</i>

1.2.1. Nanomaterials as adsorbents

Nanoadsorbents refer to particles at the nanoscale composed of either organic or inorganic materials that exhibit a strong attraction towards adsorbate compounds. Due to their high porosity, small size, and active surface area, nanoadsorbents are not only capable of adsorbing contaminants with different molecular sizes, and hydrophobicity but also allow the manufacturing process to use raw materials efficiently without releasing their toxic load [18]. Nanoadsorbents also have significant contaminant-binding capabilities and can also be chemically regenerated after depletion [19]. These particles possess distinctive characteristics, including catalytic capability and heightened reactivity, in addition to their extensive surface area, rendering them superior adsorbents compared to traditional materials. Recent reports in the literature have extensively investigated the adsorption capacity of various nanomaterials such as CeO [20], ZnO [21], SiO₂ [22], and Fe₃O₄ [23]. However, the adsorption capacity of these materials is still limited, *e.g.* TiO₂ has shown adsorption capacity with a removal of 18-30% [24]. Therefore, carbon-based nanomaterials represent a promising alternative in this

context, as they meet the appropriate requirements for a successful adsorption process, such as large surface area, high pore volume, and adequate functionalities.

1.2.1.1. Carbon

The carbon atom, with $1s^2 2s^2 2p^2$ as its fundamental electronic configuration, is one of the most versatile elements, able to adopt different hybridization forms leading to multiple carbon-based architectures. The main features of the carbon bonding hybridization are outlined below:

- sp^3 hybridization (C-C bond):** It consists of one s -band mixed with three p -orbitals to form four equivalent hybrid orbitals. The hybrid orbitals are oriented as far apart as possible, being located at the vertices of the regular tetrahedron with 109.5° bonds (Fig. 1.2.). This hybridization is involved in the diamond structure with the formation of tetrahedral arrangements of carbon atoms.

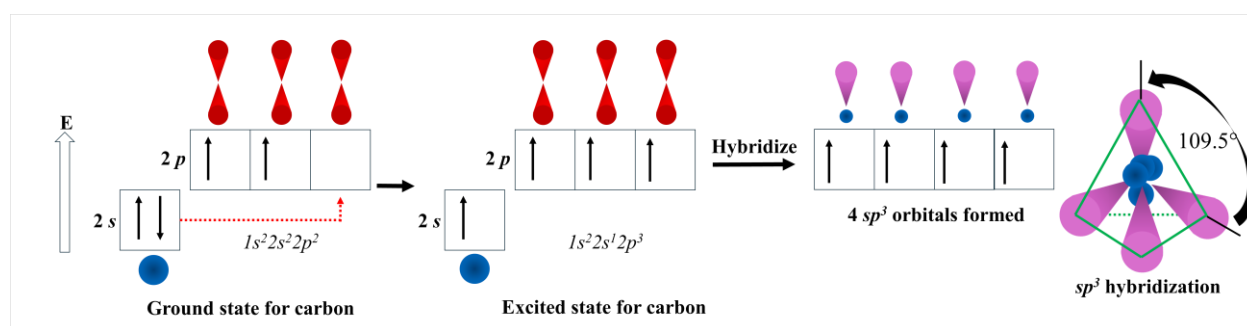


Fig. 1.2. Electronic configuration of the carbon atom and geometry of sp^3 -hybridization

- sp^2 hybridization (double C=C bond):** The sp^2 hybridization associates one s -orbital mixed with two p -orbitals. The mixing of these orbitals leads to three equivalent hybrid orbitals (sp^2) arranged in a trigonal planar geometry (120°). The p -orbital that was left out (unhybridized) and did not take part in the hybridization is a significant distinction between this hybridization and the sp^3 hybridization. This orbital is placed at 90° to the plane of the trigonal planar arrangement of the three sp^2 -orbitals (Fig. 1.3.). Extensive research has been conducted on the exceptional physicochemical features of graphene, carbon nanotubes, and fullerenes, which are carbon-based structures with sp^2 hybridization.

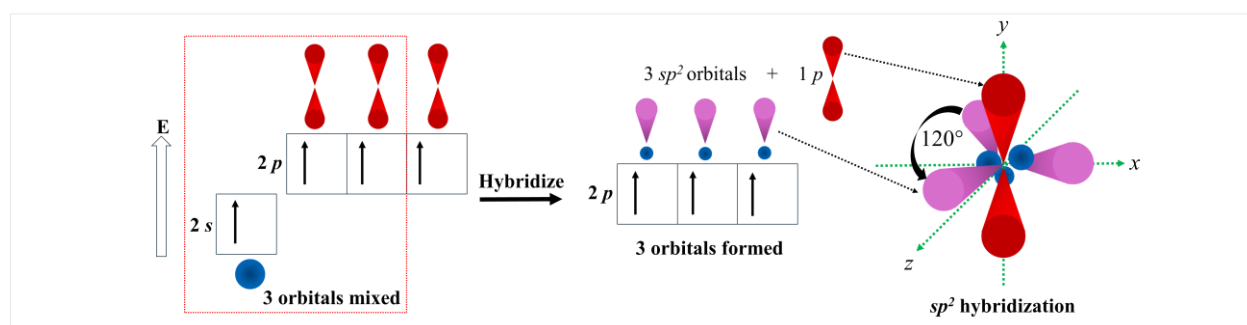


Fig. 1.3. Electronic configuration of the carbon atom and geometry of sp^2 -hybridization.

- ***sp* hybridization (triple bond $C\equiv C$):** the *s* carbon orbital is mixed with only one out of the three *2p*-orbitals. The resulting two *sp* hybrid orbitals are then arranged in a linear geometry (180°) and the two unhybridized *2p*-orbitals are placed at 90° (Fig. 1.4.).

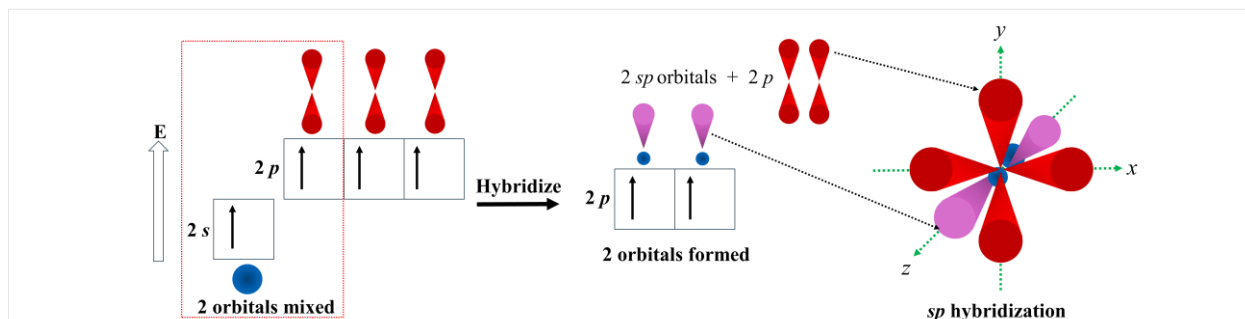


Fig. 1.4. Electronic configuration of the carbon atom and geometry of *sp*-hybridization.

1.2.1.2. Carbon-based nanomaterials (CBN)

Carbon can form various crystalline arrangements or allotropes, resulting in a variety of carbon-based nanomaterials with characteristic mechanical and thermal properties. Their exceptional surface area, porosity, and significant adsorption capacity were crucial factors in effectively eliminating a broad spectrum of pollutants from water. As examples, activated carbon, carbon nanotubes (CNTs), graphene, and its derivatives, among others, generally exhibit high adsorption capacity and thermal stability, in addition to providing ample binding sites for contaminants, making them capable of adsorbing organic compounds, heavy metals, dyes, pharmaceuticals residues, and others. In addition, these materials can be customized and functionalized to target specific contaminants, improving their selectivity and overall efficiency. In addition, modified or doped compositions to incorporate surface functional groups can be achieved by dedicated chemical methods and used for wastewater treatment.

Water and wastewater treatment systems incorporating activated carbon (CA) have been widely used due to their ease of operation, potential for adsorbent regeneration, and applicability in batch and continuous processes [25]. On the other hand, carbon nanotubes represent another option that has received considerable attention as a new type of adsorbent with potential applications in the removal of various contaminants (*e.g.*, metal ions, dyes, phenolic compounds, and pharmacological substances) in aqueous solutions [26]. Unlike CA adsorbents, the adsorption properties of CNTs differ significantly from those of activated carbon. Regardless of pore characteristics and surface areas, the overall adsorption properties of CNTs depend on the adsorption site, purity, and surface functional groups of carbon in nanometer-thick layers [27]. Table 1.2. shows a summary of work reported in the literature on activated carbon and carbon nanotubes, respectively, for the removal of contaminants from water by adsorption mechanisms.

Table 1.2. Summary of work that has used activated carbon and carbon nanotubes

CBN	Contaminant	% removal	E_q. time	Isotherm	Kinetic	Ref.
CA	Sildenafil citrate (Sil)	85%	< 10 h	Langmuir isotherms	Pseudo-first order	[28]
CA-Alginate composite	Bisphenol AF	29.2 %	within 3 h	Dubinin-Ashtakhov isotherms	Pseudo-second-order	[29]
Granular CA	Benzophenone	53±4%	90 min	Langmuir isotherms	Pseudo-second-order	[30]
Granular CA	Caffeine	53±2%	90 min	Langmuir isotherms	Pseudo-second-order	[30]
Polyethyleneimine modified CA	Hg(II)	90%	35 min	Langmuir isotherms	Pseudo-second-order	[31]
CNT	Zn ²⁺	≈59.8%	60 min	Langmuir isotherms	----	[32]
CNT	Malachite green (MG)	≈70%	50 min	Langmuir isotherms	Pseudo-first order	[33]
Magnetic CNT	Methylene blue (MB)	≈95%	120 min	Langmuir isotherms	Pseudo-second-order	[34]
CNT	Bisphenol A	≈49.26%	15 min	Langmuir isotherms	---	[35]

1.2.1.3. Graphene-based materials (GBM)

Since the last decade, there have been exhaustive investigations on graphene and graphene-based materials (GBM) for environmental issues. In this regard, environmental applications based on graphene oxide (GO) offer more realistic possibilities compared to pristine graphene due to easy and low-cost production. Compared to CNTs, GBM is expected to offer better absorbance efficiency of pollutants [36] as their available contact surfaces are more important. On the other hand, GO and rGO (reduced graphene oxide) can be readily produced through the chemical exfoliation of graphite, resulting in materials with a significant abundance of oxygen-containing functional groups. Thus, efficient adsorption processes can be achieved for the removal of inorganic species from aqueous solutions [37], including organic pollutants, heavy metals, rare earths, and dyes [38].

Carbon materials play a key role in the adsorption of various contaminants from water, and in this scenario, GBM emerges as a prominent vector. Several authors claim that GO is

preferable to pristine graphene for metal ions adsorption due to the high content of oxygen groups available to interact with ions. In addition, its properties and characteristics can be conveniently modified by the gradual incorporation of oxygen-containing functional groups [39]. The importance of these oxygenated functional groups has been previously demonstrated by Yan, H. *et al.* [40] who showed a clear tendency of GO to improve its adsorption capacity at higher degrees of oxidation, *i.e.* at higher amounts of functional groups. Likewise, Reynosa-Martinez A, *et al.* [41] demonstrated the same behavior concerning the adsorption of As(III). GO can also be incorporated with metal oxides to form hybrid nanostructured materials with specific properties and has been used as an efficient adsorbent and also enhances *advanced oxidation processes* (AOP) for the removal of various pollutants as discussed in the following sections. However, before discussing hybrid systems, it is important to characterize the organization and the electronic band structure peculiarities of GO materials, and the following section is dedicated to shed light on the relevant related features.

1.2.1.3.1. Graphene-structure

Thorough investigations were concentrated on a different form of carbon known as graphene. This 2D structure possesses a hexagonal lattice of carbon with sp^2 -hybridization. Most of graphene's electrical conductivity is ascribed to the π -bond, which is positioned vertically to the lattice plane. The stability of graphene is a result of the close arrangement of its carbon atoms and the sp^2 -orbital hybridization, which involves a mix of s , px , and py orbitals that form the σ -bond. The last valence electron forms the π -bond. The π -bonds undergo hybridization to create the π -band and π^* -bands (Fig. 1.5). The noteworthy electrical properties of graphene are mostly attributed to the bands that enable the movement of free electrons, particularly the half-filled band [42].

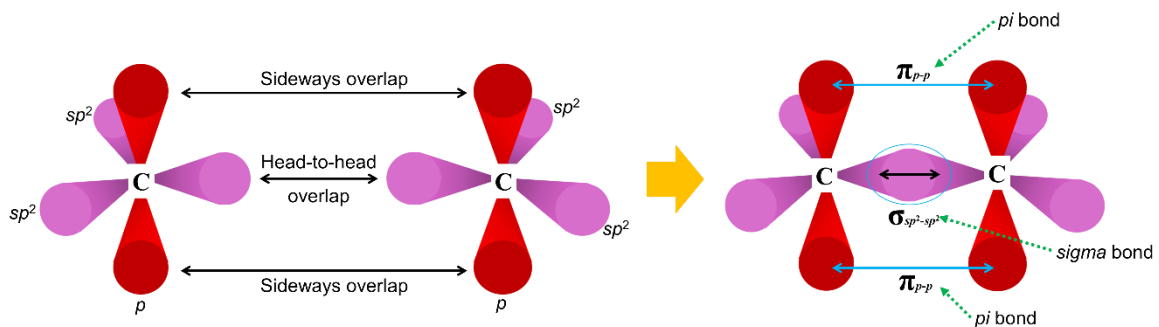


Fig. 1.5. Overlapping of sp^2 and p orbitals and formation of pi (π) and sigma (σ) bonds

Graphene is the most conductive material so far at room temperature, with a conductivity of 106 S/m and a sheet resistance of 31 Ω /sq [43]. This is attributed to its ultrahigh mobility of 2×10^5 cm²/Vs [44] which is almost 140 times the mobility in silicon. Besides this, graphene is a typical semimetal [45] in which there is a small overlap between its conduction band (C_B) and valence band (V_B). Even at the temperature of absolute zero, a certain concentration of electrons is already in the C_B while a certain concentration of holes is in the V_B . As shown in Fig. 1.6. the V_B and C_B of graphene exhibit cone-like structures that intercept at the Dirac point. The electron transport in graphene exhibits the anomalous quantum Hall effect [46] and characteristics of relativistic particles [47].

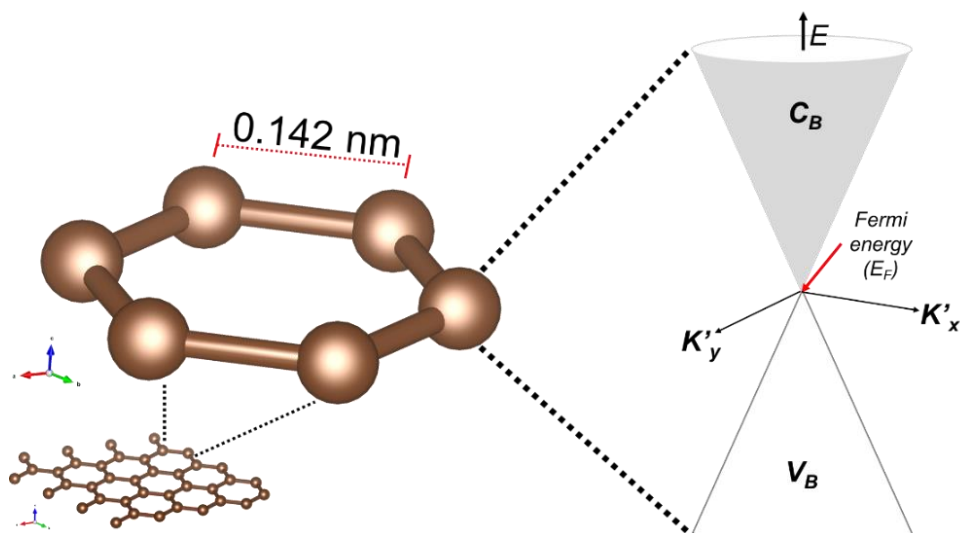


Fig. 1.6. Representation of energy band of graphene.

The conductivity of graphene can also be manipulated by inserting a hydrogen atom onto each carbon atom without breaking the hexagonal lattice, giving an insulating graphene material [48]. A great deal of resistance could also be given to graphene by applying a vertical electric field onto bilayer graphene, blocking the electrons from in-plane movement [49]. Additionally, several studies have demonstrated that the absence of a bandgap in graphene is a result of the identical conditions of the two atomic sublattices that make up graphene. This suggests that introducing structural or chemical modifications to disrupt this lateral in-plane symmetry could create a bandgap in graphene [50], similar to what occurs in GO as discussed later.

1.2.1.3.2. Graphene oxide structure

At first, GO was believed to be the outcome of the chemical process of exfoliation and oxidation of layered crystalline graphite, whether it be natural or artificial [51]. However, authors have recently shown that the same structure can also be obtained by an alternative (*bottom-up*) method by hydrothermal treatment of glucose [52] or even by chemical vapor deposition (CVD) [53]. Therefore, GO could be defined as "a single-atom carbon layer with both surfaces modified by oxygen-containing functional groups". Like any 2D carbon, GO can have a monolayer or multilayer structure [54]. The carbon layers in multilayer GO are separated by functional groups attached to each layer of carbon atoms (Fig. 1.7.a.). Although GO, like graphene, is a two-dimensional carbon material, its properties can differ significantly from those of graphene as the oxidation degree increases.

The exceptional characteristics of GO mostly stem from its hybrid electronic structure, which encompasses both the conducting π -states of the sp^2 carbon domains and the σ -states of the sp^3 carbon domains [55]. Theoretical studies have shown that the properties of GO can be modified by adjusting the sp^2/sp^3 ratios of the carbon atoms [56]. Previous experimental reports showed the observation of quantum confinement phenomena in GO due to the formation of non-oxidized sp^2 islands between the oxidized sp^3 regions [57]. The formation of sp^3 domains

in GO is due to the oxidation reaction resulting in the decoration of different types of functional groups such as hydroxyl, epoxide, carbonyl, and carboxyl groups (Fig. 1.7.b.). The presence of these oxygenated functional groups in GO makes it hydrophilic and also allows it to be functionalized with other materials using appropriate chemistry [58]. The sp^2/sp^3 ratios in GO can be adjusted by varying the oxidation degree through appropriate chemical reactions. GO with different ratios of sp^2/sp^3 domains can be tuned for specific properties relevant to water remediation applications, such as the bandgap required for photocatalysis as will be discussed in the following sections. This relevance is based on the need for the bandgap to match the energy of incident photons to facilitate light absorption and subsequent electron-hole (e^-/h^+) pair generation. Chapter 3 of this compendium presents Density Functional Theory (DFT) simulations focusing on the structure of monolayer graphene and evaluates in detail the variation of its bandgap as functional groups are introduced into its configuration, leading to the alteration of the inherent symmetry and the breaking of carbon hexagons.

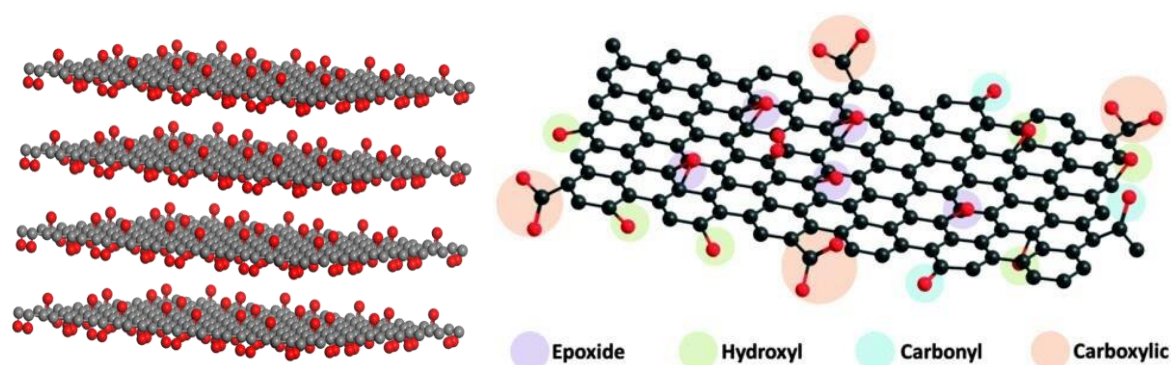


Fig. 1.7. (a) GO multilayer and, (b) structure of GO and functional groups

1.2.1.3.3. Synthesis methods to fabricate GO

GO was first synthesized by Benjamin Brody in 1859, long before the discovery of graphene [59]. Benjamin invented the method for making GO, which consisted of oxidation and exfoliation of natural crystalline graphite, which undoubtedly yielded a significant amount of monolayer GO, but at that time no one knew about graphene. The latest GO fabrication methods are based on the remarkable intercalation ability of layered graphite. It allows active metal atoms and some types of oxidants to penetrate between the flat carbon layers of crystalline graphite by increasing the interlayer distance and modifying the layer surfaces by chemically bonded functional groups. Finally, the action of suitable oxidizing agents causes the complete decomposition of the graphite crystal into separate carbon monolayers with chemically modified surfaces. It is important to note that the chemical oxidation conditions of graphite usually require a small ($< 10 \mu m$) particle size of the starting material. Intensive stirring or even ultrasonication is usually required to complete the chemical reactions (Fig. 1.8.). These factors make it difficult to obtain large GO flakes. For this reason, the average size of commercially available GO particles does not exceed a few microns. Nevertheless, the fundamental characteristics of GO, particularly the colligative capabilities of the macroscopic structures generated by GO, are significantly influenced by the average flake size.

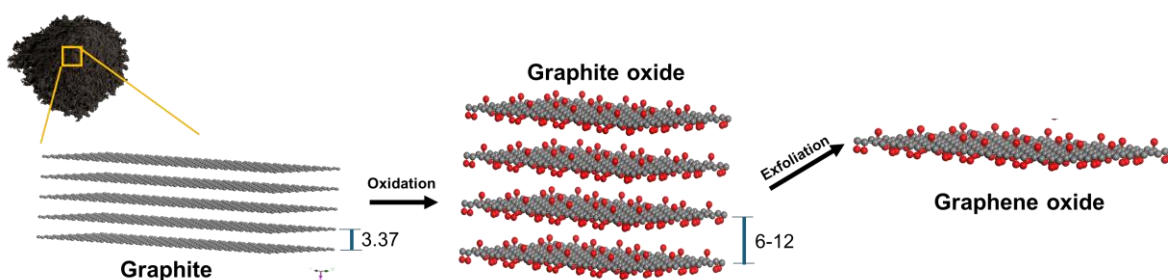


Fig. 1.8. Schematic of the process for obtaining GO, through the oxidation of graphite.

Since its discovery in 2004, GO has garnered significant attention in the field of carbon materials research. Numerous publications have been dedicated to studying its structure, reduction methods, and potential uses [60]. Common techniques for its synthesis (*Brodie*, *Staudenmaier*, *Hoffman*, *Hummers*) involve the utilization of potent acids (nitric and/or sulfuric) and potassium chlorate. The widely favored Hummers-Offeman technique employs a blend of concentrated H_2SO_4 , NaNO_3 , and KMnO_4 . Nevertheless, in 2010, Professor Tour's group at Rice University [61] introduced a novel approach that removed sodium nitrate, enhanced the quantity of potassium permanganate, and inserted phosphoric acid (H_3PO_4) into the reaction vessel. The researchers documented the production of a GO product with an increased oxidation degree. This was achieved by subjecting graphite to a reaction with potassium permanganate (KMnO_4) in a mixture of sulfuric acid (H_2SO_4) and phosphoric acid (H_3PO_4). An important benefit of this protocol is that it does not contain NaNO_3 , which prevents the formation of harmful gases like NO_2 , N_2O_4 , or ClO_2 during the reaction, thereby enhancing its environmental friendliness. Furthermore, it is claimed that H_3PO_4 offers a greater number of intact graphitic basal planes compared to Hummers' approach, resulting in a significantly larger final yield. In Chapter 4 of this material, we describe in detail the procedure carried out in this research for the fabrication of GOs by the Tour method.

1.3. Advanced oxidation processes (AOP)

Although most contaminants in wastewater can be removed by standard primary and secondary treatment, some traces of nondegradable materials, such as pharmaceutical residues, are difficult to remove. The limitations of conventional approaches have led to the development of more effective techniques such as advanced oxidation processes (AOPs) [9]. These techniques comprise a series of chemical treatments specifically formulated to eliminate organic and, in some cases, inorganic substances from water and wastewater through the process of oxidation [62]. AOPs rely on the generation of hydroxyl radicals ($\bullet\text{OH}$) in the water, which are extremely powerful oxidants capable of oxidizing almost any chemical in the water. The oxidation process frequently occurs rapidly, as assessed by the diffusion rate of the chemicals in the water [63]. Consequently, once formed, $\bullet\text{OH}$ reacts non-selectively and contaminants are rapidly and efficiently fragmented and converted into small molecules. Some examples of AOPs include UV/O_3 , $\text{UV}/\text{H}_2\text{O}_2$, Fenton, photo-Fenton, non-thermal plasmas, sonolysis, photocatalysis, radiolysis, and supercritical water oxidation [64]. The effectiveness of AOP treatment is highly dependent on the physical and chemical properties of the contaminants and the operating conditions.

Among all advanced oxidation methods, photocatalysis stands out as a strategy in the search for effective solutions to environmental remediation challenges such as water treatment. By harnessing the energy of light to generate highly reactive species, photocatalysis offers a versatile and promising approach to the degradation of persistent organic pollutants and other harmful compounds.

1.3.1. Photocatalysis

Photocatalysis refers to a series of chemical events that include speeding up photoinduced reactions in the presence of photocatalysts [65]. The fundamental principle of the heterogeneous photocatalysis process involves the use of a solid catalyst that is placed in a solution and exposed to specific wavelengths of light. The photo-generation of e^-/h^+ pairs produce free radicals within the solutions such as highly reactive hydroxyl radicals (-OH) that can oxidize any pollutant present in water, often at a diffusion-controlled reaction rate. As a result, contaminants are quickly and efficiently fragmented and converted into small inorganic molecules [66].

Photocatalytic processes mainly revolve around five steps (Fig. 1.9.) and two reaction pathways. The five phases are (i) light absorption by the photocatalyst (ii) excitons (e^-/h^+ pairs) generation within the photocatalyst, (iii) charge separation-transfer-migration, (iv) charge recombination or oxidation-reduction processes, and (v) desorption of reaction products from the catalyst surface or reaction medium [67]. The two reaction pathways for photocatalytic reactions are (a) direct pathways, in which photogenerated charge carriers are separated and trapped by surface defects or pollutants molecules that correspondingly form radicals, and (b) indirect pathways, in which photogenerated charge carriers are used to generate ions and radicals (reactive oxygen species) that react with water pollution molecules [68].

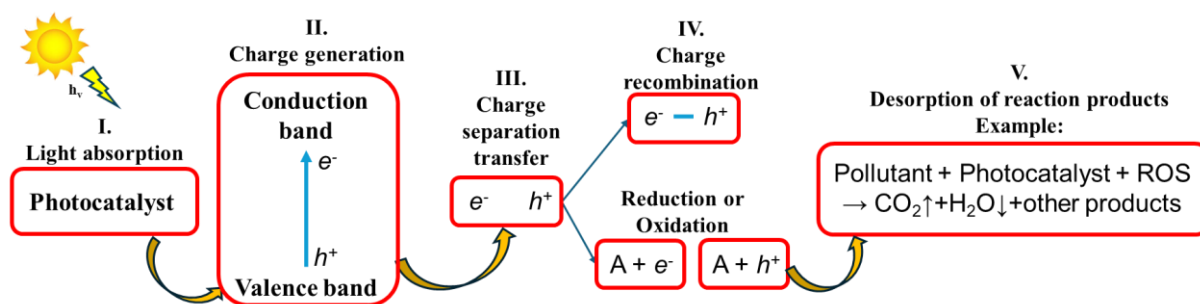


Fig. 1.9. Stages involved in photocatalysis (Adapted from [68] with copyright permission).

Provided there is no charge accumulation or poisoning, these steps can be repeated indefinitely. All steps need to be optimized to achieve the ideal efficiency: in (i), the more the full spectrum of light can be absorbed, the more e^-/h^+ pairs will be generated; in (ii), the more electrons and holes can avoid mutual annihilation by recombination, the more they will migrate to surfaces to be available for surface reactions; in (iii), surface reactions can be optimized by tailoring the energetics of the reactive species, their preconcentration, the pH, and the support of implanted surface functional groups [67].

1.3.2. Nanostructured photocatalysts

In principle, the requirements for a material to be a photocatalyst include semiconducting materials that can generate e^-/h^+ pairs upon irradiation. Furthermore, it is necessary for the photocatalyst to possess suitable bandgaps in order to effectively absorb a wide variety of visible light wavelengths from the solar spectrum. An efficient photocatalyst should possess a bandgap within the range of 1.6-2.2 eV and a high sunlight absorption coefficient [69]. The nano-structuration of semiconducting photocatalysts greatly enhances the surface contact for the photocatalytic reactions through a higher fraction of the light absorption, better charge transfer, and fine-tuned electronic structure. Additionally, both the enhanced specific surface area and quantum size (*Q-size*) play a very important role in improving the photocatalytic and photophysical capabilities of these nanostructured materials compared to bulk materials.

In nanosized semiconductors, quantum size effects are involved due to limited electron movement when the particle size of photocatalysts is less than a critical size limit (Bohr radius of exciton). Owing to the direct effect of quantum size, the semiconductor photocatalyst's C_B and V_B can become discretized into energy levels defined by the size of the nanoparticle. The redox potential of the V_B or the C_B undergoes a shift in a more positive or negative direction due to discretization. This process leads to an increase in the redox potential of the generated electrons and holes. Consequently, nanostructured photocatalysts exhibit increased reactivity towards oxidation [70]. The specific surface area not only improves the adsorption capacity of nanostructured photocatalysts but also influences the time it takes for the e^-/h^+ pairs to interact with the surface of the semiconducting particles and determines the photocatalytic efficiency of any photocatalyst. When the particle is at the nanoscale, its diameter becomes negligible, allowing for simple movement of e^-/h^+ pairs from the interior to the surface. This greatly enhances the rate of the redox process. Nano-photocatalysts have an increased ability to transfer e^-/h^+ pairs from the interior to the surface, resulting in a reduced probability of e^-/h^+ pair combination. Consequently, nanostructured photocatalysts demonstrate superior photocatalytic activity compared to bulk photocatalysts, leading to increased photocatalytic processes [71].

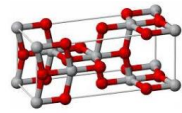
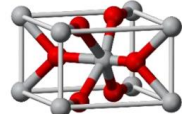
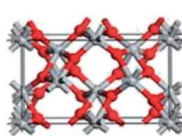
Numerous semiconductors have been used as photocatalysts, including metal oxides and sulfides. However, within this diversity of nanomaterials presented, TiO_2 occupies a place of undisputed relevance. TiO_2 is the most studied photocatalyst for the removal of aqueous pollutants due to its high oxidizing capacity, superhydrophilicity, chemical stability, long lifetime, non-toxicity, and low cost [72]. In recent decades, the fabrication of TiO_2 nanostructures with intentional morphologies and properties to enhance the photocatalytic activity of TiO_2 has been extensively investigated [73].

1.3.3. Titanium dioxide (TiO_2)

TiO_2 is extensively researched because of its remarkable photocatalytic activity and exceptional characteristics. It possesses three polymorphs such as anatase, rutile, and brookite. Both anatase and rutile belong to the same (tetragonal) crystal system involved in the low-

temperature range [74] while brookite can be stabilized at higher temperatures with an orthorhombic crystal structure. The anatase phase can be converted irreversibly to rutile for temperatures above 605°C [75] but the conversion temperature can vary depending on the preparation conditions. As a photocatalyst, the anatase TiO₂ shows excellent photocatalytic and sensitization properties, which have attracted much attention in both photocatalysis and photovoltaic conversion as well. That is why, in this study, we have focused on the study of this phase mainly. The crystal structure of anatase TiO₂ is a tetragonal system, space group I₄₁/amd [76], crystal constant $a=b=3.784 \text{ \AA}$, $c=9.515 \text{ \AA}$. Ti⁴⁺ is located in the center of the TiO₆ octahedron, and each octahedron is connected with eight surrounding octahedrons, among which there are four common edges and four common vertexes. The crystal structure is shown in Table 1.3.

Table 1.3. Properties of rutile, anatase, and brookite of TiO₂ [77].

Phases	Crystal structure	Bandgap (eV)	Space group	Density (g/cm ³)	Refractive Index	Structure Geometry
Anatase	Tetragonal	3.23	I ₄₁ /amd	3.894	2.488	
Rutile	Tetragonal	3.05	P ₄₂ /mnm	4.25	2.609	
Brookite	Orthorhombic	3.26	Pbca	4.12	2.583	

1.3.3.1. Fundamentals and photocatalysis mechanism of TiO₂.

In the field of photocatalysis, TiO₂ has been widely studied for the degradation of contaminants. As its bandgap is about 3.2 eV [78], it can adsorb only about 5% of the UV radiation included in the solar spectrum. Thus, its photoactivity is induced only by the UV illumination, promoting electrons from the V_B to the C_B (Fig. 1.10). In order to achieve efficient absorption of solar radiation and extend light absorption into the visible region for visible-light-driven photocatalysis, it is necessary for the bandgap to be less than 3 eV. In addition to the maximum bandgap requirement, the minimum bandgap of semiconductor photocatalysts for water splitting should be 1.23 eV which is the energy required for photocatalytic water splitting. Thus, effective photocatalysts have been shown to exhibit bandgaps greater than 2 eV [79].

Given the importance and progress of photocatalysis, numerous strategies have been reported to reduce the bandgap and improve its photocatalytic activity under visible light, including the formation of TiO₂-based hybrid nanostructures with less energetic bandgap semiconductors [80]. In particular, several TiO₂-based photocatalysts include two-dimensional

materials such as graphene and its derivatives GO, and rGO. This association leads to the improvement of the electrical conductivity and increase of the electrocatalytic active sites, stability, and the synergistic effect of the assembled systems [81]. Much research was devoted to the incorporation of carbon structures into semiconductor materials to increase electron and hole mobility and prevent their recombination. In addition, their large surface area allows the photocatalyst to be distributed throughout large interfaces which facilitates synergetic interactions between the two constituents [82].

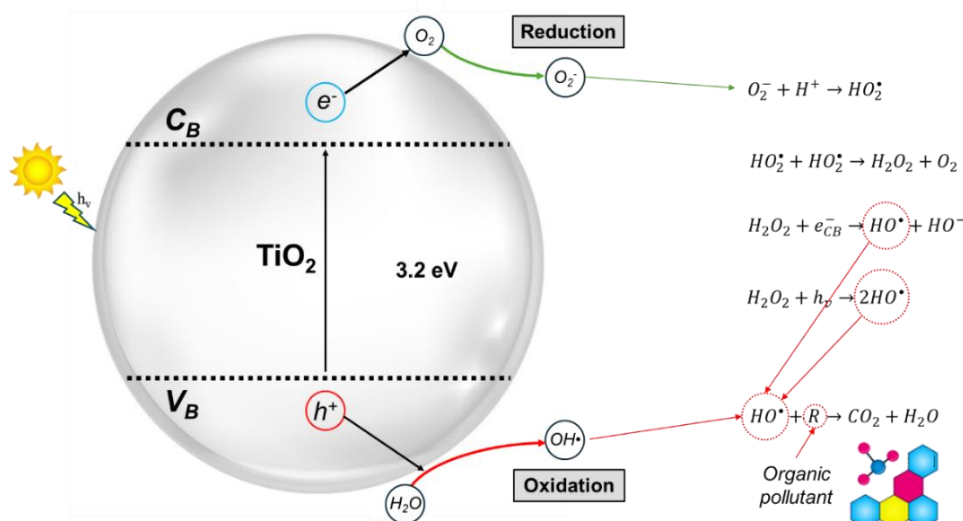


Fig. 1.10. Schematic illustration of typical photocatalysis on TiO₂. (Adapted from [83] with copyright permission).

1.3.4. Heterojunction systems with TiO₂

It is well known that coupling TiO₂ with other semiconductors characterized by different electronic band structures can lead to an increase in photocatalytic efficiency by the enhancement of the charge carrier concentration and the increase in the lifetime of the charge carriers. Moreover, the realization of heterojunction by semiconductors with compatible electronic structures (electronic band alignment) can activate the photoactivity under visible light radiation. Many benefits can be realized in such a design, including (a) improved carrier separation; (b) longer carrier lifetime; and (c) improved interfacial charge transfer efficiency between the hybrid systems [84]. In Fig. 1.11.a, there is a highly effective transfer of electrons between the low bandgap semiconductor (which acts as a sensitizer) and TiO₂. This transfer happens when the conduction band (C_B) of TiO₂ is more positively charged than the equivalent band of the sensitizer. Under visible light radiation, only the sensitizer is excited and the photogenerated electrons are transferred to the TiO₂ C_B. If the V_B of the sensitizer is more negatively charged than the V_B of TiO₂, the hole created in the semiconductor will remain localized and will not be able to migrate to TiO₂. When the system of coupled semiconductors works under UV–Vis radiation, both semiconductors are excited. In the described heterojunction system, there are two sources of electrons in the C_B of TiO₂. Firstly, electrons are injected into TiO₂ from a coupled sensitizer, similar to what happens under visible

excitation. Secondly, the process of photoexcitation under UV irradiation in titania results in the production of electrons, which then accumulate notably in the C_B of TiO_2 . While h^+ in the V_B of TiO_2 can go to the V_B of connected semiconductors and impact a significant accumulation of vacancies at the interface between the semiconductor and electrolyte (Fig. 1.11.b) [85].

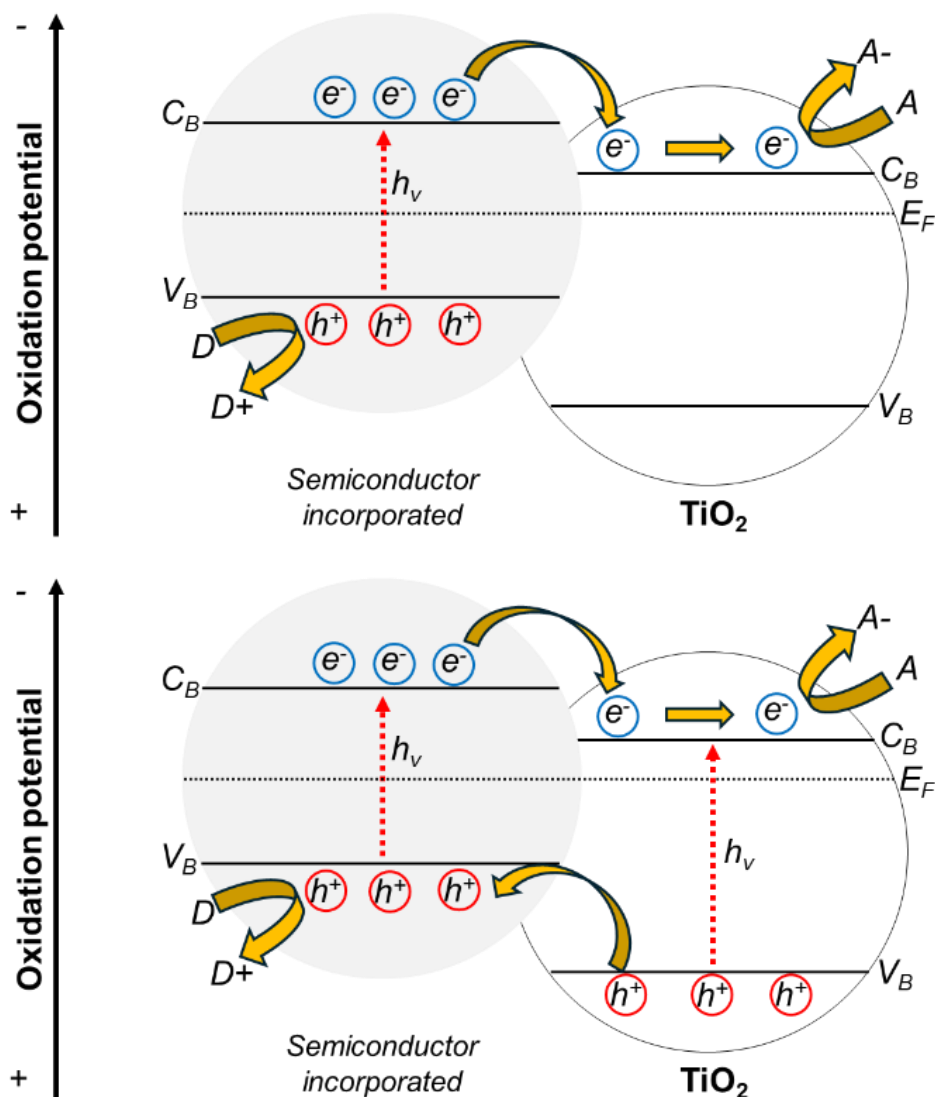


Fig. 1.11. (a) Energy diagram illustrating the coupling of two semiconductors in which vectorial electron transfer occurs from the light-activated semiconductor to the nonactivated TiO_2 ; (b) coupling of semiconductor in which vectorial movement of electrons and holes is possible. (Adapted from [85] with copyright permission).

1.3.5. Hybrid nanostructures based on TiO_2 -graphene

Former reports have pointed out that in heterostructures associating TiO_2 and graphene-based composites, the carbon-based material acts as an acceptor for the photogenerated electrons during the excitation of TiO_2 [86]. Charge carriers can transfer freely through the graphene flakes, enhancing the e^-/h^+ recombination and helping to improve the photocatalytic

performance of TiO₂-graphene systems for water purification [87]. In addition, the negatively charged surface area of the Graphene flakes favors the adsorption rate of pollutants contained in water. The interaction between the *d*-orbital in TiO₂ and the π -orbital in graphene affects the reduction of the bandgap in the hybrid nanostructures, resulting in a substantial increase in the photocatalytic activity in the visible region. The formation of chemical bonds between TiO₂ and graphene (*d*- π interactions) favors the effective transfer of photogenerated electrons from the C_B (*d*-orbital) of TiO₂ to the Fermi level (π -orbital) of the graphene sheet. TiO₂ (e⁻_{CB}) could be freely transported through the graphene matrix acting as an excited electron acceptor and finally transferred to the surface to form the ROS that can effectively oxidize organic pollutants in water [88]. A schematic illustration of the enhanced photocatalytic performance mechanism of TiO₂-graphene nanostructures in dye degradation is shown in Fig. 1.12. [89].

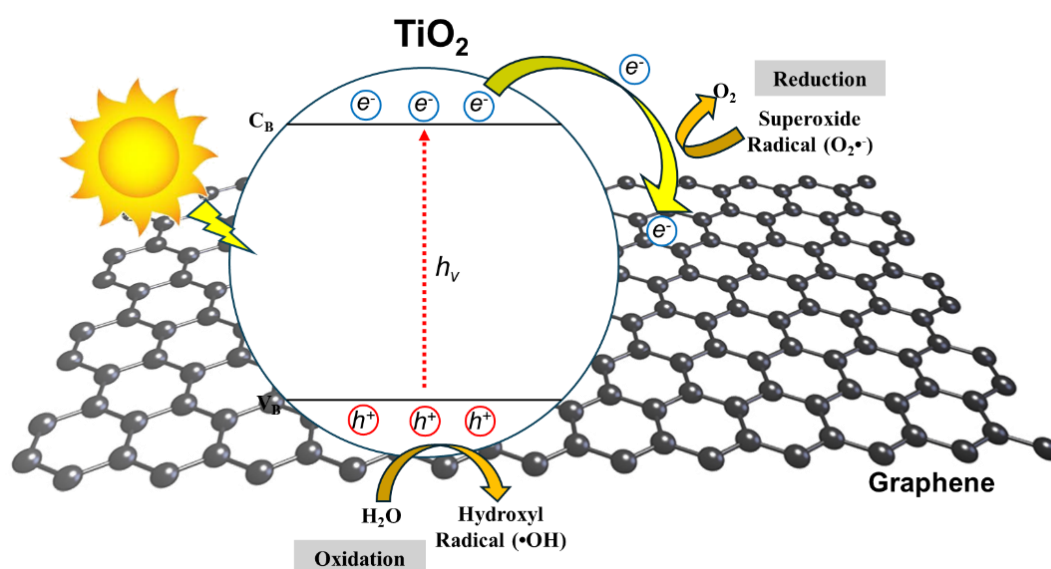
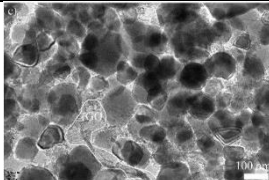
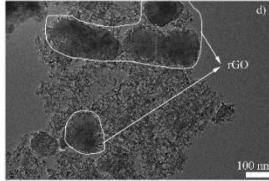
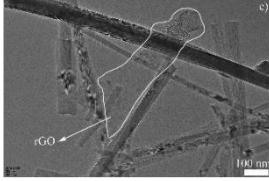
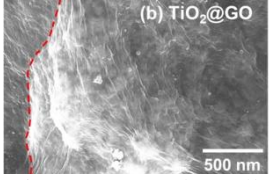
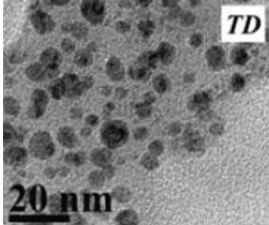
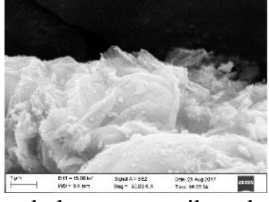
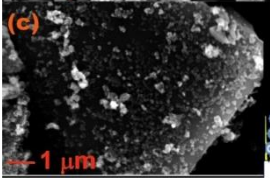
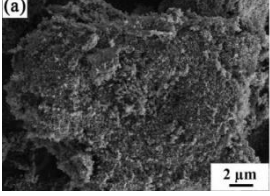
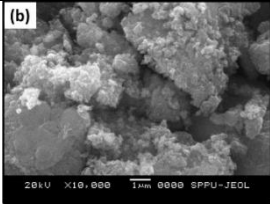
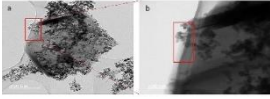
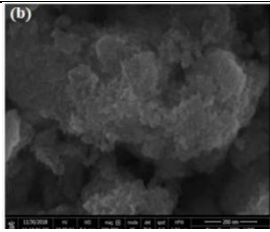
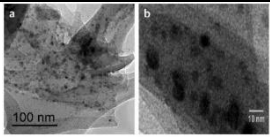
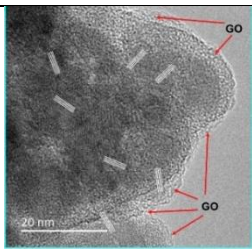


Fig. 1.12. Proposed mechanism for the photodegradation of dyes by TiO₂-graphene compounds under sunlight irradiation (*Adapted from [89] with copyright permission*).

Even though graphene greatly contributes to improving photocatalytic efficiency when incorporated in TiO₂, it is relevant to mention that this material does not react easily [90]. When it is used in nanostructures, it is necessary to modify its structure by adding defects and/or oxygenated groups that allow anchoring with other materials such as GO and/or rGO. Table 1.4. shows a summary of the work in photocatalysis carried out in the last 5 years by using GO-based nanostructures with TiO₂. The aforementioned investigations have shown a remarkable improvement in the photocatalytic properties of TiO₂ when GO is incorporated, also improving the adsorption capacity. It has also been reported that, regardless of the fabrication method, the concentration, or the oxidation degree of the incorporated GO, the hybrid structures are mainly composed of TiO₂ nanoparticles distributed on the GO sheets. The degradation-mechanism in Fig. 1.12. refers to such a structural arrangement. In summary, finding the optimal conditions for fabrication of the ideal material becomes a complex task as it will depend on factors such as (a) bandgap, (b) the proportion of incorporated GO, (c) synthesis methods, and (d) as well as the oxidation degree of the incorporated GO, commonly determined by sp^2/sp^3 ratio by Raman spectroscopy or XPS.

Table 1.4. Investigations of TiO₂ with GO for applications in photocatalysis.

Hybrid system	GO amount	GO oxidation degree	GO Synthesis Method	The synthesis method	Hybrid nanostructure morphology	Main removal mechanisms	Ref.
TiO ₂ - <i>r</i> GO	12 mL of GO aqueous solution into 0.6 g of TiO ₂	—	Modified Hummers'	Hydrothermal synthesis	 <p>TiO₂ nanoparticles are uniformly distributed on the surface of <i>r</i>GO.</p>	Photocatalysis	[91]
TiO ₂ - <i>r</i> GO	12 mL of GO aqueous solution into 0.6 g of TiO ₂	—	Modified Hummers'	Hydrothermal synthesis	 <p>The surface of <i>r</i>GO exhibits a homogeneous distribution of TiO₂ nanotubes.</p>	Photocatalysis	[91]
TiO ₂ - <i>r</i> GO	12 mL of GO aqueous solution into 0.6 g of TiO ₂	—	Modified Hummers'	Hydrothermal synthesis	 <p>TiO₂ nanobelt is uniformly distributed on the surface of <i>r</i>GO.</p>	Photocatalysis	[91]
TiO ₂ -GO	0.1 g	—	Commercial	Suspension in deionized water and stirring	 <p>TiO₂ nanocrystals, well-assembled into the GO nanosheets matrix</p>	Photocatalysis	[92]
TiO ₂ -GO	20 % w/w	—	Hummer's method	Sonochemistry	 <p>Nanoparticles on the surface of the GO laminae clusters</p>	Photocatalysis	[93]
TiO ₂ -GO	15 wt%	I _D /I _G = 1.6	Hummer's method	Hydrogel and electromagnetically stirred	 <p>Formed clusters contributed to the GO monolith-like structure</p>	Photocatalysis	[94]

TiO ₂ -GO	1% wt	—	Hummer method	Hydrothermal synthesis		Photocatalysis [95]
					TiO ₂ nanoparticles tended to accumulate along the wrinkles and edges of GO sheets	
TiO ₂ -GO	25% wt	—	Modified Hummers method	Hydrothermal synthesis		Photocatalysis [96]
					TiO ₂ particles are located on the GO sheets and distributed evenly	
TiO ₂ -GO	2% wt	I _D /I _G =0.86	Modified Hummers method	Hydrothermal synthesis		Photocatalysis [97]
					Agglomeration of TiO ₂ nanoparticles over the GO nanosheets	
TiO ₂ -GO	10% wt	—	Hummers method	Ultrasonication		Photocatalysis [98]
					TiO ₂ agglomerates over the GO sheet	
TiO ₂ -GO	8% wt	—	Hummer & Offeman method	Water bath with continuous stirring		Photocatalysis [99]
					TiO ₂ nanostructure has a uniform distribution over the GO sheets	
TiO ₂ -GO	2.5% wt	—	Commercial	Sonification and stirring		Photocatalysis [100]
					The uniform decoration of highly dense TiO ₂ nanoparticles over GO sheets	
TiO ₂ -GO	2% wt	I _D /I _G =0.86-0.98	Tour method	Ball-milling		Adsorption [101]
					TiO ₂ is surrounded by irregular GO layers, forming a core-shell-type structure	

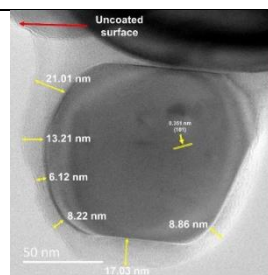
TiO₂-GO

2% wt

I_D/I_G=
0.86-
0.98

Tour method

Photosonic
ation



Adsorption &
photocatalysis

[102]

TiO₂ particle coated by GO,
forming a core-shell type
structure

----: *Not mentioned*

1.4.Conclusion

The state-of-art presented in this chapter highlights the relevance of addressing the global issue of water scarcity and pollution through the development and application of innovative technologies such as photocatalysis and adsorption. Adsorption, a process in which pollutants adhere to the surface of adsorbent materials, and photocatalysis, which involves the breakdown of pollutant molecules under light radiation, are key strategies in water remediation. In this context, nanomaterials offer significant advantages in these processes, thanks to their high surface area, and unique physicochemical properties. Their ability to adsorb pollutants and catalyze chemical reactions with improved efficiency makes them promising tools. Specifically, the characteristics of TiO₂ and its application in photocatalytic processes were pointed out, as well as the strategy of building heterostructures to enhance its photocatalytic activity. The understanding of these fundamentals is crucial to ensure the effectiveness of the fabricated nanostructures in the ability to remove pollutants from water. Finally, the fundamentals of GO structure are highlighted to understand the arrangement and nature of its bonding when modification of its structure is made by incorporating functional groups. This leads to significant alterations in its physicochemical characteristics and properties and reveals the inherent versatility of GO and the engineering capability to manipulate its structure at the molecular level. Understanding how these modifications affect the properties of GO will allow a better interpretation and discussion of the results presented in the following chapters.

References

1. Unesco, UN-Water, World Water Assessment Programme: The United Nations World Water Development Report 2017 : wastewater : the untapped resource. (2017)
2. UNESCO: The United Nations World Water Development Report 2021: Valuing water, (2021)
3. Sharma, C., Negi, Y.S.: Methods of inorganic pollutants detection in water. Inorganic Pollutants in Water. 115–134 (2020). <https://doi.org/10.1016/B978-0-12-818965-8.00007-X>
4. Elgarahy, A.M., Elwakeel, K.Z., Mohammad, S.H., Elshoubaky, G.A.: A critical review of biosorption of dyes, heavy metals and metalloids from wastewater as an efficient and green process. Clean Eng Technol. 4, 100209 (2021). <https://doi.org/10.1016/J.CLET.2021.100209>
5. WHO: A global overview of national regulations and standards for drinking-water quality. Verordnung über die Qualität t von Wasser für den menschlichen Gebrauch (Trinkwasserverordnung -TrinkwV 2001). (2018)
6. Shahul Hameed, K., Muthirulan, P., Meenakshi Sundaram, M.: Adsorption of chromotrope dye onto activated carbons obtained from the seeds of various plants: Equilibrium and kinetics studies. Arabian Journal of Chemistry. 10, S2225–S2233 (2017). <https://doi.org/10.1016/J.ARABJC.2013.07.058>

7. Alvarez, P.J.J., Chan, C.K., Elimelech, M., Halas, N.J., Villagrán, D.: Emerging opportunities for nanotechnology to enhance water security. *Nature Nanotechnology* 2018 13:8. 13, 634–641 (2018). <https://doi.org/10.1038/s41565-018-0203-2>
8. Abdul Khalil, H.P.S., Dungani, R., Hossain, M.S., Suraya, N.L.M., Aprilia, S., Astimar, A.A., Nahrul Hayawin, Z., Davoudpour, Y.: Mechanical properties of oil palm biocomposites enhanced with micro to nanobiofillers. *Biocomposites: Design and Mechanical Performance*. 401–435 (2015). <https://doi.org/10.1016/B978-1-78242-373-7.00026-3>
9. Zhao, W., Chen, I.W., Huang, F.: Toward large-scale water treatment using nanomaterials. *Nano Today*. 27, 11–27 (2019). <https://doi.org/10.1016/J.NANTOD.2019.05.003>
10. Zhang, W., Zhang, D., Liang, Y.: Nanotechnology in remediation of water contaminated by poly- and perfluoroalkyl substances: A review *. (2019). <https://doi.org/10.1016/j.envpol.2019.01.045>
11. Yang, K., Xing, B.: Adsorption of organic compounds by carbon nanomaterials in aqueous phase: Polanyi theory and its application. *Chem Rev.* 110, 5989–6008 (2010). <https://doi.org/10.1021/cr100059s>
12. Drisya, K.T., Edely, M., Solís-López, M., Jantrania, A., Auguste, S., Rousseau, A., Casteneda, H., Velumani, S., Kassiba, A.: Structural features and morphology of titanium dioxide–bismuth vanadate heterojunctions. *CrystEngComm*. 23, 7679–7690 (2021). <https://doi.org/10.1039/D1CE00982F>
13. Fernandes, A.N., Almeida, C.A.P., Menezes, C.T.B., Debacher, N.A., Sierra, M.M.D.: Removal of methylene blue from aqueous solution by peat. *J Hazard Mater.* 144, 412–419 (2007). <https://doi.org/10.1016/J.JHAZMAT.2006.10.053>
14. Rouquerol, J., Rouquerol, F., Llewellyn, P., Maurin, G., Sing, K.S.W.: Adsorption by Powders and Porous Solids: Principles, Methodology and Applications: Second Edition. *Adsorption by Powders and Porous Solids: Principles, Methodology and Applications: Second Edition*. 1–626 (2013). <https://doi.org/10.1016/C2010-0-66232-8>
15. Yagub, M.T., Sen, T.K., Afroze, S., Ang, H.M.: Dye and its removal from aqueous solution by adsorption: A review. *Adv Colloid Interface Sci.* 209, 172–184 (2014). <https://doi.org/10.1016/J.CIS.2014.04.002>
16. Dąbrowski, A.: Adsorption — from theory to practice. *Adv Colloid Interface Sci.* 93, 135–224 (2001). [https://doi.org/10.1016/S0001-8686\(00\)00082-8](https://doi.org/10.1016/S0001-8686(00)00082-8)
17. Kecili, R., Hussain, C.M.: Mechanism of Adsorption on Nanomaterials. *Nanomaterials in Chromatography: Current Trends in Chromatographic Research Technology and Techniques*. 89–115 (2018). <https://doi.org/10.1016/B978-0-12-812792-6.00004-2>
18. Pacheco, S., Medina, M., Valencia, F., Tapia, J.: Removal of Inorganic Mercury from Polluted Water Using Structured Nanoparticles. *Journal of Environmental Engineering*. 132, 342–349 (2006). [https://doi.org/10.1061/\(ASCE\)0733-9372\(2006\)132:3\(342\)](https://doi.org/10.1061/(ASCE)0733-9372(2006)132:3(342))
19. Yang, K., Xing, B.: Desorption of polycyclic aromatic hydrocarbons from carbon nanomaterials in water. *Environmental Pollution*. 145, 529–537 (2007). <https://doi.org/10.1016/J.ENVPOL.2006.04.020>
20. Hua, M., Zhang, S., Pan, B., Zhang, W., Lv, L., Zhang, Q.: Heavy metal removal from water/wastewater by nanosized metal oxides: A review. *J Hazard Mater.* 211–212, 317–331 (2012). <https://doi.org/10.1016/j.jhazmat.2011.10.016>
21. Monsef Khoshhesab, Z., Gonbadi, K., Rezaei Behbehani, G.: Removal of reactive black 8 dye from aqueous solutions using zinc oxide nanoparticles: investigation of adsorption parameters. *Desalination Water Treat.* 56, 1558–1565 (2015). <https://doi.org/10.1080/19443994.2014.967304>
22. Jeong, B., Kim, D.H., Park, E.J., Jeong, M.G., Kim, K.D., Seo, H.O., Kim, Y.D., Uhm, S.: ZnO shell on mesoporous silica by atomic layer deposition: Removal of organic dye in water by an adsorbent and its photocatalytic regeneration. *Appl Surf Sci.* 307, 468–474 (2014). <https://doi.org/10.1016/J.APSUSC.2014.04.060>
23. Singh, S., Barick, K.C., Bahadur, D.: Functional oxide nanomaterials and nanocomposites for the removal of heavy metals and dyes. *Nanomaterials and Nanotechnology*. 3, (2013). <https://doi.org/10.5772/57237>
24. Khataee, A.R., Pons, M.N., Zahraa, O.: Photocatalytic degradation of three azo dyes using immobilized TiO₂ nanoparticles on glass plates activated by UV light irradiation: Influence of dye molecular structure. *J Hazard Mater.* 168, 451–457 (2009). <https://doi.org/10.1016/J.JHAZMAT.2009.02.052>
25. Faiz Muaz, M., Zamri, A., Bahru, R., Suja' C, F., Shamsuddin, A.H., Kumar Pramanik, S., Md, I., Fattah, R.: Treatment strategies for enhancing the removal of endocrine-disrupting chemicals in water and wastewater systems. *Journal of Water Process Engineering*. 41, 2214–7144 (2021). <https://doi.org/10.1016/j.jwpe.2021.102017>
26. Kurwadkar, S., Hoang, T. V., Malwade, K., Kanel, S.R., Harper, W.F., Struckhoff, G.: Application of carbon nanotubes for removal of emerging contaminants of concern in engineered water and wastewater treatment systems. *Nanotechnology for Environmental Engineering*. 4, 1–16 (2019). <https://doi.org/10.1007/s41204-019-0059-1>
27. Arora, B., Attri, P.: Carbon Nanotubes (CNTs): A Potential Nanomaterial for Water Purification. *Journal of Composites Science* 2020, Vol. 4, Page 135. 4, 135 (2020). <https://doi.org/10.3390/JCS4030135>

28. Delgado, N., Capparelli, A., Navarro, A., Marino, D.: Pharmaceutical emerging pollutants removal from water using powdered activated carbon: Study of kinetics and adsorption equilibrium. (2019). <https://doi.org/10.1016/j.jenvman.2019.01.116>
29. Tang, Z., Peng, S., Hu, S., Hong, S.: Enhanced removal of bisphenol-AF by activated carbon-alginate beads with cetyltrimethyl ammonium bromide. *J Colloid Interface Sci.* 495, 191–199 (2017). <https://doi.org/10.1016/J.JCIS.2017.01.103>
30. Rao, A., Kumar, A., Dhodapkar, R., Pal, S., Cadaval, T.R.: Adsorption of five emerging contaminants on activated carbon from aqueous medium: kinetic characteristics and computational modeling for plausible mechanism. (2014). <https://doi.org/10.1007/s11356-020-12014-1>
31. Saleh, T.A., Sari, A., Tuzen, M.: Optimization of parameters with experimental design for the adsorption of mercury using polyethylenimine modified-activated carbon. *J Environ Chem Eng.* 5, 1079–1088 (2017). <https://doi.org/10.1016/J.JECE.2017.01.032>
32. Lu, C., Chiu, H.: Adsorption of zinc(II) from water with purified carbon nanotubes. *Chem Eng Sci.* 61, 1138–1145 (2006). <https://doi.org/10.1016/J.CES.2005.08.007>
33. Sadegh, H., Shahryari-Ghoshekandi, R., Agarwal, S., Tyagi, I., Asif, M., Kumar Gupta, V.: Microwave-assisted removal of malachite green by carboxylate functionalized multi-walled carbon nanotubes: Kinetics and equilibrium study. (2015). <https://doi.org/10.1016/j.molliq.2015.02.007>
34. Yan, L., Chang, P.R., Zheng, P., Ma, X.: Characterization of magnetic guar gum-grafted carbon nanotubes and the adsorption of the dyes. *Carbohydr Polym.* 87, 1919–1924 (2012). <https://doi.org/10.1016/J.CARBPOL.2011.09.086>
35. Zhang, Z., Chen, X., Rao, W., Chen, H., Cai, R.: Synthesis and properties of magnetic molecularly imprinted polymers based on multiwalled carbon nanotubes for magnetic extraction of bisphenol A from water. *Journal of Chromatography B.* 965, 190–196 (2014). <https://doi.org/10.1016/J.JCHROMB.2014.06.031>
36. Ali, I., Basheer, A.A., Mbianda, X.Y., Burakov, A., Galunin, E., Burakova, I., Mkrtchyan, E., Tkachev, A., Grachev, V.: Graphene based adsorbents for remediation of noxious pollutants from wastewater. *Environ Int.* 127, 160–180 (2019). <https://doi.org/10.1016/J.ENVINT.2019.03.029>
37. Verma, S., Kim, K.H.: Graphene-based materials for the adsorptive removal of uranium in aqueous solutions. *Environ Int.* 158, 106944 (2022). <https://doi.org/10.1016/J.ENVINT.2021.106944>
38. Singh, S., Naik, T.S.S.K., Shehata, N., Aguilar-Marcelino, L., Dhokne, K., Lonare, S., Chauhan, V., Kumar, A., Singh, J., Ramamurthy, P.C., Khan, A.H., Khan, N.A., Dehghani, M.H.: Novel insights into graphene oxide-based adsorbents for remediation of hazardous pollutants from aqueous solutions: A comprehensive review. *J Mol Liq.* 369, 120821 (2023). <https://doi.org/10.1016/J.MOLLIQ.2022.120821>
39. Lin, S., Tang, J., Zhang, K., Chen, Y., Gao, R., Yin, H., Qin, L.C.: Tuning oxygen-containing functional groups of graphene for supercapacitors with high stability. *Nanoscale Adv.* 5, (2023). <https://doi.org/10.1039/d2na00506a>
40. Yan, H., Tao, X., Yang, Z., Li, K., Yang, H., Li, A., Cheng, R.: Effects of the oxidation degree of graphene oxide on the adsorption of methylene blue. *J Hazard Mater.* 268, 191–198 (2014). <https://doi.org/10.1016/J.JHAZMAT.2014.01.015>
41. Reynosa-Martínez, A.C., Tovar, G.N., Gallegos, W.R., Rodríguez-Meléndez, H., Torres-Cadena, R., Mondragón-Solórzano, G., Barroso-Flores, J., Alvarez-Lemus, M.A., Montalvo, V.G., López-Honorato, E.: Effect of the degree of oxidation of graphene oxide on As(III) adsorption. *J Hazard Mater.* 384, 121440 (2020). <https://doi.org/10.1016/J.JHAZMAT.2019.121440>
42. Zhen, Z., Zhu, H.: Structure and Properties of Graphene. *Graphene: Fabrication, Characterizations, Properties and Applications.* 1–12 (2018). <https://doi.org/10.1016/B978-0-12-812651-6.00001-X>
43. Kim, K.S., Zhao, Y., Jang, H., Lee, S.Y., Kim, J.M., Kim, K.S., Ahn, J.H., Kim, P., Choi, J.Y., Hong, B.H.: Large-scale pattern growth of graphene films for stretchable transparent electrodes. *Nature* 2009 457:7230. 457, 706–710 (2009). <https://doi.org/10.1038/nature07719>
44. Bolotin, K.I., Sikes, K.J., Jiang, Z., Klima, M., Fudenberg, G., Hone, J., Kim, P., Stormer, H.L.: Ultrahigh electron mobility in suspended graphene. *Solid State Commun.* 146, 351–355 (2008). <https://doi.org/10.1016/J.SSC.2008.02.024>
45. Son, Y.W., Cohen, M.L., Louie, S.G.: Half-metallic graphene nanoribbons. *Nature* 2006 444:7117. 444, 347–349 (2006). <https://doi.org/10.1038/nature05180>
46. Novoselov, K.S., Geim, A.K., Morozov, S. V., Jiang, D., Katsnelson, M.I., Grigorieva, I. V., Dubonos, S. V., Firsov, A.A.: Two-dimensional gas of massless Dirac fermions in graphene. *Nature* 2005 438:7065. 438, 197–200 (2005). <https://doi.org/10.1038/nature04233>
47. Avouris, P., Chen, Z., Perebeinos, V.: Carbon-based electronics. *Nature Nanotechnology* 2007 2:10. 2, 605–615 (2007). <https://doi.org/10.1038/nnano.2007.300>
48. Elias, D.C., Nair, R.R., Mohiuddin, T.M.G., Morozov, S. V., Blake, P., Halsall, M.P., Ferrari, A.C., Boukhvalov, D.W., Katsnelson, M.I., Geim, A.K., Novoselov, K.S.: Control of graphene's properties by

- reversible hydrogenation: Evidence for graphane. *Science* (1979). 323, 610–613 (2009). <https://doi.org/10.1126/SCIENCE.1167130>
49. Oostinga, J.B., Heersche, H.B., Liu, X., Morpurgo, A.F., Vandersypen, L.M.K.: Gate-induced insulating state in bilayer graphene devices. *Nature Materials* 2007 7:2. 7, 151–157 (2007). <https://doi.org/10.1038/nmat2082>
 50. Cano, F.J., Romero-Núñez, A., Liu, H., Reyes-Vallejo, O., Ashok, A., Velumani, S., Kassiba, A.: Variation in the bandgap by gradual reduction of GOs with different oxidation degrees: A DFT analysis. *Diam Relat Mater.* 139, (2023). <https://doi.org/10.1016/j.diamond.2023.110382>
 51. Park, S., Ruoff, R.S.: Chemical methods for the production of graphenes. *Nature Nanotechnology* 2009 4:4. 4, 217–224 (2009). <https://doi.org/10.1038/nnano.2009.58>
 52. Tang, L., Li, X., Ji, R., Teng, K.S., Tai, G., Ye, J., Wei, C., Lau, S.P.: Bottom-up synthesis of large-scale graphene oxide nanosheets. *J Mater Chem.* 22, 5676–5683 (2012). <https://doi.org/10.1039/C2JM15944A>
 53. Liu, Y., Chen, Y.: Synthesis of large scale graphene oxide using plasma enhanced chemical vapor deposition method and its application in humidity sensing. *J Appl Phys.* 119, 103301 (2016). <https://doi.org/10.1063/1.4942999/140978>
 54. Bianco, A., Cheng, H.M., Enoki, T., Gogotsi, Y., Hurt, R.H., Koratkar, N., Kyotani, T., Monthieux, M., Park, C.R., Tascon, J.M.D., Zhang, J.: All in the graphene family – A recommended nomenclature for two-dimensional carbon materials. *Carbon N Y.* 65, 1–6 (2013). <https://doi.org/10.1016/J.CARBON.2013.08.038>
 55. Jeong, H.K., Yang, C., Kim, B.S., Kim, K.J.: Valence band of graphite oxide. *Europhys Lett.* 92, 37005 (2010). <https://doi.org/10.1209/0295-5075/92/37005>
 56. Krishnamoorthy, K., Veerapandian, M., Yun, K., Kim, S.J.: The chemical and structural analysis of graphene oxide with different degrees of oxidation. *Carbon N Y.* 53, 38–49 (2013). <https://doi.org/10.1016/J.CARBON.2012.10.013>
 57. Shukla, S., Saxena, S.: Spectroscopic investigation of confinement effects on optical properties of graphene oxide. *Appl Phys Lett.* 98, (2011). <https://doi.org/10.1063/1.3555438/935829>
 58. Veerapandian, M., Lee, M.H., Krishnamoorthy, K., Yun, K.: Synthesis, characterization and electrochemical properties of functionalized graphene oxide. *Carbon N Y.* 50, 4228–4238 (2012). <https://doi.org/10.1016/J.CARBON.2012.05.004>
 59. Li, J., Martin, I., Büttiker, M., -, al: Graphene prehistory. *Phys Scr.* 2012, 014003 (2012). <https://doi.org/10.1088/0031-8949/2012/T146/014003>
 60. Gao, W.: The chemistry of graphene oxide. *Graphene Oxide: Reduction Recipes, Spectroscopy, and Applications.* 61–95 (2015). https://doi.org/10.1007/978-3-319-15500-5_3
 61. Marcano, D.C., Kosynkin, D. V., Berlin, J.M., Sinitskii, A., Sun, Z., Slesarev, A., Alemany, L.B., Lu, W., Tour, J.M.: Improved synthesis of graphene oxide. *ACS Nano.* 4, 4806–4814 (2010). <https://doi.org/10.1021/NN1006368/>
 62. Palit, S., Hussain, C.M.: Advanced oxidation processes as nonconventional environmental engineering techniques for water treatment and groundwater remediation. *Handbook of Advanced Approaches Towards Pollution Prevention and Control.* 1, 33–44 (2021). <https://doi.org/10.1016/B978-0-12-822121-1.00002-3>
 63. Vallejo, M., Fresnedo San Román, M., Ortiz, I., Irabien, A.: Overview of the PCDD/Fs degradation potential and formation risk in the application of advanced oxidation processes (AOPs) to wastewater treatment. *Chemosphere.* 118, 44–56 (2015). <https://doi.org/10.1016/J.CHEMOSPHERE.2014.05.077>
 64. O'Shea, K.E., Dionysiou, D.D.: Advanced Oxidation Processes for Water Treatment. *Journal of Physical Chemistry Letters.* 3, 2112–2113 (2012). <https://doi.org/10.1021/JZ300929X>
 65. Carneiro, J.O., Teixeira, V., Carvalho, P., Azevedo, S., Manninen, N.: Self-cleaning smart nanocoatings. *Nanocoatings and Ultra-Thin Films.* 397–413 (2011). <https://doi.org/10.1533/9780857094902.2.397>
 66. Song, R., Ren, S., Chi, Y.R.: Carbene- and photocatalysis redefine arene acylation. *Nature Synthesis* 2023. 1–3 (2023). <https://doi.org/10.1038/s44160-023-00400-9>
 67. Schneider, J., Matsuoka, M., Takeuchi, M., Zhang, J., Horiuchi, Y., Anpo, M., Bahnemann, D.W.: Understanding TiO₂ photocatalysis: Mechanisms and materials. *Chem Rev.* 114, 9919–9986 (2014). <https://doi.org/10.1021/cr5001892>
 68. Thongam, D.D., Chaturvedi, H.: Advances in nanomaterials for heterogeneous photocatalysis. *Nano Express.* 2, 012005 (2021). <https://doi.org/10.1088/2632-959X/ABEB8D>
 69. Hassaan, M.A., El-Nemr, M.A., Elkatory, M.R., Ragab, S., Niculescu, V.C., El Nemr, A.: Principles of Photocatalysts and Their Different Applications: A Review. *Topics in Current Chemistry* 2023 381:6. 381, 1–54 (2023). <https://doi.org/10.1007/S41061-023-00444-7>
 70. Hassaan, M.A., Pantaleo, A., Santoro, F., Elkatory, M.R., de Mastro, G., El Sikaily, A., Ragab, S., El Nemr, A.: Techno-Economic Analysis of ZnO Nanoparticles Pretreatments for Biogas Production from Barley Straw. *Energies* 2020, Vol. 13, Page 5001. 13, 5001 (2020). <https://doi.org/10.3390/EN13195001>

71. Kim, D.S., Kwak, S.Y.: The hydrothermal synthesis of mesoporous TiO₂ with high crystallinity, thermal stability, large surface area, and enhanced photocatalytic activity. *Appl Catal A Gen.* 323, 110–118 (2007). <https://doi.org/10.1016/J.APCATA.2007.02.010>
72. Vilas Vilela, L., Ruiz-Rubio, L., Wang, H., Armakovi'carmakovi'c, S.J., Savanovi'csavanovi'c, M.M., Armakovi'c, S.A.: Titanium Dioxide as the Most Used Photocatalyst for Water Purification: An Overview. *Catalysts* 2023, Vol. 13, Page 26. 13, 26 (2022). <https://doi.org/10.3390/CATAL13010026>
73. Anucha, C.B., Altin, I., Bacaksiz, E., Stathopoulos, V.N.: Titanium dioxide (TiO₂)-based photocatalyst materials activity enhancement for contaminants of emerging concern (CECs) degradation: In the light of modification strategies. *Chemical Engineering Journal Advances.* 10, 100262 (2022). <https://doi.org/10.1016/J.CEJA.2022.100262>
74. Guo, Q., Zhou, C., Ma, Z., Yang, X.: Fundamentals of TiO₂ Photocatalysis: Concepts, Mechanisms, and Challenges. *Advanced Materials.* 31, 1901997 (2019). <https://doi.org/10.1002/ADMA.201901997>
75. Brayner, R., Coradin, T., Fiévet, F.: Preface. *Nanomaterials: A Danger or a Promise?: A Chemical and Biological Perspective.* v–vi (2013). <https://doi.org/10.1007/978-1-4471-4213-3>
76. Mo, S. Di, Ching, W.Y.: Electronic and optical properties of three phases of titanium dioxide: Rutile, anatase, and brookite. *Phys Rev B.* 51, 13023 (1995). <https://doi.org/10.1103/PhysRevB.51.13023>
77. Zhang, H., Banfield, J.F.: Structural characteristics and mechanical and thermodynamic properties of nanocrystalline TiO₂. *Chem Rev.* 114, 9613–9644 (2014). <https://doi.org/10.1021/CR500072J>
78. Cano, F.J., Romero-Nunez, A., Jantrania, A., Liu, H., Kassiba, A., Velumani, S.: Bandgap dependence on facet and size engineering of TiO₂: A DFT Study. *CCE 2021 - 2021 18th International Conference on Electrical Engineering, Computing Science and Automatic Control.* (2021). <https://doi.org/10.1109/CCE53527.2021.9632880>
79. Dincer, I., Zamfirescu, C.: Hydrogen Production by Photonic Energy. *Sustainable Hydrogen Production.* 309–391 (2016). <https://doi.org/10.1016/B978-0-12-801563-6.00005-4>
80. Nevárez-Martínez, M.C., Nski, M.P.K., Mazierski, P., Wólkiewicz, J., Trykowski, G., Malankowska, A., Kozak, M., Espinoza-Montero, P.J., Zaleska-Medynska, A.: molecules Self-Organized TiO₂-MnO₂ Nanotube Arrays for Efficient Photocatalytic Degradation of Toluene. (2017). <https://doi.org/10.3390/molecules22040564>
81. Li, X., Yu, J., Wageh, S., Al-Ghamdi, A.A., Xie, J.: Graphene in Photocatalysis: A Review. *Small.* 12, 6640–6696 (2016). <https://doi.org/10.1002/SMLL.201600382>
82. Bie, C., Yu, H., Cheng, B., Ho, W., Fan, J., Yu, J.: Design, Fabrication, and Mechanism of Nitrogen-Doped Graphene-Based Photocatalyst. *Advanced Materials.* 33, 2003521 (2021). <https://doi.org/10.1002/ADMA.202003521>
83. Nasir, A., Khalid, S., Yasin, T., Mazare, A.: A Review on the Progress and Future of TiO₂/Graphene Photocatalysts. *Energies* 2022, Vol. 15, Page 6248. 15, 6248 (2022). <https://doi.org/10.3390/EN15176248>
84. Bessekhoud, Y., Robert, D., Weber, J. V.: Bi₂S₃/TiO₂ and CdS/TiO₂ heterojunctions as an available configuration for photocatalytic degradation of organic pollutant. *J Photochem Photobiol A Chem.* 163, 569–580 (2004). <https://doi.org/10.1016/J.JPHOTOCHEM.2004.02.006>
85. Bessekhoud, Y., Robert, D., Weber, J. V.: Photocatalytic activity of Cu₂O/TiO₂, Bi₂O₃/TiO₂ and ZnMn₂O₄/TiO₂ heterojunctions. *Catal Today.* 101, 315–321 (2005). <https://doi.org/10.1016/J.CATTOD.2005.03.038>
86. Atout, H., Álvarez, M.G., Chebli, D., Bouguettoucha, A., Tichit, D., Llorca, J., Medina, F.: Enhanced photocatalytic degradation of methylene blue: Preparation of TiO₂/reduced graphene oxide nanocomposites by direct sol-gel and hydrothermal methods. *Mater Res Bull.* 95, 578–587 (2017). <https://doi.org/10.1016/j.materresbull.2017.08.029>
87. Nosaka, Y., Nosaka, A.Y.: Generation and Detection of Reactive Oxygen Species in Photocatalysis. (2017). <https://doi.org/10.1021/acs.chemrev.7b00161>
88. Rincón, A.G., Pulgarin, C., Adler, N., Peringer, P.: Interaction between E. coli inactivation and DBP-precursors - dihydroxybenzene isomers - in the photocatalytic process of drinking-water disinfection with TiO₂. *J Photochem Photobiol A Chem.* 139, (2001). [https://doi.org/10.1016/S1010-6030\(01\)00374-4](https://doi.org/10.1016/S1010-6030(01)00374-4)
89. Posa, V.R., Annavaram, V., Koduru, J.R., Bobbala, P., Somala, A.R.: Preparation of graphene-TiO₂ nanocomposite and photocatalytic degradation of Rhodamine-B under solar light irradiation. (2016). <https://doi.org/10.1080/17458080.2016.1144937>
90. Suzuki, S., Yoshimura, M.: Chemical Stability of Graphene Coated Silver Substrates for Surface-Enhanced Raman Scattering OPEN. <https://doi.org/10.1038/s41598-017-14782-2>
91. Li, D., Sun, J., Shen, T., Song, H., Liu, J., Wang, C., Wang, X., Zhao, R.: Influence of morphology and interfacial interaction of TiO₂-Graphene nanocomposites on the visible light photocatalytic performance. *J Solid State Chem.* 286, 121301 (2020). <https://doi.org/10.1016/J.JSSC.2020.121301>

92. Shi, Y., Yu, Z., Li, Z., Zhao, X., Yuan, Y.: In-situ synthesis of TiO₂@GO nanosheets for polymers degradation in a natural environment. *Polymers (Basel)*. 13, (2021). <https://doi.org/10.3390/polym13132158>
93. Ramos, D.K.C., González, M.V., Muñoz, R.A.E., Cruz, J.S., Moure-Flores, F.J. De, Mayén-Hernández, S.A.: Obtaining and Characterization of TiO₂-GO Composites for Photocatalytic Applications. *International Journal of Photoenergy*. 2020, (2020). <https://doi.org/10.1155/2020/3489218>
94. Fu, Z., Zhang, S., Fu, Z.: Preparation of Multicycle GO/TiO₂ Composite Photocatalyst and Study on Degradation of Methylene Blue Synthetic Wastewater. *Applied Sciences* 2019, Vol. 9, Page 3282. 9, 3282 (2019). <https://doi.org/10.3390/APP9163282>
95. Sharma, M., Behl, K., Nigam, S., Joshi, M.: TiO₂-GO nanocomposite for photocatalysis and environmental applications: A green synthesis approach. *Vacuum*. 156, (2018). <https://doi.org/10.1016/j.vacuum.2018.08.009>
96. Wang, R., Shi, K., Huang, D., Zhang, J., An, S.: Synthesis and degradation kinetics of TiO₂/GO composites with highly efficient activity for adsorption and photocatalytic degradation of MB. *Scientific RepoRtS* |. 9, 18744 (2019). <https://doi.org/10.1038/s41598-019-54320-w>
97. Hunge, Y.M., Yadav, A.A., Dhodamani, A.G., Suzuki, N., Terashima, C., Fujishima, A., Mathe, V.L.: Enhanced photocatalytic performance of ultrasound treated GO/TiO₂ composite for photocatalytic degradation of salicylic acid under sunlight illumination. *Ultrason Sonochem*. 61, (2020). <https://doi.org/10.1016/j.ultsonch.2019.104849>
98. Hernández-Majalca, B.C., Meléndez-Zaragoza, M.J., Salinas-Gutiérrez, J.M., López-Ortiz, A., Collins-Martínez, V.: Visible-light photo-assisted synthesis of GO-TiO₂ composites for the photocatalytic hydrogen production. *Int J Hydrogen Energy*. 44, 12381–12389 (2019). <https://doi.org/10.1016/J.IJHYDENE.2018.10.152>
99. Khan, S.A., Arshad, Z., Shahid, S., Arshad, I., Rizwan, K., Sher, M., Fatima, U.: Synthesis of TiO₂/Graphene oxide nanocomposites for their enhanced photocatalytic activity against methylene blue dye and ciprofloxacin. *Compos B Eng*. 175, 107120 (2019). <https://doi.org/10.1016/J.COMPOSITESB.2019.107120>
100. Ch-Th, T., Manisekaran, R., Santoyo-Salazar, J., Schoefs, B., Velumani, S., Castaneda, H., Jantrania, A.: Graphene oxide decorated TiO₂ and BiVO₄ nanocatalysts for enhanced visible-light-driven photocatalytic bacterial inactivation. *J Photochem Photobiol A Chem*. 418, (2021). <https://doi.org/10.1016/j.jphotochem.2021.113374>
101. Cano, F.J., Reyes-Vallejo, O., Ashok, A., Olvera, M.D.L.L., Velumani, S., Kassiba, A.: Mechanisms of dyes adsorption on titanium oxide– graphene oxide nanocomposites. *Ceram Int*. 49, (2023). <https://doi.org/10.1016/j.ceramint.2023.03.249>
102. Cano, F.J., Coste, S., Reyes-Vallejo, O., Makowska-Janusik, M., Velumani, S., De La, M., Olvera, L., Kassiba, A.: Influence of GO oxidation degrees on the organization and physical features of TiO₂-GO-based nanocomposites for water dye removal. *Surfaces and Interfaces*. 46, 104004 (2024). <https://doi.org/10.1016/j.surfin.2024.104004>

Chapter II:

Reagents, Methods, and Instrumentation

In the analysis of nanostructured materials, such as graphene oxides (GO) and TiO₂-GO hybrid nanostructures, advanced characterization techniques play a crucial role in revealing physicochemical and morphological properties which are essential for understanding the material's behavior in water remediation applications through adsorption and photocatalysis phenomena. The combination of X-ray diffraction (XRD) and Raman spectroscopy has provided a comprehensive characterization of the crystal structure and vibrational properties. These techniques have been used to understand how oxygen functionalization affects the structural and chemical properties of GOs concerning their oxidation degree. The use of techniques such as X-ray photoelectron spectroscopy (XPS) and Fourier transform infrared spectroscopy (FTIR) was essential and complementary to inform the evolution of the chemical composition and surface functionalization of GOs concerning their oxidation degree. As for the hybrid nanostructures, these techniques were crucial to elucidate the nature of the bonds formed at the interface between the two structures. The gas adsorption technique using the Brunauer-Emmett-Teller (BET) theory provided detailed information on the specific surface area (SSA) and porosity of the nanostructures which are fundamental aspects for understanding the dye adsorption mechanisms. Scanning electron microscopy (SEM) and transmission electron microscopy (TEM) allowed the surface morphology and topography of the nanostructures studied, facilitating the visualization and analysis of their shapes and dimensions. Electron paramagnetic resonance (EPR) spectroscopy proved to be a powerful technique to study the interaction of paramagnetic species, to confirm the purity of the synthesized GOs, and, in the case of TiO₂-GO nanostructures, to confirm the formation of Ti³⁺ structural defects and draw a mechanism of formation of the hybrid nanostructures. Optical characterization by UV-Vis spectroscopy provided an in-depth understanding of the absorption and emission properties of the materials, while electrical techniques evaluated the conductivity features. This chapter details also the conditions used for the investigations performed by each technique and the used theoretical and simulation procedures for understanding the experimental features before conducting the adsorption-photocatalysis tests.

2.1. Graphene oxide synthesis by Tour method

The reagents used for the synthesis of graphene oxides by the Tour method are listed in Table 2.1.

Table 2.1. Substances used for synthesis by the Tour method

Chemicals/reagents	Supplier
Natural graphite powder	Sigma-Aldrich
Potassium permanganate, ACS reagent, $\geq 99.0\%$	Sigma-Aldrich
Sulfuric acid ACS reagent, 95.0-98.0%	Sigma-Aldrich
Ortho-phosphoric acid, 85%	Sigma-Aldrich
HCl (36.5%-38.0%)	Sigma-Aldrich
Analytical grade H ₂ O ₂ (30 wt.%)	Sigma-Aldrich
Citric acid ACS reagent (99.5%)	Sigma-Aldrich

The synthesis was made by mixing 43.2 mL of concentrated H₂SO₄ (sulfuric acid ACS reagent, 95.0-98.0%) with 4.8 mL concentrated H₃PO₄ (ortho-phosphoric acid, 85%). Then, the mixture of acids is poured into 1 g of Graphite (Gr) powder continuously for 3 hours using a cold bath at 4°C. Afterward, different amounts of KMnO₄ were added to the whole preparation to vary the oxidation degree. After 2 hours, a mixture of 12 mL of analytical grade H₂O₂ (30 wt.%) and 13 mL of HCl (36.5%-38.0%) was added dropwise under stirring for 30 minutes. The reactions were stopped by adding deionized water to the mixture. A solution of citric acid (CA) diluted in water was then added, using 2 g of CA for each gram of KMnO₄ used. This was followed by continuous washing with water until the residual liquid reached a pH of 7. Materials were exfoliated by sonication for 30 minutes. Finally, the collected materials were dried in an oven at 65 °C for 12 hours. The compounds obtained were designated as GO_(0.5), GO₍₁₎, GO₍₃₎, GO₍₆₎ and GO₍₁₀₎, where the subscripts correspond to the weight of KMnO₄ used in the synthesis.

The decision to use different amounts of KMnO₄ in the investigation was a deliberate choice to explore the impact of different oxidant concentrations on the synthesis process. The aim was to study the influence of KMnO₄ on the oxidation degree of the final GO and its properties. By systematically increasing the amount of KMnO₄, the reaction kinetics, the oxidation degree, and possible changes in the physicochemical properties of the synthesized materials were investigated. Although the differences between 6g and 10g may seem subtle, it was intended to cover a wide range to ensure a comprehensive understanding of the parameter space. Overall, this approach helped us to identify the optimal conditions for the synthesis and provided valuable information on the role of KMnO₄ in the oxidation degree.

2.2. Hybrid nanostructures based on TiO₂ and graphene oxide

The synthesized GOs were associated with anatase-phase TiO₂ nanoparticles using two different methods: *ball-milling* and *photosonation*, respectively. The obtained materials were named TG_(0.5), TG₍₁₎, TG₍₃₎, TG₍₆₎, and TG₍₁₀₎, where the subscripts represent the weight (g) of KMnO₄ used in the synthesis of GOs and take into account the GO oxidation degrees. For this research, commercial TiO₂ (*Merck, EMSURE® Reag. Ph Eur.*) was used to isolate the effect

of the GO oxidation degree by minimizing possible variations in TiO_2 properties due to synthesis. This provides a better understanding of how variations in GO specifically affect hybrid nanostructures. In addition, commercial TiO_2 is usually produced under controlled conditions, which contributes to the reproducibility of the results.

2.2.1. Hybrid nanostructures by ball-milling

Hybrid nanostructures were fabricated using a *PM-400 Planetary Ball Mill* equipment available at the laboratory "*Materials for Renewable Energy and Biomedical Applications (MREB)*" belonging to the "Sección de Electronica del Estado Sólido (SEES)" of Cinvestav-Zacatenco unit. The powders were milled using a high-speed ball mill with 10 Silicon Carbide balls of 14 mm diameter at 300 rpm for 8 h. The procedure was repeated for each GO, obtaining TiO_2 -GO hybrid nanostructures with a ratio of 98 wt% TiO_2 and 2 wt% GO. The obtained materials were named $\text{TG}_{(0.5)}$, $\text{TG}_{(1)}$, $\text{TG}_{(3)}$, $\text{TG}_{(6)}$, and $\text{TG}_{(10)}$, where the subscripts represent the weight (g) of KMnO_4 used in GOs synthesis and take into account the GO oxidation degrees. Fig. 2.2. shows a schematic representation of the used synthesis methodology for the nanostructures. The structural, morphological, optical, and electrical properties are discussed in detail in Chapter 5 of this manuscript.

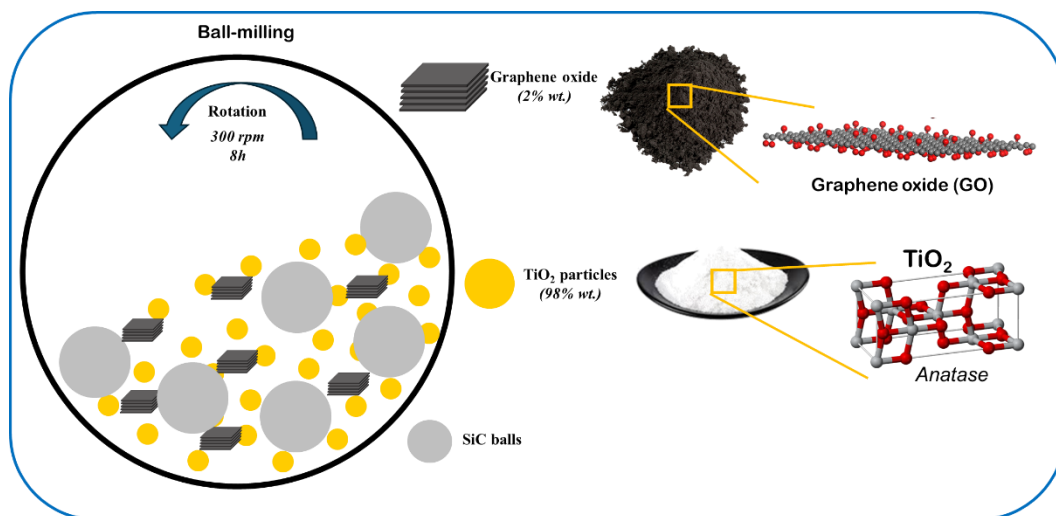


Fig. 2.2. Schematic representation of the ball-milling methodology

2.2.2. Hybrid nanostructures by photosonication

To perform this process, we used an ultrasonic bath of the *Branson Ultrasonics Cpx-952-316r series* available at IMMM of Le Mans Université. The synthesized GO powders and TiO_2 powder were suspended separately in ethanol and an ultrasonic bath (*Branson 2510*) at a frequency of 40 kHz for 20 min was used to obtain a homogeneous suspension. The GO suspension was then poured into the TiO_2 suspension and the ultrasonication extended up to 45 minutes. The resulting solution was stirred continuously for 30 minutes in a photoreaction system under irradiation with a 150 W Xe light source. Light irradiation plays a key role in activating the surfaces of both materials, facilitating the formation of bonds between them,

resulting in increased interaction and synergy between the surfaces involved. This was followed by 24 hours of continuous stirring. Finally, the solution was dried at 80 °C for 18 hours. Similar to ball-milling, the procedure was repeated for each GO oxidation degree, obtaining TiO₂-GO hybrid nanostructures with a ratio of 98 wt% TiO₂ and 2 wt% GO. The obtained materials were also named TG_(0.5), TG₍₁₎, TG₍₃₎, TG₍₆₎, and TG₍₁₀₎, and the characteristics, structural properties, and formation mechanism of the obtained structures are described in detail in chapter 6. Fig. 2.3. shows a schematic representation of the synthesis methodology by photosonication.

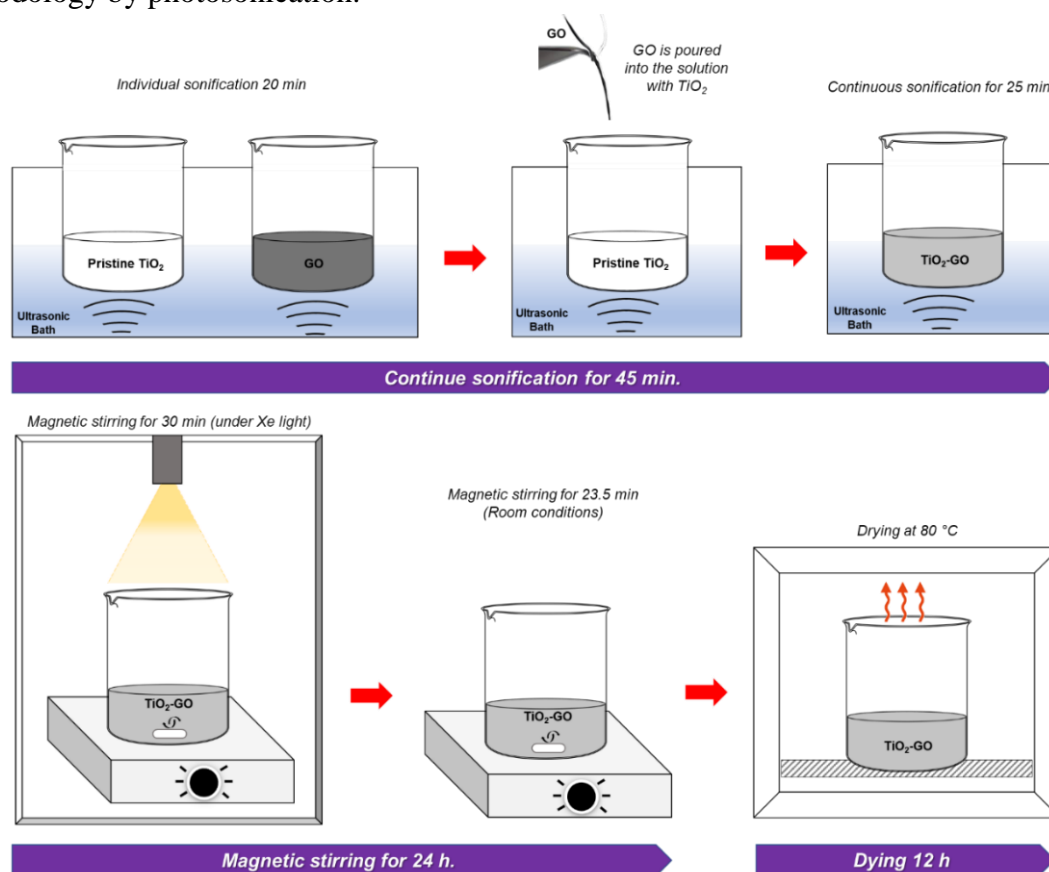


Fig. 2.3. Schematic representation of the synthesis methodology by photosonication

2.3.Characterization techniques

2.3.1. X-ray diffraction (XRD)

XRD is a non-destructive technique that offers comprehensive and precise information regarding the crystal structure, phase composition, and physical characteristics of materials. The hybrid nanostructures prepared by ball-milling (chapter 5) were analyzed using a *Bruker D2 PHASER diffractometer* with Cu-K α radiation ($\lambda=1.54056 \text{ \AA}$) obtained under a voltage of 40 kV and a current of 30 mA, available at CINVESTAV-Zacantenco, Mexico (Fig. S.2.1.a.). The analysis of the nanostructures prepared by photosonication was conducted using a Bragg-Brentano PANalytical Empyrean diffractometer. The diffractometer was equipped with a PIXcel-1D detector and utilized Cu-K α_1 radiation ($\lambda=1.540562 \text{ \AA}$). The radiation was obtained under a voltage of 40 kV and a current of 30 mA (Fig. S.2.1.b.). The instrument was available

at the IMMM of Le Mans Université, France. XRD analysis of GO powders was performed in the range of 5-60° to identify the evolution of the (001) plane during the transition from graphite to GO and the changes with the subsequent increase in the oxidation degree. Subsequently, the analysis of the phases involved in the TiO₂-GO hybrid nanostructure powders was carried out in the range of 5-70°. For this purpose, the peaks in the diffractograms were identified using *Xpert High Score* software. The width and shape of the diffraction peaks are a consequence of the combination of instrumental broadening and factors based on the microstructure of the samples [1]. From the obtained diffractograms, the size of the crystalline domains of carbon materials along the *c*-axis of GO bulk (the average height of the stacked layers) was calculated using the Debye-Scherrer equation [2].

$$L_c = \frac{A \lambda}{\beta \cos \theta} \quad (\text{eq. 1})$$

Where L_c is the average height of the ordered GO domains, λ is the X-ray wavelength, and θ is the Bragg angle at the reflection (001). The Scherrer constant, denoted as A , is highly influenced by the morphology of the crystallite, the index (hkl) of the selected lattice plane, and the definition of β . A is taken as a constant number of 0.9 and β represents the full-width of the reflection at half of its highest intensity, measured in radians. The Scherrer equation, with a Warren constant of 1.84 [3], was used to estimate the average diameter of the stacking layers, indicated as D , for the two-dimensional reflection (100). To evaluate the evolution of the degree of exfoliation of the GO sheets, the Bragg equation [4] was applied to the reflection (001) with the inter-reticular distance d .

$$n\lambda = 2d \sin\theta \quad (\text{eq. 2})$$

The crystallite size (L_c) in the TiO₂-GO hybrid nanostructures was also determined using the Debye-Scherrer (eq. 1) and a constant value of $A=0.9$. Additionally, the deformation (ε) and the dislocation density (δ) were calculated using the following equations 3 and 4 [5].

$$\delta = \frac{1}{D^2} \quad (\text{eq. 3})$$

$$\varepsilon = \frac{\beta}{4 \text{tg}\theta} \quad (\text{eq. 4})$$

These parameters collectively elucidate the degree of structural integration, the presence of defects, and the overall homogeneity of the TiO₂-GO hybrid system, providing a comprehensive picture of its microstructural characteristics.

2.3.2. Raman spectroscopy

Raman spectroscopy is a highly effective technique for analyzing the structure, bonding, and degree of disorder in carbon-based materials, as well as any modifications that may have

occurred [6]. The technique gives a detailed evaluation of molecular vibrations and structural properties by highlighting the characteristic vibrational modes in graphitic compounds generally referred to as D and G Raman bands. Their characteristics such as position, shape, and intensity inform the hybridization modes sp^2 and sp^3 as well as the presence of impurities, crystalline disorder, and deformations, among others. The D-mode has A_{1g} symmetry and can be described as an in-plane breathing vibration of the six-membered aromatic carbon rings (Fig. 2.4.). The Raman-forbidden band in perfect graphite becomes active in the presence of any deviation from an ideal structure. Thus, this characteristic might be regarded as a band caused by a disease (where "D" represents "disorder"). The G-mode (E_{2g} symmetry) is due to the in-plane stretching vibration of carbon atom pairs (Fig. 2.4.). This mode is always allowed and can be observed in the Raman spectrum for all carbon structures containing the sp^2 network, and it is characteristic not only of the aromatic rings of carbon but also of other sp^2 structures [6, 7].

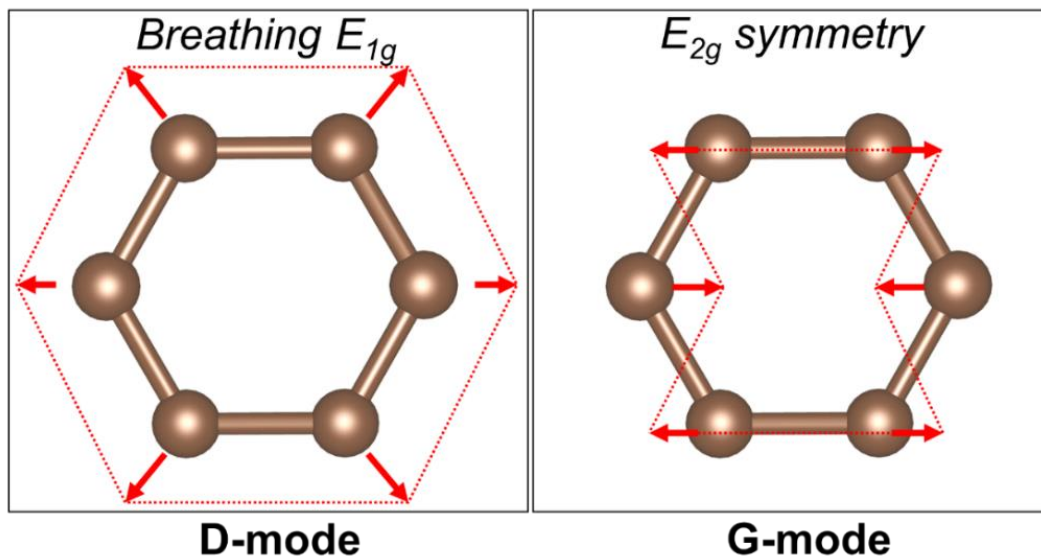


Fig. 2.4. Movements of carbon atoms in the vibrational modes of D and G.

The intensity ratio of D (I_D) and G (I_G) Raman bands has been extensively used for the quantification of defects in carbon-based materials since the pioneering work of Tuinstra and Koenig was published in 1970 [8]. Also, the I_D/I_G ratio is a key indicator of the degree of structural disorder and its evolution with the oxidation degrees. Although the I_D/I_G ratio is most commonly used in the literature to evaluate the crystalline order and defect effects in GO, the A_D/A_G ratio was also utilized to determine the combined intensity of the D and G-bands, which represents quantitatively the whole scattering process. Since the I_D/I_G ratio depends on the excitation wavelength, the excitation laser energy was taken into account when calculating the in-plane crystallite size. The crystallite size (L_a) by Raman spectroscopy was estimated using the following equation (eq. 5) [8], with λ_l representing the wavelength of the laser source (nm).

$$L_a = (2.4 \times 10^{-10}) \lambda_l^4 \left(\frac{I_D}{I_G} \right)^{-1} \quad (\text{eq. 5})$$

On the other hand, Raman spectroscopy was used on pristine TiO₂ and TiO₂-GO hybrid nanostructures to obtain information on crystal lattice vibrations that allowed the identification and confirmation of the crystalline phases shown by XRD, as well as the structural changes induced in both TiO₂ and GO as a consequence of mechanical milling and photosonication, respectively. The measurements were carried out on powders at room temperature and did not require any specific sample preparation. The *X'Plora* equipment available at the IMMM of Le Mans Université (Fig. S.2.1.c.) was used. It is a compact multi-wavelength Raman spectrometer from Horiba Jobin-Yvon, consisting of a confocal microscope (100x), a motorized table (XY), a 1650 x 200-pixel air-cooled CCD detector and 4 gratings 600-1200-1800-2400 lines/mm. The objective of the microscope used was 100x and a krypton-argon laser with a wavelength of $\lambda=532$ nm as an excitation. Spectral line fits were performed with Lorentzian functions using the *OriginLab* software. The comprehensive analysis of Raman spectroscopy on GOs is discussed in detail in chapter 4, while hybrid TiO₂-GO nanostructures are explored in chapters 5 and 6, respectively.

2.3.3. Fourier transform infrared spectroscopy (FTIR-ART)

Fourier transform infrared spectroscopy (FTIR) is an analytical technique that quantifies the absorption of infrared radiation at specific vibrational frequencies of the molecules present in the sample. This technique operates by transmitting infrared radiation (IR) through a sample, and the resulting spectrum indicates the absorption and transmission of molecules, thereby generating a distinct chemical fingerprint [9]. The FT-IR spectra of the samples were measured in the mid-infrared range (400-4000 cm⁻¹) using a Vertex 70v infrared spectrometer available at the IMMM of Le Mans Université (Fig. S.2.1.d.). Samples as powders were investigated by using the ATR technique and without any special preparation.

In the GO materials, it was an effective technique for identifying molecular species as well as functional groups present at each oxidation degree (chapter 4). These IR investigations allow complementary structural characterization to those obtained by Raman spectroscopy. In the hybridized nanostructures, FTIR was used as our main tool to elucidate the chemical nature of the bonds at the interfaces between the two structures (chapters 5 and 6, respectively). To validate and fully elucidate the atomic interaction, Lorentzian deconvolution analysis of the spectra was performed using *OriginLab* software.

2.3.4. X-ray photoelectron spectroscopy (XPS)

X-ray photoelectron spectroscopy (XPS) is a precise and surface-sensitive spectroscopic method used to determine the elemental composition, chemical state, and electronic state of elements in a material. In our research, XPS was used on the GO materials to provide complementary information to FTIR on the nature of the chemical bonds, the presence of different functional groups as well as the effects of the oxidation degrees. For the experiments, GO powders were examined using a PHI Versa Probe II spectrometer. The analysis was conducted with monochromatic *AlK_α* radiation at an energy of 1486.6 eV, with a 2×10^{-8} mTorr

vacuum chamber, aluminum anode as the monochromatic X-ray source. The explored energy range was 290 to 282 eV and the integrated intensity of the XPS lines was calculated by using a deconvolution by Lorentzian forms to quantify the sp^2 and sp^3 states of the GOs.

2.3.5. Brunauer-Emmett-Teller (BET)

The BET (Brunauer-Emmett-Teller) technique is a method used to measure the specific surface area (unit: $m^2.g^{-1}$) of solid materials, especially for porous materials such as catalysts, adsorbents, and nanopowders. The process relies on the physical adsorption of gas molecules onto the surface of the substance. The specific surface area (SSA) of TiO_2 -GO nanostructures prepared by ball milling was measured by nitrogen adsorption at 15 points after the powder was degassed in nitrogen at $150^\circ C$ for 12 h (Fig. 2.5.). The instrument used was a *Brunauer-Emmett-Teller (BET) micromeritometer, Gemini 3240*, available at the Chemistry Department of Cinvestav-Zacatenco.

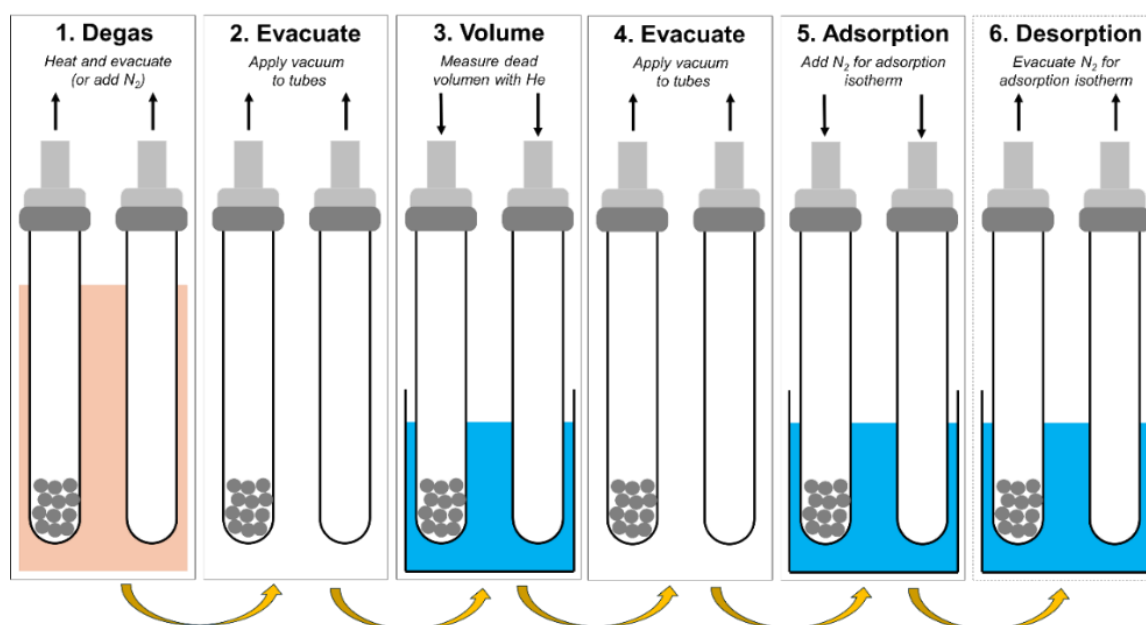


Fig. 2.5. Illustration of measuring surface area with BET

2.3.6. Scanning electron microscopy (SEM)

Scanning Electron Microscopy (SEM) is a technique used to visually examine and study solid-state materials at extremely small scales, specifically in the micro- to nanometer range. It uses accelerated electrons to produce high-resolution images of the sample surface, providing detailed information about its topography, morphology, and composition. The evaluation of the different morphological characteristics of the hybrid nanostructures prepared by ball milling, such as shape, diameter, and length, was performed employing a Hitachi S5500 FESEM, a field emission scanning electron microscope, with an acceleration voltage of 5 kV, equipped with a Bruker Quantax EDAX analyzer, available at the *Universidad Autónoma de Morelos*, Mexico. The detailed results are discussed in Chapter 5. While, a *JEOL scanning electron microscope, JSM 6510*, with an acceleration voltage of 20 kV, available at IMMM,

Le Mans Université, was used for the characterization of GOs. The acceleration voltage and the variable slit size were adjusted to ensure proper focusing of the samples, with manual correction of astigmatism and beam shape.

2.3.7. Transmission electron microscopy (TEM)

TEM uses electrons transmitted through the sample to create an image of its internal structure, providing detailed information about the crystalline structure and morphology of the material. The spatial resolution of the TEM is much higher than that of the SEM, allowing the observation of details at the atomic scale [10]. For the sample preparation, a very small amount of powder was diluted in ethanol and the solution was then exposed to an ultrasonic bath for 2 min to achieve maximum dispersion, and then a drop was deposited on a carbon-thin grid to be observed immediately after drying. The morphological analysis of the hybridized nanostructures was carried out using a *transmission electron microscope JEOL JEM 2100 HR* in the high-resolution mode available at IMMM-Le Mans Université (Fig. S.2.1.f.).

2.3.8. Diffuse reflectance spectroscopy (DRS)

Diffuse reflectance spectroscopy (DRS) is a technique that entails gathering light that is diffusely reflected off a sample and then analyzing its spectrum using a spectrometer. It is typically used in the UV-visible, near-infrared (NIR), and mid-infrared regions to obtain molecular spectroscopic information, particularly from powders with minimal sample preparation [11].

The optical spectra of the ball-milling powder samples (Chapter 5) were obtained with an *Agilent Cary UV-Vis spectrophotometer* equipped with an integrating sphere, available at the SEES department of Cinvestav-Zacatenco, Mexico (Fig. S.2.1.g.). For the nanostructures prepared by photsonication, an *Ocean Optics Spectrometer ISP-REF Illuminated Integrating Sphere* available at IMMM of Le Mans Université was used (Fig. S.2.1.h). The UV-visible spectroscopy yielded diffuse reflectance data, which was then transformed into the absorption coefficient $F(R)$ using the Kubelka-Munk equation [12]:

$$F(R) = \frac{(1 - R)^2}{2R} = \frac{k}{s} \quad (\text{eq. 6})$$

Where R is the reflectance of the sample and $F(R)$ is equivalent to the absorption coefficient. The direct and indirect bandgap of pristine TiO_2 and nanostructures were estimated using the following equation:

$$[F(R_\infty)hv]^n = k(hv - E_g) \quad (\text{eq. 7})$$

Where $h\nu$ is the photon energy; E_g is the bandgap energy; k is a characteristic constant for each semiconductor material and the exponent n depends on the nature of the transitions ($n=1/2$

for direct transitions allowed and $n=2$ for indirect transitions allowed). By identifying the intercept of the linear portion of the graph with the x -axis ($h\nu=0$), we estimate the optical bandgap of the samples.

2.3.9. Electron paramagnetic resonance (EPR) spectroscopy

Electron paramagnetic resonance (EPR) spectroscopy, sometimes referred to as electron spin resonance (ESR) spectroscopy, is a scientific method employed to investigate chemical entities that include unpaired electrons [13, 14]. The unpaired spins carried by ions or molecules of the considered sample lead to magnetic moments involved in such paramagnetic species. Their interactions with an applied magnetic field with defined values and microwave radiation create the spin resonance conditions giving rise to an EPR Signal. For this purpose, an EPR Bruker EMX spectrometer available at IMMM of Le Mans Université (Fig. S.2.1.i) equipped with an X-band microwave bridge (9.5 GHz) and an electromagnet with variable magnetic field 0-1 Tesla was used. The characteristic features of an EPR spectrometer with continuous wave mode (CW) [14] are schematically represented in Fig. 2.6. The investigated sample is placed into the center of the microwave cavity, which is designed with a geometry that matches the wavelength of the used microwave radiation. An EPR spectrometer works by generating microwaves from a source; typically, a microwave bridge using a semiconductor-based Gunn diode, guided propagation is made and transferred to the resonant cavity where the sample is located. While the microwave radiation frequency is kept constant, the sweep of the applied magnetic field creates the spin resonance condition which modifies the electromagnetic microwave power in the cavity giving rise to the EPR spectrum. The analysis of an EPR experiment allows us to identify the nature of the unpaired spin carriers, ions, molecules, itinerant electrons, and their concentration as well as their local environments such as crystalline or disordered. The EPR measurements can be performed at variable temperatures from 4K to 1000K to characterize the changes in the local environment or the mobility of the unpaired spins.

For the context of this thesis work, EPR spectroscopy was used for the detection of Mn^{2+} ions from the $KMnO_4$ compound used for the oxidation degree of GO. EPR is a highly sensitive tool for paramagnetic species and stands out as a specific technique for the accurate detection of these ions in GO. Additionally, to demonstrate the creation of Ti^{3+} surface defects by sonication in TiO_2 and the structural changes due to the incorporation of GO, EPR spectra were measured at room temperature in the range of 3320 to 3500 G. While the magnetic properties of the embedded GO were studied by the temperature-induced changes of the EPR spectra in air and the temperature range from 100 to 300 K. The findings are thoroughly examined and analyzed in Chapter 6.

In a typical EPR experiment, the area under the curve is proportional to the number of spins that contribute to the EPR signal. The integration of this line allows the estimation of the species concentration of samples. The resonance condition defined by the magnetic field associated with the position of the resonance line can be used to determine the spectroscopic parameter such as the Landé factor (g -values). These parameters inform the electronic states of

the paramagnetic species leading to the EPR signal as will be discussed in the dedicated studies in chapter 6.

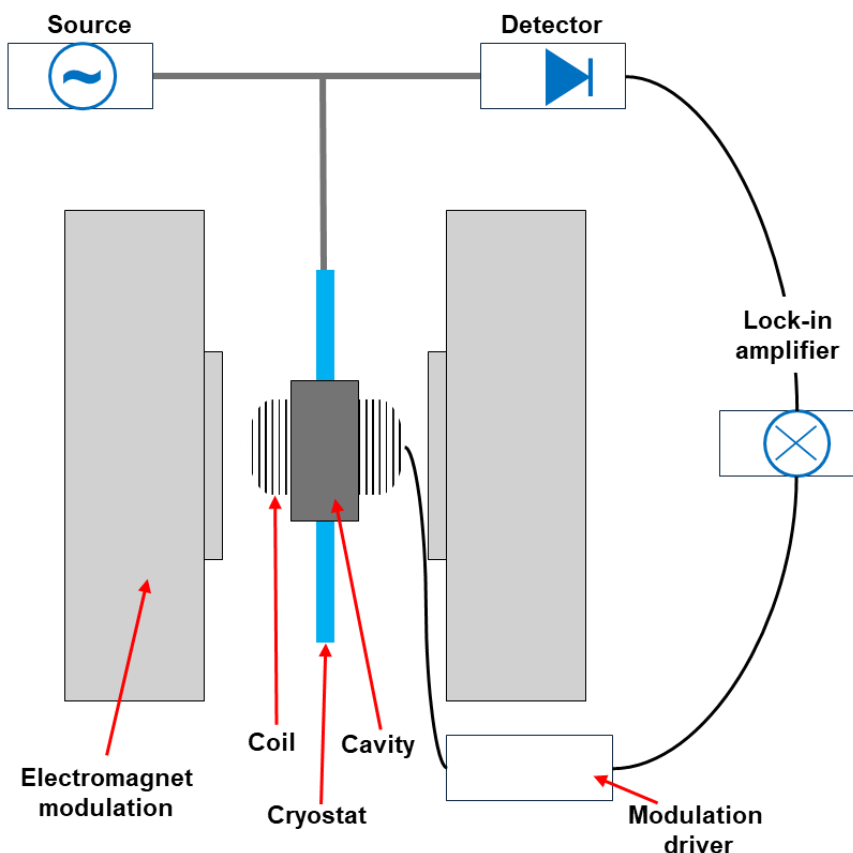


Fig. 2.6. Block diagram of EPR spectrometer

2.3.10. Electrical conductivity measurements

The electrical conductivity of GO and derivatives is a crucial factor influenced by their oxidation degree. Tuning the oxidation degree allows tuning the performance of GO and its subsequent incorporation into nanostructured TiO_2 for photocatalytic applications. Electrical measurements were performed with a Novocontrol broadband dielectric spectrometer (*Alpha-A high-performance frequency analyzer*) and a BDS 1200 sample measurement cell, available from IMMM at Le Mans Université (Fig. S.2.1.j).

To measure the different samples, pellets were manufactured. In order to create the pellets, a quantity of 1 gram of the powdered material was placed inside a pellet mold with a diameter of 5 mm and a thickness of 3 mm. The mold, together with the weighted material, was exposed to a uniaxial pressure of 5 Torr. Silver paint was then applied to both surfaces of the pellets to form a conductive layer. After application, the paint was allowed to dry and cure, creating a thin conductive layer on the ceramic pellet. This layer plays a critical role in providing an electrically conductive interface to facilitate conductivity measurement. The measurement was performed at room temperature and then the temperature was varied in the range of 100 to 200 °C. The results are discussed in detail in Chapters 5 and 6.

2.4. Experiment setup for MB removal

2.4.1. MB stock solution and calibration curve

The studies were performed with methylene blue (MB) powder (87% MB, Sigma-Aldrich, CI 52015). 25 mg of MB powder was dissolved in 250 mL of distilled water to prepare a 100 ppm MB stock solution. For each experiment, 10 mL of the 100 ppm MB stock solution was measured, and 90 mL of H₂O was added to give a final solution of 10 ppm in a total volume of 100 mL. Each experiment was performed with this concentration of dyes. Several standard solutions of MB were prepared at pH \approx 7 with concentrations ranging from 10 ppm to 0 ppm. The concentrations of MB dye in the solutions were determined by measuring the absorbance at the dye's maximum wavelengths (λ_{\max} = 664 nm) using the calibration curve depicted in Fig. 2.7.a. The reported experimental data were fitted by a straight line with a high regression coefficient ($R^2=0.9996$) (Fig. 2.7.b).

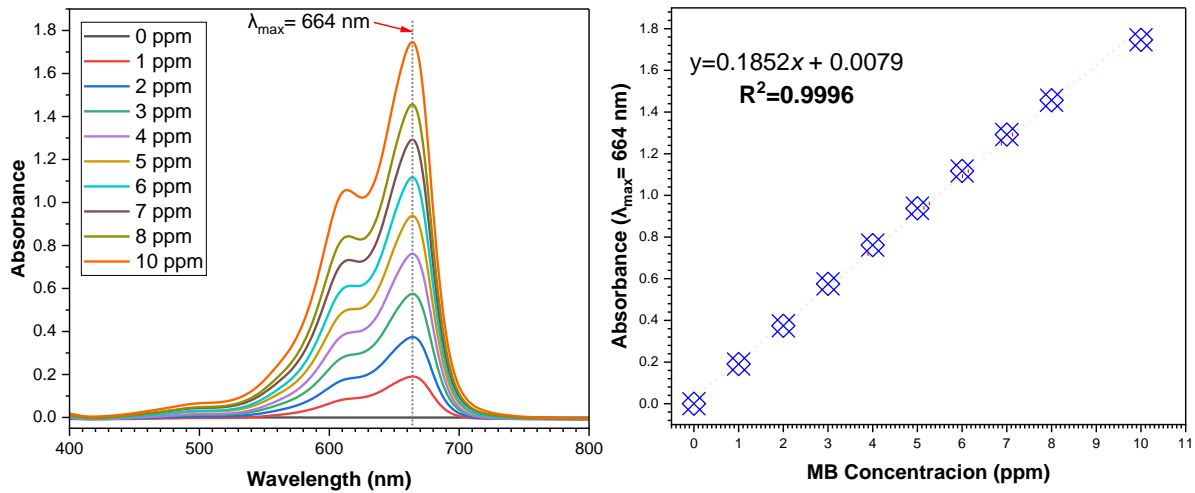


Fig. 2.7. (a) UV-Vis absorption spectra of standards containing various concentrations of MB, and (b) the calibration curve of absorbance (Abs) against MB concentrations (ppm)

For adsorption experiments, the removal efficiency [$R(\%)$], and the equilibrium adsorption capacity [q_e (mg/g)] were calculated using the following equations:

$$R (\%) = \left(\frac{C_0 - C_e}{C_0} \right) \times 100 \quad (\text{eq. 8})$$

$$q_e = \left(\frac{C_0 - C_e}{W} \right) \times V \quad (\text{eq. 9})$$

C_0 and C_e represent the initial and equilibrium concentrations of MB dye, measured in milligrams per liter (mg/L) accordingly. W , stands for the mass of the adsorbent (g), and V represents the volume of the solution (L). For the photocatalysis experiments, the R (%) was

also determined using eq. 8. In this case, however, the initial concentration (C_0) refers to the concentration measured after 30 minutes of adsorption.

2.4.2. Experimental set-ups for adsorption

MB experiments were conducted in a batch mode using 100 ml of a 10 ppm MB solution and 5 g of the powdered material. The solution was agitated vigorously for 40 min in the absence of light. The solution was sampled at 3-min intervals, promptly centrifuged, and then analyzed using a UV-Vis spectrophotometer (JASCO spectrometer model V-670) to determine the concentration of MB dyes in the solution over time. The highest wavelength chosen for quantifying the quantity of MB dye was 664 nm, which corresponds to the absorption band of MB. The measurement was conducted using deionized water as a reference. The experiments were performed in the dark to exclude the effects of photocatalysis and to avoid possible interference from light-induced reactions that could affect the surface properties we were studying as well as the adsorbed molecules. Conducting our experiments in the absence of light helped to eliminate potential sources of error and ensured that the investigation of the adsorption phenomenon was carried out accurately.

2.4.3. Experimental set-ups for photocatalysis

A home-built photocatalytic reactor was used for the photocatalytic studies. The photocatalytic activities of the samples were determined by decolorization of the organic dye solution under the irradiation of simulated sunlight using a mercury (Xe) arc lamp with an irradiance of 112 mW/cm² as the light source. The organic dye solution is introduced into a cylindrical flask and continuously stirred with a magnetic stirrer at moderate speed. The entire photocatalytic system is shown schematically in Fig. 2.8.

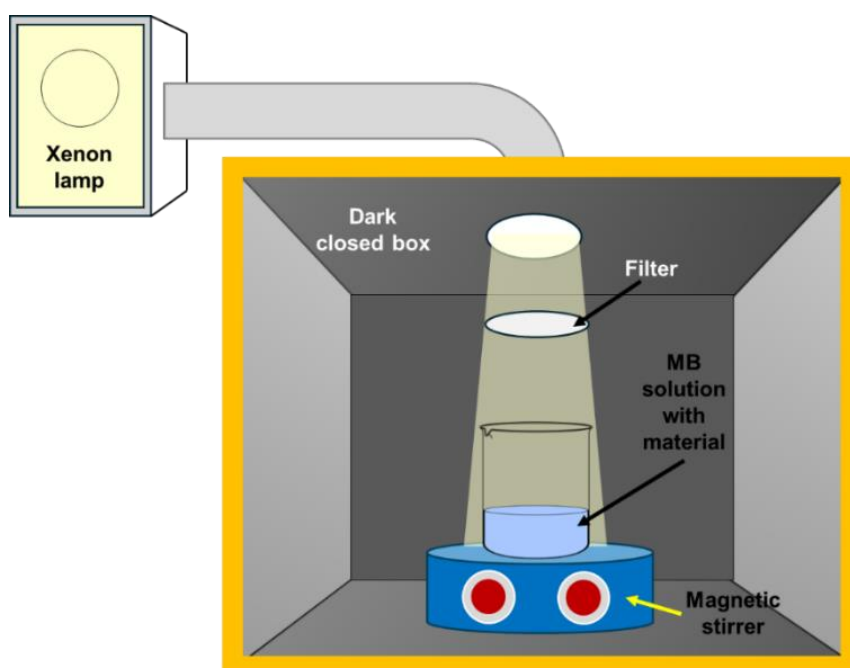


Fig. 2.8. Schematic representation of photocatalytic system.

2.4.3.1. Bandpass filter transmission

A long-pass optical filter was used to block UV radiation to restrict the photocatalytic activity to visible light only. A long-pass filter was used to selectively block wavelengths below 400 nm. The filter had a cut-off point at ≈ 408 nm and a transmission value of nearly 70% at 440 nm (Fig. 2.9.)

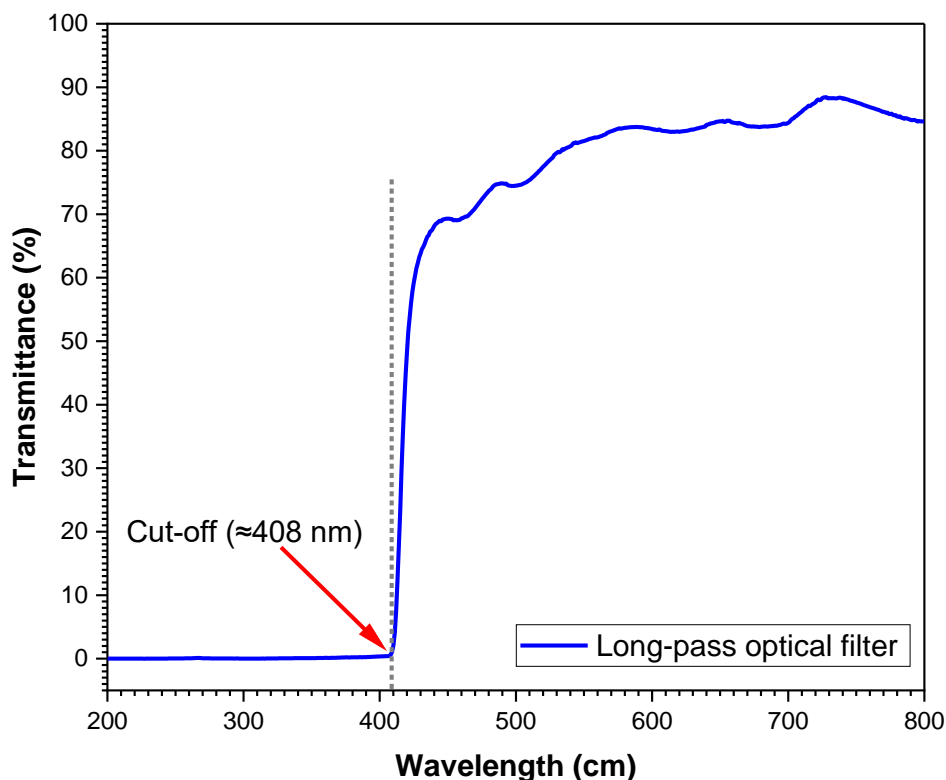


Fig. 2.9. The transmittance spectrum of the long-pass filter is utilized to obstruct wavelengths below 400 nm that are employed in photocatalytic investigations.

2.4.3.2. Photocatalysis with ball-milled nanostructures

To properly evaluate the photocatalytic activity of all mechano-synthesized nanostructures, pellet fabrication was chosen. To prepare the pellets, 1 g of the powdered material was placed in a pellet mold 5 mm in diameter and 3 mm thick. The mold, along with the weighted powder, underwent a uniaxial pressure of 5 Torr. No further treatments were performed due to the good quality and resistance of these in a liquid medium under constant stirring. The same procedure was followed for each of the powders produced by ball milling and discussed in detail in Chapter 5.

2.4.3.3. Photocatalysis with photosonicated nanostructures

Photocatalytic experiments on the activity of TiO_2 -GO nanostructures fabricated by photosonation are discussed in Chapter 6. A 25 mL solution containing 10 ppm MB and 0.1 g TiO_2 -GO was used. The mixture was initially agitated vigorously for 30 min in the absence

of light to achieve adsorption-desorption equilibrium for each item. Then, to study the photocatalytic activity, the mixture was exposed to irradiation for 180 min. During the experiment, 2 mL samples were extracted and promptly subjected to centrifugation at 4000 rpm in order to determine the dye concentration over time. The analysis was performed using a *JASCO spectrometer model V-670*, with the maximum wavelength selected at 664 nm of the MB absorption band and the deionized water used for the reference recording.

2.5. Experiment setup for microalga photolysis and photocatalysis study

2.5.1. Pulse-amplitude-modulation (PAM) fluorometry

In principle, chlorophyll fluorescence can be used as an indicator of the different levels of photosynthesis. Chlorophyll serves as the primary pigment that captures light energy and directs it to the reaction centers of photosystems I (PSI) and II (PSII). These reaction centers are responsible for converting the absorbed energy into chemical energy through photochemical reactions. The indicator function of chlorophyll fluorescence is derived from the fact that fluorescence emission is the opposite of the alternative processes of de-excitation, which include photochemistry and heat dissipation. In general, the fluorescence yield is enhanced when the yields of photochemistry and heat dissipation are decreased and vice versa. The variable part of chlorophyll fluorescence originates mainly in PSII, thus reflecting changes in PSII photochemical efficiency and heat dissipation [15].

Fluorometry combined with the saturation pulse approach has proven to be highly effective in real world scenarios. The principle of PAM fluorometry is based on a short light pulse of 1 μ s (low intensity and non-actinic) that is precisely timed with a lock-in amplifier. The use of a lock-in amplifier allows accurate measurements of quantum yield under illumination conditions by eliminating extraneous signals unrelated to the lock-in signal. After the process of dark adaptation, it is possible to measure the minimum fluorescence value (F_0) of the sample. If the sample is then exposed to a saturating pulse of light, causing all the reaction centres to capture the energy of a photon absorbed by their antennae (resulting in closed reaction centres), the maximum fluorescence value (F_M) can be quantified. The variable fluorescence (F_v) represents the difference between these two extremes. F_v/F_M quantifies the maximum efficiency of photosystem II (PSII) in converting light energy into chemical energy. When the sample is exposed to actinic illumination, its fluorescence yield can range between two extreme values, F_0 and F_M . The momentary fluorescence yield, F , can be measured briefly before triggering the saturating pulse, during which the maximal fluorescence yield, F_M' is reached. The effective yield of PSII photochemical energy conversion under illumination is calculated as $(F_M' - F)/F_M'$ [16].

The alterations in the sample caused by the photolysis or photocatalysis processes were monitored using a dual-beam spectrophotometer (Perkin Elmer). This was done either by analyzing the sample after it was collected or by observing changes in Chlorophyll fluorescence yields using a Dual PAM-100 (Walz, Germany) device [17], which are available at the laboratory of *"Metabolism, bioengineering of microalga molecules and applications, Mer*

Molécules Santé (MIMMA, MMS, IUML - FR 3473 CNRS)" at Le Mans Université (Fig. S.2.1.k.).

2.5.2. Sample preparation

The utilization of nanoparticles in many applications can be a subject of controversy due to their ability to permeate any organism when disseminated in water, thereby posing toxicity risks to unintended organisms. Internalized nanomaterials pose a risk of being released back into the environment once the targeted organisms have been broken down. This has the potential to be a source of pollution [18, 19]. To avoid this drawback, the nanoparticles used in this research have been immobilized on metallic substrates, creating thin films that provide the opportunity to study the effects of the materials alone on microalgae and determine their potential for water decontamination.

For film formation, 0.52 g of Pluronic F-127 (CAS No.9003-11-6 Sigma) was mixed with 3.5 ml of ethanol and stirred until complete dissolution was achieved. Then 1 g of TG_(0.5) nanostructured powder prepared by sonication was added, mixed, and stirred for 30 min. The resulting solution was deposited by spin-coating technique on Si(100) substrates, previously washed, and cut into 2.5x1 cm dimensions. The conditions for the preparation of the thin films are as follows:

- Spin speed: 4000 rpm.
- Centrifugation time: 60 seconds
- Approximate thickness determined by profilometry: \approx 450 nm.

Spin conditions were set according to preliminary tests (results not shown). Upon completion, the films were air dried and then dried in air at 80 °C for 24 hours. The films were then ready for use in the microalgae experiments discussed in detail in Chapter 8.

2.5.3. Diatoms solution used

Phaeodactylum tricornutum is a type of pennate diatom that can take on many forms (fusiform, triradiate, and oval) as depicted in Fig. 2.10. Alterations in cell shape can be induced by environmental factors [21–23]. The selection of *Phaeodactylum tricornutum* for this investigation was based on its ability to undergo approximately one division per day when cultured in artificial saltwater under axenic conditions [24], such as in the F/2 medium (*it is an ideal and widely used nutrient medium for algae cultivation*). In addition, following the sequencing of its genome, it has become a model organism for diatom physiology and has been used in numerous studies due to its ease of laboratory culture [25]. The diatom *Phaeodactylum tricornutum* was maintained in a 50 mL flask with F/2 medium. Gas exchange was facilitated through a membrane in the lid. Tests were performed in duplicate using the same conditions.

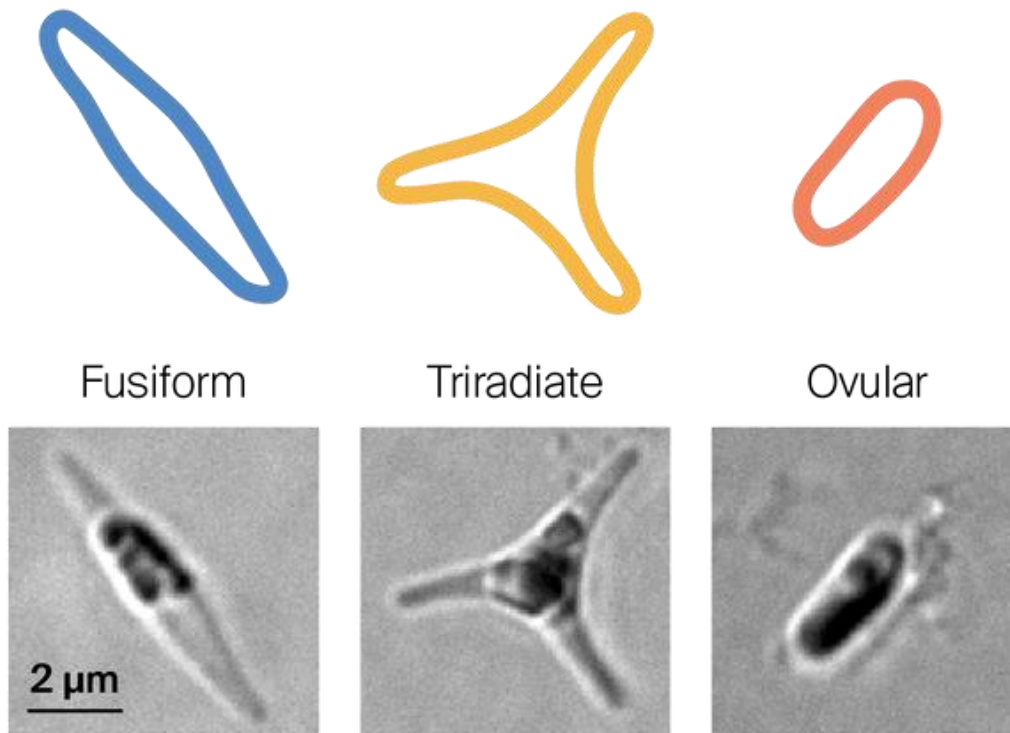


Fig. 2.10. Schematic illustration of morphologies of *Phaeodactylum tricornutum* [20].

2.5.4. Experimental setup for microalgal degradation

For the photolysis and photocatalysis experiments, the microalgae culture solution was placed in cuvettes with a volume of 3 mL. These cuvettes had four transparent sides and were equipped with a magnetic stirrer. The fabricated film was placed on one side of the cuvette as shown in the schematic representation in Fig. 2.11. The solution was exposed to a focused light beam (L-ACT) emitted by an Oriel Xenon Arc Lamp (Model #6255), which emits light with a spectral composition similar to sunlight. The emitted light beam underwent filtration using a series of filters to minimize sample heating, facilitate absorption by the nanomaterial employed for ROS production, and initiate photosynthesis. A fan was placed behind the sample to accelerate the removal of residual heat and maintain the temperature at $37 \pm 2^\circ\text{C}$. The changes in the sample caused by the photolysis or photocatalysis procedures were monitored using a dual-beam spectrophotometer (Perkin Elmer) either after collecting samples or in real-time by observing alterations in chlorophyll fluorescence yields with the apparatus depicted in Fig. 2.11. Prior to taking measurements, the sample in the cuvette, which had a smooth surface on all four sides, was supplied with sodium bicarbonate (NaHCO_3) to prevent carbon deprivation during the experiment [26]. Details of chlorophyll fluorescence measurements are discussed in detail in Chapter 8. The process was carried out under identical conditions for microalgae in the absence (photolysis) and presence (photocatalysis) of the photocatalyst.

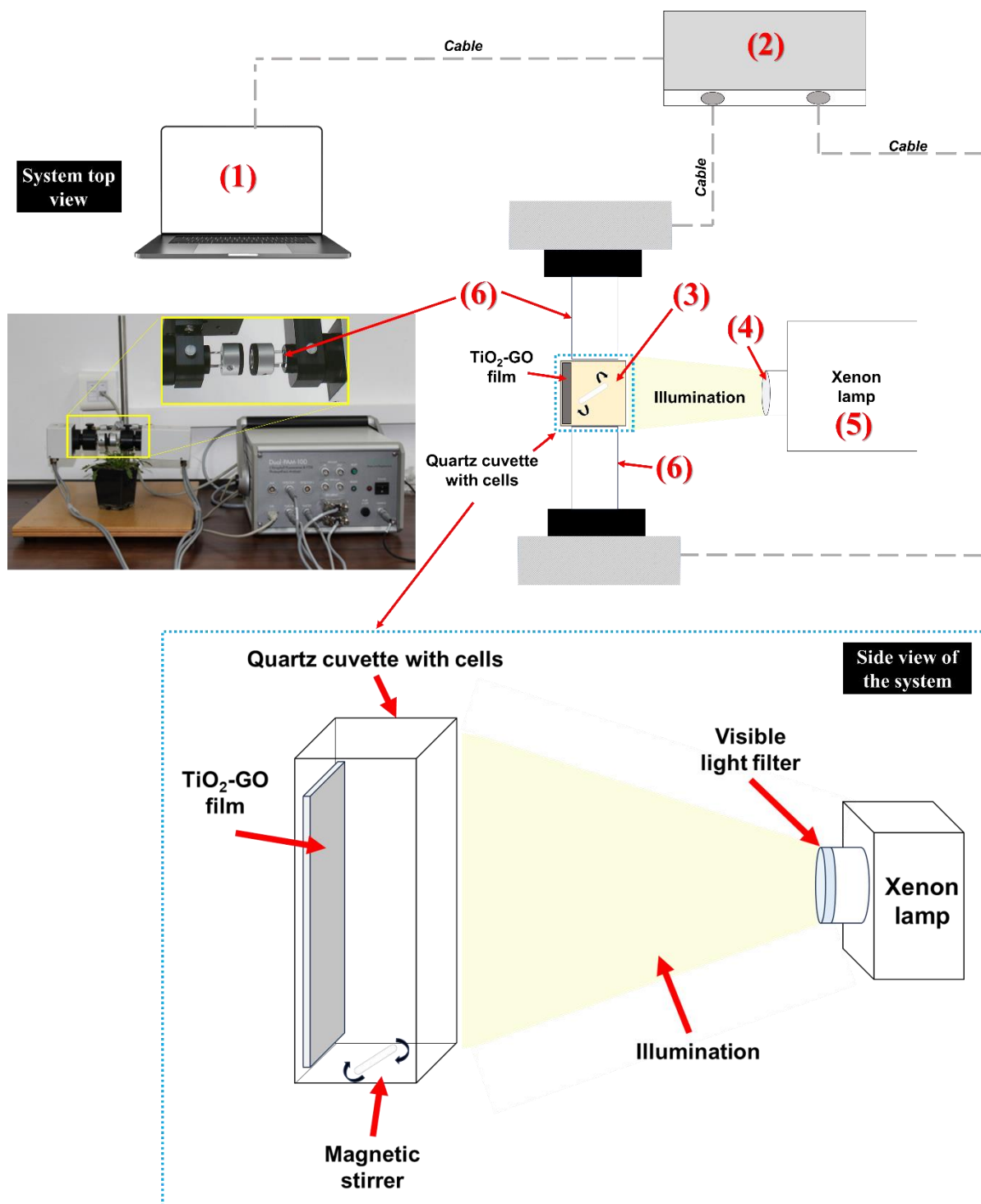


Fig. 2.11. Schematic of the experimental setup employed to quantify the impact of photolysis and photocatalysis: (1) a computer that controls the PAM, (2) the PAM control unit, (3) a magnetic stirrer, (4) a light filtering system, (5) a UV lamp source and voltage control for the lamp's power supply, and (6) a cuvette holder used with the PAM measurement head.

References

1. Azároff, L. V., Zipin, R.B.: Elements of X-ray Crystallography. *Phys Today*. 22, (1969). <https://doi.org/10.1063/1.3035379>
2. Langford, J.I., Wilson, A.J.C., IUCr: Scherrer after sixty years: A survey and some new results in the determination of crystallite size. *urn:issn:0021-8898*. 11, 102–113 (1978). <https://doi.org/10.1107/S0021889878012844>
3. Warren, B.E.: X-ray diffraction in random layer lattices. *Physical Review*. 59, 693–698 (1941). <https://doi.org/10.1103/PhysRev.59.693>
4. Elton, L.R.B., Jackson, D.F.: X-Ray Diffraction and the Bragg Law. Citation: *American Journal of Physics*. 34, 1036 (1966). <https://doi.org/10.1119/1.1972439>
5. Joseph Raj, P.L., Kalimuthu, K., Kulkarni, S.A., -, al, Mir, Q., Ahmad -, B., Kurian, S., Amrita, C., Raguram, T., Rajni, K.S.: Preparation and Characterisation of PVA⁺TiO₂ Nanofiber by Electrospinning Technique. *IOP Conf Ser Mater Sci Eng*. 577, 012077 (2019). <https://doi.org/10.1088/1757-899X/577/1/012077>
6. Ferrari, A.C., Robertson, J.: Raman spectroscopy of amorphous, nanostructured, diamondlike carbon, and nanodiamond. *Philosophical Transactions of the Royal Society of London. Series A: Mathematical, Physical and Engineering Sciences*. 362, 2477–2512 (2004). <https://doi.org/10.1098/RSTA.2004.1452>
7. Trusovas, R., Račiukaitis, G., Niaura, G., Barkauskas, J., Valušis, G., Pauliukaite, R.: Recent Advances in Laser Utilization in the Chemical Modification of Graphene Oxide and Its Applications. *Adv Opt Mater*. 4, 37–65 (2016). <https://doi.org/10.1002/ADOM.201500469>
8. TUINSTR A F, KOENIG JL: Raman Spectrum of Graphite. *J Chem Phys*. 53, 1126 (2003). <https://doi.org/10.1063/1.1674108>
9. Nicolet, T., & All, C. (2001). Introduction to Fourier Transform Infrared Spectrometry. Thermo Nicolet Corporation.
10. Inkson, B.J.: Scanning electron microscopy (SEM) and transmission electron microscopy (TEM) for materials characterization. *Materials Characterization Using Nondestructive Evaluation (NDE) Methods*. 17–43 (2016). <https://doi.org/10.1016/B978-0-08-100040-3.00002-X>
11. D.E.O'C.: Reflectance spectroscopy (principles, methods, applications). *J Mol Struct*. 13, (1972). [https://doi.org/10.1016/0022-2860\(72\)87038-8](https://doi.org/10.1016/0022-2860(72)87038-8)
12. Kubelka, P., Munk, F.: An Article on Optics of Paint Layers. (1931)
13. Roessler, M.M., Salvadori, E.: Principles and applications of EPR spectroscopy in the chemical sciences. *Chem Soc Rev*. 47, 2534–2553 (2018). <https://doi.org/10.1039/C6CS00565A>
14. Neukermans, S., Samanipour, M., Vincent Ching, H.Y., Hereijgers, J., Van Doorslaer, S., Hubin, A., Breugelmans, T.: A Versatile In-Situ Electron Paramagnetic Resonance Spectro-electrochemical Approach for Electrocatalyst Research. *ChemElectroChem*. 7, 4578–4586 (2020). <https://doi.org/10.1002/CELC.202001193>
15. Haidekker, M.A., Dong, K., Mattos, E., van Iersel, M.W.: A very low-cost pulse-amplitude modulated chlorophyll fluorometer. *Comput Electron Agric*. 203, 107438 (2022). <https://doi.org/10.1016/J.COMPAG.2022.107438>
16. Schreiber, U.: Pulse-Amplitude-Modulation (PAM) Fluorometry and Saturation Pulse Method: An Overview. *Chlorophyll a Fluorescence*. 279–319 (2004). https://doi.org/10.1007/978-1-4020-3218-9_11
17. DUAL-PAM-100 Downloads | WALZ, https://www.walz.com/products/chl_p700/dual-pam-100/downloads.html
18. Gupta, R., Xie, H.: Nanoparticles in daily life: Applications, toxicity and regulations. *Journal of Environmental Pathology, Toxicology and Oncology*. 37, (2018). <https://doi.org/10.1615/JEnvironPatholToxicolOncol.2018026009>
19. Jeevanandam, J., Barhoum, A., Chan, Y.S., Dufresne, A., Danquah, M.K.: Review on nanoparticles and nanostructured materials: History, sources, toxicity and regulations. *Beilstein Journal of Nanotechnology*. 9, 1050–1074 (2018). <https://doi.org/10.3762/BJNANO.9.98>
20. Avasthi, P., MacQuarrie, C.D., Radkov, A.: Inducing protoplast formation in *Phaeodactylum tricornutum* by silica deprivation, enzymatic treatment, or cytoskeletal inhibition. (2023). <https://doi.org/10.57844/ARCADIA-FH8F-XZ51>
21. Martino, A. De, Meichenin, A., Shi, J., Pan, K., Bowler, C.: Genetic and phenotypic characterization of *Phaeodactylum tricornutum* (Bacillariophyceae) accessions I. *J Phycol*. 43, 992–1009 (2007). <https://doi.org/10.1111/J.1529-8817.2007.00384.X>
22. Tesson, B., Gaillard, C., Martin-Jézéquel, V.: Insights into the polymorphism of the diatom *Phaeodactylum tricornutum* Bohlin. *Botanica Marina*. 52, 104–116 (2009). <https://doi.org/10.1515/BOT.2009.012/MACHINEREADABLECITATION/RIS>

23. Pocha, C.K.R., Chia, W.Y., Chew, K.W., Munawaroh, H.S.H., Show, P.L.: Current advances in recovery and biorefinery of fucoxanthin from *Phaeodactylum tricornutum*. *Algal Res.* 65, 102735 (2022). <https://doi.org/10.1016/J.ALGAL.2022.102735>
24. Thomas, C.T.: Photocatalytic treatment of biological organisms in water using graphene oxide doped TiO₂ and BiVO₄ nanocomposites. (2021)
25. Bowler, C., Allen, A.E., Badger, J.H., Grimwood, J., Jabbari, K., Kuo, A., Maheswari, U., Martens, C., Maumus, F., Otiillar, R.P., Rayko, E., Salamov, A., Vandepoele, K., Beszteri, B., Gruber, A., Heijde, M., Katinka, M., Mock, T., Valentin, K., Verret, F., Berges, J.A., Brownlee, C., Cadoret, J.P., Chiovitti, A., Choi, C.J., Coesel, S., De Martino, A., Detter, J.C., Durkin, C., Falciatore, A., Fournet, J., Haruta, M., Huysman, M.J.J., Jenkins, B.D., Jiroutova, K., Jorgensen, R.E., Joubert, Y., Kaplan, A., Kröger, N., Kroth, P.G., La Roche, J., Lindquist, E., Lommer, M., Martin-Jézéquel, V., Lopez, P.J., Lucas, S., Mangogna, M., McGinnis, K., Medlin, L.K., Montsant, A., Secq, M.P.O. Le, Napoli, C., Obornik, M., Parker, M.S., Petit, J.L., Porcel, B.M., Poulsen, N., Robison, M., Rychlewski, L., Rynearson, T.A., Schmutz, J., Shapiro, H., Siat, M., Stanley, M., Sussman, M.R., Taylor, A.R., Vardi, A., Von Dassow, P., Vyverman, W., Willis, A., Wyrwicz, L.S., Rokhsar, D.S., Weissenbach, J., Armbrust, E.V., Green, B.R., Van De Peer, Y., Grigoriev, I. V.: The *Phaeodactylum* genome reveals the evolutionary history of diatom genomes. *Nature* 2008 456:7219. 456, 239–244 (2008). <https://doi.org/10.1038/nature07410>
26. Heydarizadeh, P., Boureba, W., Zahedi, M., Huang, B., Moreau, B., Lukomska, E., Couzinet-Mossion, A., Wielgosz-Collin, G., Martin-Jézéquel, V., Bougaran, G., Marchand, J., Schoefs, B.: Response of CO₂-starved diatom *Phaeodactylum tricornutum* to light intensity transition. *Philosophical Transactions of the Royal Society B: Biological Sciences.* 372, (2017). <https://doi.org/10.1098/RSTB.2016.0396>

Chapter III:

Theoretical approach by DFT applied to Graphene oxides (GO) and hybrid structures TiO₂-GO

Density functional theory (DFT) has been the most successful and frequently used method in condensed matter physics, quantum chemistry, and computational physics for several decades. This theory describes the properties of materials, which include not only standard bulk structures and molecules but also complex systems such as proteins, interfaces, and nanoparticles. The primary concept behind DFT is to characterize a system consisting of several particles by its electronic density, rather than relying on the electronic wave function. The theory was initially formulated by Hohenberg-Kohn [1], who proposed that all aspects of a system can be understood as distinct functionals of its ground state density. The Born-Oppenheimer approximation [2] and the Kohn-Sham technique [3] have facilitated the implementation of practical and precise DFT calculations by employing estimates for the exchange–correlation (XC) potential. This potential incorporates the influence of the Pauli principle and the Coulomb potential, going beyond the sole electrostatic interaction between the electrons. Due to the intractability of solving the many-body problem precisely, the exact XC potential cannot be calculated. As a result, a commonly used approximation is the local density approximation. This approximation replaces the XC energy density of an inhomogeneous system with that of a homogeneous electron gas, evaluated at the local density. In many cases, the results of DFT calculations for condensed-matter systems agreed quite satisfactorily with experimental data, especially with better approximations for the XC energy function since the 1990s. Also, the computational costs were relatively low compared to traditional ways which were based on the complicated many-electron wavefunction, such as Hartree-Fock theory [4] and related approaches. Despite the improvements in DFT, there are still difficulties in using this theory to properly describe intermolecular interactions; charge transfer excitations; transition states, global potential energy surfaces, and some other strongly correlated systems as well as the calculations of the bandgap of bulk materials and nanostructures.

In this chapter, the comprehensive use of DFT as a first preliminary approach to study the gradual variation of the bandgap of GOs as a function of the O/C ratio is discussed. The bandgap of GO was modified by the gradual incorporation of functional groups on the surface

of the material. The direct relation between the bandgap and the number of epoxide functional groups in the GO was demonstrated. In addition, the interaction around the integration of graphene and graphene oxide monolayers on the surface of TiO₂ anatase was explored. Although the main focus of this research was not on theoretical aspects, the insights gained from this chapter have significantly contributed to our understanding of the intricate interactions between these materials and served as a starting point for experimental development. These findings not only enrich our understanding of the behavior of GO but also serve as an important stepping stone that complements the discussion of experimental results related to the properties and structural features of hybrid nanostructures based on TiO₂ and GO.

3.1. Computational details

3.1.1. Graphene oxide structures

The structures of the graphene and graphene oxide monolayers were performed using the DFT approach developed by Walter Kohn *et al.* in the 1960s [5, 6] and implemented in Material Studio software. To ensure the accuracy and reliability of our calculation results, the Dmol³ module is used, which was chosen to combine the Perdew-Burke-Ernzerhof (PBE) functional with the generalized gradient approximation (GGA) [7, 8]. DFT-D Grimme was employed to correct the total energy of the system to more properly assess weak interactions like the van der Waals force. The DIIS size was set to 6 and the SCF tolerance was 1×10^{-6} Ha. The calculations utilized the DNP basis set and the GGA-PBE functional. During the process of geometry optimization, the positions of all atoms were adjusted in order to achieve electronic band structures, density of states, and bandgap energies. The band structure was calculated with a separation distance of 0.025 \AA^{-1} . The *k*-point set was set to $4 \times 4 \times 1$ by using the Monkhorst-Pack method [9].

A graphene monolayer with 41 C atoms, with a vacuum spacing of 5 nm in the *c*-direction, was optimized and used as a periodic supercell of $9.8 \times 9.8 \text{ \AA}$. Following that, epoxide groups were introduced onto the material's surface at O/C ratios of 0.06, 0.11, 0.17, 0.28, 0.33, 0.38, and 0.50. Only epoxide functional groups were used because they have been reported to be more effective in gradually tuning the bandgap than other groups such as hydroxyl, carbonyl, or carboxyl groups [10–12]. The optimized structures are discussed below.

3.1.2. TiO₂-GO hybrid structures

For the theoretical investigation of TiO₂ and its coupling with graphene and GO, respectively, the model structure was based on a supercell constructed by $2 \times 2 \times 1$ unit cells of anatase TiO₂ and cut on the (010) plane surface. The Vienna ab initio simulation tool (VASP) version Vasp.5.4.4 (*VASP Software GmbH, Vienna, Austria*) was used to perform structural and electronic properties for the investigated atomic structures. Using *sw*-GW basis sets, the electronic structure was characterized after optimizing the geometry by a complete relaxation of the atomic positions. The application of the conjugate gradient approach was used resulting in the relaxation of lattice parameters. The Monkhorst and Pack scheme was used to generate

a k -point sampling with an $8 \times 8 \times 8$ point mesh. The Brillouin zone, denoted as G-F-Q-Z-G, was used to calculate the electronic properties of the optimized crystalline structure under study straightforwardly. At the surface of the optimized TiO_2 structure, a $2 \times 1 \times 1$ monolayer of graphene or GO was respectively placed at a distance of 1.34 \AA . The added GO contains an epoxide functional group ($-\text{O}$) connected respectively to two C atoms.

3.2. Graphene

3.2.1. Optimized geometry

The optimized graphene corresponds to a monolayer of a hexagonal arrangement of carbon atoms with sp^2 hybridization. This type of hybridization results in a trigonal planar arrangement in which each carbon atom forms a covalent σ -bond with three neighboring atoms in the same plane. The angle between these bonds is 120° and their average length is 1.42 \AA (Fig. 3.1.).

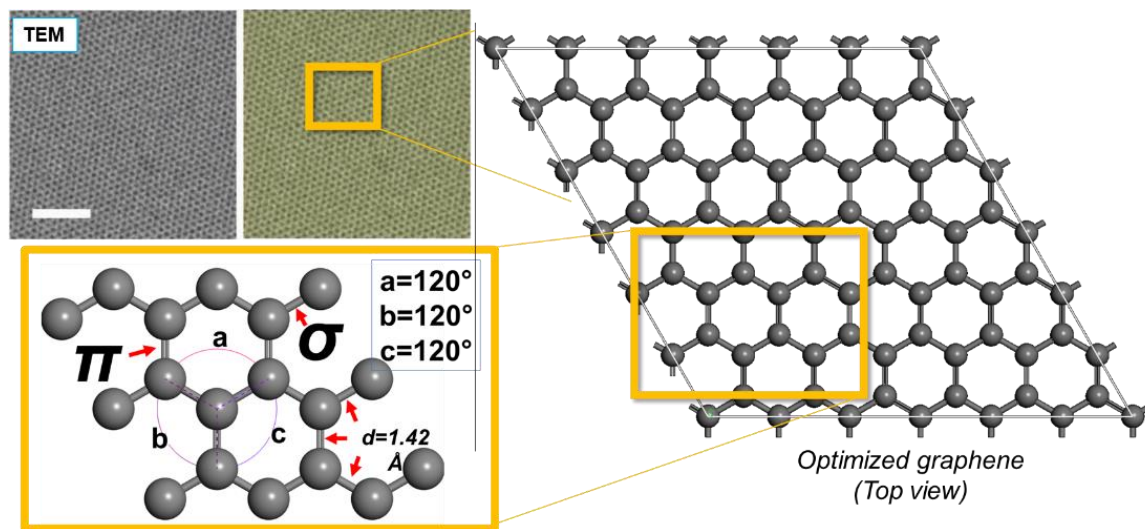


Fig. 3.1. The structural arrangement of two-dimensional sheets of graphene (*TEM image is adapted from [13] with copyright permission*).

3.2.2. Graphene band-structure

As expected, no bandgap was calculated for a two-dimensional monolayer of graphene. Its band structure is shown in Fig. 3.2. where the energy bands observed above 0 eV correspond to the C_B , while those below are the V_B . C_B and V_B are linked at two specific places in the reciprocal space referred to as k and k' , where the energies $E(k)$ and $E(k')$ coincide with the Fermi level. The electrons in the graphene sheet move relatively freely so that even at room temperature almost no collisions with the crystal lattice occur. This characteristic electronic structure of graphene leads to unique physical properties. The delocalized π -electron cloud and the rapid carrier dynamics are accountable for the ballistic transport reported in graphene [14, 15]. Recent research has indicated that the absence of a bandgap in graphene is due to the identical surroundings of its two atomic sublattices. This suggests that introducing changes to the structure or making chemical modifications to graphene could result in the creation of a bandgap, similar to what occurs in GO [16–18].

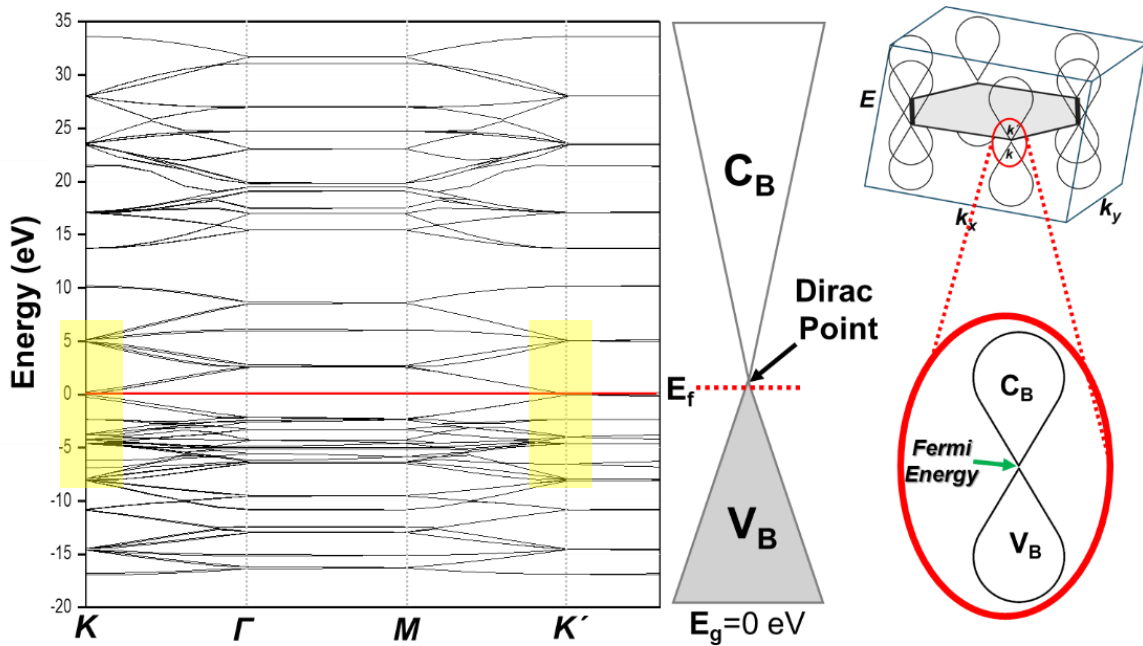


Fig. 3.2. Graphene band structures, and scattering ratio $E(k)$ for an electron in graphene (reprinted from our publisher work on Elsevier 2023 [19]).

3.3. Graphene oxide

3.3.1. Optimized geometry

After optimization, computational results of GOs showed that epoxide groups do not break the hexagonal carbon ring structure; however, a single epoxide functional group on graphene can induce significant local distortion. Furthermore, this addition replaced the π -conducting states with σ -states, as shown in the red boxes in Fig. 3.3.

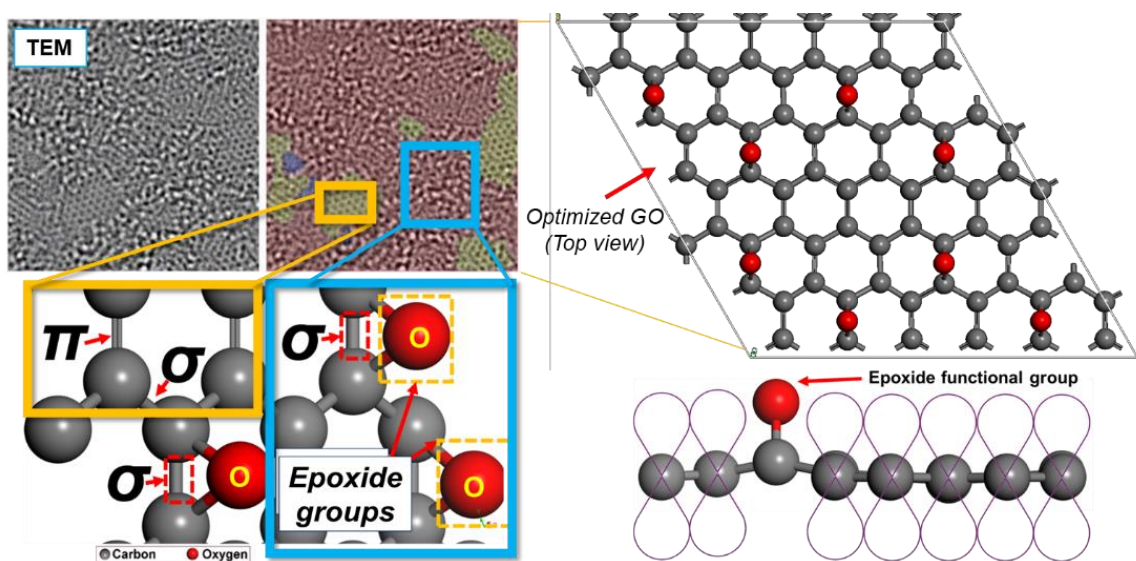
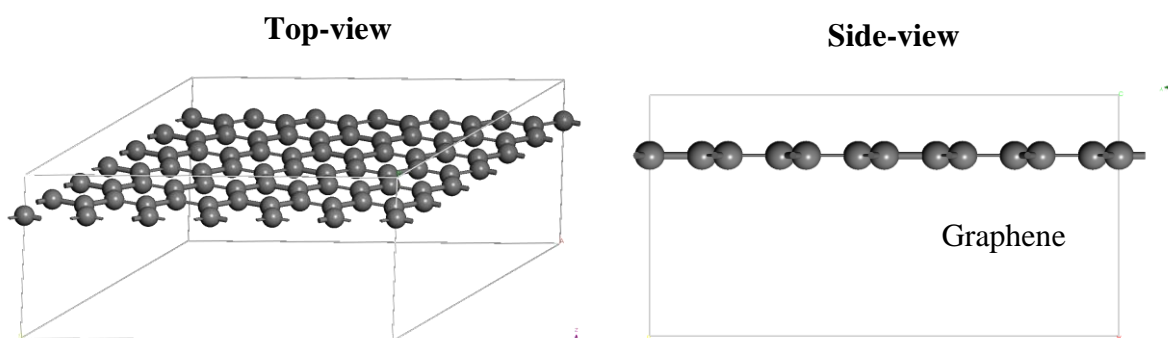
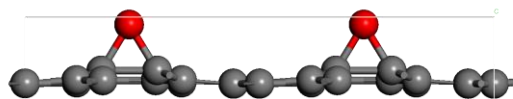
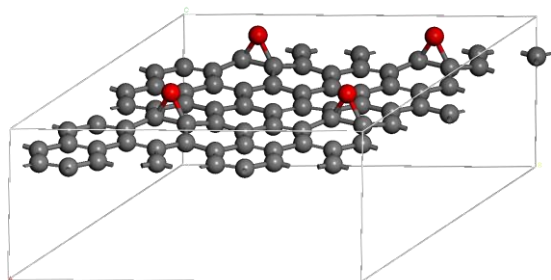


Fig. 3.3. The structural arrangement of two-dimensional GO (TEM image is adapted from [13] with copyright permission).

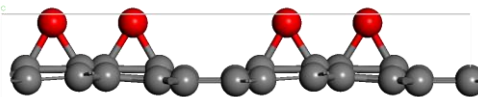
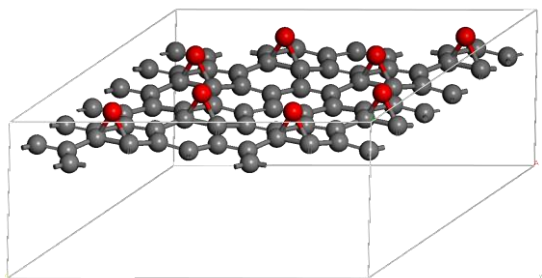
Oxidation refers to the process of introducing oxygen functional groups onto graphene sheets [20, 21]. Unlike graphene, which contains only a sp^2 carbon lattice with a highly uniform surface, GO has a hybrid carbon lattice with a disordered structure containing sp^2 regions with a conserved honeycomb structure, sp^3 regions with bonded oxygenated groups, and defective regions. These perturbations of the graphene lattice contribute to a relatively rough surface.

Moreover, Fig. 3.4. shows the deformation and gradual loss of linearity of the materials due to the effect of the oxygenated groups. This effect is attributed to the difference in electronegativity between oxygen (*i.e.*, 3.5) and carbon (*i.e.*, 2.5) [22], which causes the oxygen atoms to attract their bounded carbon atoms. As new C-O-C bonds are formed, the bonding characteristics of the connected C atoms change from planar sp^2 to distorted sp^3 hybridization. These hybridizations can be detected experimentally using techniques such as Raman spectroscopy [7, 23] and XPS studies [24] providing information on the vibrational and electronic properties of the carbon atoms in the material through the identification and quantification of the proportion of atoms with different hybridizations. In Raman spectroscopy, the G-mode (G-band; $\approx 1591\text{ cm}^{-1}$) is characteristic of the vibration of carbon-carbon (C-C) bonds in the hexagonal lattice. The existence and strength of the G-peak in the Raman spectrum provide evidence of the sp^2 hybridization of the carbon atoms in the material. A strong G-peak suggests a high concentration of sp^2 hybridization. Whereas the D-mode (D-band; $\approx 1339\text{ cm}^{-1}$) is characteristic of the presence of defects and sp^3 hybridization [25]. Several authors have successfully calculated the I_D/I_G ratio [26, 27], which provides a quantitative measure of the degree of structural disorder in GO or rGO. It was concluded that the higher the value of I_D/I_G , the higher the content of defects and disorder in the GO structure. A lower I_D/I_G ratio indicates the retention of the original structure and a lower oxidation degree or defects in the material, confirming the accuracy of our estimates. On the other hand, the XPS technique provides information about the composition and electronic states of the atoms on the GO surface [28, 29]. The sp^3 hybridization causes a shift towards higher values of the C1s binding energy compared to the sp^2 hybridization (the C1s peak indicates the binding energy of electrons in the carbon 1s orbital). In addition, the amount of sp^3 -hybridized carbon can be estimated by fitting specific peaks in the XPS spectrum. These experimental techniques are essential to characterize the hybridization of carbon atoms in GO and its derivatives and provide complementary information to the theoretical calculations performed by DFT. The combination of experimental data and theoretical results provides a more complete understanding of the structural and electronic properties of GO and its derivatives.

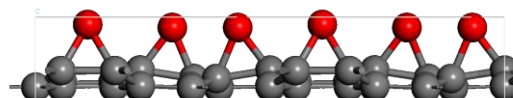
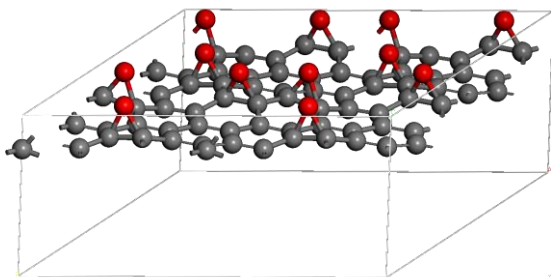




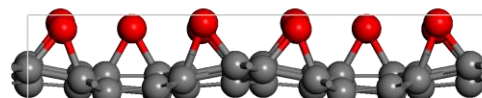
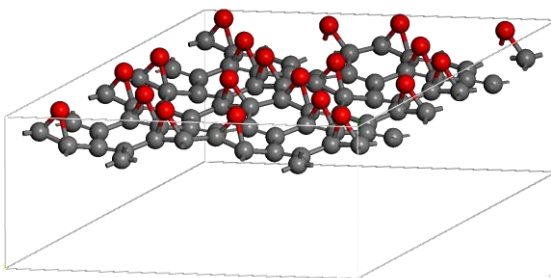
O/C=0.06



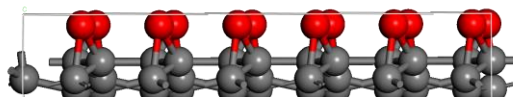
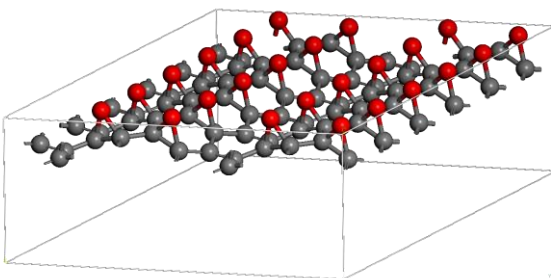
O/C=0.11



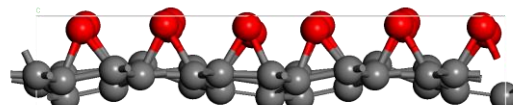
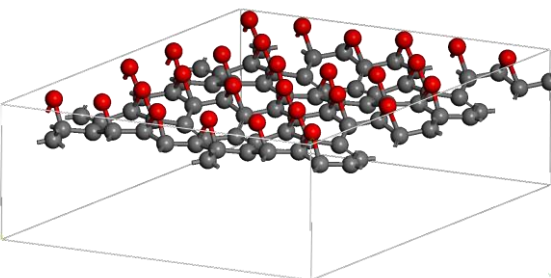
O/C=0.17



O/C=0.28



O/C=0.33



O/C=0.38

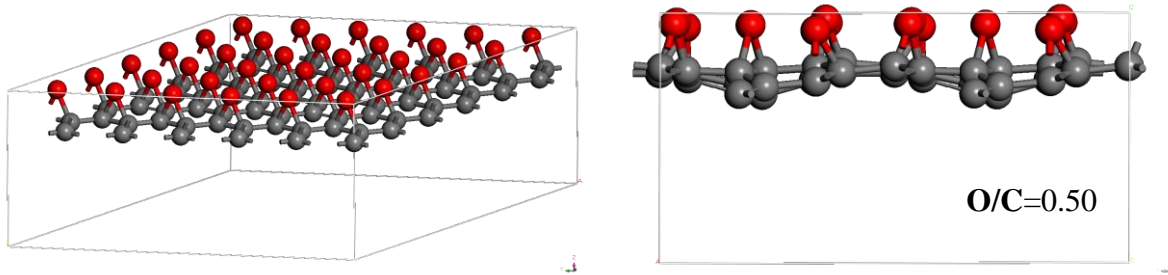


Fig. 3.4. Optimized (a) graphene and (b-h) GO with different O/C ratios

3.3.2. Bandgap variation

Fig. 3.5. shows the estimated bandgap of graphene and GO with the O/C ratio in the range of 0.06 to 0.5. An increase in the bandgap of GO was observed with the incorporation of the functional groups, in agreement with theoretical and experimental works previously reported in the literature.

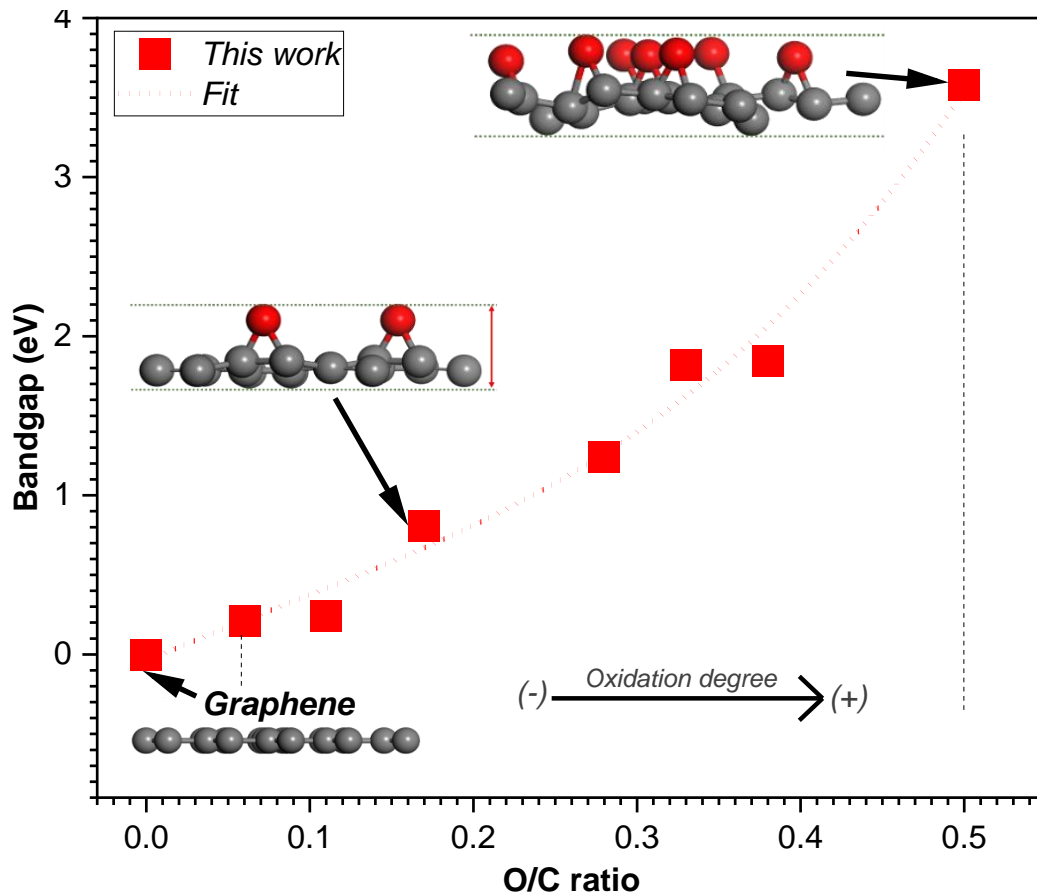


Fig. 3.5. Behavior of the bandgap as a function of the O/C ratio.

Boukhalov *et al.* 2008 [30] predicted a linear increase in the bandgap as a function of the O/C ratio. Huang *et al.* 2012 [31] performed a theoretical study using the Vienna Ab initio Simulation Package (VASP) software and calculated a bandgap of 0.109 eV for an O/C ratio of 0.0625 and a maximum of 3.004 eV for an O/C ratio of 0.50. Lundie *et al.* 2014 [32] reported

a theoretical study showing the possibility of tuning the bandgap in the range of 4.38 to 1.31 eV by gradually removing 2 to 4 oxygen atoms. Jin Yiqian *et al.* 2020 [10] found that the epoxide groups gradually shifted the bandgap from 0.944 eV to 2.659 eV as the O/C ratio increased from 0.17 to 0.50. V. Gupta *et al.* 2017 [12] reported a bandgap of 3.89 eV for a GO with an O/C ratio of 0.6238 and Cano *et al.* (2022) [33] conducted a quantitative analysis to identify the oxidation degree of GOs, which were found to be 4.1%, 49.5%, and 53.9%. Additionally, they calculated bandgaps ranging from 0.8 to 2.18 eV. In this work, the estimated bandgap values of GOs are in the range of 0.211 to 3.58 eV for an O/C ratio of 0.06 to 0.5, following an almost linear relationship between the bandgap and the O/C ratio. This linear dependence is mainly attributed to the loss of linearity and symmetry in the material and the increase in the amount of non-conducting sp^3 states [34]. Table 1 gives a comparative summary of theoretical-experimental studies that have measured the bandgap in graphene and its derivatives and is consistent with the results described above.

Table 3.1. Comparison of the reported bandgap of GO and derivatives (*reprinted from our publisher work on Elsevier 2023 [19]*).

Type of investigation	Material	Method	Oxidation degree	Bandgap	Gradient approximation	Functional	Ref.
Theory	GO	DFT	O/C=0.0625-0.50	0.109-3.004 eV	GGA	PBE	[31]
Theory	rGO	DFT	Removal of 2 to 4 oxygen atoms	4.38 a 1.31 eV	GGA	PBE	[32]
Theory	rGO	DFT	O/C=0.017-0.50	0.944-2.659 eV	GGA	PBE	
Experiment	rGO	Commercial	HNO ₃ concentration varied from 5 to 40%.	0.264 to 0.786 eV	-	-	[10]
Experiment	GO	Modified Hummer's Method	62.38 % by XPS	3.89 eV	-	-	[12]
Experiment	GO	Tour Method	4.1-53.9% by XPS	0.8 a 2.18 eV	-	-	[33]
Experiment	GO	Staudenmaier Method	Reduction controlled by sonification	2 to 0.02 eV	-	-	[35]
Theory	rGO	DFT	1 oxygen atom	0.3 eV	LSDA	Perdew and Wang	[36]
Experiment	GO	Hummers' Method	I _D /I _G =0.99	1.75 eV	-	-	[37]
Experiment	GO	Hummers' Method	I _D /I _G =0.99-1.05	1.75-2.2eV	-	-	[38]

3.3.3. Electronic band structure

The incorporation of oxygenated groups in the basal plane of graphene leads to the formation of sp^3 bonding which gradually converts GO into an electronic insulator at higher oxygen concentration. In GO with higher O/C ratios, sp^2 clusters develop within the sp^3 C-O matrix and may induce insulator character for strong functionalization with oxygen groups. This is explained by the breakdown of the π -electronic bonding of the carbon atoms during the oxidation of graphene, leading to the opening of a bandgap at the Brillouin zone boundaries as illustrated in Fig. 3.6.

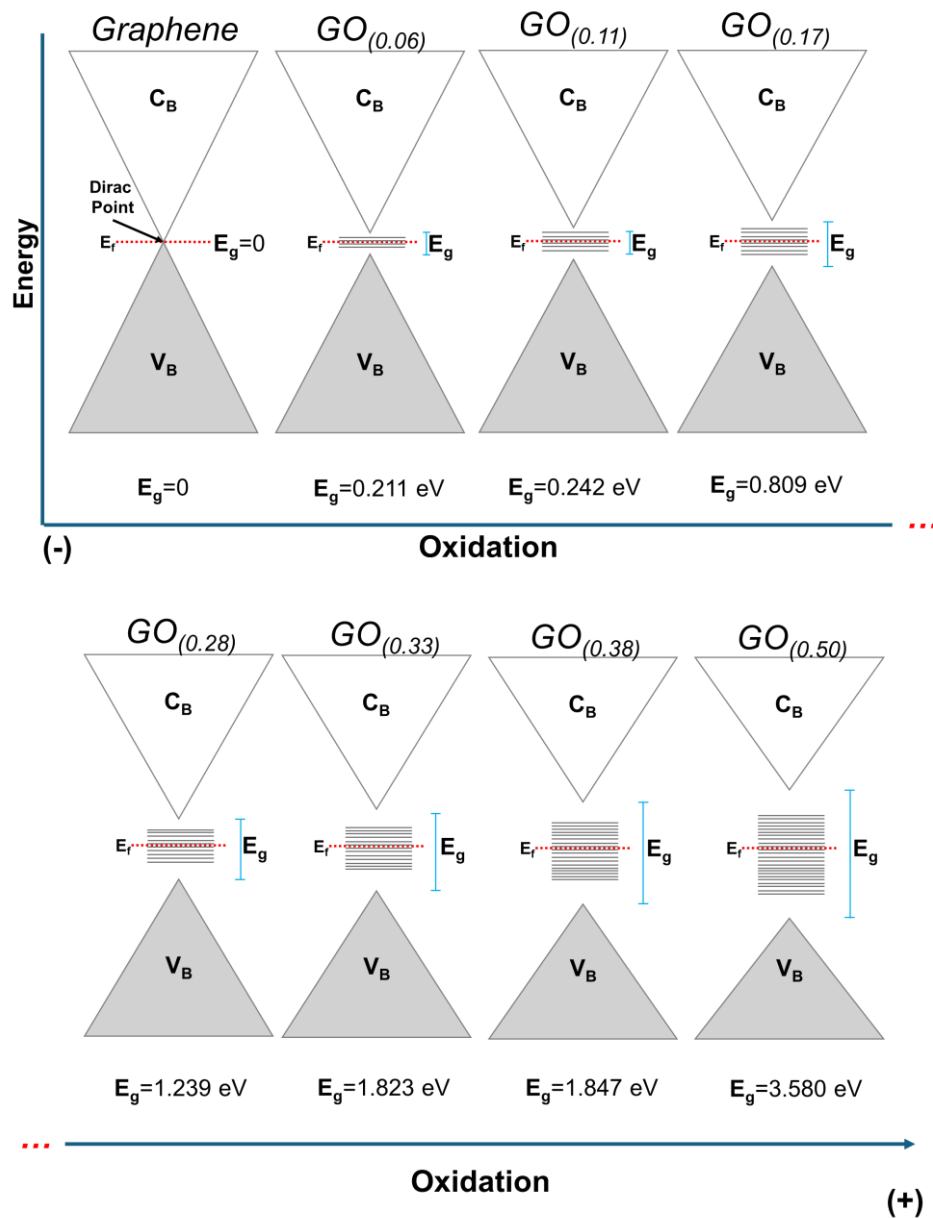


Fig. 3.6. Energy level diagrams with electronic transitions.

The optoelectronic properties of carbon materials with a combination of sp^2 and sp^3 bonding are mainly controlled by the π and π^* -states of the sp^2 sites, which lie in the σ - σ^* -gap. To contextualize, the π - π^* transition is an electronic transition that occurs in molecules or materials containing conjugated π -systems. The latter consists of a network of atoms with adjacent p -orbitals that overlap to form delocalized π -molecular orbitals (Fig. 3.7.). During the π - π^* electronic transition, an electron in the π -bonding molecular orbital is energetically promoted to the equivalent π^* -anti-bonding molecular orbital. This transition generally leads to the absorption of light within the ultraviolet or visible spectrum. In the case of GO, the π - π^* -transition is related to the delocalized π -bonding network present in the graphene plane [39]. In contrast, the n - π^* electronic transition refers to the process of exciting an electron from a non-bonding orbital (n), also known as a lone pair orbital, to the anti-bonding π^* orbital. The n - π^* transition generally leads to the absorption of light within the ultraviolet or visible spectrum. In the case of GO, the n - π^* transition is related to the oxygen-containing functional groups that are present on the graphene surface [40]. An energy level diagram showing the electronic transitions is shown in Fig. 3.7. Functional groups in GO can cause modifications in the electrical structure of the graphene lattice, leading to the creation of a bandgap. This alteration can have a substantial impact on the electronic and optical characteristics of the material.

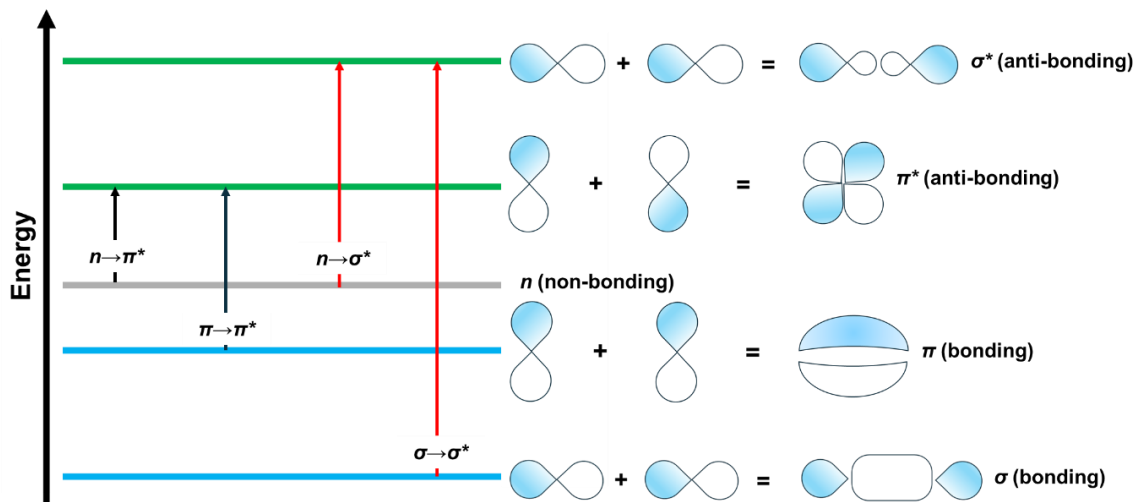


Fig. 3.7. Molecular orbitals are illustrated at different energy levels.

3.4. Anatase TiO₂ structure

3.4.1. Optimized structure and band structure

The lattice parameters obtained for the resulting structure after a geometry optimization were $c=9.486 \text{ \AA}$ and $a=b=3.776 \text{ \AA}$, in agreement with values previously mentioned by other authors [41]. The optimized TiO₂ layered structure with the surface (010) is shown in Fig. 3.8.

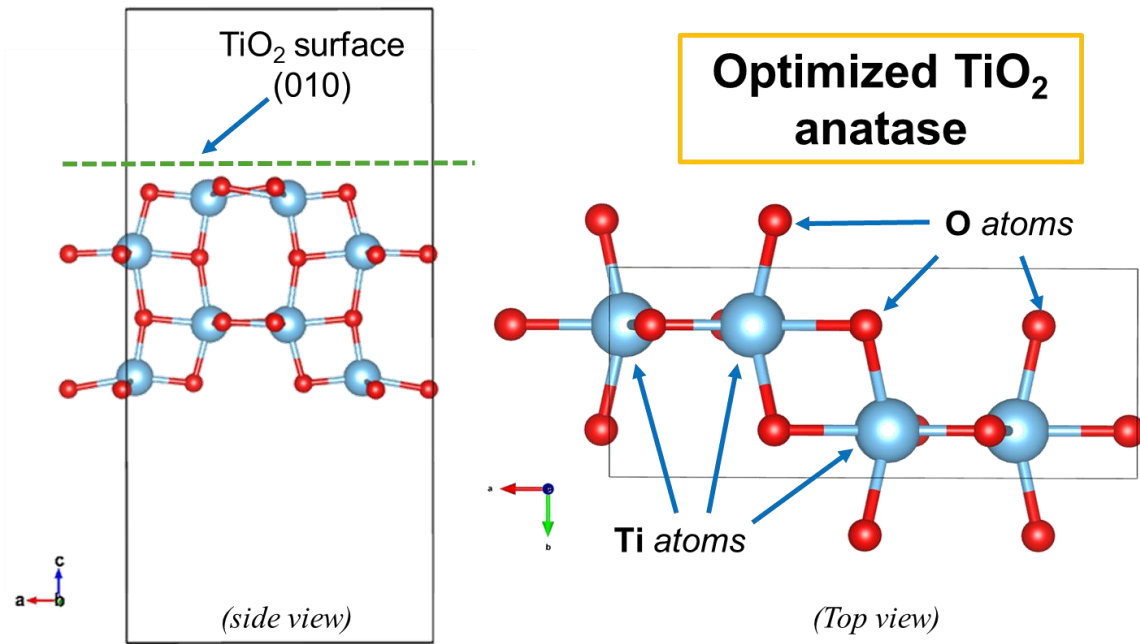


Fig. 3.8. TiO₂ (010) structure optimized cell (reprinted from our publisher work with permission from IEEE, copyright 2023 [42]).

Fig. 3.9. shows the band structure and electron density of states (DOS) of the TiO₂ layer under investigation. The (G) and (F) points in the Brillouin zone of TiO₂ correspond to the conduction band minimum (C_B-min) and valence band maximum (V_B-Max) of the material, respectively. The calculations support an indirect bandgap of 3.23 eV, which is in agreement with previous results [43]. According to the DOS, the V_B consists of O 2p states, whereas the C_B is composed of Ti 3d states [44].

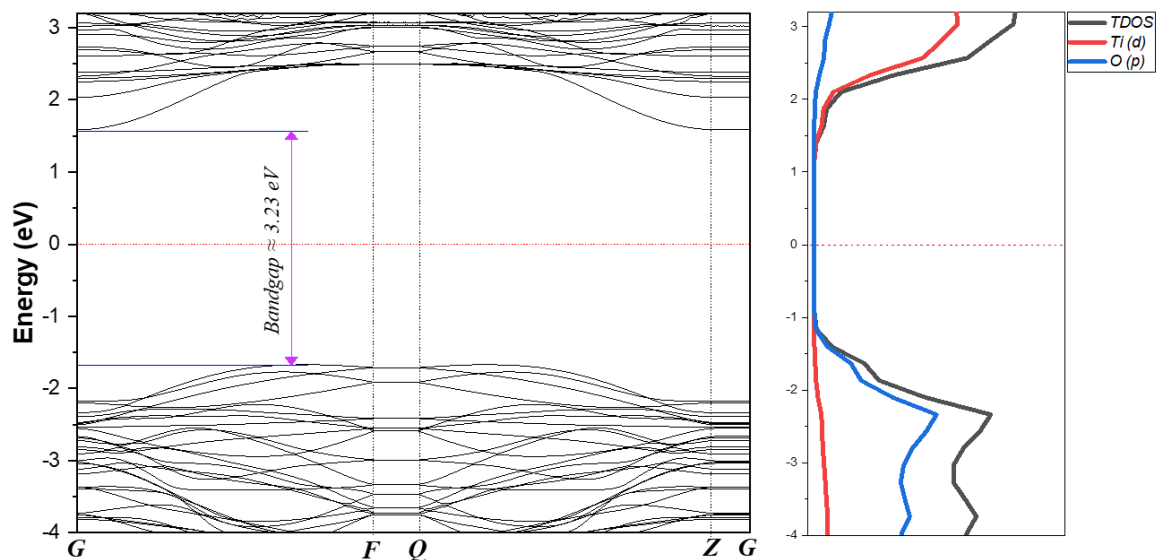


Fig. 3.9. Band structure and DOS for TiO₂ (010) (reprinted from our publisher work with permission from IEEE, copyright 2023 [42]).

3.5. Hybrid structures based on TiO₂ and Graphene/GO

3.5.1. Optimized geometry of hybrid TiO₂-Graphene-based structures

Following the addition of a graphene or GO layer onto the (010) surface of the relaxed TiO₂, the hybrid structures underwent another optimization procedure, enabling the surface layer of atoms to relax unrestrictedly. In consequence, changes in the atomic positions of TiO₂ were observed, while the graphene and GO layers were moved away from the surface favoring a more stable and less energetic arrangement of the whole system [45]. A separation distance of 2.8 Å is visible in the TiO₂-graphene hybrid structure's most stable configuration (Fig. 3.10.), which points out weak Van der Waals interactions at the interfaces [46].

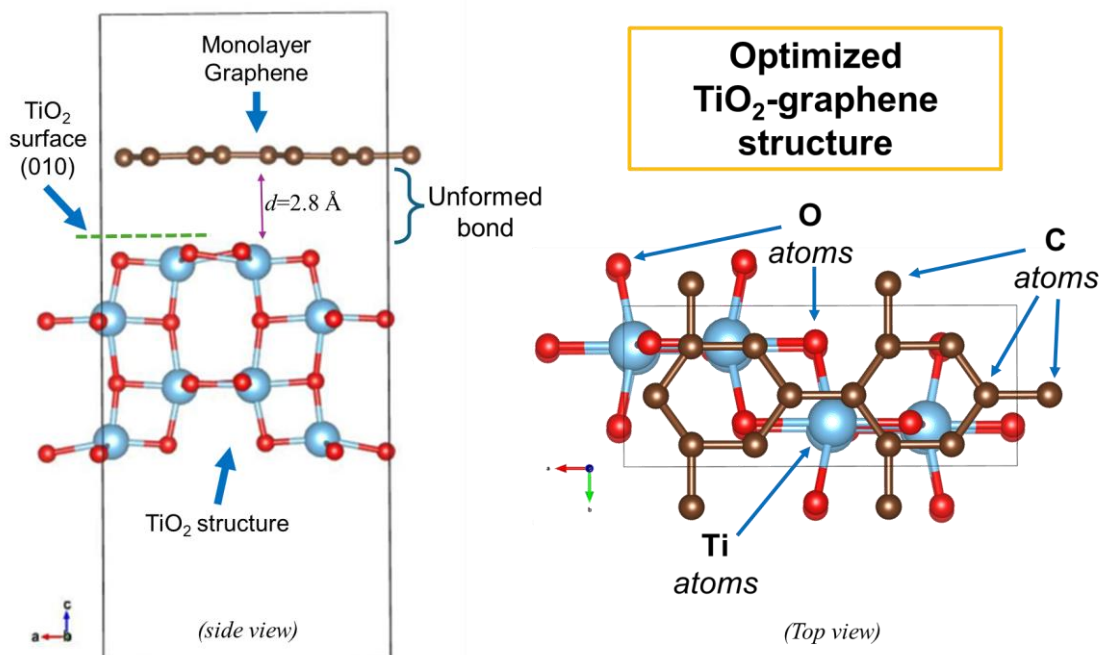


Fig. 3.10. TiO₂-graphene structure optimized cell (*reprinted from our publisher work with permission from IEEE, copyright 2023 [42]*).

In principle, the significant distance could suggest that these materials do not show a great affinity for each other at the atomic level. The fact that the lattice symmetry and atomic arrangements of TiO₂ and graphene do not coincide, lead also to a weak interface between the two materials [47]. Additionally, the difference in their electronic properties and the absence of coincident energy levels could limit the formation of strong covalent or electron interactions between the two materials [48]. It is important to note that the lattice mismatch and the difference in electrical properties between TiO₂ and graphene may not be adequately compensated for by weak van der Waals interactions, which are typically essential for maintaining graphene structures [49, 50]. As a result, weak forces fail to form a well-connected interface between the two materials. The significant separation between the layers being described reduces the anticipated synergistic effects, hence restricting the enhancement of the material properties. Furthermore, according to previous experimental investigations, it is

possible to state that graphene is a material that does not readily react with TiO_2 , so, if it is to be used in nanostructures, it is necessary to alter its structure by adding defects and/or oxygenated groups that allow layers anchoring [51, 52]. These results also offer opportunities for alternative approaches, such as the introduction of interlayers to facilitate stronger interactions and/or chemical bonding.

3.5.2. TiO_2 -GO structure optimized geometry

The modeling of the TiO_2 -GO hybrid structure (Fig. 3.11.) containing an epoxide group (C-O-C), provides interesting information about the interaction between the layers. The geometry relaxation of the mentioned hybrid material showed that both layers are going to be connected through the oxygen atom coming from the degraded epoxide group. It was observed that one C-O bond in the epoxide group is broken creating a new O-Ti bond. The observed connection between TiO_2 and GO through the epoxide group suggests the formation of Ti-O-C bonding, indicating chemical interaction between these two structures. The epoxide group acts as a bridge, facilitating the link between TiO_2 and GO. It is also important to note that there was no evidence of a direct bonding between the TiO_2 and the carbon atoms of the GO. The absence of a chemical bonding suggests a limited interaction between the studied layers similar to the previously discussed TiO_2 -graphene hybrid. Nevertheless, the creation of the Ti-O-C bond demonstrates the ability of the epoxide group to promote the bonding of TiO_2 and GO.

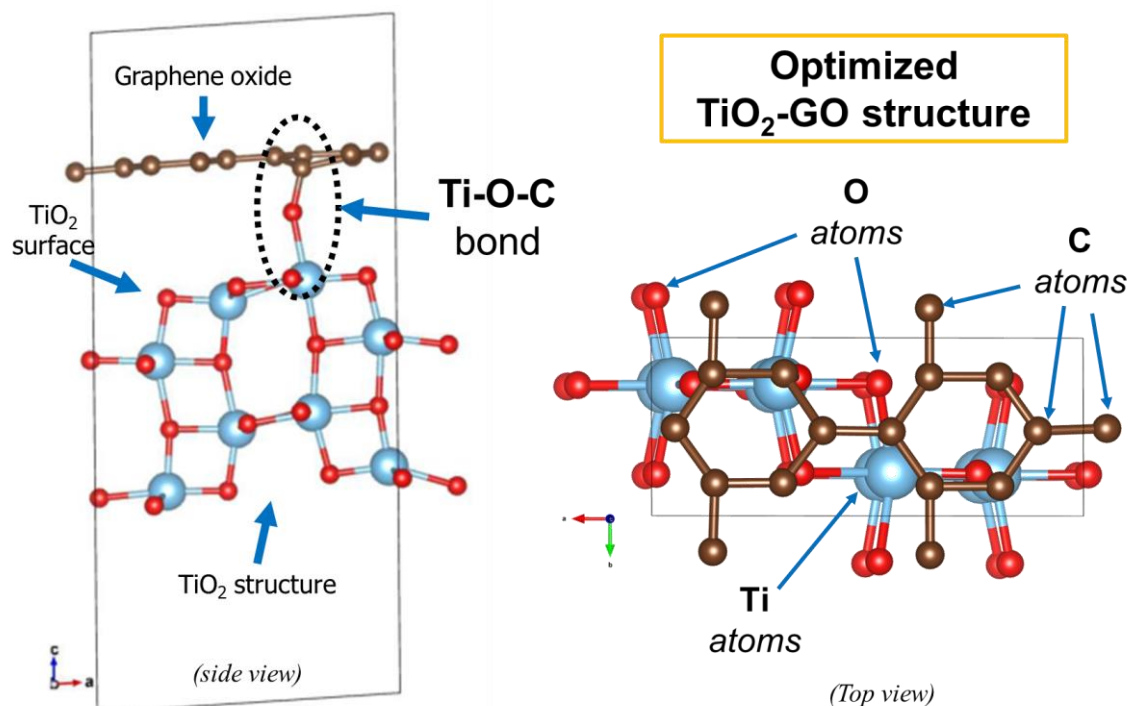


Fig. 3.11. TiO_2 -GO structure optimized cell (reprinted from our publisher work with permission from IEEE, copyright 2023 [42]).

3.5.3. Electronic structures of hybrid nanostructures

With the incorporation of the graphene layer on the (010) surface of TiO_2 , new electronic energy levels are created as shown coming from the overlapping of the TiO_2 and graphene energy levels (Fig. 3.12.a). The lack of overlap between the V_B and C_B and the difference in energy levels create this energy gap. The precise mechanisms underlying the extension of the C_B below the Fermi level and the absence of connection with the V_B in the TiO_2 -graphene system may involve complex electronic interactions, charge transfer effects, or interfacial states. These interface effects modify the TiO_2 electronic band structure. However, the magnitude of the reduction in the forbidden band would normally be small and localized to the interface region.

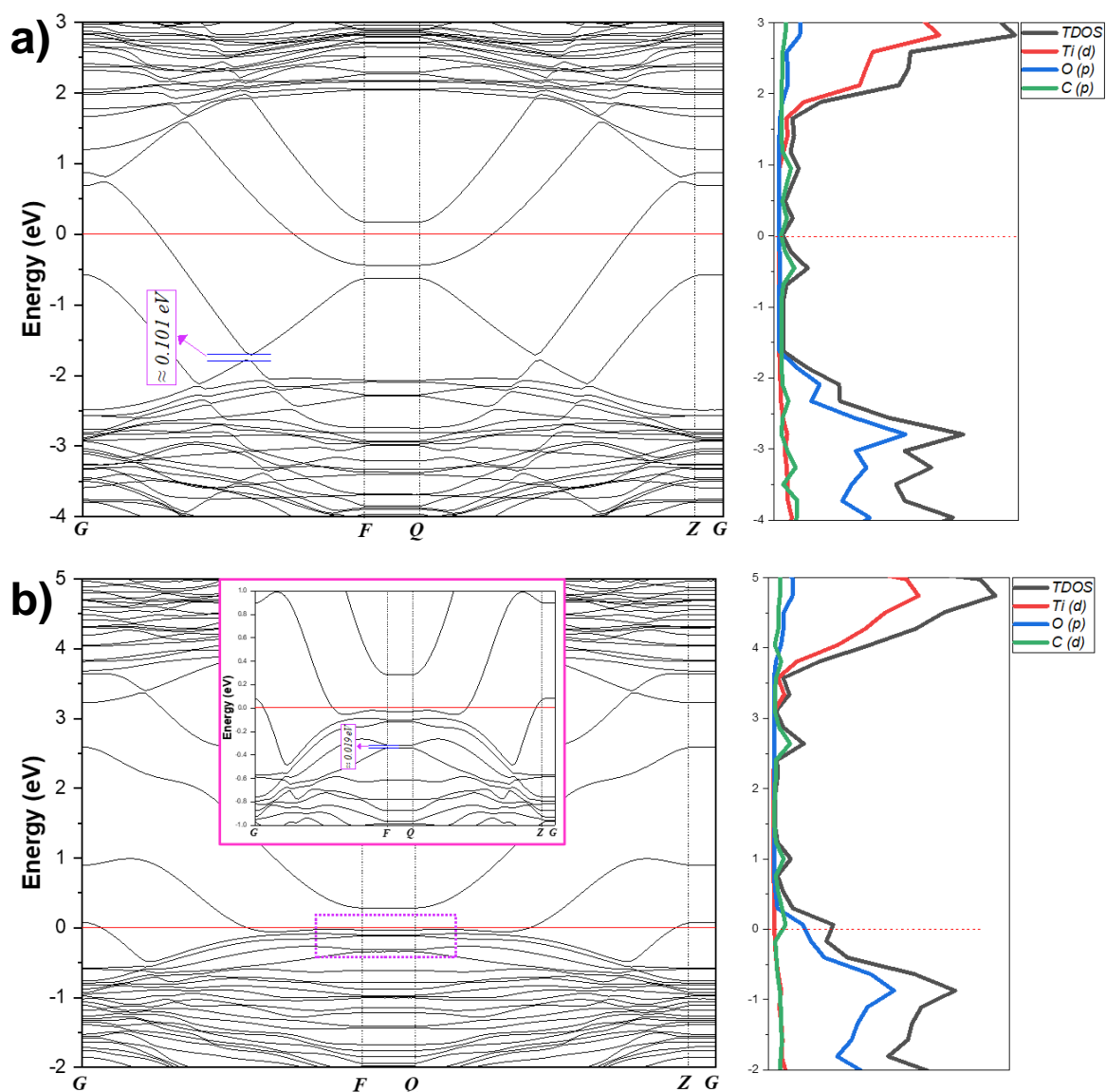


Fig. 3.12. Band structures and DOS for (a) TiO_2 -graphene and (b) TiO_2 -GO (reprinted from our publisher work with permission from IEEE, copyright 2023 [42]).

On the other hand, Fig. 3.12.b. shows the calculated energy bands for TiO₂ and GO hybrid. The direct connection between GO and TiO₂ through the functional group generates more hybridized electron states from both layers. This hybridization leads to the formation of new bands and the modification of existing bands, including C_B and V_B [53]. The introduction of functional groups in GO creates localized energy states, which contribute to the DOS near the band edges of TiO₂ [54, 55] potentially narrowing the bandgap and increasing the DOS near the band boundaries. The DOS in the bandgap region is filled with previously unoccupied states, allowing electron transitions at lower energies.

3.4. Conclusion

In this Chapter, using Density Functional Theory (DFT), the variation of the bandgap of GO as a function of the O/C ratio has been studied, and the concluding remarks are hereafter outlined:

- The direct relationship between the bandgap and the number of epoxide functional groups in the GO was demonstrated. A gradual increase in the bandgap from 0.211 eV to ≈3.58 eV was observed by varying the O/C ratio from 0.06 to 0.50. This phenomena can be attributed to the presence of functional groups, which cause a breaking of symmetry in the lattice plane. This, in turn, leads to a change in hybridization from sp^2 to sp^3 , resulting in the creation of a bandgap that is so high that the material exhibits semiconductor or electrical insulator properties. The incorporation of these functional groups causes a disturbance in the original perfect hexagonal arrangement of graphene and triggers the formation of specific electronic states within the energy band structure, resulting in the creation of a bandgap.
- The analysis of the TiO₂-graphene and TiO₂-GO systems, respectively, highlights important information about the interaction between the associated structures. The calculations revealed improved connectivity, suggesting the potential for interaction and interface formation between TiO₂ and GO, contrary to what was observed in TiO₂-graphene. Our DFT calculations further demonstrated that the incorporation of graphene and GO created intermediate bands reducing the bandgap of TiO₂.
- It is worth noting that the strategies to strengthen the connection between TiO₂ and graphene structures, as well as the integration of functional groups, may offer opportunities to optimize the electronic properties and improve the performance of these materials in various applications. The results of this study contribute to the fundamental understanding of TiO₂-graphene and TiO₂-GO systems and serve as support for the experimental behaviors discussed in subsequent chapters.

References

1. Ernzerhof, M., Scuseria, G.E.: Perspective on “inhomogeneous electron gas.” Theor Chem Acc. 103, 259–262 (2000). <https://doi.org/10.1007/S002149900030>

2. Born, M., Heisenberg, W.: Zur Quantentheorie der Molekeln. Original Scientific Papers Wissenschaftliche Originalarbeiten. 216–246 (1985). https://doi.org/10.1007/978-3-642-61659-4_16
3. Kohn, W.: Density functional theory.
4. Hartree, D.R.: The Wave Mechanics of an Atom with a Non-Coulomb Central Field. Part I. Theory and Methods. Mathematical Proceedings of the Cambridge Philosophical Society. 24, 89–110 (1928). <https://doi.org/10.1017/S0305004100011919>
5. Jones, R.O., Gunnarsson, O.: The density functional formalism, its applications and prospects. Rev Mod Phys. 61, 689 (1989). <https://doi.org/10.1103/RevModPhys.61.689>
6. Kohn, W., Becke, A.D., Parr, R.G.: Density Functional Theory of Electronic Structure. Journal of Physical Chemistry. 100, 12974–12980 (1996). <https://doi.org/10.1021/JP960669L>
7. Ramezanzadeh, M., Bahlakeh, G., Ramezanzadeh, B.: Construction of an epoxy composite with excellent thermal/mechanical properties using graphene oxide nanosheets reduced/functionalized by Tamarindus indica extract/zinc ions; detailed experimental and DFT-D computer modeling explorations. Results Phys. 19, (2020). <https://doi.org/10.1016/j.rinp.2020.103400>
8. Gui, Y., Hao, Z., Li, X., Tang, C., Xu, L.: Gas sensing of graphene and graphene oxide nanoplatelets to ClO₂ and its decomposed species. Superlattices Microstruct. 135, (2019). <https://doi.org/10.1016/j.spmi.2019.106248>
9. Monkhorst, H.J., Pack, J.D.: Special points for Brillouin-zone integrations. Phys Rev B. 13, 5188 (1976). <https://doi.org/10.1103/PhysRevB.13.5188>
10. Jin, Y., Zheng, Y., Podkolzin, S.G., Lee, W.: Band gap of reduced graphene oxide tuned by controlling functional groups. J. Mater. Chem. C. 8, 4885 (2020). <https://doi.org/10.1039/c9tc07063j>
11. Zhou, X., Zheng, J., Wu, H., Yang, H., Zhang, J., Guo, S.: Reducing graphene oxide via hydroxylamine: A simple and efficient route to graphene. Journal of Physical Chemistry C. 115, 11957–11961 (2011). <https://doi.org/10.1021/jp202575j>
12. Gupta, V., Sharma, N., Singh, U., Arif, M., Singh, A.: Higher oxidation level in graphene oxide. Optik (Stuttg). 143, 115–124 (2017). <https://doi.org/10.1016/J.IJLEO.2017.05.100>
13. Erickson, K., Erni, R., Lee, Z., Alem, N., Gannett, W., Zettl, A.: Determination of the Local Chemical Structure of Graphene Oxide and Reduced Graphene Oxide. Advanced Materials. 22, 4467–4472 (2010). <https://doi.org/10.1002/ADMA.201000732>
14. Mayorov, A.S., Gorbachev, R. V., Morozov, S. V., Britnell, L., Jalil, R., Ponomarenko, L.A., Blake, P., Novoselov, K.S., Watanabe, K., Taniguchi, T., Geim, A.K.: Micrometer-scale ballistic transport in encapsulated graphene at room temperature. Nano Lett. 11, 2396–2399 (2011). <https://doi.org/10.1021/nl200758b>
15. Castro Neto, A.H., Guinea, F., Peres, N.M.R., Novoselov, K.S., Geim, A.K.: The electronic properties of graphene. Rev Mod Phys. 81, (2009). <https://doi.org/10.1103/RevModPhys.81.109>
16. Li, Y., Zhao, Y., Cheng, H., Hu, Y., Shi, G., Dai, L., Qu, L.: Nitrogen-doped graphene quantum dots with oxygen-rich functional groups. J Am Chem Soc. 134, (2012). <https://doi.org/10.1021/ja206030c>
17. Eda, G., Mattevi, C., Yamaguchi, H., Kim, H., Chhowalla, M.: Insulator to Semimetal Transition in Graphene Oxide. Journal of Physical Chemistry C. 113, 15768–15771 (2009). <https://doi.org/10.1021/JP9051402>
18. Gokus, T., Nair, R.R., Bonetti, A., Böhmeler, M., Lombardo, A., Novoselov, K.S., Geim, A.K., Ferrari, A.C., Hartschuh, A.: Making graphene luminescent by oxygen plasma treatment. ACS Nano. 3, 3963–3968 (2009). <https://doi.org/10.1021/nm9012753>
19. Cano, F.J., Romero-Núñez, A., Liu, H., Reyes-Vallejo, O., Ashok, A., Velumani, S., Kassiba, A.: Variation in the bandgap by gradual reduction of GOs with different oxidation degrees: A DFT analysis. Diam Relat Mater. 139, (2023). <https://doi.org/10.1016/j.diamond.2023.110382>
20. Dreyer, D.R., Park, S., Bielawski, C.W., Ruoff, R.S.: The chemistry of graphene oxide. Chem Soc Rev. 39, 228–240 (2010). <https://doi.org/10.1039/B917103G>
21. Jin, Y., Zheng, Y., Podkolzin, S.G., Lee, W.: Band gap of reduced graphene oxide tuned by controlling functional groups. J. Mater. Chem. C. 8, 4885 (2020). <https://doi.org/10.1039/c9tc07063j>
22. Pritchard, H.O., Skinner, H.A.: The Concept of Electronegativity. Chem Rev. 55, (1955). <https://doi.org/10.1021/cr50004a005>
23. Ramezanzadeh, M., Bahlakeh, G., Ramezanzadeh, B.: Green synthesis of reduced graphene oxide nanosheets decorated with zinc-centered metal-organic film for epoxy-ester composite coating reinforcement: DFT-D modeling and experimental explorations. J Taiwan Inst Chem Eng. 114, (2020). <https://doi.org/10.1016/j.jtice.2020.09.003>
24. Cano, F.J., Reyes-Vallejo, O., Ashok, A., Olvera, M. de la L., Velumani, S., Kassiba, A.: Mechanisms of dyes adsorption on titanium oxide– graphene oxide nanocomposites. Ceram Int. 49, 21185–21205 (2023). <https://doi.org/10.1016/J.CERAMINT.2023.03.249>

25. Keshmiri, N., Najmi, P., Ramezanzadeh, B., Ramezanzadeh, M., Bahlakeh, G.: Nano-scale P, Zn-codoped reduced-graphene oxide incorporated epoxy composite; synthesis, electronic-level DFT-D modeling, and anti-corrosion properties. *Prog Org Coat.* 159, (2021). <https://doi.org/10.1016/j.porgcoat.2021.106416>
26. Keshmiri, N., Najmi, P., Ramezanzadeh, M., Ramezanzadeh, B., Bahlakeh, G.: Ultrastable Porous Covalent Organic Framework Assembled Carbon Nanotube as a Novel Nanocontainer for Anti-Corrosion Coatings: Experimental and Computational Studies. *ACS Appl Mater Interfaces.* 14, (2022). <https://doi.org/10.1021/acsami.1c24185>
27. Cano, F.J., Reyes-Vallejo, O., Romero-Nunez, A., Covarrubias Garcia, J., Garcia-Sotelo, A., Velumani, S., Kassiba, A.: MB adsorption by TiO₂/GO nanocomposites: A comparison of the synthesis method. 2022 19th International Conference on Electrical Engineering, Computing Science and Automatic Control (CCE). 1–6 (2022). <https://doi.org/10.1109/CCE56709.2022.9975906>
28. Reynosa-Martínez, A.C., Gómez-Chayres, E., Villaurrutia, R., López-Honorato, E.: Controlled Reduction of Graphene Oxide Using Sulfuric Acid. *Materials* 2021, Vol. 14, Page 59. 14, 59 (2020). <https://doi.org/10.3390/MA14010059>
29. Carvalho, A., Costa, M.C.F., Marangoni, V.S., Ng, P.R., Nguyen, T.L.H., Castro Neto, A.H.: The degree of oxidation of graphene oxide. *Nanomaterials*. 11, (2021). <https://doi.org/10.3390/nano11030560>
30. Boukhvalov, D.W., Katsnelson, M.I.: Modeling of graphite oxide. *J Am Chem Soc.* 130, 10697–10701 (2008). <https://doi.org/10.1021/ja8021686>
31. Huang, H., Li, Z., She, J., Wang, W.: Oxygen density dependent band gap of reduced graphene oxide. *J Appl Phys.* 111, 054317 (2012). <https://doi.org/10.1063/1.3694665>
32. Lundie, M.J., Tomić, S., Šljivančanin, Ž.: Ab initio study of structural and electronic properties of partially reduced graphene oxide. *Phys Scr.* 2014, 014019 (2014). <https://doi.org/10.1088/0031-8949/2014/T162/014019>
33. Cano, F.J., Reyes-Vallejo, O., Diaz, J.J., Velumani, S., Kassiba, A.: Effect of the oxidation degree on the bandgap of graphene oxides by Tour method. 2022 19th International Conference on Electrical Engineering, Computing Science and Automatic Control (CCE). 1–6 (2022). <https://doi.org/10.1109/CCE56709.2022.9975930>
34. Wang, Y., Wang, L., Wang, H.Y., Chen, Q.D., Sun, H.B.: Ultrafast Spectroscopic Study of Insulator-Semiconductor-Semimetal Transitions in Graphene Oxide and Its Reduced Derivatives. *Journal of Physical Chemistry C.* 123, 22550–22555 (2019). <https://doi.org/10.1021/acs.jpcc.9b03926>
35. Shen, Y., Yang, S., Zhou, P., Sun, Q., Wang, P., Wan, L., Li, J., Chen, L., Wang, X., Ding, S., Zhang, D.W.: Evolution of the band-gap and optical properties of graphene oxide with controllable reduction level. *Carbon N Y.* 62, (2013). <https://doi.org/10.1016/j.carbon.2013.06.007>
36. Tang, S., Cao, Z.: Adsorption of nitrogen oxides on graphene and graphene oxides: Insights from density functional calculations. *Journal of Chemical Physics.* 134, (2011). <https://doi.org/10.1063/1.3541249>
37. Park, J., Kim, Y., Park, S.Y., Sung, S.J., Jang, H.W., Park, C.R.: Band gap engineering of graphene oxide for ultrasensitive NO₂ gas sensing. *Carbon N Y.* 159, (2020). <https://doi.org/10.1016/j.carbon.2019.11.063>
38. Gallegos-Pérez, W.R., Reynosa-Martínez, A.C., Soto-Ortiz, C., Angélica Álvarez-Lemus, M., Barroso-Flores, J., García Montalvo, V., López-Honorato, E.: Effect of UV radiation on the structure of graphene oxide in water and its impact on cytotoxicity and As(III) adsorption. *Chemosphere.* 249, 126160 (2020). <https://doi.org/10.1016/J.CHEMOSPHERE.2020.126160>
39. Tene, T., Guevara, M., Benalcázar Palacios, F., Morocho Barrionuevo, T.P., Vacacela Gomez, C., Bellucci, S.: Optical properties of graphene oxide. *Front Chem.* 11, 1214072 (2023). <https://doi.org/10.3389/FCHEM.2023.1214072/BIBTEX>
40. Abid, P., Sehrawat, S.S., Islam, M., Ahmad, S.: Reduced graphene oxide (rGO) based wideband optical sensor and the role of Temperature, Defect States and Quantum Efficiency OPEN. 8, (2018). <https://doi.org/10.1038/s41598-018-21686-2>
41. Liu, X., Fu, J.: Electronic and elastic properties of the tetragonal anatase TiO₂ structure from first principle calculation. *Optik (Stuttg).* 206, 164342 (2020). <https://doi.org/10.1016/J.IJLEO.2020.164342>
42. Cano, F.J., Korolevych, O., Makowska-Janusik, M., Coste, S., Ashok, A., Velumani, S., Kassiba, A.: G and GO interaction into TiO₂ (010) anatase and its influence on the bandgap: DFT Study. 2023 20th International Conference on Electrical Engineering, Computing Science and Automatic Control, CCE 2023. (2023). <https://doi.org/10.1109/CCE60043.2023.10332908>
43. Cano, F.J., Romero-Nunez, A., Jantrania, A., Liu, H., Kassiba, A., Velumani, S.: Bandgap dependence on facet and size engineering of TiO₂: A DFT Study. CCE 2021 - 2021 18th International Conference on Electrical Engineering, Computing Science and Automatic Control. (2021). <https://doi.org/10.1109/CCE53527.2021.9632880>

44. Raghav, A., Tri Hanindriyo, A., Utimula, K., Abbasnejad, M., Maezono, R., Panda, E.: Intrinsic electronic defect states of anatase using density functional theory. *Comput Mater Sci.* 184, 109925 (2020). <https://doi.org/10.1016/J.COMMATSCI.2020.109925>
45. Mishra, S.B., Roy, S.C., Nanda, B.R.K.: Electronic structure of graphene/TiO₂ interface: Design and functional perspectives. *Appl Surf Sci.* 542, (2021). <https://doi.org/10.1016/j.apsusc.2020.148709>
46. Datteo, M., Liu, H., Di Valentin, C.: Water on Graphene-Coated TiO₂: Role of Atomic Vacancies. *ACS Appl Mater Interfaces.* 10, (2018). <https://doi.org/10.1021/acsami.7b18087>
47. Liu, H., Zhu, D., Shi, H., Shao, X.: Fabrication of a Contamination-Free Interface between Graphene and TiO₂ Single Crystals. *ACS Omega.* 1, (2016). <https://doi.org/10.1021/acsomega.6b00074>
48. Bukowski, B., Deskins, N.A.: The interactions between TiO₂ and graphene with surface inhomogeneity determined using density functional theory. *Physical Chemistry Chemical Physics.* 17, (2015). <https://doi.org/10.1039/c5cp04073f>
49. Zhang, H., Xu, P., Du, G., Chen, Z., Oh, K., Pan, D., Jiao, Z.: A facile one-step synthesis of TiO₂/graphene composites for photodegradation of methyl orange. *Nano Res.* 4, (2011). <https://doi.org/10.1007/s12274-010-0079-4>
50. Yu, S., Wang, X., Zhang, R., Yang, T., Ai, Y., Wen, T., Huang, W., Hayat, T., Alsaedi, A., Wang, X.: Complex Roles of Solution Chemistry on Graphene Oxide Coagulation onto Titanium Dioxide: Batch Experiments, Spectroscopy Analysis and Theoretical Calculation. *Sci Rep.* 7, (2017). <https://doi.org/10.1038/srep39625>
51. Haghghi, M., Khodadadi, A., Golestanian, H., Aghadavoudi, F.: Effects of defects and functional groups on graphene and nanotube thermoset epoxy-based nanocomposites mechanical properties using molecular dynamics simulation. *Polymers and Polymer Composites.* 29, (2021). <https://doi.org/10.1177/0967391120929075>
52. Liao, C., Li, Y., Tjong, S.C.: Graphene Nanomaterials: Synthesis, Biocompatibility, and Cytotoxicity. *International Journal of Molecular Sciences* 2018, Vol. 19, Page 3564. 19, 3564 (2018). <https://doi.org/10.3390/IJMS19113564>
53. Bukowski, B., Deskins, N.A.: The interactions between TiO₂ and graphene with surface inhomogeneity determined using density functional theory. *Physical Chemistry Chemical Physics.* 17, 29734–29746 (2015). <https://doi.org/10.1039/C5CP04073F>
54. Drisya, K.T., Solís-López, M., Ríos-Ramírez, J.J., Durán-Álvarez, J.C., Rousseau, A., Velumani, S., Asomoza, R., Kassiba, A., Jantrania, A., Castaneda, H.: Electronic and optical competence of TiO₂/BiVO₄ nanocomposites in the photocatalytic processes. *Scientific Reports* 2020 10:1. 10, 1–16 (2020). <https://doi.org/10.1038/s41598-020-69032-9>
55. Timoumi, A., Timoumi, A.: Reduction Band Gap Energy of TiO₂ Assembled with Graphene Oxide Nanosheets. *Graphene.* 7, 31–38 (2018). <https://doi.org/10.4236/GRAPHENE.2018.74004>

Chapter IV:

Tuning oxidation degree: A structural study of graphene oxides

As mentioned above, most of the outstanding properties of GO arise from its hybrid electronic structure, as it contains both the conducting π -states of the sp^2 carbon domains and the σ -states of the sp^3 carbon domains [1]. The previous chapter's theoretical DFT analysis shown that the electrical characteristics of GO can be altered by manipulating the sp^2/sp^3 ratios of the carbon atoms. The existence of oxygenated functional groups on the graphene sheets results in the formation of sp^3 domains in GO.

In this context, the experimental preparation of GOs is crucial to complement the theoretical results obtained by DFT. In addition, the experimental synthesis of GOs provides an opportunity to explore and control specific aspects of their structure and composition that cannot be fully captured by theoretical models. To elucidate the evolution of the morphological and structural characteristics of the graphene oxides as a function of the amount of the oxidizing agent $KMnO_4$ added, several characterization techniques were used, such as X-ray diffraction (XRD), Raman spectroscopy, SEM/TEM, and specific surface area (SSA) measurement by BET. The nature of the oxygenated species present at each oxidation degree was investigated by X-ray photoelectron spectroscopy (XPS) and Fourier Transform Infrared (FTIR) spectroscopy, respectively. The purity of the synthesized GOs was confirmed by electron paramagnetic resonance (EPR). The electrical properties of the resulting materials were studied at each degree of oxidation. The description of measurement conditions and the equipment used are described in detail in Chapter 2.

4.1. Removal of residual Mn^{2+} ions

The electronic and magnetic properties of GO can be affected by the presence of various types of defects, and its surface provides a unique opportunity to harbor chemical impurities. Previous research has indicated the presence of Mn^{2+} ions trapped between graphite sheets during the oxidation process using $KMnO_4$ for GO production [2, 3]. Paratala B, *et al* [4] have demonstrated that GO displays paramagnetic properties as a result of the existence of paramagnetic impurities, such as Mn^{2+} ions. While, Panich A, *et al* [5] argue that these ions do not exist as a separate phase but form paramagnetic charge transfer complexes with the graphene sheets, which should affect the structural, electronic, and magnetic properties of the

materials. To demonstrate the importance of the GO washing step in the presence of ligands, EPR spectroscopy was used. This technique detects unpaired electrons carried by defects of the carbon lattice due to broken bonds (dangling bonds), vacancies, or impurities such as Mn^{2+} in GO as will be discussed below. Localized or delocalized spins show EPR signals which depend on the effective spin multiplicity such as $S=1/2$ for unpaired electrons or $S=5/2$ for Mn^{2+} with the electronic configuration $3d^5$. So, the recorded signal is a combination of all the signals from the different coexisting paramagnetic species (unpaired electrons and Mn^{2+} ions). A brief comparative analysis by EPR was performed between GO washed in the presence and absence of CA. For this purpose, the GO synthesized with the highest amount of $KMnO_4$ was used, *i.e.* 10 g.

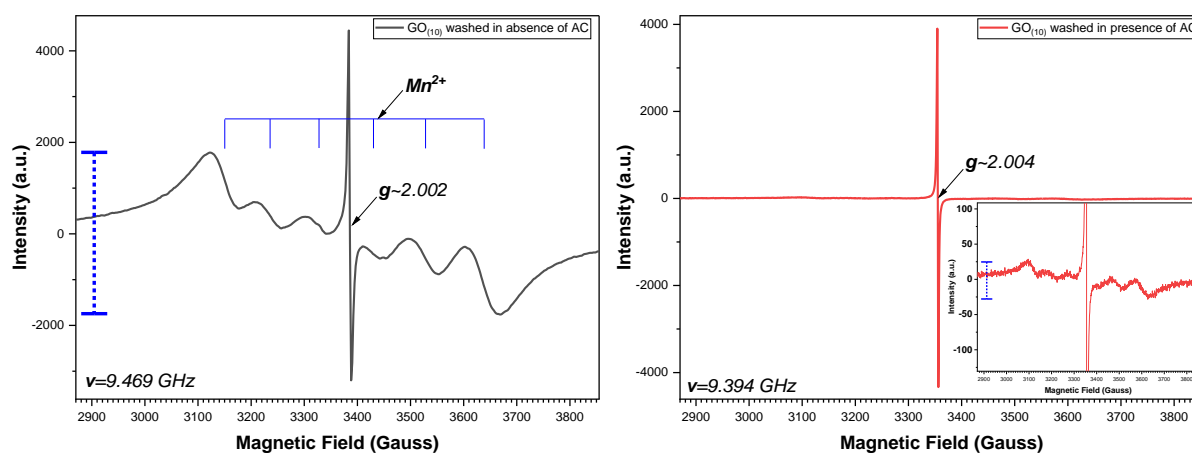


Fig. 4.1. EPR spectra of GO (a) GO washed in the absence of CA and (b) GO washed in the presence of CA - The box is the magnification of the horizontal line.

Fig. 4.1.a shows the room temperature EPR spectrum of the washed GO sample in the absence of CA. In this spectrum, there is a superposition of an intense and relatively narrow asymmetric signal together with a resolved hyperfine pattern of six broad lines characteristic of isolated complexes containing Mn^{2+} . The narrow singlet line in the center of the EPR spectrum is attributed to carbon radicals with a center of $g\sim 2.002$ and a line width $\Delta H\approx 1.2$ G, indicating the presence of free radicals [6]. The sextet hyperfine pattern is characteristic of polycrystalline samples containing magnetically diluted Mn^{2+} complexes ($S=5/2$, $I=5/2$) [7]. The well-defined resolution of the hyperfine structure suggests that the Mn^{2+} ions in the compound exist as remarkably magnetically dilute paramagnetic complexes, ruling out the presence of concentrated Mn^{2+} clusters or aggregates within the sample [5, 8]. As we observe only one sextuplet for the EPR signal of Mn^{2+} , we conclude that there is no anisotropy of the local environment of Mn^{2+} ions. In this case, all the electronic spin transitions are superimposed at the position of the central transition which occurs between the spin states $\left|\frac{5}{2}, \frac{1}{2}\right\rangle \rightarrow \left|\frac{5}{2}, -\frac{1}{2}\right\rangle$. The splitting of this electronic transition to six hyperfine lines is due to the nuclear spin of the Mn^{2+} nuclei ($I=5/2$). In contrast to the above features of the above EPR signal, Fig. 4.1.b. shows the EPR spectrum of the CA-washed variant, which is composed of nearly isotropic $s=1/2$ EPR spectrum single resonance line signal corresponding to carbon radicals in the GO. However, on closer inspection at near-zero intensities, faint signals from Mn^{2+} ions can be seen, albeit

much weaker and potentially negligible. This confirms the success of the process to obtain impurity-free GO in the presence of CA.

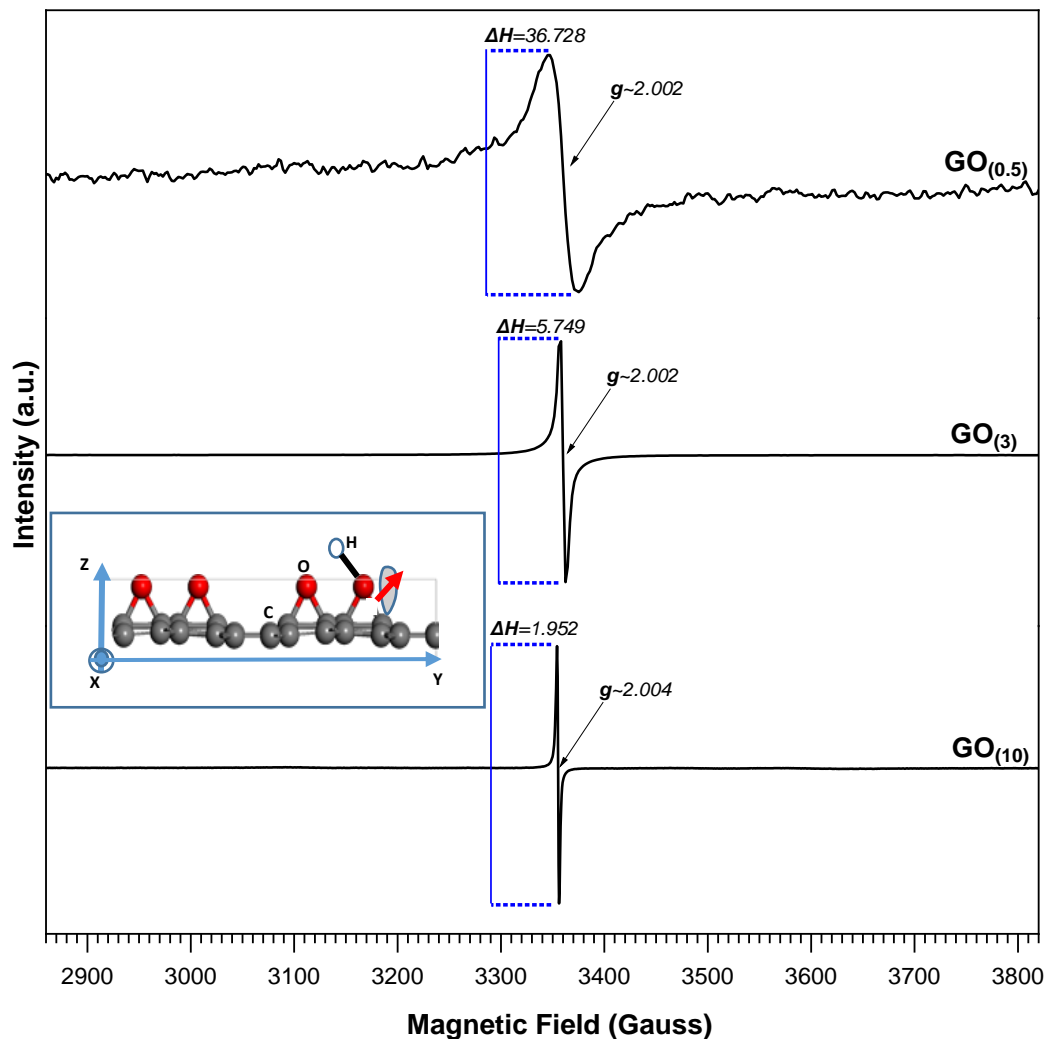


Fig. 4.2. EPR spectra of synthesized graphene oxides (less oxidized vs high oxidized)

Fig. 4.2. shows, the room-temperature evolution of the EPR signal of the synthesized GOs. The EPR signal consists of a single resonance line at $g \sim 2.002$ [6] which is characteristic of defects as unpaired spins of dangling bonds on carbon atoms. In a sample with a large number of spins, the EPR signal amplitude (ΔH) can be affected by spin-spin interactions, spin dynamics, and also by the disorder in the environments of localized unpaired spins. An increase in the concentration of paramagnetic species strengthens the spin-spin interactions which can induce dipolar broadening or exchange narrowing depending on the magnitude of the interactions. Several EPR investigations on carbon-based nanomaterials such as graphene, GO or rGO structures were documented from former works [9].

Initially, $GO_{(0.5)}$ exhibited a signal with a line width of about $\Delta H = 36.76$ G, which progressively varied until reaching a value $\Delta H = 1.95$ G for $GO_{(10)}$. This decrease in the line width correlates with the variation in the oxidation degree of the GOs. At low oxidation, dangling bonds are created as a consequence of the incorporation of oxygen-based groups in the graphene lattice. The concentration of these defects is low for low oxidized graphene and

then the unpaired spins are localized and non-interacting. As their local environments are different depending on the nature of the functional groups, the EPR signal will reflect the distribution of the local environments through a broad resonance line. Furthermore, the EPR signal in GO_(0.5) also reflects the anisotropy of the environment through that of the g -tensor. Indeed, the simulation of a typical EPR spectrum of GO_(0.5) is accounted for by an anisotropy of the g -tensor components $\Delta g = g_{X,Y} - g_Z = 0.005$. In this expression, the directions X, Y, and Z are related to the main frame of the g -tensor and tentatively we may assign X, and Y to the graphene layer and Z to the perpendicular direction to the basal graphene plane as depicted in the insert Fig. 4.2. Increasing the oxidation of GO enhances the concentration of oxygen atoms bound to graphene lattice and induces a higher concentration of unpaired spins. As a consequence, the mutual interactions between neighboring spins are expected to have the features of dipolar or exchange interactions. The dipolar interactions lead to an inhomogeneous broadening of the EPR resonance lines due to a distribution of the local magnetic fields in the environment of the paramagnetic species. However, the observed narrowing of the line width rules out the relevance of dipolar broadening. The exchange interactions between neighboring spins are characterized by the exchange integral defined by the overlap of their wave functions. This parameter can become important enough compared to other interactions and in consequence, can couple coherently the neighboring unpaired spins and then limit the dispersion of their resonance position. The resulting EPR signal will be affected by the exchange narrowing effect. This situation is indeed observed in the case of GO with an increased effect of the exchange narrowing as the oxidation degree increases. In the meantime, the exchange interaction is accompanied by a rapid dynamic that averages the EPR line width and lowers the anisotropy related to the local environment as traduced from the almost isotropic g -tensor $\Delta g = g_{X,Y} - g_Z = 0.001$ for GO₍₁₀₎.

To sum up, EPR investigations of GO with different oxidation degrees show great sensitivity to the oxidizing agent KMnO₄ and allow us to characterize the quality of purification of GO from the metallic ions (Mn). On the other hand, EPR reveals the relationship between the concentration of unpaired spins and the oxidation of GO. The analysis of the EPR spectra line-shape points out the involvement of exchange narrowing phenomena with increased strength as the concentration of the unpaired spins increases.

4.2. Morphological and microstructural features

4.2.1. X-ray diffraction

Fig. 4.3. shows the X-ray diffractograms corresponding to GOs synthesized with different amounts of KMnO₄, compared with the diffractogram of pristine graphite (Gr). In the graphite pattern, the characteristic planes (002) and (004) of this material are identified at angles (2θ) of 26.40° and 54.11°, respectively. The sharp signal (002) indicates reflections in the perpendicular direction (c -axis) of the hexagonal planes of graphite, representing stacking with an interlayer spacing of ≈ 0.34 nm [10]. The intensity and position of this peak provide valuable information about the stacking order and structural properties of graphite.

On the other hand, the X-ray patterns of GOs show remarkable changes as a function of the used amount of KMnO_4 . With increasing oxidation, the intensity of the graphite reflection (002) decreases and becomes broader, disappearing at higher oxidation degrees [$\text{GO}_{(10)}$]. Simultaneously, the appearance of a new reflection between 9° - 15° , assigned to the (001) plane of GO, and another reflection near $\approx 43^\circ$, assigned to the (100) plane [11–13] were observed. In contrast to the (002) plane in graphite, the (001) reflection in GO increases and shifts towards lower 2θ angles with increasing the oxidation degree. No reflections corresponding to manganese (Mn) were detected in the X-ray patterns [14] due to the limited sensitivity of the XRD compared to the EPR spectroscopy as discussed in the above section.

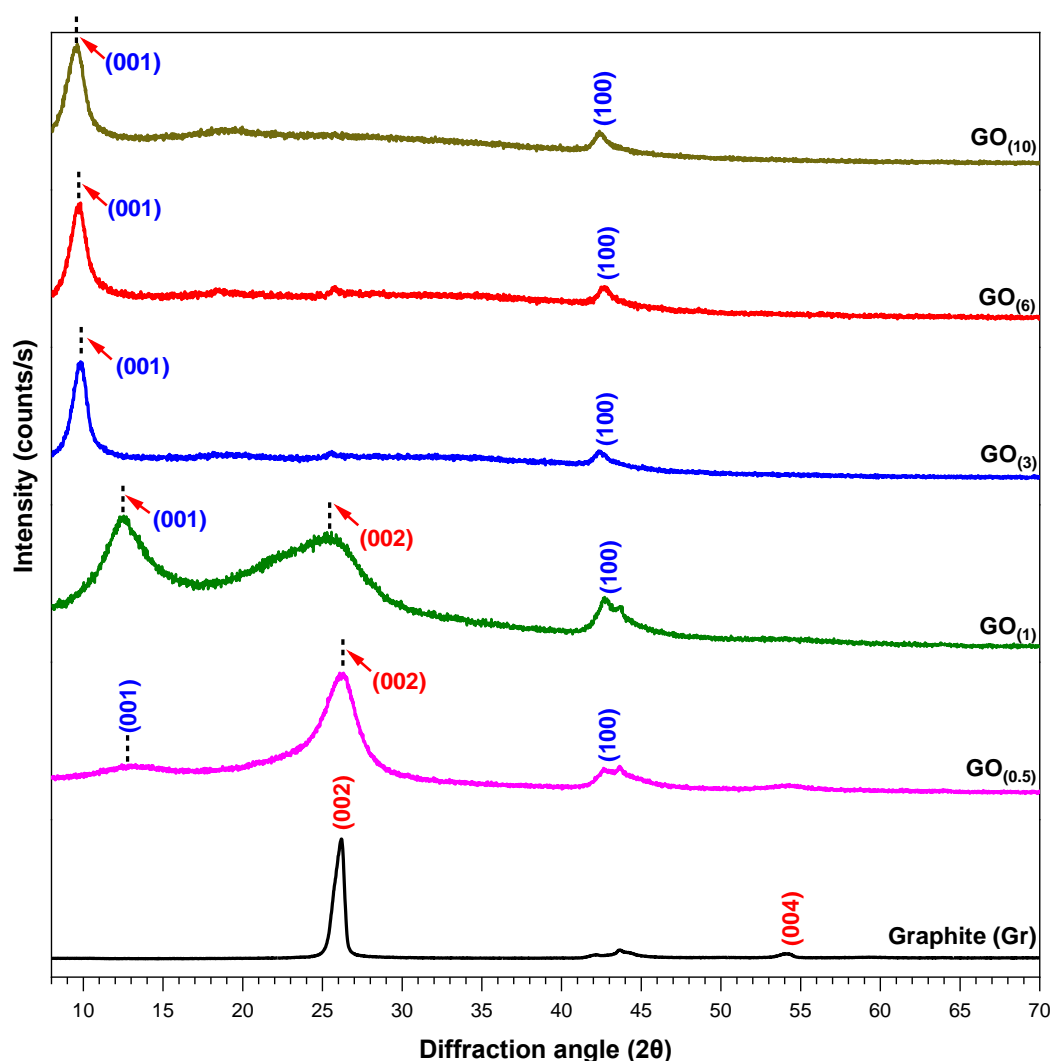


Fig. 4.3. Evolution of the XRD patterns of Gr and GOs as a function of the oxidation degree.

Initially, in the material with the lowest oxidation degree [$\text{GO}_{(0.5)}$], a broadening of the reflection (002) is observed compared to graphite. This phenomenon is mainly related to the rapid oxidation of graphite and the reduction in the size of the crystalline domains (Fig. 4.4.a-b.). The introduction of oxygenated groups between the graphite layers causes distortions and changes in the regular crystalline structure, generating greater variability in the distances between the crystalline planes and resulting in the broadening of the reflection (002).

Simultaneously, a scarcely perceptible new wide reflection (001) emerges at an angle of $\approx 13^\circ$ (2θ). Then, with the increase of the oxidation degree in $GO_{(1)}$, the graphite peak (002) becomes much broader and decreases in intensity. In parallel, at the same time, the reflection (001) of GO develops and shifts to diffraction angles at $2\theta \approx 12.41^\circ$ with increasing intensity and sharp line shape. These changes are due to the heterogeneous nature of oxidized graphite, which consists of both sp^2 domains of graphite and sp^3 domains of oxidized graphite. Up to this point, the coexistence of graphitic and oxidized domains is demonstrated in both materials (Fig. 4.4.c.). Finally, as the oxidation increases, the (001) reflection shifts to lower 2θ angles (between 9.59° - 9.79°) starting from $GO_{(3)}$. In all cases, the reflection attributed to graphite (002) is almost imperceptible (Fig. 4.4.d.).

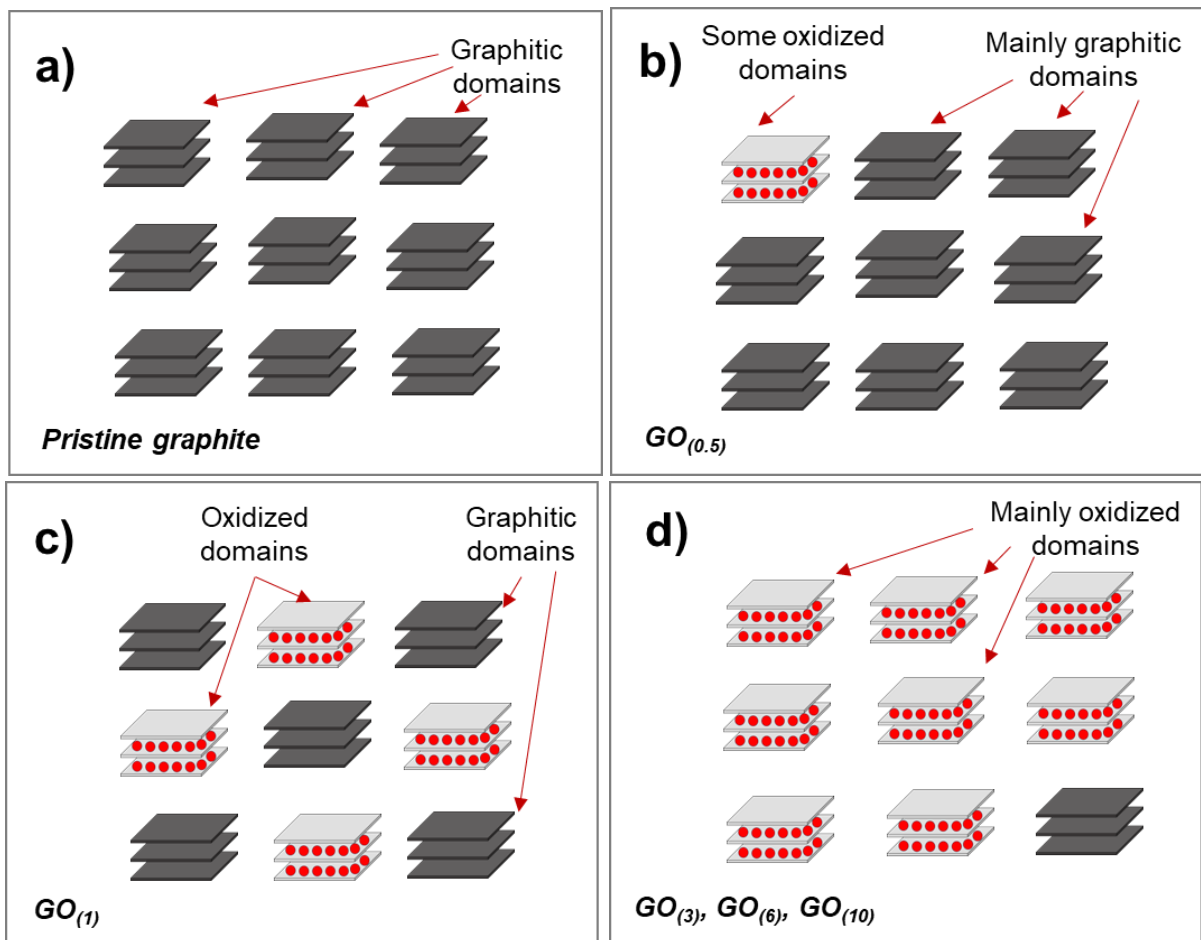


Fig. 4.4. Representation of the structural evolution of GO as a function of gradual oxidation.

4.2.1.1. Quantitative analysis

The reflection (001) was used to calculate the size of the crystalline (L_c) domains of carbon materials along the c -axis of graphite (the average height of the stacked layers). For this, the Scherrer equation (eq. 1) [15] with an A constant of 0.9 was used. The Scherrer equation, using a Warren constant of 1.84 [16], was employed to determine the average diameter of the stacking layers, indicated as D , based on the two-dimensional reflection (100). To evaluate the evolution of the degree of exfoliation of the GO sheets, the Bragg equation (eq. 2) [17] was applied to

the reflection (001), denoted as d . Fig. 4.5. shows an illustration of the different parameters in a GO domain.

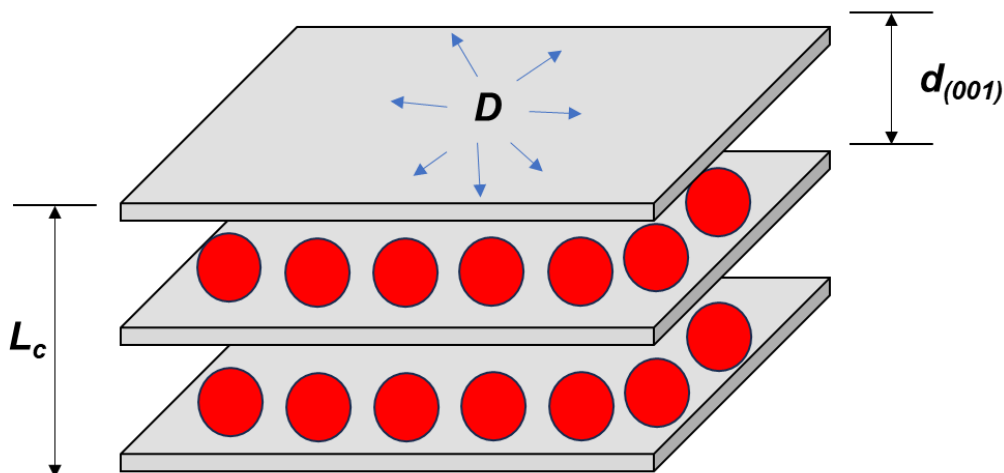


Fig. 4.5. Illustration of the different parameters (L_c , D , d_{001}) in a GO domain

Table 4.1. summarizes the XRD data for the reflection (001) associated with the graphitic layer spacing d_{001} , the FWHM determined by the Lorentzian fit, and the crystalline domain size (L_c) calculated. These data show an increase in the inter-reticular distance d_{001} in GOs with an increasing oxidation degree. This phenomenon is a result of the insertion of functional groups between the layers of graphite, such as epoxy, hydroxyl, carbonyl, and carboxyl groups, during the chemical oxidation reaction [18] which leads to the loss of aromaticity of the carbon bonding. These oxygenated groups contribute also to the breakdown of the carbon lattice (basal plane) of GO and reduce the Van der Waals interactions between the stacking planes. As a result, the GO sheets exfoliate more, leading to a higher average number of separated graphene layers (n). The performed XRD analysis is in good agreement with the behaviors demonstrated in the literature [19]. On the one hand, using the Scherrer equation, we show that with increasing oxidation degrees of GO, the size of GO crystallites in the (001) direction gradually increases, while the size of graphitic crystallites derived from the (002) reflection gradually decreases. For example, the lowest oxidation [$GO_{(0.5)}$] consists of stacks of between 2 and 3 layers with a mean diameter (L_c) of ≈ 27.155 nm and height (D) of ≈ 2.040 nm and an average interlayer distance $d_{001} = 0.680$ nm. For the highest oxidation [$GO_{(10)}$], a stacking of between 8 and 9 layers with a mean diameter (L_c) of ≈ 20.765 nm and height (D) of ≈ 7.704 nm and an average inter-planar distance of 0.903 nm. The approximate number of stacked GO layers (n) was calculated from the ratio L_c/d_{001} .

Table 4.1. Quantitative values calculated by XRD

Materials	Reflection of plane (001)					Reflection of plane (100)		
	2 θ (degrees)	d ₍₀₀₁₎ (nm)	FWHM (degrees)	L _c (nm)	n (layers)	2 θ (degrees)	FWHM (degrees)	D (nm)
GO _(0.5)	13.001	0.680	3.920	2.040	2-3	42.653	0.642	27.155
GO ₍₁₎	12.570	0.704	2.975	2.686	3-4	42.670	0.774	22.524
GO ₍₃₎	9.525	0.928	1.263	6.313	6-7	42.414	0.792	22.006
GO ₍₆₎	9.702	0.911	1.142	6.983	7-8	42.673	0.799	21.822
GO ₍₁₀₎	9.790	0.903	1.035	7.704	8-9	42.422	0.839	20.765

4.2.1.2. Correlation between the size of nanocrystallites L_c and the oxidation degree

The above-estimated values of the crystalline domain (L_c) correlate with the oxidation degree of GO networks. As shown in Table 4.1, L_c increases significantly with the increase in the amount of oxidant, but this behavior stabilizes and varies to a lesser extent after a certain amount of KMnO_4 , showing an exponential behavior. The regression of the measured data gives the following correlation:

$$L_c = 5.369 + 1.027 \ln(x - 0.685)$$

Where x refers to the amount of oxidant (KMnO_4). The equations could be a useful indicator of the degree of crystallinity and morphological characteristics expected in GOs produced by using different amounts of KMnO_4 during synthesis. Fig. 4.6 shows a graphical representation of the above equation.

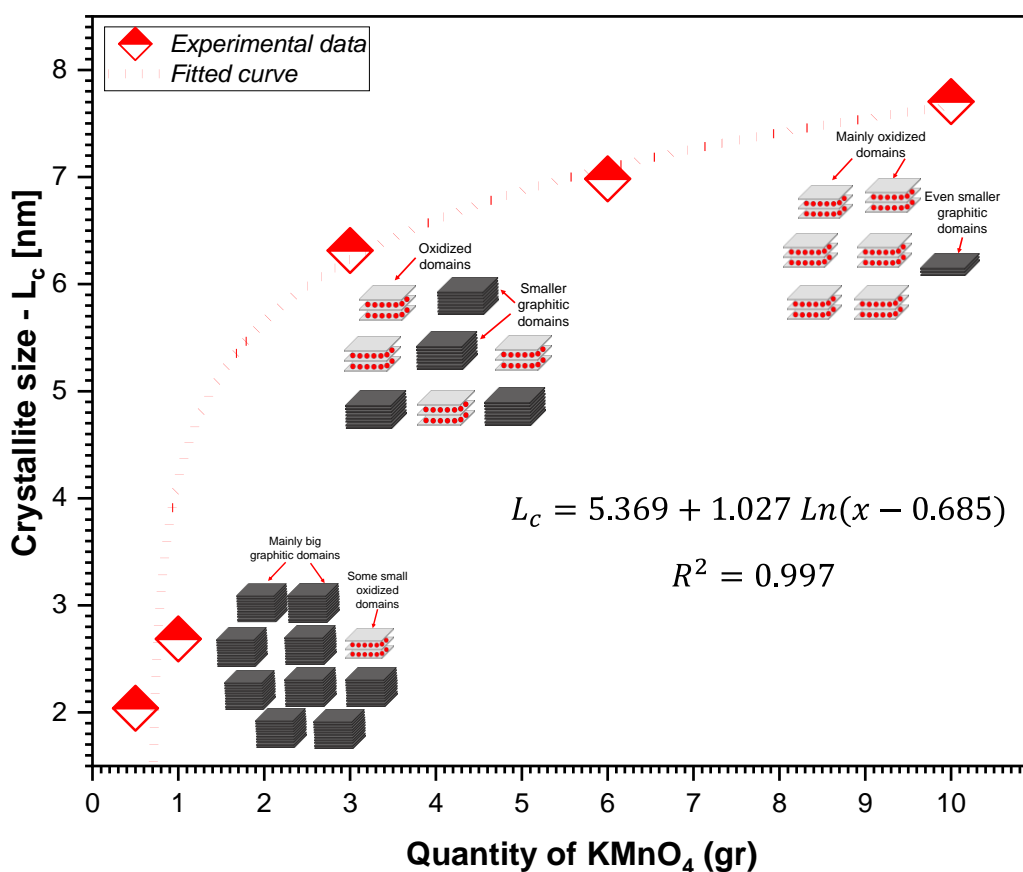


Fig. 4.6. Correlation between Crystalline domain size in the GOs vs the amount of KMnO_4 .

4.2.2. Raman spectroscopy

Fig. 4.7 shows the Raman spectra of the synthesized GOs compared to the spectrum of pristine graphite in the range of $1000\text{--}2000\text{ cm}^{-1}$. The graphite spectrum shows an intense band at $\approx 1579\text{ cm}^{-1}$ assigned to the G -mode, corresponding to the E_{2g} vibrational degenerated mode observed

in the graphite single crystal [20]. An additional band at $\approx 1347 \text{ cm}^{-1}$, assigned to the *D*-mode, corresponds to the A_{1g} mode, emanating from polycrystalline samples of small crystallites or larger crystallite boundaries. This band is associated with defective bonding in the graphitic lattice such as bond angle or length disorder, vacancies, edge defects... [21, 22].

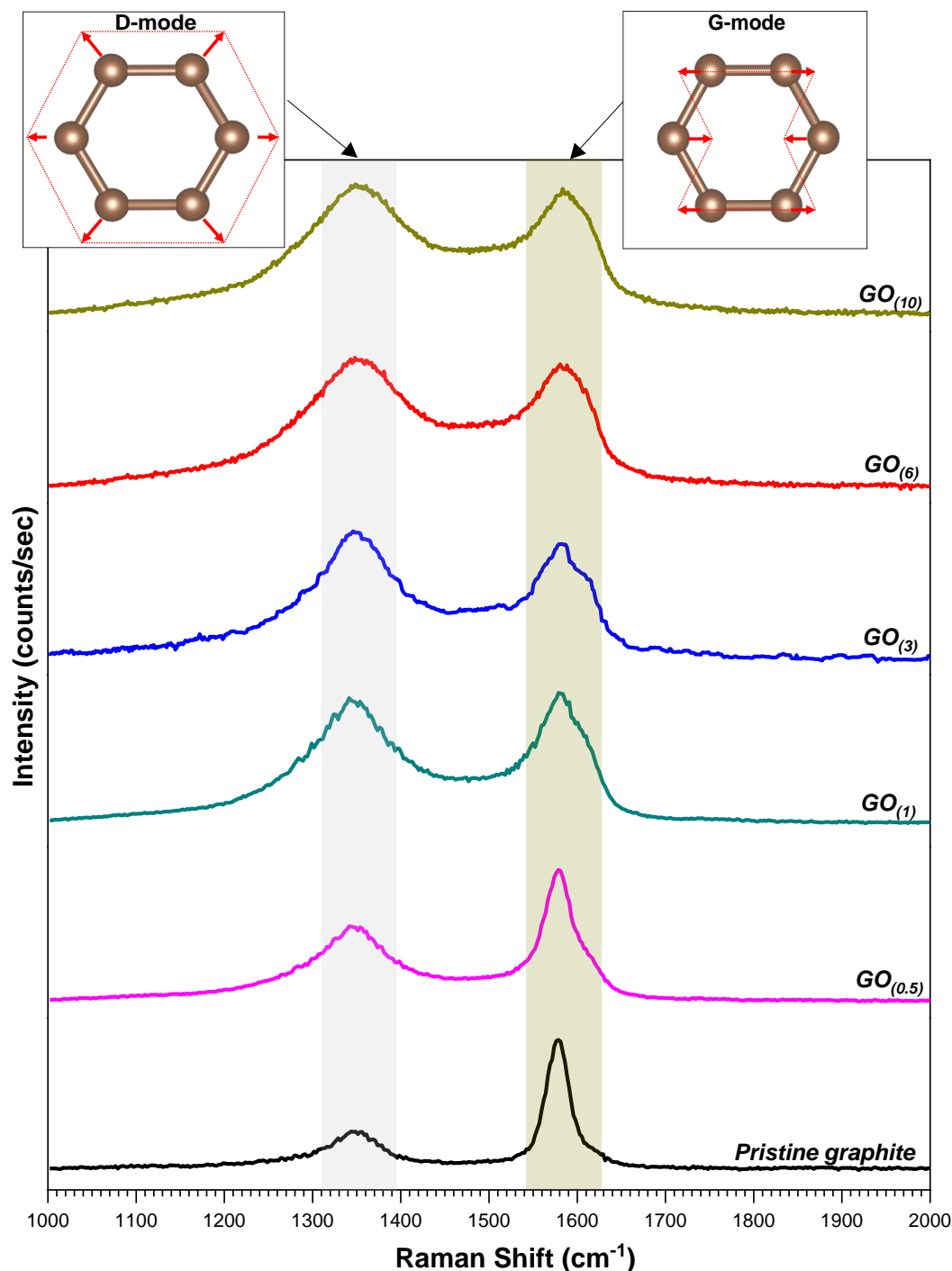


Fig. 4.7. Raman spectra of the pristine graphite and GOs samples.

On the other hand, the Raman spectra of the synthesized GOs show two peaks at positions around the D and G-bands of pristine graphite with differences in position and relative intensity. *D*-band is indicative of structural defects and disorder caused by the introduction of

oxygen functional groups during the oxidation process. Although these defects may introduce some carbon-bonded regions, the *D*-band itself arises mainly from changes and disorder in the sp^2 carbon lattice (such as vacancies, edges, etc.). In particular, our observations have shown that the *G*-band shift toward higher wavenumbers with increasing oxidation is associated with the formation of new sp^3 carbon atoms in the graphitic lattice [23]. Similarly, the oxidation degree affects the characteristics of the *D*-band, resulting in an increase in intensity as oxidation increases and reaching a stable level at higher oxidation degrees. The spectra obtained here show similar characteristics to many others described in the literature for GOs [21, 24].

4.2.2.1. Quantitative analysis of the D/G ratio

A detailed analysis showed that GO spectra can be deconvolved using Lorentzian curves with multiple Raman bands as *D**, *D*, *D''*, *G*, and *D'* [25, 26]. The *D* and *G* bands have already been described. The *D** band at 1050-1200 cm^{-1} originates from the sp^3 orbital, which is similar to the *D** band observed in small grain size nanocrystalline diamond [27], sp^3 -rich phases [28] and disordered graphite lattice provided by sp^2 - sp^3 bonds [29]. The *D''* band at 1500-1550 cm^{-1} appears due to an amorphous structure with sp^2 bonds and interstitial defects [30] and its intensity is inversely related to crystallinity, *i.e.* its intensity decreases with increasing crystallinity [31]. This band is associated with the anchored functional groups, such as -COOH, -COC, and -OH [32, 33] on the exfoliated graphite sheets. The *D'* band at 1620 cm^{-1} corresponds to an intra-valley resonance with the *G*-band split by impurities [34]. The Bands *D* and *D'* appear when defects break the periodic lattice of graphene [35] and are mainly associated with structural defects such as sp^3 hybridization, vacancy-like defects, and boundary-like defects [36]. The values resulting from the deconvolutions are shown in Table 4.2. and the spectra can be seen in supplementary information (Fig. S.4.1.).

Table 4.2. Values obtained from the Lorentzian deconvolutions of the Raman spectra.

Material	Parameters	<i>D*</i>	<i>D</i>	<i>D''</i>	<i>G</i>	<i>D'</i>
Graphite	Position	1249.30	1346.70	1489.00	1577.90	1622.00
	FWHM	215.49	69.70	16.66	30.43	9.81
	Area	972.32	2777.90	27.66	4631.90	41.89
GO _(0.5)	Position	1262.81	1345.37	1499.08	1578.44	1613.95
	FWHM	304.15	98.90	120.96	38.96	20.74
	Area	992.50	3247.16	649.23	2378.50	152.73
GO ₍₁₎	Position	1185.62	1345.32	1517.33	1579.15	1611.50
	FWHM	345.47	121.93	120.45	49.29	23.31
	Area	513.61	3965.84	894.13	1527.20	226.01

GO ₍₃₎	Position	1173.41	1349.00	1523.88	1578.89	1612.80
	FWHM	241.49	132.25	131.22	56.55	24.33
	Area	705.26	5497.06	1111.97	1867.62	264.45
GO ₍₆₎	Position	1155.62	1350.07	1511.86	1579.48	1609.55
	FWHM	123.91	147.93	115.08	57.64	28.45
	Area	962.11	45966.32	9643.88	13452.41	2730.19
GO ₍₁₀₎	Position	1147.83	1350.60	1509.23	1580.14	1611.18
	FWHM	110.54	151.12	120.13	59.68	33.13
	Area	1143.73	57683.41	12541.94	16467.22	4279.33

Based on the origins of the D and G-bands, the average size of the aromatic clusters in the different GOs was calculated and determined by the Raman ratio of the D/G peaks [37]. The I_D/I_G ratio is the most commonly used in the literature to evaluate GO quality. However, the A_D/A_G area (integrated intensity) ratio has also been used in recent research [38, 39]. In this treatment, the ratio of the integrated areas is preferred to the intensity because the area under the band represents the entire scattering process. The integrated intensity ratios (A_D/A_G) of the D and G-bands of GO were compared as a function of the amount of $KMnO_4$. Fig. 4.8 shows the area and intensity interactions of the different deconvolution values of the D-band concerning the G-band and their evolution as a function of the amount of $KMnO_4$. The trends showed the dependence of the D/G ratios on the amount of $KMnO_4$, *i.e.* these ratios increase as the oxidation degree increases, showing a logarithmic dependence following correlations based on areas and intensities respectively, where x represents the amount of $KMnO_4$.

$$\frac{A_D}{A_G} = 2.770 + 0.326 \ln(x - 0.486)$$

The increase in the D/G ratio highlights the appearance of a more intricate and disordered carbon network in the highly oxidized GO samples. The I_D/I_G ratio in the GOs increases compared to the pristine graphite, indicating that the sp^2 bonds are disrupted, leading to the formation of a significant amount of sp^3 hybridized carbon atoms due to the presence of oxygen-containing functional groups. This situation is accompanied by the average size reduction of the carbon domains with sp^2 bonding. Eigler, S. *et al.* 2012 [40], reported an increase of I_D/I_G from 1.14 to 1.19 for higher oxidized GO. Hu, X., *et al* 2014 [41], also reported a higher I_D/I_G ratio for mostly oxidized GO while Reynosa-Martínez *et al* 2020 [42] show an increase in the I_D/I_G ratio from 0.42, 1.29, and 1.34 respectively as a function of the oxidation degree. The observed behaviour remains consistent in the current study and indicates a greater degree of disorder resulting from the oxidation process of the graphitic clusters.

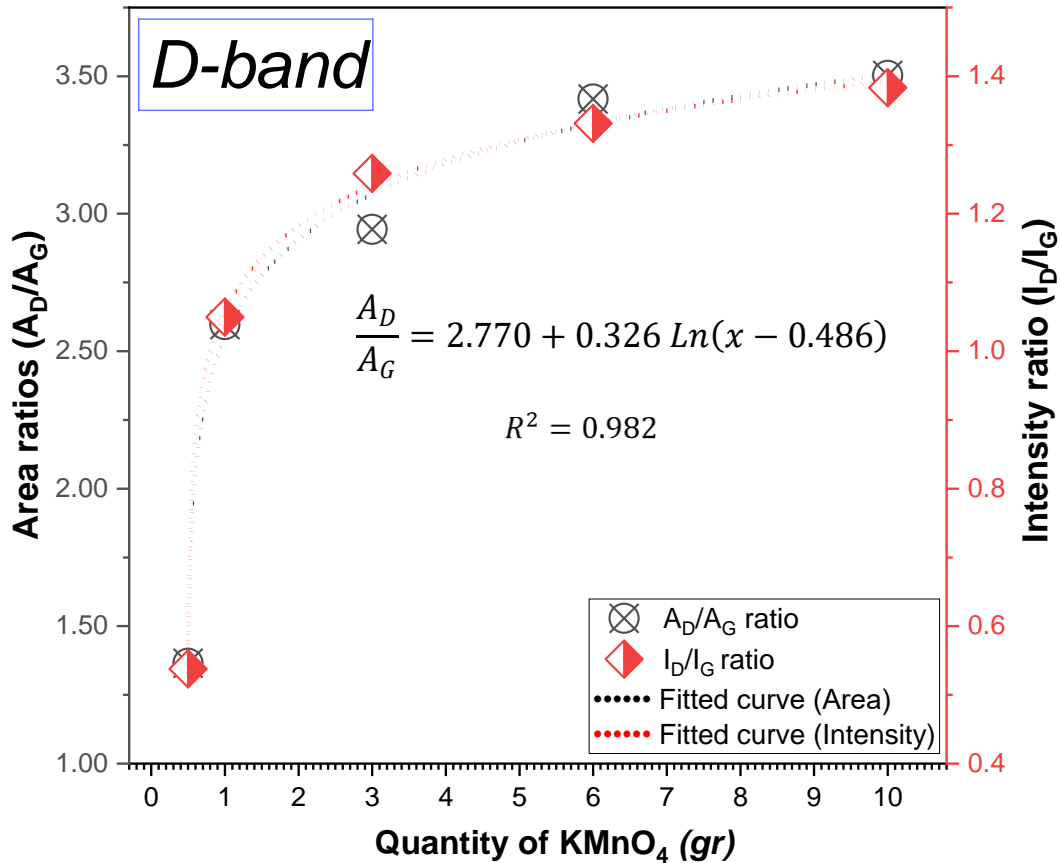


Fig. 4.8. Dependence of the D/G ratios (areas and intensities) with the amount of KMnO₄.

4.2.2.2. Identification of structural defects

From the evolution of the intensities of the D' and D-bands it is possible to identify the type of structural defects in GOs [36]. It should be noted that the intensities of the D and D'-bands are proportional to the concentration and type of defects, such as grain boundaries, vacancies, or sp³ hybridization [43]. Hence, in GOs, the occurrence of the D'-band in their Raman spectra can be attributed to the existence of C-sp³ and structural defects formed during oxidation. Before analyzing the relationship between the D' and D-bands for our GOs, it is necessary to take into account former interpretations made from previous works. For example, Ferrari *et al.* [33, 44–46] have shown that the I_D/I_G ratio follows a two-stage evolution. Stage 1 corresponds to graphene with few defects, while stage 2 corresponds to highly disordered graphene. The authors also found the transition between the two stages at I_D/I_G values ≈3.5 [46]. They also showed that in stage 1, the intensities of the D and D'-peaks are proportional to the defect concentration and, consequently, to each other. However, in stage 2, the relationship between the intensities of the two bands becomes more complex and it is not possible to relate them precisely. In our GO materials, the D/G ratios for both areas and intensities are ≤ 3.5, so it is expected they contain low defect concentrations.

Fig. 4.9. shows the integrated D' band areas, (A_{D'}/A_G), versus the D band areas, (A_D/A_G). To obtain information about the nature of the defects, our data were compared with theoretical-

experimental values of the $A_{D'}/A_G$ ratio studied in the literature [36]. Thus, it was shown that defects associated with sp^3 hybridization have a maximum $A_{D'}/A_G$ ratio of ≈ 0.0769 , whereas defects from vacancies or cluster edges have maximal $A_{D'}/A_G$ about 0.1428 or 0.2857, respectively. Based on this, we find that the defects mainly present in pristine graphite are of the sp^3 hybridization type. Since pristine graphite has not undergone any chemical oxidation process, these hybridizations are attributed to the disordered graphite network provided by sp^2 - sp^3 (C-C) bonds [29]. This type of hybridization has also been reported in nanocrystalline diamonds of small grain size [27]. Subsequently, in the lower oxidation [$GO_{(0.5)}$], this type of defect remains highly predominant in the structure. This is largely consistent with the corresponding X-ray diffraction pattern, which shows the high presence of graphitic domains with the original characteristics of pristine graphite.

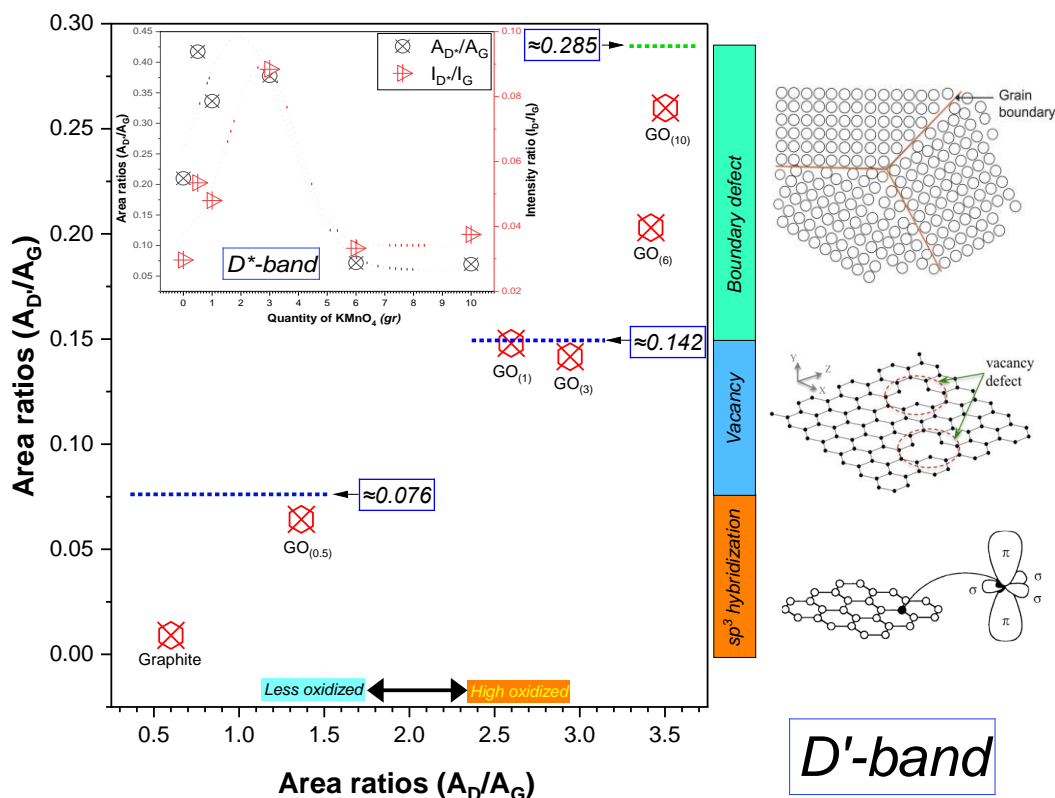


Fig. 4.9. Ratio of the (D'/G) band areas as a function of the band ratios (D/G).

In parallel, the analysis of the D^* peak associated with sp^3 orbitals shows that in GOs where less $KMnO_4$ is used [$GO_{(0.5)}$, $GO_{(1)}$, and $GO_{(3)}$], the concentration of sp^3 hybridizations increases for $GO_{(0.5)}$ but remains relatively unchanged for higher values. Although the defects associated with sp^3 hybridizations are higher in $GO_{(1)}$ and $GO_{(3)}$, the analysis of the $A_{D'}/A_G$ ratios is consistent with the presence of defects mainly associated with vacancies. This suggests that during the synthesis process, the different precursors or oxidants break the C-C bonds, creating gaps or vacancies in the lattice. Similarly, the intercalation of oxygenated species between the graphene layers would cause the separation of the graphene sheets and the creation of such vacancies. These vacancies will eventually serve as active sites for further functionalization when more oxidant is used.

Finally, the most oxidized GOs [GO₍₆₎ and GO₍₁₀₎] coincide with the primary presence of boundary-like defects. These types of defects can occur in GO as a consequence of the heterogeneous nature of the oxidation process. The presence of functional groups near already-formed vacancies would lead to oxidative functionalization of the surrounding carbon atoms. Oxidation may occur unevenly in different regions, resulting in a heterogeneous distribution of functional groups along the layer.

4.2.2.3. Graphitic domain size

The crystallite size of unoxidized graphitic domains was determined by calculating the ratio of the integrated intensities of the D and G bands (A_D/A_G) in the Raman spectra. Using eq. 5 [35], this ratio was employed to estimate the crystallite size (L_a).

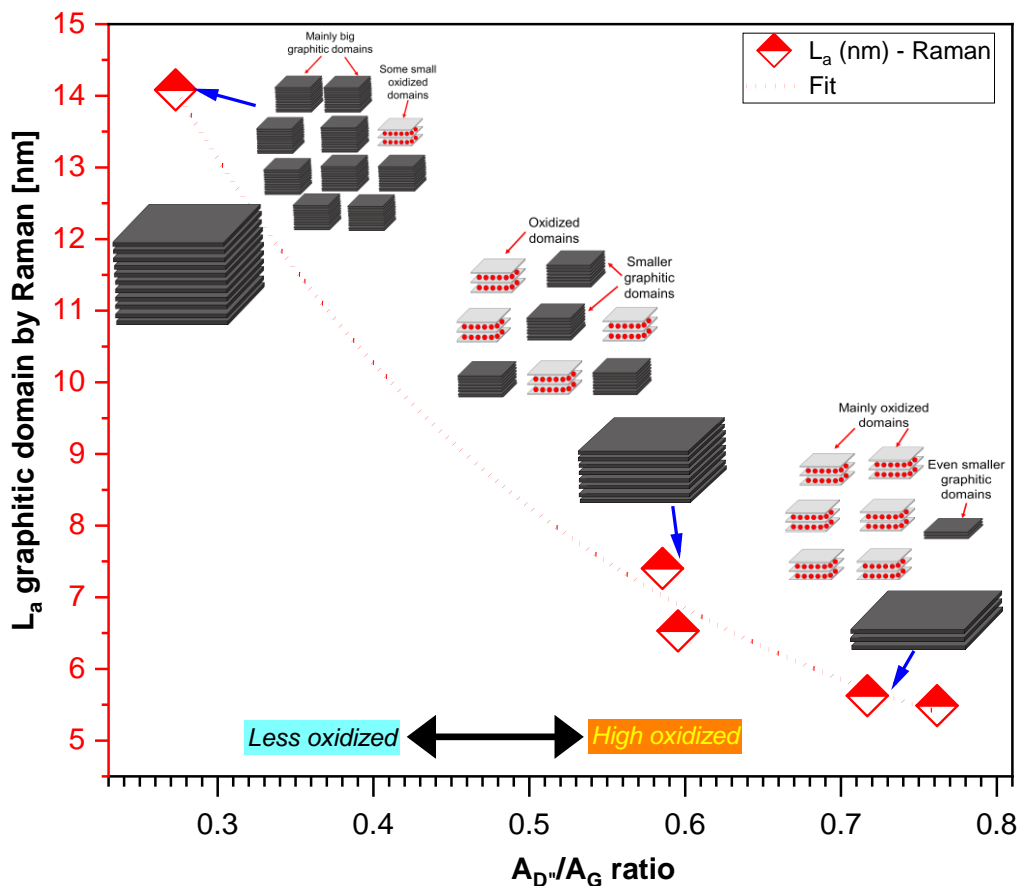


Fig. 4.10. Dependence of the $A_{D''}/A_G$ ratio as a function of graphitic domains calculated by Raman spectroscopy.

Fig. 4.10. shows that the crystallinity of the graphitic domains decreases with increasing $A_{D''}/A_G$ ratio, which coincides with the increase in the crystallinity of the oxidized domains determined by XRD, as the oxidation degree increases. This finding supports the hypothesis that the intensity of the D'' -band is intrinsically related to the crystallinity and structure of the graphitic and oxidized domains. The determination of the crystallite size by X-ray diffraction

provides information about the oxidized domains, while the results obtained by Raman are more related to the graphitic domains, especially the (002) reflection, which is no longer observable in the more oxidized GOs [GO₍₃₎, GO₍₆₎, and GO₍₁₀₎] by X-ray diffraction. In addition, details of other Raman bands, such as the *D*-peak, can also indicate the presence of defects and disorder in the material. In summary, the combination of XRD and Raman allows a more complete and detailed analysis of the graphite structure, providing information about the oxidized domains, graphitic domains, as well as the presence of defects and disorder in the material, both being complementary tools for the study of the GO structure [47].

4.2.3. Morphology (SEM/TEM) and specific surface area (SSA)

As shown previously, an increase in the D/G intensity ratio correlates with a higher degree of structural defects or disorder in the GO. As the oxidation degree increases, the amount of these functional groups on the surface increases, leading to an increase in active sites and surface chemical reactivity. This increase in functional groups also leads to increased dispersion and exfoliation of the material, which contributes to an increase in surface area. Fig. 4.11. compares the specific surface area (SSA) and pore volume concerning the A_D/A_G ratio and confirms the expected behavior. This is consistent with former reports demonstrating the increase in the specific surface area of graphite when oxidized to form GO [43, 46].

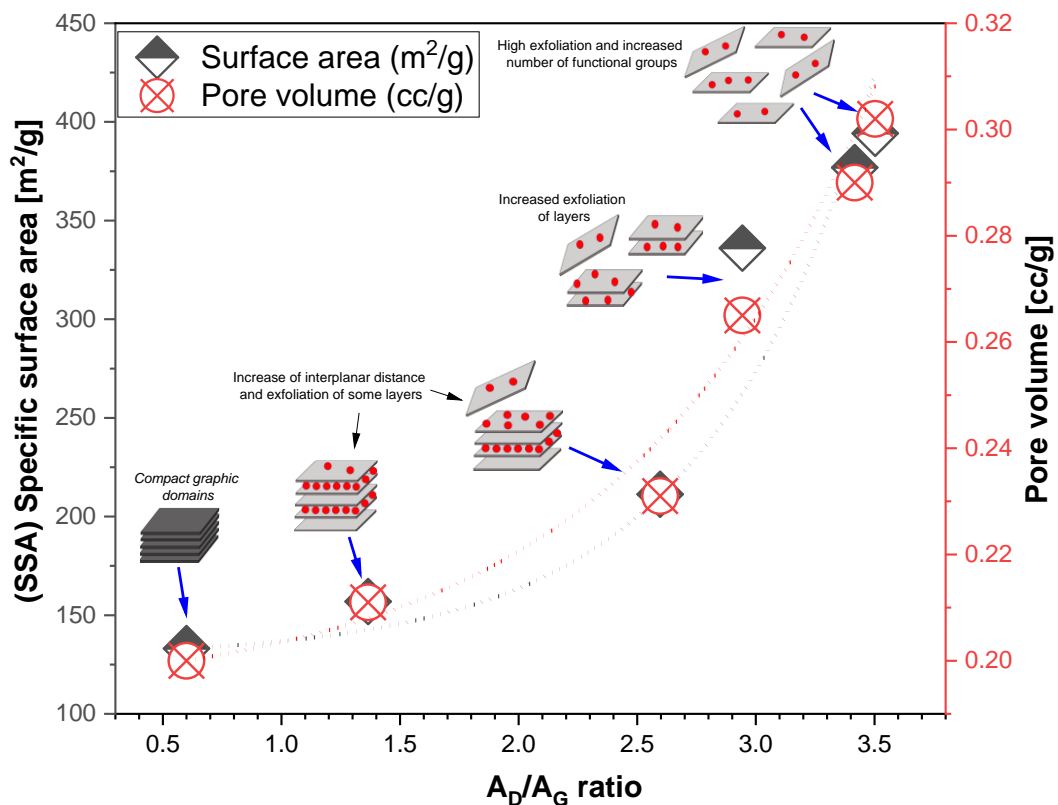


Fig. 4.11. Dependence of specific surface area (SSA) as a function of A_D/A_G ratio calculated by Raman spectroscopy.

Fig. 4.12 displays the micrographs of GO samples at a magnification of 2000x. In images, wrinkled and layered flakes are visible on the surface, indicating the presence of oxidized graphene layers [48]. However, in Fig. 4.12.a., the less oxidized GO shows larger carbon platelets and more stacking associated with graphitic domains. Fig. 4.12.e. shows the more oxidized [GO₍₁₀₎] with a higher degree of flaking and wrinkling, with flat lamellae, indicating a higher degree of exfoliation. TEM images show thinner material layers with higher oxidation, suggesting changes in SSA due to layer exfoliation.

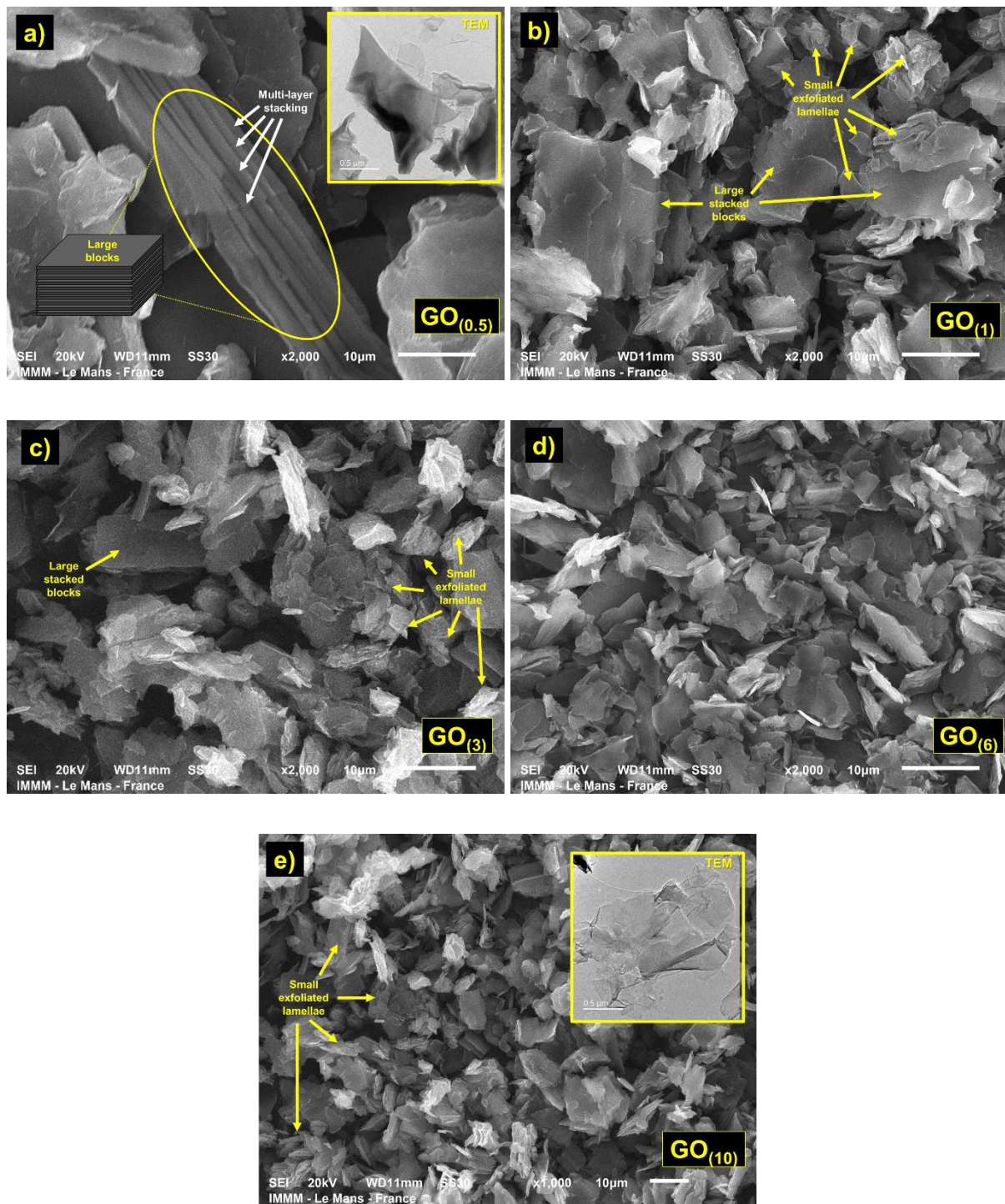


Fig. 4.12. SEM images of graphene oxides

4.3. Surface chemical composition features

The analyses carried out to date have made a significant contribution to understanding the evolution of the structural properties of GO concerning the increase in the amount of KMnO_4 . However, it is important to note that these techniques do not provide an exhaustive description of the nature of the functional groups present in the material. Therefore, additional techniques such as X-ray photoelectron spectroscopy (XPS) and Fourier transform infrared spectroscopy (FTIR) have been used to identify and characterize the functional groups in GO. These techniques provide valuable and complementary information on the chemical composition and bonding involved in GO.

4.3.1. FT-IR characterization

Fig. 4.13. shows the FT-IR spectra for pristine graphite and GOs in the $2000\text{-}400\text{ cm}^{-1}$ region. At higher wavenumbers, only the OH/ H_2O bands corresponding to intercalated water are observed and will not be discussed further in this work. No spectral bands were detected in the graphite, which aligns with the findings published in earlier research [49, 50].

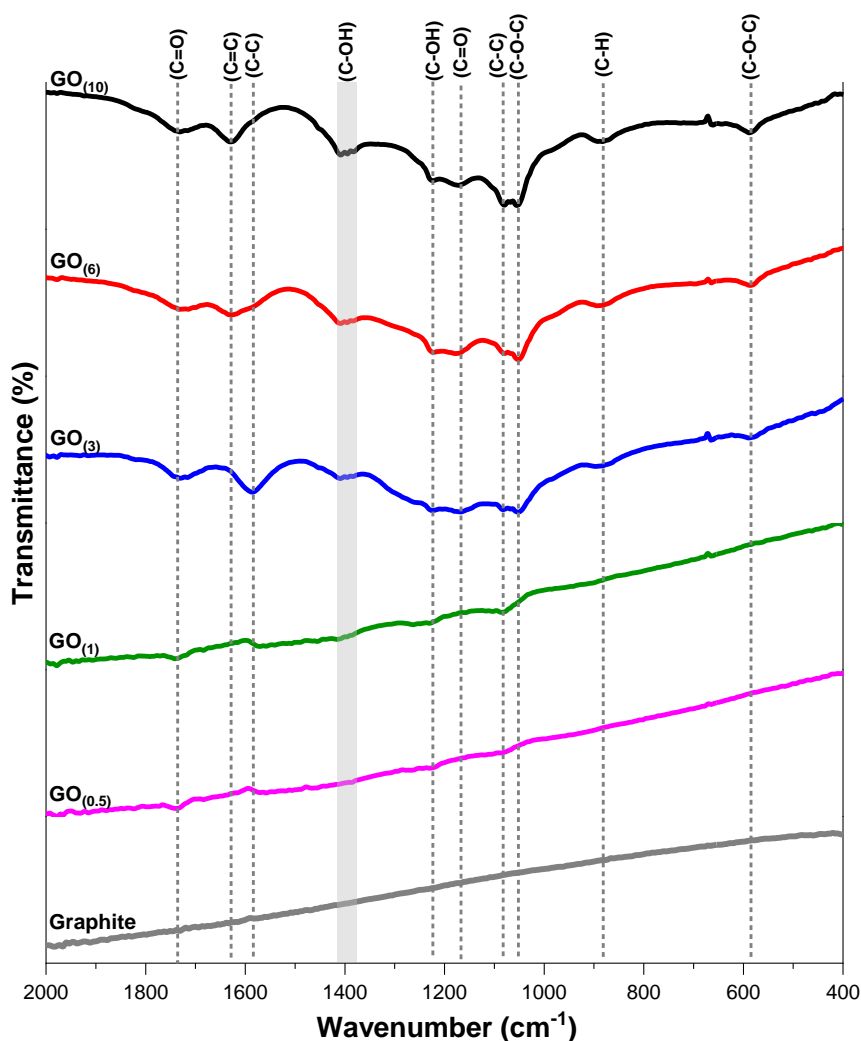


Fig. 4.13. FT-IR spectra of pristine graphite and synthesized graphene oxides.

The presence of bands at ≈ 593 and ≈ 1058 cm^{-1} corresponds to the epoxy stretching mode (C-O-C) located above the basal plane of the GO. The bands at ≈ 1230 and ≈ 1387 cm^{-1} are related with the bending mode of hydroxyl groups (C-OH) above the basal plane. For the bands at ≈ 1170 and ≈ 1730 cm^{-1} , they correspond to carbonyl or carboxylic functional groups (C=O) located at the edge of the lamellae. For ≈ 1082 and ≈ 1623 cm^{-1} , bands associated with skeletal (C-C) and the asymmetric stretching vibrational mode of sp^2 hybridization (C=C) of the graphene sheet skeleton were identified [51]. Finally, the peak at ≈ 831 cm^{-1} can be ascribed to the C-H group [52] while the inclusion of bands associated with C-O-C, C-OH, and C=O would demonstrate the presence of oxygen molecules occupying both the edges and the basal plane of GOs [53, 54], thus confirming the oxidation of graphite.

However, in $\text{GO}_{(0.5)}$ and $\text{GO}_{(1)}$, very low intensities of functional groups were observed in the corresponding FTIR spectra. If GO has low oxidation, the concentration of oxygenated groups on the surface may be relatively low. In this situation, the functional groups may not contribute significantly to the signals in the FTIR spectra, and the corresponding bands may be weak or almost imperceptible. As the degree of oxidation increases, the concentration of oxygenated groups increases. This leads to an increase in the intensity of the bands in the FTIR spectrum as more functional groups interact with the infrared radiation and produce stronger signals. This would be related to the model proposed in Fig. 4.6 for L_c deduced from XRD studies, where it is observed that at low oxidation [$\text{GO}_{(0.5)}$ and $\text{GO}_{(1)}$], the crystallite sizes associated with oxidized domains are still relatively small, while from $\text{GO}_{(3)}$, the domain size becomes more important.

4.3.1.1. Chemical composition

To evaluate the structural evolution of the synthesized GOs in more detail, the spectra were deconvolved into Lorentzian peaks to obtain the area under the curve, in the spectral regions $1000\text{-}1500$ cm^{-1} and $1500\text{-}2000$ cm^{-1} , respectively. Band assignment and spectral analysis were mainly performed by comparing FTIR studies on carbon materials reported in the literature [51, 55]. The deconvolved spectra are shown in Fig. 4.14.

The lower oxidation GOs [$\text{GO}_{(0.5)}$ and $\text{GO}_{(1)}$] are very similar to each other and show the presence of peaks not observed in pristine graphite. Mainly intense bands related to C-C and C-O skeletal vibrations are observed (≈ 1083 cm^{-1}), as well as distinct intense bands related to -COOH (≈ 1226 and ≈ 1737 cm^{-1}). Clear phenol-related bands at 1262 , 1467 , and 1563 cm^{-1} and an intense H-C=C-H band at ≈ 1409 cm^{-1} are also resolved. The presence of these bands, which are associated with bending modes above the basal plane and edges, suggests that oxidation starts selectively in certain regions of the material. That is, during the oxidation process, the edges of the lamellae are oxidized first. This results in a microstructure with predominantly edge-oxidized graphitic domains and a few exfoliated graphene layers. The graphite edges are more likely to oxidize first during the GO formation process due to their higher reactivity and accessibility to chemical reactions that introduce oxygen into the material structure. The mild oxidation process preserves the sp^2 network of the carbon and the edges are functionalized with hydrophilic groups, making the material dispersible in water [56–58].

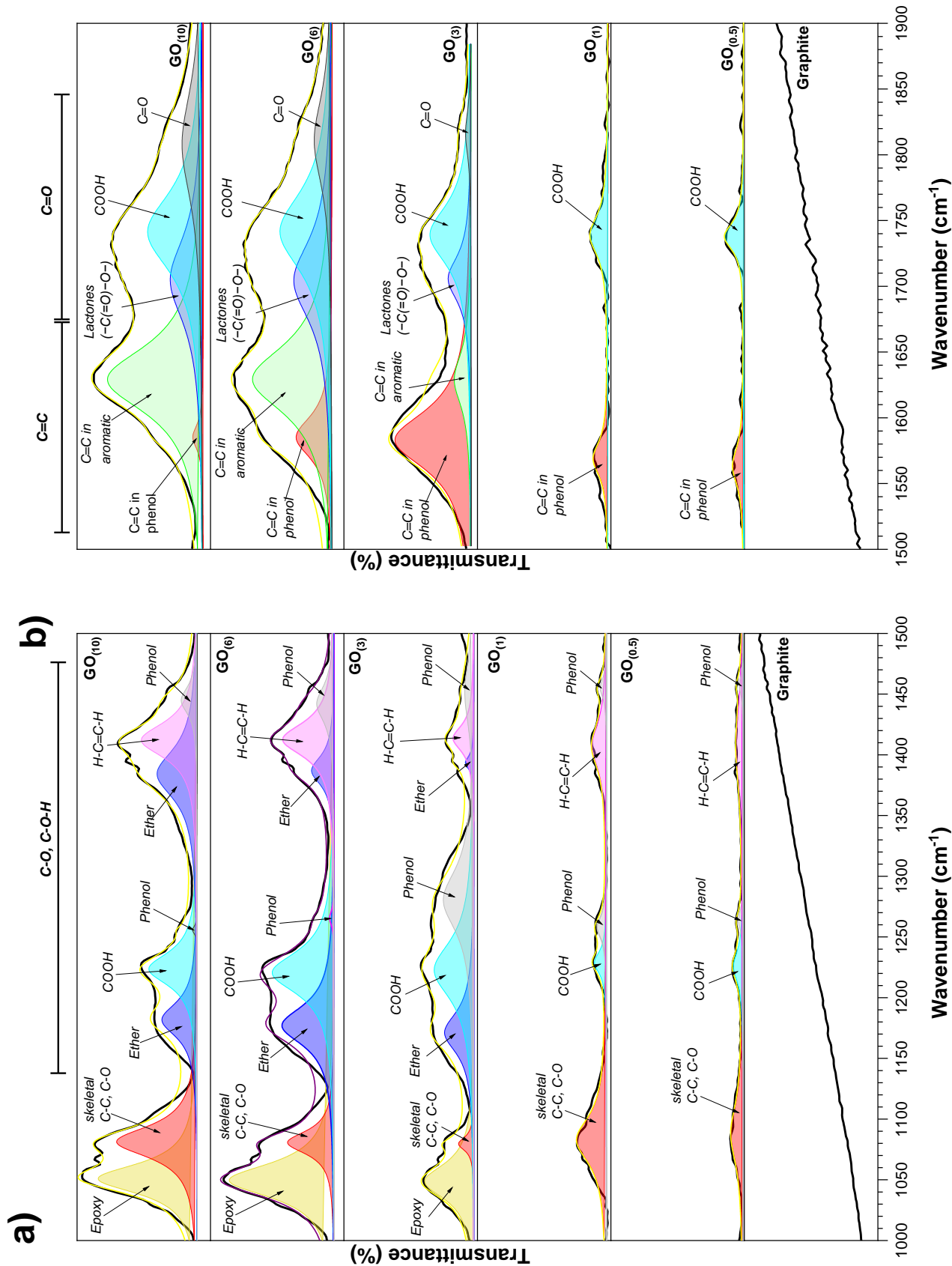


Fig. 4.14. Deconvoluted FTIR spectra of GOs with different oxidation degree (a) range 1000-1500 cm⁻¹ and (b) range 1500-2000 cm⁻¹

Subsequently, in a higher oxidation GO [GO₍₃₎], the same bands as in the less oxidized GOs are still seen, in addition to the appearance of new bands related to ethers at ≈ 1171 and ≈ 1394 cm^{-1} , and lactones at ≈ 1704 cm^{-1} . The newly developed bands may indicate a great diversity of functional groups formed at the edges. These functional groups are present at high oxidation degrees with variations in the ether/lactone fractions. Similarly, the appearance of an intense band at ≈ 1049 cm^{-1} associated with epoxide functional groups is observed. These groups appear in the basal plane and not only at the edges [59]. The intensity of this band gradually increases in GO₍₆₎ and GO₍₁₀₎, indicating a more extensive functionalization of the basal plane with the progression of the oxidation process. Finally, it is also observed that starting from GO₍₃₎, a band appears at ≈ 1629 cm^{-1} that gradually increases in intensity and is associated with C=C stretching. The increase in intensity is enhanced by a higher abundance of oxygen-containing elements [51]. This increase in intensity has been reported previously in other studies [60–63]. The general trend shows that as the oxidation degree increases, the presence of oxygen-containing functional groups increases and influences other structural properties such as the degree of exfoliation and crystallite size described above. The increased diversity of functional groups at the basal plane and edges is the result of the prolonged oxidation process, which leads to a more complex and varied chemical structure in GO layers [63–65].

4.3.2. Quantitative determination of oxidation degree by XPS

XPS was used to bring a complementary knowledge of the nature of the oxygenated groups of GO. Relative O/C ratios were calculated, as reported in other work [66, 67]. Fig. 4.15 shows the XPS C1s spectra of the graphite samples and the GOs produced. The C1s XPS deconvolution was carried out using the Gaussian function as reported in previous research [68]. The graphite spectrum shows the presence of peaks derived from the C=C bond at ≈ 284.6 eV, from the C-C bond at ≈ 285.3 eV, the C-OH bond at ≈ 286.5 eV and 291 eV the π - π^* transitions [69, 70].

Comparing the spectra of the GOs, the relative intensity of the graphitic domain (C=C/C-C) decreases with increasing KMnO₄, indicating gradual oxygenation of the material, which is consistent with the behavior of the sp^2 and sp^3 peaks obtained by Raman spectroscopy. The percentage of C=C/C-C decreases from $\approx 52.64\%$ in GO_(0.5) to $\approx 41.64\%$ in GO₍₁₀₎. On the other hand, it is observed that in the lowest oxidation GO [GO_(0.5)], the presence of C-OH bonds is mainly predominant ($\approx 33.93\%$), followed by carbonyl groups (C=O; $\approx 9.51\%$), and a minimal, almost negligible amount of epoxide groups (C-O-C; $\approx 3.93\%$). The limited existence of only two types of oxygenated functional groups could be attributed to the fact that not enough KMnO₄ was used during synthesis to promote other types. According to the model proposed by Lerf *et al* [71], the C-O-C bonds would be positioned in the basal plane, while the hydroxyl (C-OH) and carbonyl (C=O) groups would be found predominantly at the edges of the GO flakes or multi-vacancy groups. Then, with increasing oxidation, in GO₍₁₎ a significant occurrence of carbonyl group bonds (C=O; $\approx 12.55\%$) is observed, while the C-O bond content was briefly reduced to $\approx 27.92\%$. Additionally, an increase in the concentration of epoxide groups (C-O-C; $\approx 11.12\%$) is observed.

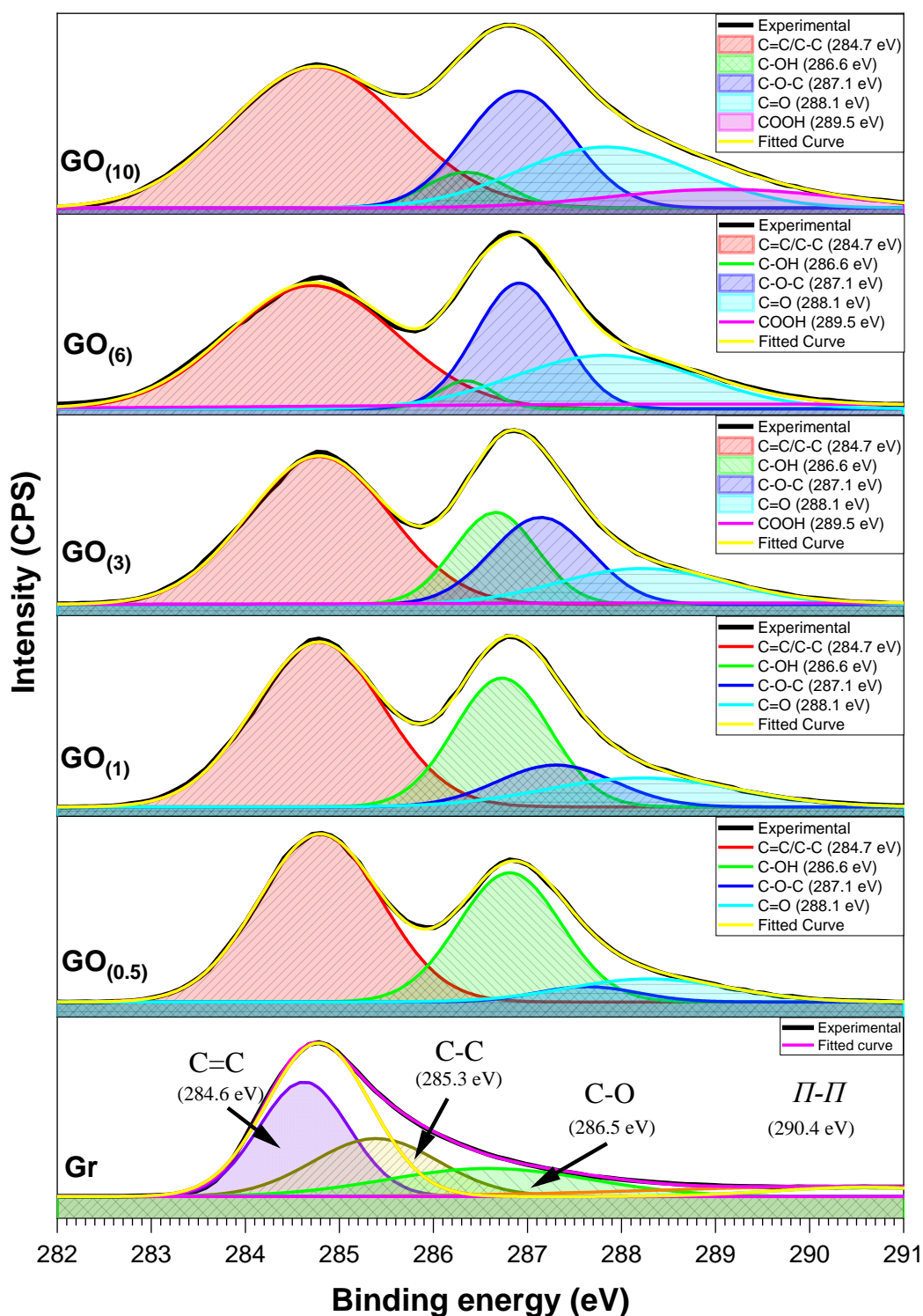


Fig. 4.15. XPS of GOs with different oxidation degrees.

In $GO_{(3)}$ and $GO_{(6)}$, however, the C-OH bond content decreased further to $\approx 3.27\%$, while the C=O bond content increased further to a maximum of $\approx 21.17\%$. This is attributed to a deprotonation phenomenon due to the increased quantity of oxidant in GO synthesis [70]. The oxidative environment provided by $KMnO_4$ can lead to the deprotonation of some hydroxyl (-OH) groups. The deprotonation process involves the removal of a proton (H^+) from the hydroxyl group, resulting in the formation of an alkoxide ion ($-O^-$). The alkoxide ions ($-O^-$) can

then react further in the presence of KMnO_4 and the oxygen atoms in the structure can rearrange to form a carbonyl group ($\text{C}=\text{O}$). In parallel, the amount of epoxide groups in the basal planes increases with oxidation up to $\approx 23.44\%$, attributed to more basal planes being exposed. Finally, in $\text{GO}_{(10)}$, concentrations of functional groups similar to $\text{GO}_{(6)}$ are observed, attributed to a saturation effect, coincident with previous characterizations that have shown less evident changes with higher level of oxidant.

The initial appearance of C-OH functional groups and their evolution to C=O groups at low oxidation level would demonstrate that the edges of the lamellae serve as reactive sites that are rapidly saturated at the onset of oxidation and that any subsequent increase in oxidation mainly affects other areas of the structure such as the basal planes, being demonstrated by the formation and increase of C-O-C bonds. This is consistent with the idea that edges and vacancies are the first sites to be occupied during the oxidation process discussed by FTIR. The results are shown in Table 4.3., where the increase in the oxidation degree of the GOs as a function of the amount of KMnO_4 is quantitatively demonstrated by the O/C in Table 4.3.

Table 4.3. Quantification of functional groups in GOs

Materials	C=C/C-C (%)	C-OH (%)	C-O-C	C=O (%)	-COOH (%)	O/C
$\text{GO}_{(0.5)}$	52.64%	33.93%	3.93%	9.51%	--	0.741
$\text{GO}_{(1)}$	48.41%	27.92%	11.12%	12.55%	--	0.911
$\text{GO}_{(3)}$	47.32%	17.14%	19.50%	13.62%	2.42%	1.001
$\text{GO}_{(6)}$	44.61%	3.27%	23.44%	21.17%	7.51%	1.231
$\text{GO}_{(10)}$	41.64%	5.29%	23.93%	21.52%	7.63%	1.330

4.4. Mechanism of graphene oxide formation

The use of various characterization techniques is a key approach to understand the evolution of the microstructural, morphological, and physicochemical characteristics of GOs concerning their oxidation degree. The experimental methods contributed to a deeper understanding of the formation mechanism of these materials, revealing crucial aspects of their structure and behavior. In this context, different authors commonly distinguish three distinct and independent steps in the course of the conversion of bulk graphite into GO [72]. However, the purification process, which is a fundamental step to obtain high-purity materials, has also been included in this work. Accordingly, the steps leading to the formation of GO can be summarized as follows:

The initial stage involves the transformation of *graphite* into a *graphite intercalation compound* (GIC). This stage begins immediately after the graphite is exposed to the acidic oxidizing medium and is completed within a few minutes. In the formed GIC, each graphene

layer alternates with an intermediate interlayer of intercalant (Fig. 4.16.). The interlayer arrangement is densely packed with H₂SO₄ and H₃PO₄ molecules, which do not form an ordered structure [73, 74].

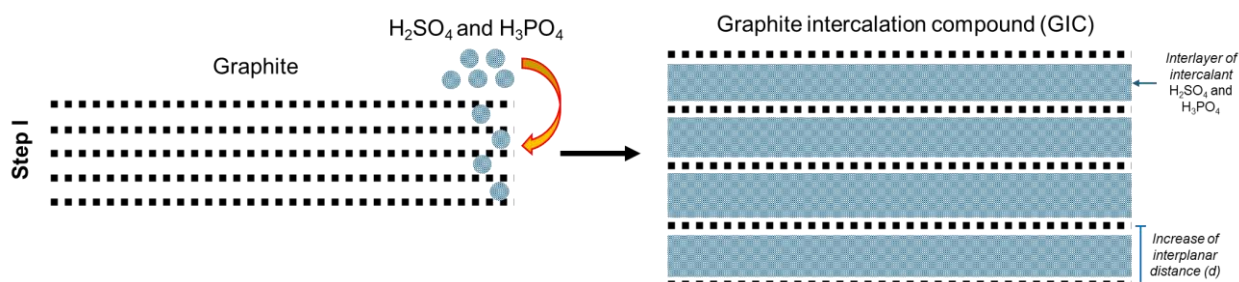


Fig. 4.16. Schematic representation of the conversion of graphite into GIC.

The second stage involves the transformation of GIC into the oxidized state of graphite, which is referred to as pristine graphite oxide (GrO). The conversion of GIC to GrO is much slower. The prerequisite for the successful oxidation of graphite is the capacity of acidic oxidizing media to intercalate graphite, resulting in the creation of graphite intercalation compounds (GIC). This applies to all currently recognized techniques for the preparation of GO. Intercalation expands the spacing between the layers of graphene in graphite, allowing the oxidant to reach the interlayer galleries (Fig. 4.17.).

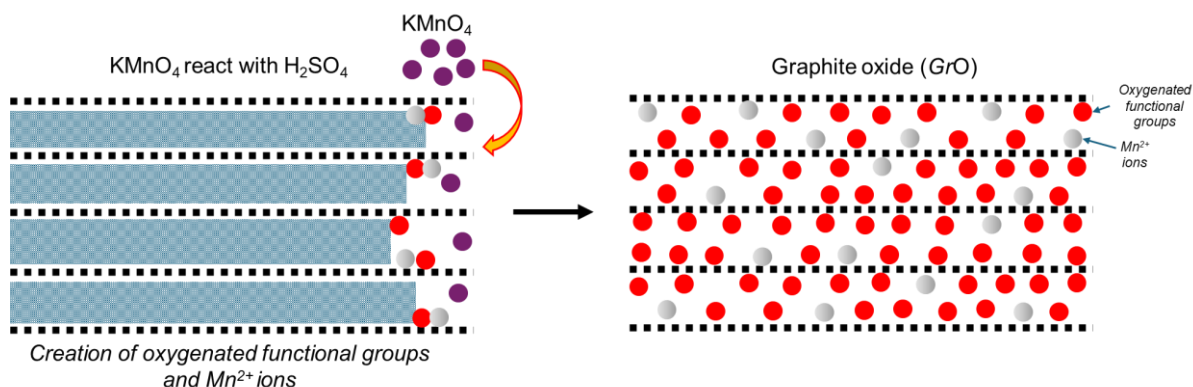
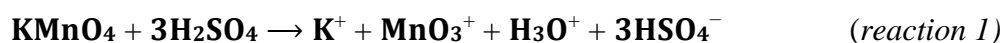


Fig. 4.17. Schematic representation of conversion GIC to the graphite oxide GrO

Although KMnO₄ is the used oxidant, the actual active species is Mn₂O₇ [75], which can selectively oxidize aliphatic unsaturated double bonds over aromatic double bonds. The small amount of H₃PO₄ acts as a catalyst in the oxidation reaction. It helps in promoting the reaction kinetics, making the oxidation process more efficient and controllable. The presence of phosphoric acid accelerates the formation of graphene oxide while maintaining the integrity of the graphene structure to a certain extent. While KMnO₄ upon reaction with sulfuric acid (H₂SO₄) generates di-manganese heptoxide (Mn₂O₇) and combined with the strongly acidic medium facilitates the oxidation process (reactions 1 and 2). In summary, as there is a greater amount of KMnO₄, more oxidation is promoted in the material.





Upon adding the combination to deionized water, the H_2SO_4 's dilution heat leads to a quick increase in the temperature of the mixture, resulting in the intercalated graphite experiencing secondary volume expansion [76]. Under these conditions, the Mn(VII) compound can produce ozone and oxidizing radicals such as hydroxyl radicals or atomic oxygen, which contribute to the oxidation of graphite to form some oxygen-containing groups [77]. At this stage, both FTIR and XPS showed that the functional groups formed at low oxidation are mainly present at the edges, and as oxidation increases, more functional groups are formed and occupy the basal planes of the lamellae as well. The oxidizing capacity of ozone can be enhanced by the formation of hydroxyl radicals when it encounters both water and newly formed MnO_2 . This destructive oxidation leads to the formation of more permanent defects covered by carboxyl groups. However, a certain amount of insoluble manganese compounds, such as MnO_2 , would be generated and grow on the graphite oxide surface [78]. Subsequently, the addition of H_2O_2 reduces Mn^{7+} and Mn^{4+} to Mn^{2+} .

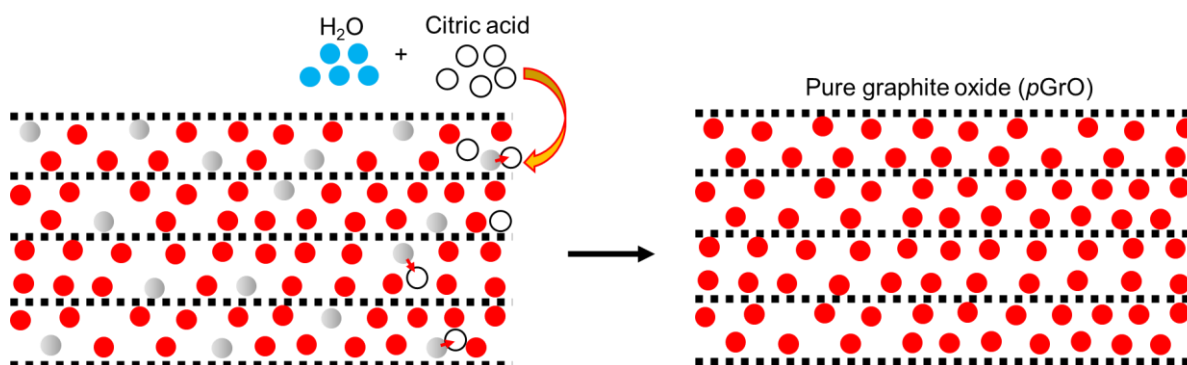


Fig. 4.18. Schematic representation of purification using ligands during the washing process.

The third step consists of the purification using ligands during the washing process which results in pure graphite oxide ($p\text{GrO}$) (Fig. 4.18.). When the GrO and CA dispersions are mixed and stirred, the manganese ions desorb from the GrO and coordinate with the ligands. Due to ligand chelation, manganese complexes with ligands are relatively stable. Therefore, most of the manganese ions will be desorbed from the GrO by forming complexes with competitive ligands. This makes the purification process efficient and the removal of manganese successful, as demonstrated by EPR.

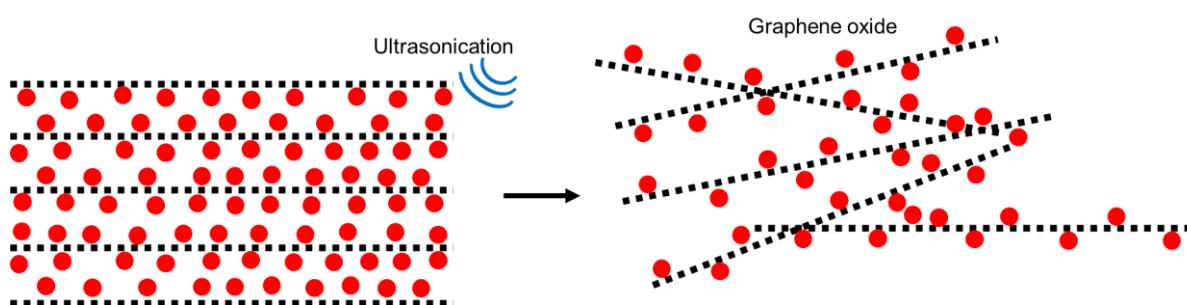


Fig. 4.19. Conversion of pure graphite oxide ($p\text{GrO}$) to GO .

Finally, the fourth step is the conversion of GrO to GO. This process entails the breaking of the interlayer bonds along the c -axis and the separation of the p GrO into individual atomic layer sheets, as seen in Fig. 4.19. Several synthesis techniques indicate that sonication is essential for dispersing the produced p GrO in aqueous solutions. Sonication is required only for partially oxidized graphene oxide (GO) samples that are generated from graphite with high particle sizes, as specified in the original protocols [72]. When the prepared GO is sufficiently oxidized, it spontaneously flakes off in monolayer sheets by simple stirring in water.

4.5. Electrical conductivity behavior

Fig. 4.20.a. shows the dependence of the electrical conductivity (AC) at room temperature on the frequency of the GOs. All GOs showed little variation over the frequency range analyzed, with almost constant values. This behavior was reported by Kavinkumar T. *et al.* for a GO heat-treated at 220 °C [79]. A possible explanation for this phenomenon is that, within this range, the charge carriers (electrons or holes) of the GO undergo scattering by defects and impurities at a rate approximately balanced by their mobility. As a result, the overall conductivity remains relatively stable.

Fig. 4.20.b. shows the reduction of the electrical conductivity of GO as the oxidation degree increases. This phenomenon is directly related to changes in the structure and conduction properties of GO, *i.e.* at low oxidation a highly conjugated π -bond structure is maintained, which allows high electronic mobility and thus high conductivity. Subsequently, the introduction of oxygenated groups breaks the π -bonds and alters this conjugated structure, leading to a dispersion of electronic states that reduces the mobility of electrons through the material. Thus, with increasing oxidation, more and more π -bonds are broken, and the structure becomes less conductive. The variation of electrical conductivity with the oxidation degree is given by the following equation, where x represents the amount of KMnO_4 .

$$\sigma' = -0.0053 + 0.066e^{(-0.1908x)}$$

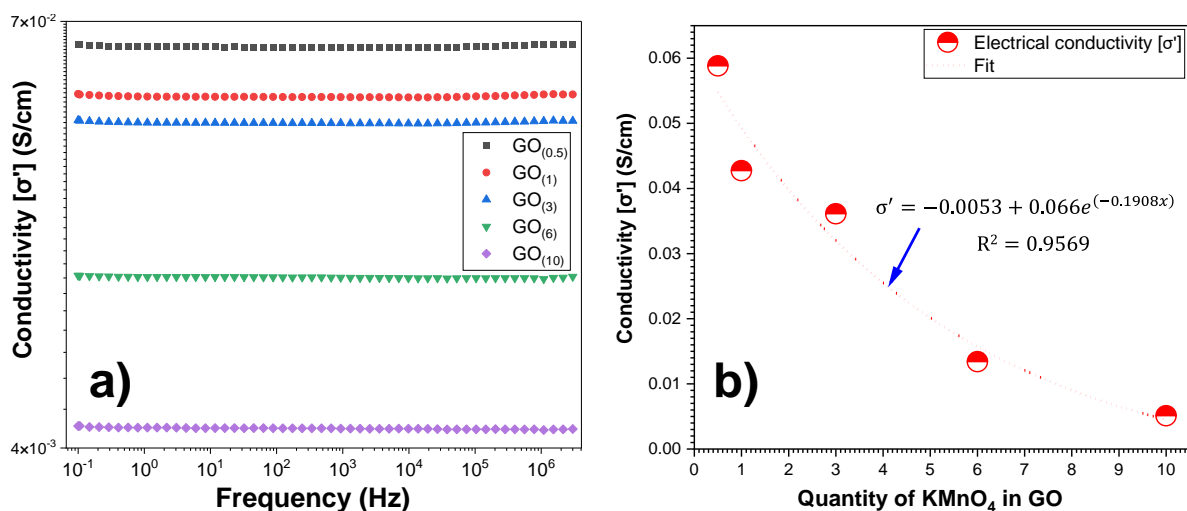


Fig. 4.20. (a) Electrical conductivity (σ') of GO as a function of frequency, and (b) dependence of the electrical conductivity as a function of the amount of KMnO_4 .

4.6. Conclusion

GO was successfully prepared by the Tour method. A thorough analysis of the physic-chemical properties of the obtained pure GOs confirmed the precise ability to control the oxidation degree by adjusting the amounts of KMnO_4 used during the synthesis.

- The presence and evolution of the (001) planes characteristic of GO was confirmed by X-ray diffraction. Quantitative analysis revealed a significant increase in the crystallite size of the oxidized domains with increasing KMnO_4 quantity, following an exponential pattern ranging from ≈ 2.04 nm to ≈ 7.70 nm. This study also revealed the expansion of the inter-reticular spacing from ≈ 0.34 nm initially for the precursor graphite to ≈ 0.903 nm for the more oxidized GO.
- Raman spectroscopy analysis of the D and G-bands has provided a more profound comprehension of the degree of structural defects and carbon ordering. The A_D/A_G ratio has been used as a quantitative measure to characterize these properties and shows a progressive increase from ≈ 1.36 at the lowest oxidation GO to a maximum of ≈ 3.50 at the highest KMnO_4 concentration conditions. These results underline the direct influence of oxidation on the structural configuration of the material, demonstrating a transition from the predominance of defects associated with sp^3 hybridizations in the less oxidized states to the predominance of "vacancies" and "grain boundary" defects in the more oxidized states. In addition, the reduction in the size of the graphite domain was confirmed in parallel with the XRD.
- SEM images showed significant changes in the morphology of the GO structures. The transition from multilayered structures to agglomerates and wrinkled nanosheets indicates a more pronounced exfoliation process, suggesting a higher degree of disorder. This phenomenon is quantitatively confirmed by the analysis of the specific surface area (SSA), of which significant increase from 133.08 m^2/g for graphite to a maximum of 394.22 m^2/g for the more oxidized graphene oxide supports the increase of the interplanar distance and the prevalence of grain boundary defects.
- The combined application of FTIR and XPS has provided an accurate understanding of the chemical composition of GOs. The results confirm the presence of hydroxyl, carbonyl, and epoxy groups, showing variations in area with increasing concentration. In particular, it is conclusively shown that under low oxidation conditions, species mainly located at the edges of the lamellae predominate, while an increase in KMnO_4 concentration systematically leads to the gradual appearance of oxygenated species occupying the basal planes. This shows a clear evolution in the distribution and configuration of the oxygenated functional groups within the GO structure, in direct response to the controlled variation of the oxidation conditions, confirming the tunability of the oxidation degree of the GOs produced by the Tour method.

- The electrical conductivity was also affected with increasing oxidation level, decreasing from ≈ 0.0582 S/cm to ≈ 0.0051 S/cm. These changes in optical and electrical properties are directly related to changes in the GO structure, *i.e.* at low oxidation a highly conjugated π -bond structure is maintained, allowing high electronic mobility and hence high conductivity. The introduction of oxygenated groups, on the other hand, breaks the π -bonds and alters this conjugated structure, leading to a dispersion of electronic states that reduces the mobility of electrons through the material. In both cases, the data were fitted to an exponential model. This indicates that the properties can be significantly altered during the first few oxidation degrees, but at higher oxidation the properties show relative stability, suggesting a saturation of the changes.

References

1. Ping Loh, K., Bao, Q., eda, G., chhowalla, manish: Graphene oxide as a chemically tunable platform for optical applications. *Nat Chem.* 2, (2010). <https://doi.org/10.1038/nchem.907>
2. Panich, A.M., Shames, A.I., Aleksenskii, A.E., Dideikin, A.: Magnetic resonance evidence of manganese–graphene complexes in reduced graphene oxide. *Solid State Commun.* 152, 466–468 (2012). <https://doi.org/10.1016/J.SSC.2012.01.005>
3. Mohanta, Z., Gaonkar, S.K., Kumar, M., Saini, J., Tiwari, V., Srivastava, C., Atreya, H.S.: Influence of oxidation degree of graphene oxide on its nuclear relaxivity and contrast in MRI. *ACS Omega.* 5, 22131–22139 (2020). <https://doi.org/10.1021/ACSOMEGA.0C02220>
4. Paratala, B.S., Jacobson, B.D., Kanakia, S., Francis, L.D., Sitharaman, B.: Physicochemical Characterization, and Relaxometry Studies of Micro-Graphite Oxide, Graphene Nanoplatelets, and Nanoribbons. *PLoS One.* 7, e38185 (2012). <https://doi.org/10.1371/JOURNAL.PONE.0038185>
5. Panich, A.M., Shames, A.I., Sergeev, N.A.: Paramagnetic Impurities in Graphene Oxide. *Appl Magn Reson.* 44, 107–116 (2013). <https://doi.org/10.1007/S00723-012-0392-Z>
6. Thiyagarajan, K., Sivakumar, K.: Oxygen vacancy-induced room temperature ferromagnetism in graphene–SnO₂ nanocomposites. *J Mater Sci.* 52, (2017). <https://doi.org/10.1007/s10853-017-1016-7>
7. Abragam, A., Bleaney, B.: *Electron Paramagnetic Resonance of Transition Ions* (Oxford Classic Texts in the Physical Sciences). 944 (2012)
8. Panich, A.M., Shames, A.I., Aleksenskii, A.E., Dideikin, A.: Magnetic resonance evidence of manganese–graphene complexes in reduced graphene oxide. *Solid State Commun.* 152, 466–468 (2012). <https://doi.org/10.1016/J.SSC.2012.01.005>
9. Savchenko D., K.A.: *Frontiers in Magnetic Resonance.* 1, (2018)
10. Namvari, M., Biswas, C.S., Wang, Q., Liang, W., Stadler, F.J.: Crosslinking hydroxylated reduced graphene oxide with RAFT-CTA: A nano-initiator for preparation of well-defined amino acid-based polymer nanohybrids. *J Colloid Interface Sci.* 504, 731–740 (2017). <https://doi.org/10.1016/J.JCIS.2017.06.007>
11. Krishnamoorthy, K., Veerapandian, M., Yun, K., Kim, S.J.: The chemical and structural analysis of graphene oxide with different degrees of oxidation. *Carbon N Y.* 53, 38–49 (2013). <https://doi.org/10.1016/J.CARBON.2012.10.013>
12. Guoxiu, W., Juan, Y., Jinsoo, P., Xinglong, G., Bei, W., Hao, L., Jane, Y.: Facile Synthesis and Characterization of Graphene Nanosheets. *Journal of Physical Chemistry C.* 112, 8192–8195 (2008). <https://doi.org/10.1021/JP710931H>
13. Dikin, D.A., Stankovich, S., Zimney, E.J., Piner, R.D., Dommett, G.H.B., Evmenenko, G., Nguyen, S.T., Ruoff, R.S.: Preparation and characterization of graphene oxide paper. *Nature* 2007 448:7152. 448, 457–460 (2007). <https://doi.org/10.1038/nature06016>
14. Scarpulla, M.A., Dubon, O.D., Yu, K.M., Monteiro, O., Pillai, M.R., Aziz, M.J., Ridgway, M.C.: Ferromagnetic Ga_{1-x}Mn_xAs produced by ion implantation and pulsed-laser melting. *Appl Phys Lett.* 82, 1251–1253 (2003). <https://doi.org/10.1063/1.1555260>
15. Langford, J.I., Wilson, A.J.C., IUCr: Scherrer after sixty years: A survey and some new results in the determination of crystallite size. *urn:issn:0021-8898.* 11, 102–113 (1978). <https://doi.org/10.1107/S0021889878012844>
16. Warren, B.E.: X-ray diffraction in random layer lattices. *Physical Review.* 59, 693–698 (1941). <https://doi.org/10.1103/PhysRev.59.693>

17. Elton, L.R.B., Jackson, D.F.: X-Ray Diffraction and the Bragg Law. Citation: American Journal of Physics. 34, 1036 (1966). <https://doi.org/10.1119/1.1972439>
18. Sheshmani, S., Amini, R.: Preparation and characterization of some graphene based nanocomposite materials. Carbohydr Polym. 95, 348–359 (2013). <https://doi.org/10.1016/J.CARBPOL.2013.03.008>
19. Stobinski, L., Lesiak, B., Malolepszy, A., Mazurkiewicz, M., Mierzwa, B., Zemek, J., Jiricek, P., Bieloshapka, I.: Graphene oxide and reduced graphene oxide studied by the XRD, TEM and electron spectroscopy methods. J Electron Spectros Relat Phenomena. 195, 145–154 (2014). <https://doi.org/10.1016/J.ELSPEC.2014.07.003>
20. Nakagawa, M.A., Brito De Souza, C., Gonçalves, E.S., Rahmawati, R., Suendo, V., Hidayat, R.: Reduced Graphene Oxide/Polyaniline Nanocomposite as Efficient Counter Electrode for Dye Sensitized Solar Cells. IOP Conf Ser Mater Sci Eng. 384, 012040 (2018). <https://doi.org/10.1088/1757-899X/384/1/012040>
21. Song, X., Zhou, Q., Zhang, T., Xu, H., Wang, Z.: Pressure-assisted preparation of graphene oxide quantum dot-incorporated reverse osmosis membranes: antifouling and chlorine resistance potentials. J Mater Chem A Mater. 4, 16896–16905 (2016). <https://doi.org/10.1039/C6TA06636D>
22. Sato, K., Saito, R., Oyama, Y., Jiang, J., Cañado, L.G., Pimenta, M.A., Jorio, A., Samsonidze, G.G., Dresselhaus, G., Dresselhaus, M.S.: D-band Raman intensity of graphitic materials as a function of laser energy and crystallite size. Chem Phys Lett. 427, 117–121 (2006). <https://doi.org/10.1016/J.CPLETT.2006.05.107>
23. Krishnamoorthy, K., Veerapandian, M., Kim, G.-S., Jae Kim, S.: A One Step Hydrothermal Approach for the Improved Synthesis of Graphene Nanosheets. Curr Nanosci. 8, 934–938 (2012). <https://doi.org/10.2174/157341312803989088>
24. Kadam, M.M., Lokare, O.R., Kireeti, K.V.M.K., Gaikar, V.G., Jha, N.: Impact of the degree of functionalization of graphene oxide on the electrochemical charge storage property and metal ion adsorption. RSC Adv. 4, 62737–62745 (2014). <https://doi.org/10.1039/C4RA08862J>
25. Malard, L.M., Pimenta, M.A., Dresselhaus, G., Dresselhaus, M.S.: Raman spectroscopy in graphene. Phys Rep. 473, 51–87 (2009). <https://doi.org/10.1016/J.PHYSREP.2009.02.003>
26. Lee, A.Y., Yang, K., Anh, N.D., Park, C., Lee, S.M., Lee, T.G., Jeong, M.S.: Raman study of D* band in graphene oxide and its correlation with reduction. Appl Surf Sci. 536, 147990 (2021). <https://doi.org/10.1016/J.APSUSC.2020.147990>
27. Manea, A., Leishman, M.R.: Competitive interactions between native and invasive exotic plant species are altered under elevated carbon dioxide. Oecologia. 165, 735–744 (2011). <https://doi.org/10.1007/S00442-010-1765-3>
28. Nemanich, R.J., Glass, J.T., Lucovsky, G., Shroder, R.E.: Raman scattering characterization of carbon bonding in diamond and diamondlike thin films. Journal of Vacuum Science & Technology A. 6, 1783–1787 (1988). <https://doi.org/10.1116/1.575297>
29. Al-Jishi, R., Dresselhaus, G.: Lattice-dynamical model for graphite. Phys Rev B. 26, 4514 (1982). <https://doi.org/10.1103/PhysRevB.26.4514>
30. Jawhari, T., Roid, A., Casado, J.: Raman spectroscopic characterization of some commercially available carbon black materials. Carbon N Y. 33, 1561–1565 (1995). [https://doi.org/10.1016/0008-6223\(95\)00117-V](https://doi.org/10.1016/0008-6223(95)00117-V)
31. Vollebregt, S., Ishihara, R., Tichelaar, F.D., Hou, Y., Beenakker, C.I.M.: Influence of the growth temperature on the first and second-order Raman band ratios and widths of carbon nanotubes and fibers. Carbon N Y. 50, 3542–3554 (2012). <https://doi.org/10.1016/J.CARBON.2012.03.026>
32. Kaniyoor, A., Ramaprabhu, S.: A Raman spectroscopic investigation of graphite oxide derived graphene. AIP Adv. 2, 32183 (2012). <https://doi.org/10.1063/1.4756995/21084>
33. Ferrari, A.C., Robertson, J.: Origin of the 1150 – cm⁻¹ Raman mode in nanocrystalline diamond. Phys Rev B Condens Matter Mater Phys. 63, (2001). <https://doi.org/10.1103/PhysRevB.63.121405>
34. Ferrari, A.C., Meyer, J.C., Scardaci, V., Casiraghi, C., Lazzeri, M., Mauri, F., Piscanec, S., Jiang, D., Novoselov, K.S., Roth, S., Geim, A.K.: Raman spectrum of graphene and graphene layers. Phys Rev Lett. 97, 187401 (2006). <https://doi.org/10.1103/PHYSREVLETT.97.187401>
35. TUINSTRAL F, KOENIG JL: Raman Spectrum of Graphite. J Chem Phys. 53, 1126 (2003). <https://doi.org/10.1063/1.1674108>
36. Eckmann, A., Felten, A., Mishchenko, A., Britnell, L., Krupke, R., Novoselov, K.S., Casiraghi, C.: Probing the nature of defects in graphene by Raman spectroscopy. Nano Lett. 12, 3925–3930 (2012). <https://doi.org/10.1021/NL300901A>
37. AlHumaidan, F.S., Rana, M.S., Vinoba, M., Rajasekaran, N., AlHenyyan, H.Y., Ali, A.A.: Synthesizing few-layer carbon materials from asphaltene by thermal treatment. Diam Relat Mater. 129, 109316 (2022). <https://doi.org/10.1016/J.DIAMOND.2022.109316>

38. Li, C., Lu, Y., Yan, J., Yu, W., Zhao, R., Du, S., Niu, K.: Effect of long-term ageing on graphene oxide: structure and thermal decomposition. *R Soc Open Sci.* 8, (2021). <https://doi.org/10.1098/rsos.202309>
39. Cheng, S., Li, N., Pan, Y., Wang, B., Hao, H., Hu, F., Liu, C., Chen, Y., Jian, X.: Establishment of silane/GO multistage hybrid interface layer to improve interfacial and mechanical properties of carbon fiber reinforced poly (Phthalazinone ether ketone) thermoplastic composites. *Materials.* 15, (2022). <https://doi.org/10.3390/ma15010206>
40. Eigler, S., Dotzer, C., Hirsch, A.: Visualization of defect densities in reduced graphene oxide. *Carbon N Y.* 50, 3666–3673 (2012). <https://doi.org/10.1016/J.CARBON.2012.03.039>
41. Hu, X., Yu, Y., Zhou, J., Song, L.: Effect of Graphite Precursor on Oxidation Degree, Hydrophilicity and Microstructure of Graphene Oxide. <https://doi.org/10.1142/S1793292014500374>
42. Reynosa-Martínez, A.C., Tovar, G.N., Gallegos, W.R., Rodríguez-Meléndez, H., Torres-Cadena, R., Mondragón-Solórzano, G., Barroso-Flores, J., Alvarez-Lemus, M.A., Montalvo, V.G., López-Honorato, E.: Effect of the degree of oxidation of graphene oxide on As(III) adsorption. *J Hazard Mater.* 384, 121440 (2020). <https://doi.org/10.1016/J.JHAZMAT.2019.121440>
43. Venezuela, P., Lazzeri, M., Mauri, F.: Theory of double-resonant Raman spectra in graphene: Intensity and line shape of defect-induced and two-phonon bands. *Phys Rev B Condens Matter Mater Phys.* 84, 035433 (2011). <https://doi.org/10.1103/PHYSREVB.84.035433>
44. Ferrari, A.C., Basko, D.M.: Raman spectroscopy as a versatile tool for studying the properties of graphene. *Nature Nanotechnology* 2013 8:4. 8, 235–246 (2013). <https://doi.org/10.1038/nnano.2013.46>
45. Ferrari, I., Motta, A., Zanoni, R., Scaramuzzo, F.A., Amato, F., Dalchiele, E.A., Marrani, A.G.: Understanding the nature of graphene oxide functional groups by modulation of the electrochemical reduction: A combined experimental and theoretical approach. *Carbon N Y.* 203, 29–38 (2023). <https://doi.org/10.1016/J.CARBON.2022.11.052>
46. Ferrari, A., Robertson, J.: Interpretation of Raman spectra of disordered and amorphous carbon. *Phys Rev B.* 61, 14095 (2000). <https://doi.org/10.1103/PhysRevB.61.14095>
47. Park, S., An, J., Jung, I., Piner, R.D., An, S.J., Li, X., Velamakanni, A., Ruoff, R.S.: Colloidal suspensions of highly reduced graphene oxide in a wide variety of organic solvents. *Nano Lett.* 9, 1593–1597 (2009). <https://doi.org/10.1021/NL803798Y>
48. Dubey, S.P., Nguyen, T.T.M., Kwon, Y.N., Lee, C.: Synthesis and characterization of metal-doped reduced graphene oxide composites, and their application in removal of Escherichia coli, arsenic and 4-nitrophenol. *Journal of Industrial and Engineering Chemistry.* 29, 282–288 (2015). <https://doi.org/10.1016/J.JIEC.2015.04.008>
49. Hidayah, N.M.S., Liu, W.W., Lai, C.W., Noriman, N.Z., Khe, C.S., Hashim, U., Lee, H.C.: Comparison on graphite, graphene oxide and reduced graphene oxide: Synthesis and characterization. *AIP Conf Proc.* 1892, 150002 (2017). <https://doi.org/10.1063/1.5005764>
50. Guerrero-Contreras, J., Caballero-Briones, F.: Graphene oxide powders with different oxidation degree, prepared by synthesis variations of the Hummers method. *Mater Chem Phys.* 153, 209–220 (2015). <https://doi.org/10.1016/J.MATCHEMPHYS.2015.01.005>
51. Fuente, E., Menéndez, J.A., Díez, M.A., Suárez, D., Montes-Morán, M.A.: Infrared spectroscopy of carbon materials: A quantum chemical study of model compounds. *Journal of Physical Chemistry B.* 107, 6350–6359 (2003). <https://doi.org/10.1021/JP027482G>
52. Lim, S., Abdullah, A.M., Ong, H.C., Pang, Y.L., Fang Tee, S., Abdullah, A.Z., Wu, C.-H., Chong, W.C., Wahab Mohammad, A., Mahmoudi, E.: Enhancement of photocatalytic degradation of organic dyes using ZnO decorated on reduced graphene oxide (rGO). *Desalination Water Treat.* 108, 311–321 (2018). <https://doi.org/10.5004/dwt.2018.21947>
53. Low, F.W., Lai, C.W., Abd Hamid, S.B.: Easy preparation of ultrathin reduced graphene oxide sheets at a high stirring speed. *Ceram Int.* 41, 5798–5806 (2015). <https://doi.org/10.1016/J.CERAMINT.2015.01.008>
54. Nine, M.J., Tran, D.N.H., ElMekawy, A., Losic, D.: Interlayer growth of borates for highly adhesive graphene coatings with enhanced abrasion resistance, fire-retardant and antibacterial ability. *Carbon N Y.* 117, 252–262 (2017). <https://doi.org/10.1016/J.CARBON.2017.02.064>
55. Prodan, D., Moldovan, M., Furtos, G., Saroși, C., Filip, M., Perhaița, I., Carpa, R., Popa, M., Cuc, S., Varvara, S., Popa, D.: Synthesis and Characterization of Some Graphene Oxide Powders Used as Additives in Hydraulic Mortars. *Applied Sciences* 2021, Vol. 11, Page 11330. 11, 11330 (2021). <https://doi.org/10.3390/APP112311330>
56. Park, J., Kim, Y.S., Sung, S.J., Kim, T., Park, C.R.: Highly dispersible edge-selectively oxidized graphene with improved electrical performance. *Nanoscale.* 9, 1699–1708 (2017). <https://doi.org/10.1039/C6NR05902C>

57. Tian, S., Sun, J., Yang, S., He, P., Wang, G., Di, Z., Ding, G., Xie, X., Jiang, M.: Controllable Edge Oxidation and Bubbling Exfoliation Enable the Fabrication of High Quality Water Dispersible Graphene. *Scientific Reports* 2016 6:1. 6, 1–8 (2016). <https://doi.org/10.1038/srep34127>
58. An, J., Nam, B.H., Alharbi, Y., Cho, B.H., Khawaji, M.: Edge-oxidized graphene oxide (EOGO) in cement composites: Cement hydration and microstructure. *Compos B Eng.* 173, 106795 (2019). <https://doi.org/10.1016/J.COMPOSITESB.2019.05.006>
59. Cano, F.J., Romero-Núñez, A., Liu, H., Reyes-Vallejo, O., Ashok, A., Velumani, S., Kassiba, A.: Variation in the bandgap by gradual reduction of GOs with different oxidation degrees: A DFT analysis. *Diam Relat Mater.* 139, 110382 (2023). <https://doi.org/10.1016/J.DIAMOND.2023.110382>
60. Çiplak, Z., Yildiz, N., Çalimli, A.: Investigation of Graphene/Ag Nanocomposites Synthesis Parameters for Two Different Synthesis Methods. *Fullerenes, Nanotubes and Carbon Nanostructures.* 23, 361–370 (2015). <https://doi.org/10.1080/1536383X.2014.894025>
61. Khalili, D.: Graphene oxide: a promising carbocatalyst for the regioselective thiocyanation of aromatic amines, phenols, anisols and enolizable ketones by hydrogen peroxide/KSCN in water. *New Journal of Chemistry.* 40, 2547–2553 (2016). <https://doi.org/10.1039/C5NJ02314A>
62. Zhong, L., Yun, K.: Graphene oxide-modified zn particles: Synthesis, characterization, and antibacterial properties. *Int J Nanomedicine.* 10, 79–92 (2015). <https://doi.org/10.2147/IJN.S88319>
63. Nazri, S.R.B., Liu, W.W., Khe, C.S., Hidayah, N.M.S., Teoh, Y.P., Voon, C.H., Lee, H.C., Adelyn, P.Y.P.: Synthesis, characterization and study of graphene oxide. *AIP Conf Proc.* 2045, 20033 (2018). <https://doi.org/10.1063/1.5080846/816933>
64. Gupta, V., Sharma, N., Singh, U., Arif, M., Singh, A.: Higher oxidation level in graphene oxide. *Optik (Stuttg).* 143, 115–124 (2017). <https://doi.org/10.1016/J.IJLEO.2017.05.100>
65. Díez-pascual, A.M., Sainz-urruela, C., Vallés, C., Vera-lópez, S., Andrés, M.P.S.: Tailorable Synthesis of Highly Oxidized Graphene Oxides via an Environmentally-Friendly Electrochemical Process. *Nanomaterials* 2020, Vol. 10, Page 239. 10, 239 (2020). <https://doi.org/10.3390/NANO10020239>
66. Reynosa-Martínez, A.C., Tovar, G.N., Gallegos, W.R., Rodríguez-Meléndez, H., Torres-Cadena, R., Mondragón-Solórzano, G., Barroso-Flores, J., Alvarez-Lemus, M.A., Montalvo, V.G., López-Honorato, E.: Effect of the degree of oxidation of graphene oxide on As(III) adsorption. *J Hazard Mater.* 384, 121440 (2020). <https://doi.org/10.1016/J.JHAZMAT.2019.121440>
67. Salazar-Aguilar, A.D., Tristan, F., Labrada-Delgado, G.J., Meneses-Rodríguez, D., Vega-Díaz, S.M.: Three-dimensional structure made with nitrogen-doped reduced graphene oxide with spherical porous morphology. *Carbon N Y.* 149, 86–92 (2019). <https://doi.org/10.1016/J.CARBON.2019.04.016>
68. Kim, N.H., Kuila, T., Lee, J.H.: Simultaneous reduction, functionalization and stitching of graphene oxide with ethylenediamine for composites application. *J Mater Chem A Mater.* 1, 1349–1358 (2012). <https://doi.org/10.1039/C2TA00853J>
69. Sánchez-Albores, R., Cano, F.J., Sebastian, P.J., Reyes-Vallejo, O.: Microwave-assisted biosynthesis of ZnO-GO particles using orange peel extract for photocatalytic degradation of methylene blue. *J Environ Chem Eng.* 10, 108924 (2022). <https://doi.org/10.1016/J.JECE.2022.108924>
70. Carvalho, A., Costa, M.C.F., Marangoni, V.S., Ng, P.R., Nguyen, T.L.H., Castro Neto, A.H.: The Degree of Oxidation of Graphene Oxide. *Nanomaterials.* 11, 1–8 (2021). <https://doi.org/10.3390/NANO11030560>
71. He, H., Klinowski, J., Forster, M., Lerf, A.: A new structural model for graphite oxide. *Chem Phys Lett.* 287, 53–56 (1998). [https://doi.org/10.1016/S0009-2614\(98\)00144-4](https://doi.org/10.1016/S0009-2614(98)00144-4)
72. Dimiev, A.M.: Mechanism of Formation and Chemical Structure of Graphene Oxide. *Graphene Oxide: Fundamentals and Applications.* 36–84 (2016). <https://doi.org/10.1002/9781119069447.CH2>
73. Dimiev, A.M., Bachilo, S.M., Saito, R., Tour, J.M.: Reversible formation of ammonium persulfate/sulfuric acid graphite intercalation compounds and their peculiar Raman spectra. *ACS Nano.* 6, 7842–7849 (2012). <https://doi.org/10.1021/nn3020147>
74. Yosida, Y., Tanuma, S., Okabe, K.: In situ observation of x-ray diffraction in a synthesis of H₂SO₄-GICS. *Synth Met.* 34, 341–346 (1989). [https://doi.org/10.1016/0379-6779\(89\)90406-2](https://doi.org/10.1016/0379-6779(89)90406-2)
75. Ardestani, M.M., Mahpishanian, S., Rad, B.F., Janmohammadi, M., Baghdadi, M.: Preparation and characterization of room-temperature chemically expanded graphite: Application for cationic dye removal. *Korean Journal of Chemical Engineering* 2022 39:6. 39, 1496–1506 (2022). <https://doi.org/10.1007/S11814-022-1084-5>
76. Dimiev, A., Kosynkin, D. V., Alemany, L.B., Chaguine, P., Tour, J.M.: Pristine graphite oxide. *J Am Chem Soc.* 134, 2815–2822 (2012). <https://doi.org/10.1021/ja211531y>
77. Pumera, M., Ambrosi, A., Chng, E.L.K.: Impurities in graphenes and carbon nanotubes and their influence on the redox properties. *Chem Sci.* 3, 3347–3355 (2012). <https://doi.org/10.1039/C2SC21374E>

78. Luo, D., Zhang, F., Ren, Z., Ren, W., Yu, L., Jiang, L., Ren, B., Wang, L., Wang, Z., Yu, Y., Zhang, Q.: An improved method to synthesize nanoscale graphene oxide using much less acid. *Materials Today Physics*. 9, 100097 (2019). <https://doi.org/10.1016/J.MTPHYS.2019.100097>
79. Kavinkumar, T., Sastikumar, D., Manivannan, S.: Effect of functional groups on dielectric, optical gas sensing properties of graphene oxide and reduced graphene oxide at room temperature. *RSC Adv*. 5, 10816–10825 (2015). <https://doi.org/10.1039/C4RA12766H>

Chapter V:

Mechanosynthesis: TiO₂-GO Hybrid nanostructures by ball-milling

Mechanochemistry is a branch of solid-state chemistry in which intramolecular bonds are broken mechanically using external mechanical energy, followed by additional chemical reactions [1]. High energy ball milling is a process in which a mixture of powders placed in the ball-mill is subjected to the high-energy collision of balls. This process was developed by Benjamin *et al.* at the International Nickel Company in the 1960s [2]. The ball mill system comprises a solitary turntable, sometimes referred to as a turntable, and either two or four bowls. The turntable exhibits unidirectional rotation while the bowls exhibit counter-rotational motion. The centrifugal forces produced by the bowl's movement on its axis, in conjunction with the turntable's rotation, exert an effect on both the powder combination and the grinding balls within the bowl. The powder mixture is fragmented and bonded together by the high velocity impact. The centrifugal forces alternate in synchronization due to the various rotation orientations of the bowl and turn disc. Friction arises from the interaction between the rigid grinding balls and powder mixture as they repeatedly move in opposite directions down the inside surface of the bowl and collide with the opposing surface. The kinetic energy of the milling balls in the vertical direction is up to 40 times greater than the energy caused by gravitational acceleration. Hence, the planetary ball mill is well-suited for high-speed grinding. For TiO₂, high-energy ball-milling has been used to modify the phase composition and particle size, resulting in the formation of composite nanostructures with extended light absorption and small bandgaps, properties that are very useful in the photocatalytic degradation of pollutants. Research has also shown that mechanical milling can promote the efficient formation of hybridized nanostructures based on TiO₂ with other materials to obtain improved properties in various applications (Table S.5.1.).

On the other hand, the ball-milling process has also been shown to influence GO particle size [3]. Mondal O, *et al.*, 2015 [4] demonstrated that high-energy ball-milling in an inert atmosphere converts GO to reduced graphene oxide (rGO), as the process introduces defects and contributes to its reduction. Ball-milling is a method to exfoliate graphite by applying lateral force. During the ball-milling process, two factors contribute to the exfoliation. The main contributing factor is the shear force applied by the balls. The sheer force alone can produce large flakes of graphene. The secondary factor is the collisions that occur during

milling. Strong collisions can break these large flakes and potentially change the crystal structure, resulting in a more amorphous mass [5].

Due to the prominent role of mechanosynthesis as a tool for the fabrication of nanostructures, this chapter is dedicated to the study of the elaboration of hybrid nanostructures based on TiO_2 and GO by the ball milling process. The fabrication procedures are described in detail in the second chapter of this work. A comprehensive research was conducted to examine the surface properties of GOs and the impact of functional groups on their composition. Different research methods were employed, such as XRD, Raman spectroscopy, FTIR-ATR, and BET analysis were used to determine the surface area. The morphology resulting from the combination of both structures was observed by SEM/TEM. In addition, the optical and electrical conductivity properties of the hybrid nanostructures were studied.

5.1. Microstructural analysis

The study of TiO_2 and GO hybrid nanostructures by the obtained high energy ball-milling process has been enriched by the study of the structural and morphological features. X-ray diffraction (XRD) has revealed the presence of the TiO_2 crystalline phases, while Raman spectroscopy has shed light on the interactions between TiO_2 and GO, as well as the changes in the D/G ratios after incorporation into the nanostructure. BET characterization has provided valuable information on the specific surface area and porosity of the nanostructures. Finally, direct observation at the nanometer scale by Scanning/Transmission Electron Microscopy (SEM/TEM) has allowed us to accurately visualize the resulting morphology of the nanostructures, thus validating the effectiveness of the ball milling.

5.1.1. X-ray powder diffraction

Fig. 5.1 shows the XRD patterns of pristine TiO_2 samples compared with the diffractograms of milled TiO_2 and hybrid TiO_2 -GO-based nanostructures obtained by high energy mechanical milling. Pristine TiO_2 shows reflections from the (101), (004), (200), (211), and (105) planes at $2\theta \approx 25.24^\circ$, 37.75° , 47.99° , 53.85° , and 55.03° , respectively, all corresponding to the anatase phase of TiO_2 (JCPDS 21-1272). In principle, the patterns would demonstrate the crystalline nature of pristine TiO_2 .

After the mechanical milling process, the milled TiO_2 showed significant changes in the diffraction planes compared to the pristine TiO_2 . Reflections of the anatase phase were identified at $2\theta \approx 25.90^\circ$, 37.68° , 47.94° , 53.77° , 54.94° , and 62.69° corresponding to the (101), (004), (200), (105), (211), and (204) planes (JCPDS fiche n°. 21-1272). Mechanical milling leads to a reduction of the intensity of anatase phase reflections and an increase in peak width. This is due to a decrease in the average crystallite size (D), the introduction of defects such as oxygen vacancies, increased microstrain caused by the milling process, and a transition to a more amorphous phase [6, 7]. Similarly, multiple reflections at $2\theta \approx 27.41^\circ$, 36.29° , 41.47° and 54.63° were attributed to planes (110), (012), (111) and (211) of the rutile phase (JCPDS fiche n°. 21-1276) as well as a layer (121) of the brookite phase at $2\theta \approx 31.49^\circ$ (JCPDS fiche n°. 29-

1360). The presence of multiple TiO₂ phases after the milling process would indicate the transformation of a fraction of the anatase phase into rutile and brookite. The presence of many phases is ascribed to chemical reactions occurring within the structure due to the rise in stored energy during the ball milling process, resulting in an anticipated increase in temperature and local pressure [8, 9]. Our results are in broad agreement with the diffractograms reported in the literature for mechanically milled TiO₂ [10, 11].

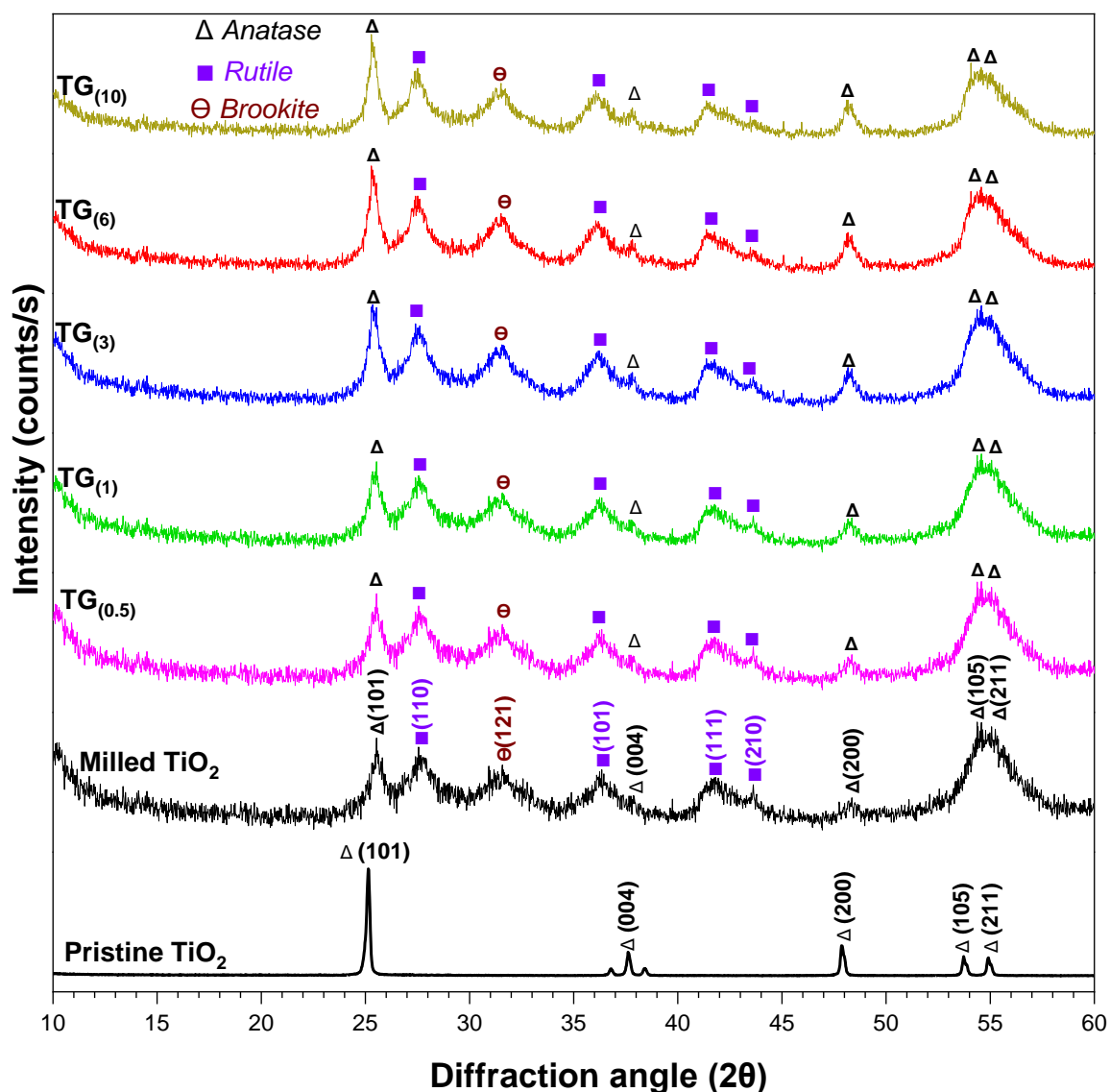


Fig. 5.1. XRD patterns of TiO₂-GO nanostructures (TG) and milled TiO₂.

In contrast, the diffractograms of the hybridized nanostructures did not show any significant changes in comparison with the diffraction planes of milled TiO₂ and did not show any characteristic GO reflection. This lack of GO-related peaks can be attributed to the fact that the limited presence of GO in the sample (2%) may not be high enough to produce distinctive signals in XRD. Therefore, other techniques such as Raman and FT-IR were used to confirm the presence of GO in the nanostructures.

5.1.2. Raman spectroscopy analysis

Fig. 5.2.a shows the Raman spectra in the range of 100 to 1000 cm^{-1} where bands related to pristine TiO_2 are observed. The analysis showed active Raman modes at 142.7, 197.4, 396.6, 520.0, and 640.8 cm^{-1} corresponding to $E_{g(1)}$, $E_{g(2)}$, $B_{1g(1)}$, $B_{1g(2)}+A_{1g}$, and $E_{g(3)}$ modes, confirming the presence of the anatase phase [12, 13]. The narrow and intense band at ≈ 142.7 cm^{-1} can be attributed to the O-Ti-O bending vibration in TiO_2 [14]. After high energy ball-milling, the main band of anatase showed a shift to a higher position (≈ 158.95 cm^{-1}), as well as a loss of intensity and increase of amplitude (FWHM), concerning pristine TiO_2 . The slight shift to a higher position is related to a change in the crystal structure and the presence of defects [15, 16]. Other authors have mentioned that the shift to higher positions indicates a reduction in crystallite size [17]. Added to the bands of the anatase phase, bands at ≈ 438 and ≈ 610 cm^{-1} corresponding to the E_g and A_{1g} vibrational modes, of the rutile phase were identified [18], as well as small bands at ≈ 323 and ≈ 366 cm^{-1} associated with the brookite phase [19, 20]. Raman spectra complement and confirm that high energy ball-milling of anatase TiO_2 creates a mixture of rutile and brookite phases. This phase transformation produced by high-energy ball-milling at room temperature has been previously reported in the literature [21, 22]. In parallel, the spectra of TiO_2 and GO hybridized nanostructures showed the same bands as milled TiO_2 .

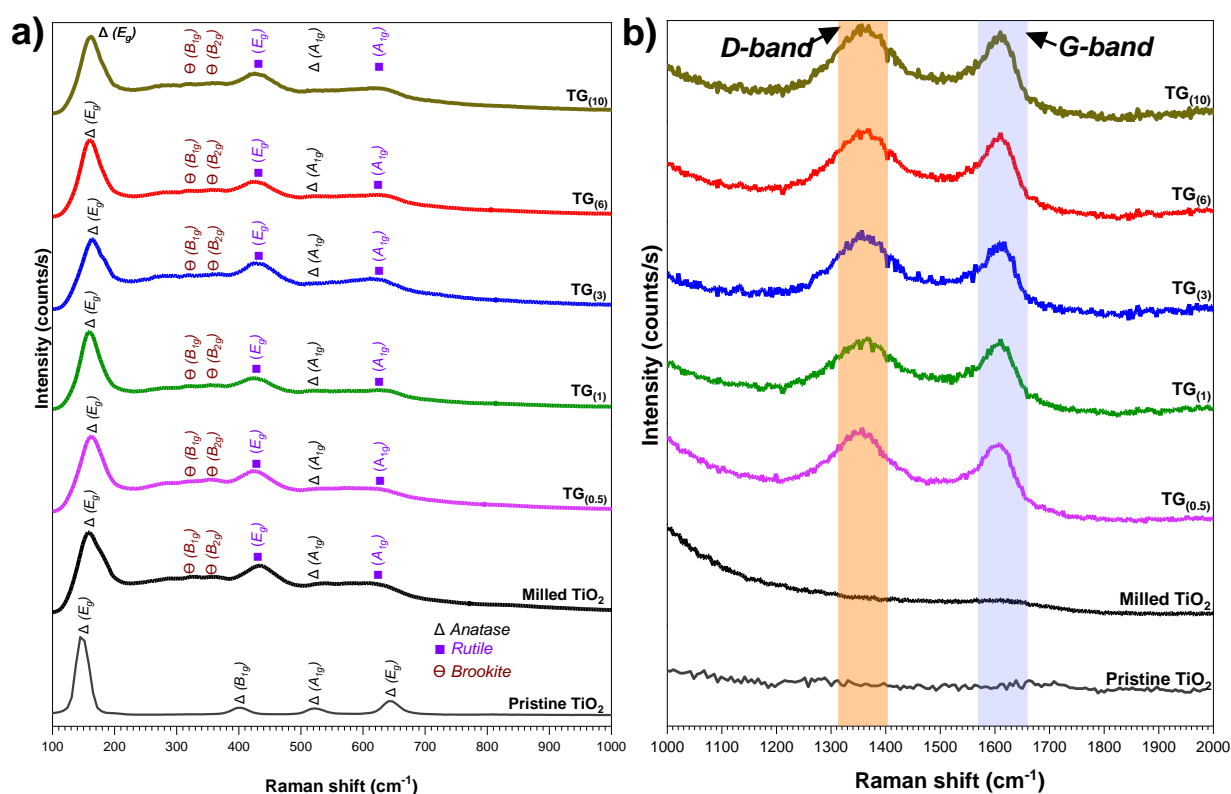


Fig. 5.2. Raman spectra of the hybrid nanostructures in the range of (a) 100-1000 cm^{-1} , and (b) range of 1000-2000 cm^{-1} .

Unlike X-ray diffraction, Raman spectroscopy is very sensitive to the vibrational modes of materials based on carbon, so it can detect even small concentrations of GO [23]. This is

demonstrated by spectra in the range 1000 to 2000 cm^{-1} (Fig. 5.2.b). The spectra showed the characteristic G and D-bands associated with GO at ≈ 1349 and ≈ 1604 cm^{-1} , respectively. The evolution and characteristics of each band as a function of the oxidation degree have been studied in detail in the Raman section of Chapter 4.

5.1.2.1. Effect of mechanical milling on graphitic domains

In an attempt to demonstrate the structural changes in the carbonaceous structure caused by the mechanical milling process, the spectra were deconvoluted using Lorentzian peaks to identify in detail the evolution of the identified bands D*, D, D'', G, and D'. The deconvoluted spectra are shown in Fig. S.5.1 and the data obtained are given in Table 5.1.

Table 5.1. Values obtained from the Lorentzian deconvolutions of the Raman spectra.

Material	Parameters	D*	D	D''	G	D'
TG _(0.5)	Position	1206.38	1371.01	1529.26	1616.40	1640.77
	FWHM	157.06	100.63	131.43	54.18	33.10
	Area	5172.97	58818.94	12606.41	16782.64	8422.68
TG ₍₁₎	Position	1206.91	1372.04	1526.35	1620.55	1644.42
	FWHM	245.57	91.64	193.55	54.20	25.67
	Area	4069.58	17452.36	6263.78	6580.21	1550.05
TG ₍₃₎	Position	1206.98	1374.53	1523.84	1615.61	1642.34
	FWHM	49.16	140.43	133.67	61.95	35.05
	Area	979.97	56108.66	11071.21	15042.65	6434.48
TG ₍₆₎	Position	1205.62	1376.23	1521.98	1612.25	1640.90
	FWHM	23.63	154.52	122.53	64.87	39.31
	Area	711.44	95317.57	15796.89	22294.92	12961.58
TG ₍₁₀₎	Position	1229.20	1370.83	1554.28	1611.20	1637.54
	FWHM	59.58	133.93	228.00	55.58	40.15
	Area	775.51	50439.97	19409.30	8383.30	9802.23

5.1.2.1.1. D- and G-band positions

The results show the shift to higher positions of the D and G-bands of GOs after their incorporation into the nanostructures with TiO₂ (Fig. 5.3.). The shift in band positions may be

due to the high number of exfoliated layers [24]. Specifically, the G-band shift is associated with the formation of new sp^3 -carbon atoms in the graphitic lattice [25]. Authors such as F. Mayoli *et al* [26] related this shift to a lower content of oxygen groups and the regeneration of the graphite structure. While the shift of the D-band is due to activation by defects [27, 28]. The analysis of the positions would qualitatively demonstrate the creation of an exfoliated structure with a high amount of defects as a result of mechanical milling.

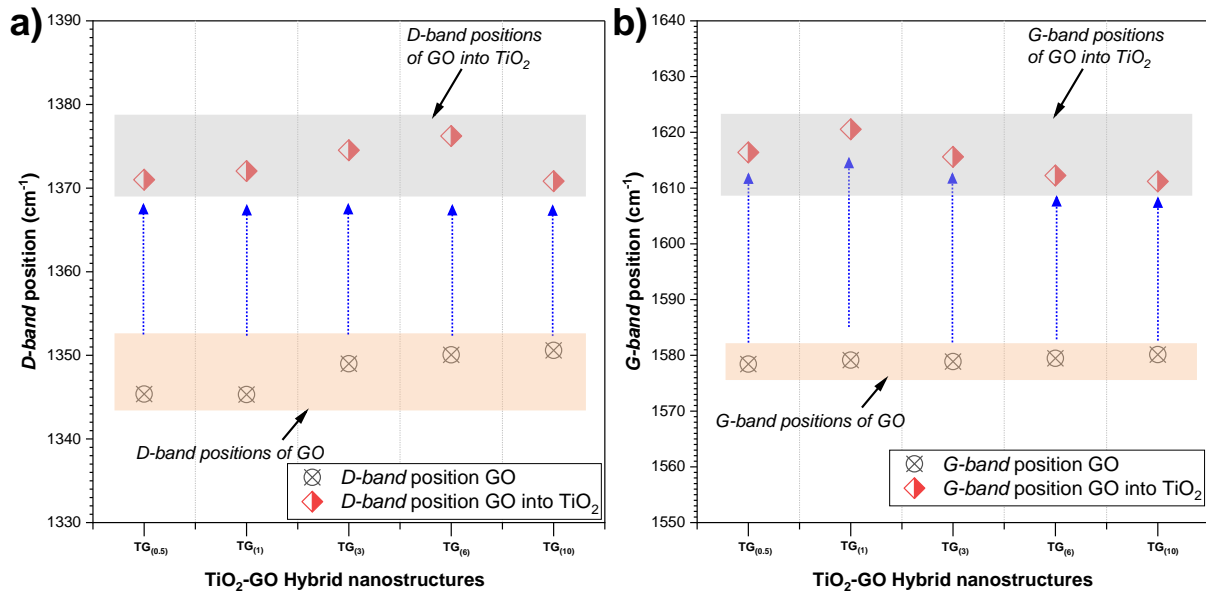


Fig. 5.3. Band positions of GO before and after incorporation into TiO₂ nanostructures. (a) D-band position (b) G-band position.

5.1.2.1.2. A_D/A_G and graphite crystallite size

To understand the structural characteristics in detail, the ratio between the D and G-bands was evaluated, since it is related to the number of defects present in the carbon materials. In all cases, an increase in the A_D/A_G ratio was observed after mechanical milling (Fig. 5.4.a.). This increase would confirm the introduction of structural defects and disorder in the lattice of GOs [29]. The crystallite size of the graphitic domain present in the hybrid nanostructures was estimated using equation (5) and the A_D/A_G ratio. Fig. 5.4.b. shows the decrease in crystallite size associated with the increase in defect density and structural disorder [30, 31]. Milling induces the formation of structural defects, such as vacancies, edges, and functional groups, as well as the creation of disorder in the carbon lattice, as translated with increasing A_D/A_G ratios [31]. It is also observed that the most significant change occurs in the nanostructure containing the lowest oxidized GO [GO_(0.5)]. In principle, mechanical milling causes additional exfoliation of the graphite layers that were not separated during GO synthesis [32]. This observation could be due to the initial state of the less oxidized GO, *i.e.* being less exfoliated, with the possibility of changes in its microstructure, which is traduced by a more noticeable effect on the crystallite size. In this context, the more oxidized GOs, which already have a more exfoliated structure, would cause the changes to be minimal despite the same milling conditions.

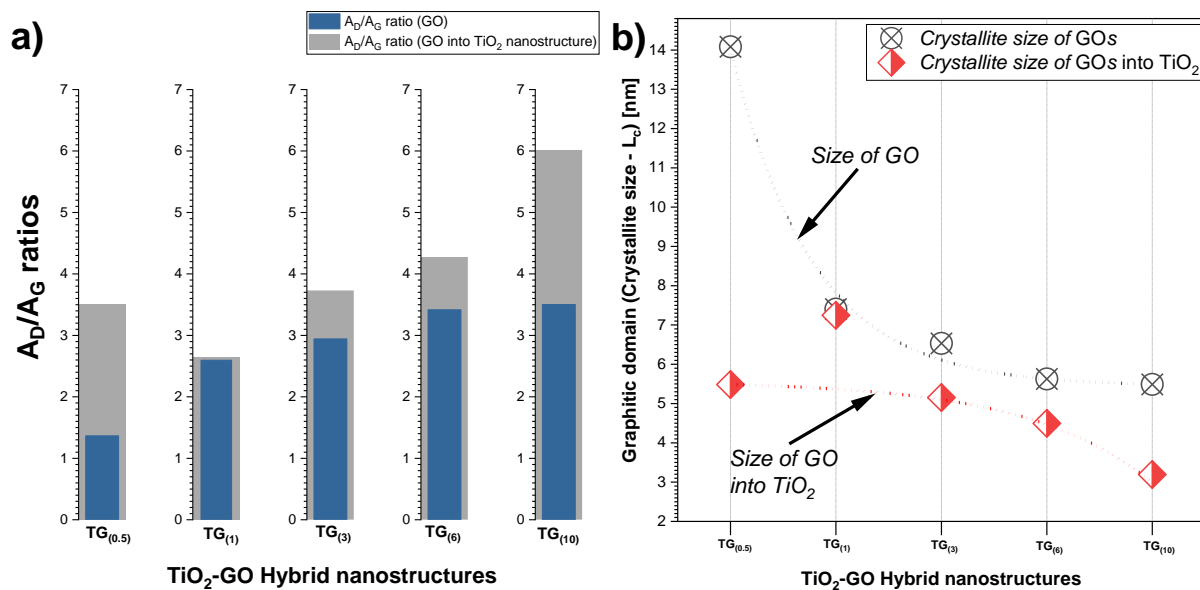


Fig. 5.4. (a) A_D/A_G ratio of GO before and after incorporation into TiO₂ nanostructures and (b) evolution of GO graphitic domain size (L_c) before and after incorporation into TiO₂ hybrid nanostructure.

By analyzing the deconvolved D'-bands, the type of structural defects in the material were identified. However, according to the model of Ferrari *et al.* [33] used to analyze the GOs in the previous chapter, since the A_D/A_G ratios are <3.5 in all cases, they would mean GOs with a high degree of disorder, making the identification imprecise. Nevertheless, when trying to identify the type of defects associated with the A_D/A_G ratios, they all show values greater than ≈0.2857, which is consistent with boundary-type defects. Such defects appear in GO as a consequence of mechanical milling, which has been associated with the generation of boundary-type defects and other structural irregularities in GO [30, 34]. The presence of this type of defect after milling could be largely related to the reduction in crystallite size shown in the hybrid structures.

5.1.3. Specific surface area (SSA)

Mechanical milling is a process that reduces particle size and increases the specific surface area of the milled material. This is due to several factors such as particle size reduction by ball collision with the material, particle fracture and deformation, cold fusion and mechanical alloying, homogenization of particle distribution, and increased porosity. These processes create new surfaces and edges resulting in increased specific surface area [35, 36]. This is demonstrated by the increase in SSA of pristine TiO₂ from 8.634 to 12.32 m²/g after milling. Nonetheless, the addition of GO to the mixture seems to have a synergistic effect as it further increases the surface area of the hybridized nanostructures. Carbon materials are known for their high specific surface area [37], as shown in the previous chapter. Thus, the combination of TiO₂ and GO may create additional interfaces, which could explain the additional increase in surface area shown in Fig. 5.5.a.

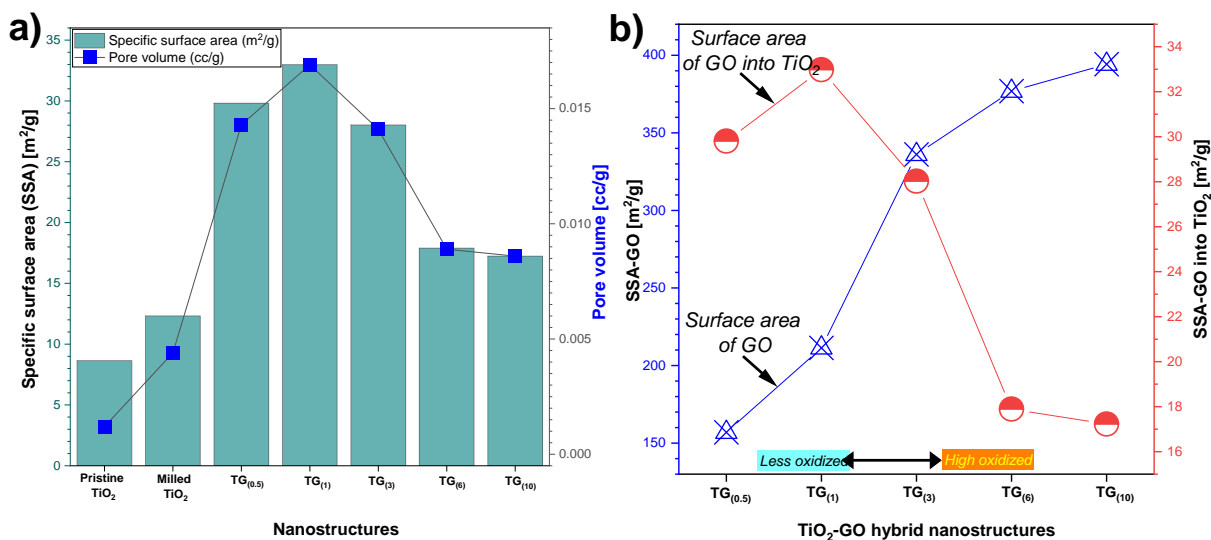


Fig. 5.5. (a) Specific surface area (SSA) and pore volume of TiO₂-GO hybrid nanostructures and (b) Specific surface area (SSA) of GO after and before incorporation into TiO₂

Before their incorporation into TiO₂, the GOs exhibited an increase in specific surface area with increasing oxidation. However, when these GOs were incorporated into the hybrid nanostructures, a trend opposite to that of the original GOs was observed. Fig. 5.5.b. shows the relationship between the specific surface areas and the oxidation degree of the GOs before and after their incorporation into TiO₂. The observed discrepancy is explained by the nature of the initial oxidation level of the GOs. In particular, highly oxidized GOs have a more negative surface charge due to the presence of negatively charged functional groups. These groups can form hydrogen bonds or van der Waals interactions between GO sheets, leading to agglomeration.

This results in less surface area available for chemical reactions highlighting the critical importance of initial oxidation on the properties and dispersion of GOs in TiO₂ nanostructures, which could have significant implications for their performance and applications. The importance of the surface area is evident in various applications, such as adsorption reactions or catalysis using nanomaterials.

5.2. FT-IR component interactions

Fig. 5.6. shows the FT-IR-ATR spectra of the hybridized nanostructures and TiO₂ before and after mechanical milling. In pristine TiO₂, two well-defined bands corresponding to Ti-O stretching vibrations were observed at ≈ 731 and ≈ 445 cm⁻¹, while the band at ≈ 574 cm⁻¹ was attributed to Ti-O-Ti bonds in the lattice [38]. In the spectrum of milled TiO₂, intensities corresponding to specific vibrational modes persist in the range of 400 to 900 cm⁻¹. However, their intensities show a reduced definition, which is consistent with the formation of an amorphous phase and the decrease in crystallinity phenomena due to the mechanical milling process, as demonstrated by X-ray diffraction and Raman spectroscopy. Conversely, the hybrid nanostructures additionally showed the presence of C-OH bonds at ≈ 1404 cm⁻¹, C-O at ≈ 1056 cm⁻¹, and a low-frequency peak at ≈ 846 cm⁻¹ attributed to the Ti-O-C bond formed between

GOs and TiO₂ [39, 40]. The presence of oxygen-containing functional groups on GOs is advantageous for the creation of nanostructures in conjunction with TiO₂ particles [41, 42].

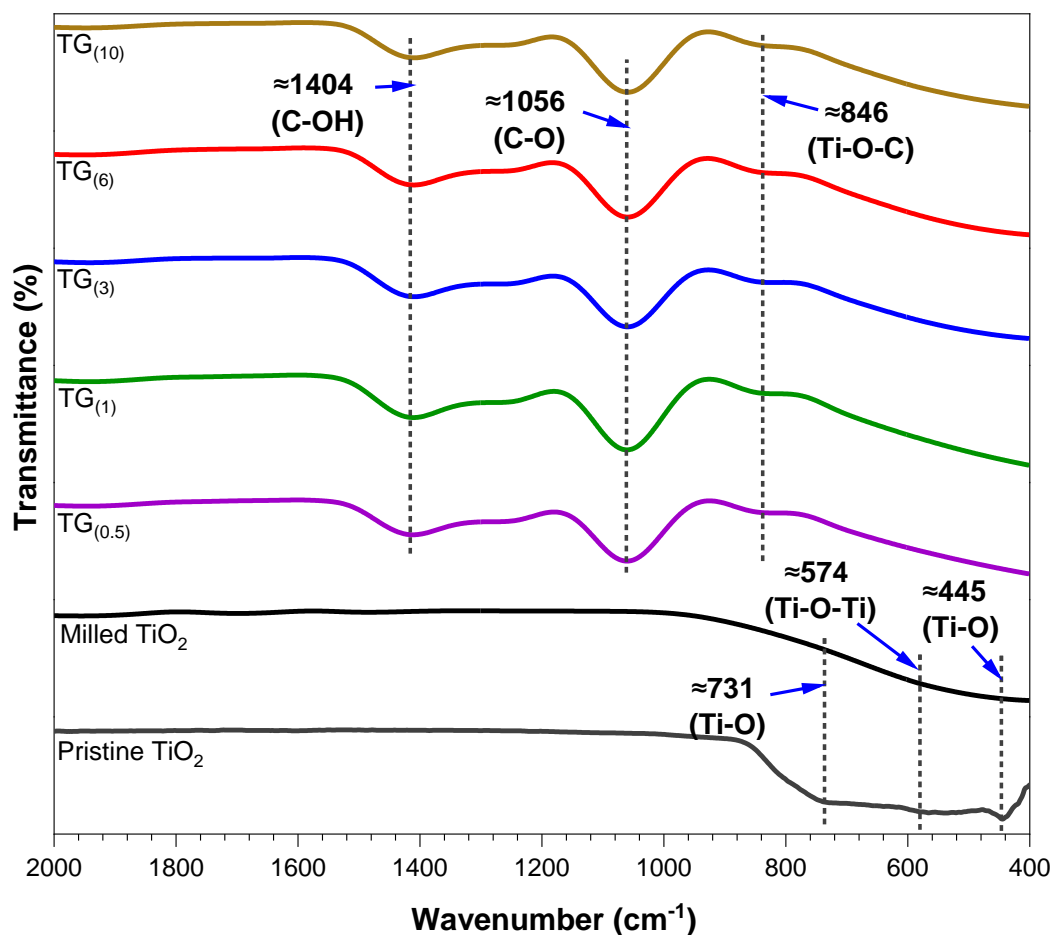


Fig. 5.6. FT-IR of hybrid nanostructures using GOs with different oxidation degrees

5.2.1. Quantification of Ti-O-C bonds

To fully elucidate the atomic interaction between the two structures, a Lorentzian deconvolution analysis of the FT-IR spectra was performed in the range of 400 to 1200 cm⁻¹ (Fig. S.5.2). The analysis revealed quite similar areas under the curve in the quantification of Ti-O-C bonds, regardless of the oxidation degrees of the incorporated GO (Fig. 5.7.). This observation suggests that the amount of oxygen in the GOs does not significantly influence the bond formation process during mechanical milling. It could be suggested that breaking bonds in the TiO₂ crystal lattice create sites with unsaturated Ti-O bonds. These free bonds are more reactive and prone to interact with other chemical species present in the environment and then participate in the formation of Ti-O-C bonds during their interaction with the graphitic material [43]. This interpretation could relate the spectra observations, and the possible origin of the oxygen involved in the Ti-O-C bonds in the hybrid nanostructures, explaining the lack of significant variation in the oxidation degrees of GO. On the other hand, although there are no significant changes, it is observed that the quantification of C-O bond contents is slightly higher in nanostructures with mostly oxidized GOs, consistent with the high concentration of epoxide

groups in highly oxidized GOs demonstrated in Chapter 4. This result could indicate that milling conditions, such as elevated temperature, could lead to the reduction of some oxygenated groups [44, 45]. This would be due to the breaking of chemical bonds and the release of gaseous molecules due to the high energy involved in the process. Hard milling conditions and increasing temperature can lead to the degradation of some functional groups, especially those that are more sensitive to extreme conditions, such as carboxyl groups, which can undergo decarboxylation at elevated temperatures [46].

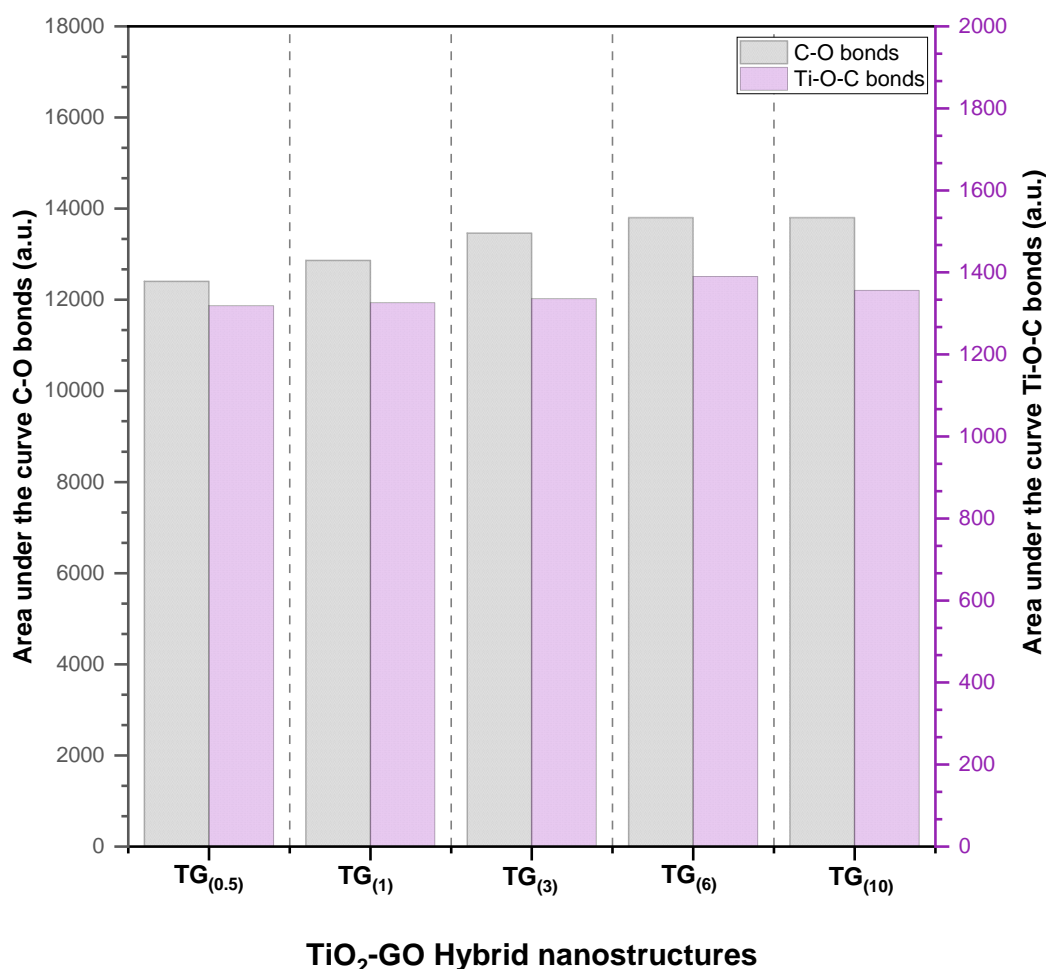


Fig. 5.7. Quantification of Ti-O-C and C-O bonds by Lorentzian deconvolution spectra of FTIR spectra.

5.3. Morphology (SEM/TEM)

Fig. 5.8. shows SEM images of pristine TiO₂ and the different TiO₂-GO hybrid nanostructures. Initially, the pristine TiO₂, particles up to ≈ 300 nm are observed with a majority distribution of ≈ 110 nm, while in the nanostructures the size decreases, presenting particle distributions mostly smaller than 100 nm (between 81 and 89 nm). Likewise, through elemental mapping of Ti, C, and O, it was observed that the elements present in the nanostructure are homogeneously distributed, as no isolated regions or clumps are observed in our material. This is an indicator of the integration and homogenization of both materials in the nanostructure.

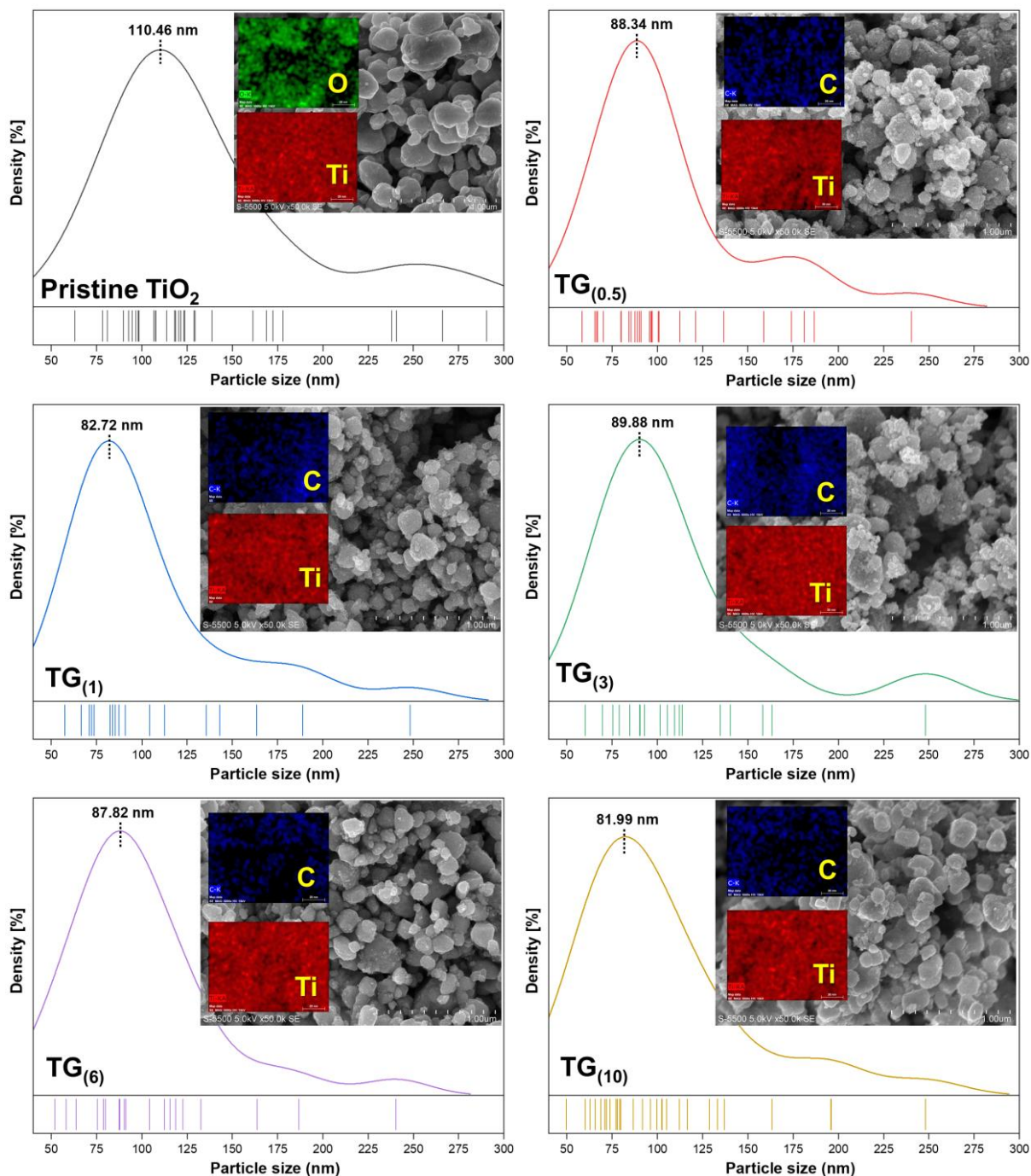
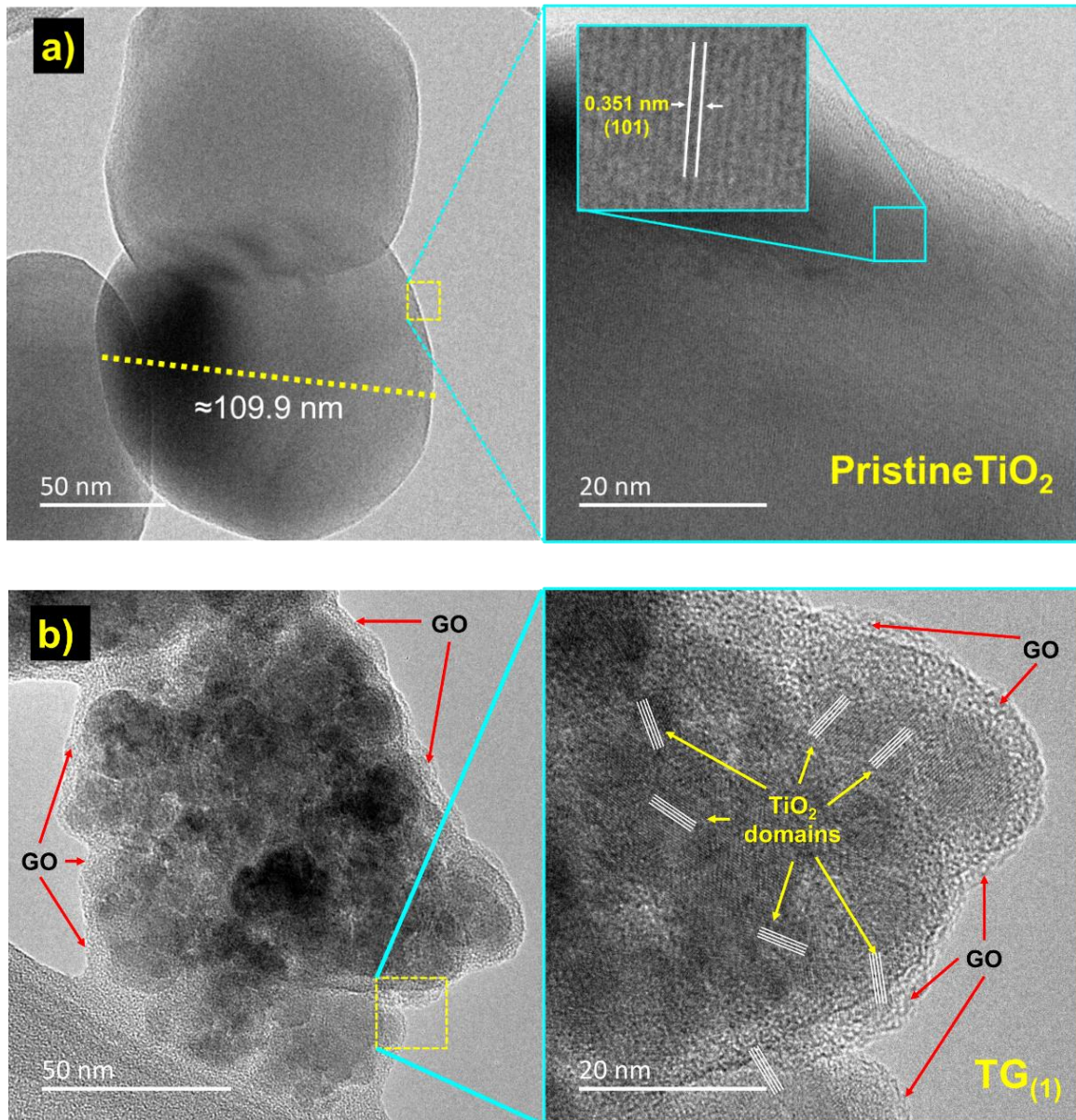


Fig. 5.8. Elemental distribution of Ti (red), C (blue), and O (green) in the pristine TiO_2 and TiO_2 -GO nanostructures and particle size distribution curves (*adapted from our publisher work on Elsevier 2023 [47]*).

On the one hand, in the TEM images of pristine TiO_2 , particles with a size of ≈ 110 nm are observed (Fig. 5.9.a-left), which confirms the information presented in the SEM distribution. Furthermore, an ordered structure with a long-range arrangement and an interplanar distance of about ≈ 0.351 nm, corresponding to the crystalline plane (101) of the anatase phase of TiO_2 , is observed (Fig. 5.9.a-right). On the other hand, Fig. 5.9.b-d shows TEM images of several TiO_2 -GO nanostructures, in which irregular and agglomerated GO-layered TiO_2 particles with

an average size between $\approx 85\text{-}90\text{ nm}$ is observed. The images showed that the morphology of the nanostructures did not show significant changes between them, regardless of the oxidation degree of the incorporated GO. The presence of the (101) TiO_2 planes is also evident; however, due to the fracturing of the particles as a result of milling, different short-range regions surrounded by a GO layer can now be observed. In summary, the TEM images confirm the formation of core-shell structures and support the formation of a hybrid $\text{TiO}_2\text{-GO}$ nanostructure rather than a separate mixture of TiO_2 and GO, thus validating the formation mechanism proposed in Fig. 5.10.



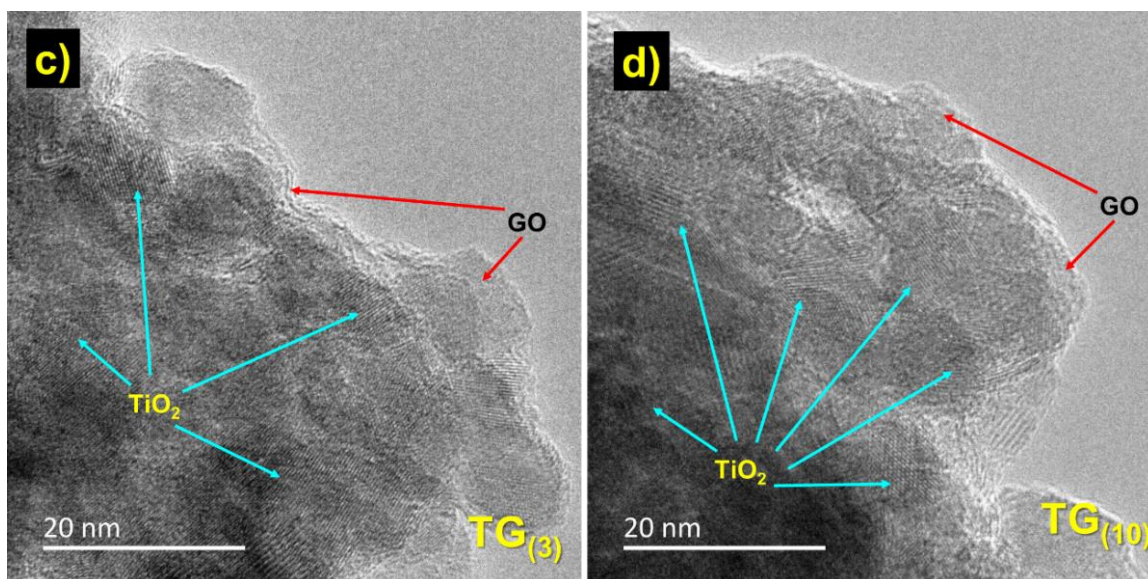


Fig. 5.9. TEM images of (a) pristine TiO_2 in comparison with (b,c, and d) the TiO_2 -GO nanostructure structure after the ball-milling process (*reprinted from our publisher work on Elsevier 2023 [47]*).

5.4. Mechanism of formation of TiO_2 -GO hybrid nanostructures

During mechanical ball-milling, various phenomena and changes occur in processed powder materials due to the interaction between the milling media and the powders and can vary depending on the materials and specific process conditions. Jia, H *et al* 2009 [48] and Saba, F *et al* 2016 [49] proposed a mechanism for the formation of Ti-C alloys by the ball-milling process. Based on this model, a schematic representation proposing the formation of hybrid nanostructures based on TiO_2 and GO is shown in Fig. 5.10. During the first few minutes of milling, TiO_2 and GO powders are mixed with the milling balls in the jar. The milling balls impact and crush the powders, resulting in an initial mixing of the two materials. This mixing is important to achieve a uniform distribution of the components (Fig. 5.10.a.). The particle size of the TiO_2 is then reduced as the ball impacts and crushes the powders (Fig 5.12.b-c). For GO, the impact and shear forces exerted by the balls cause the GO flakes to exfoliate and break into smaller fragments. During this stage, the average particle size decreases and the specific surface area increases. Subsequently, mechanical milling introduces a significant amount of mechanical energy into the system, which can lead to plastic deformation and the introduction of crystalline defects in the TiO_2 and GO particles. These defects can increase the reactivity of the materials, making them more susceptible to chemical reactions that make it easier for the two materials to combine and adhere to each other (Fig. 5.10.d.). Increased milling time can result in progressively smaller particles with surfaces containing Ti-O-C bonds. Consequently, with continuous milling, the GO powders would bond with the TiO_2 , creating a welding effect between the two materials (Fig. 5.10.e.). This combination would result in the formation of a composite structure where the GO would be dispersed in the TiO_2 (Fig. 5.10.f.). Finally, it is important to note that as the ball-milling continues, there is an increase in temperature caused by the friction generated by the milling balls, which causes phase changes in the TiO_2 . Whereas in GO this would cause the reorganization of its functional groups, affecting its chemical

properties and reactivity. However, if the time increases significantly, this could hurt GO, as the excessive local accumulation of heat could lead to structural degradation and loss of properties.

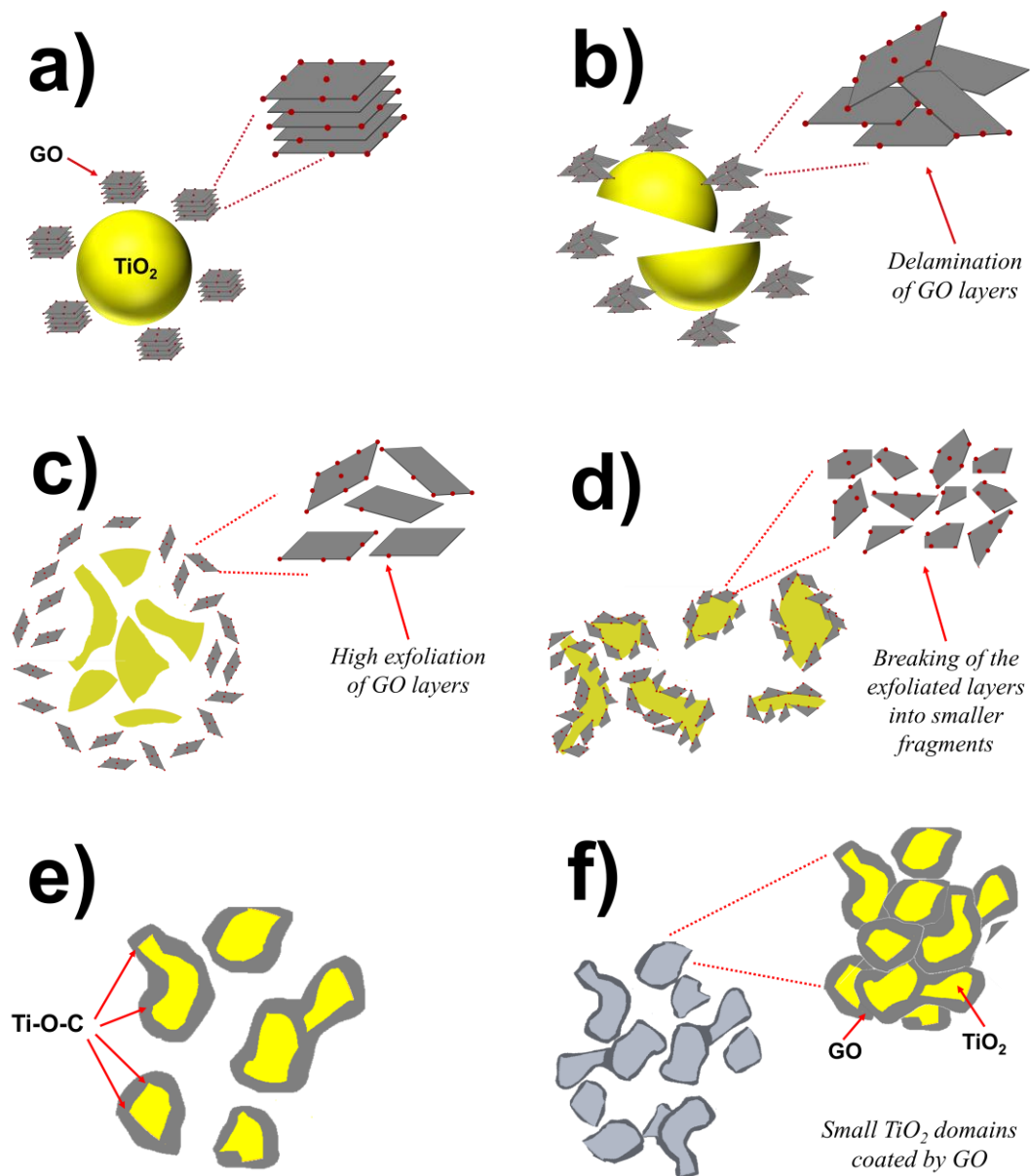


Fig. 5.10. Schematic mechanisms of formation of hybrid nanostructure by ball-milling.

5.5. Optical properties of hybrid nanostructures

5.5.1. Absorbance

Fig. 5.11. shows the UV-Vis absorption spectra of the different nanomaterials in the range 300-600 nm. The pristine TiO_2 shows an absorption spectrum with a strong absorption peak in the UV region and an absorption edge at ≈ 392 nm, similar to that reported in the literature [50]. Subsequently, after mechanical milling, TiO_2 showed a redshift of the absorption edge to ≈ 441 nm. In addition, the spectrum exhibited an increase in absorption in the visible region. This

increase in absorbance can be attributed to various factors such as particle size reduction, the creation of structural defects, and/or changes in the crystalline structure of the material. Mechanical milling led to the creation of more edges and active surfaces on the TiO₂ particles, which increased their ability to absorb light. This phenomenon corroborates the fact that the structure and properties of TiO₂ were modified due to the creation of defects and/or changes in the crystalline structure of TiO₂ during the milling process.

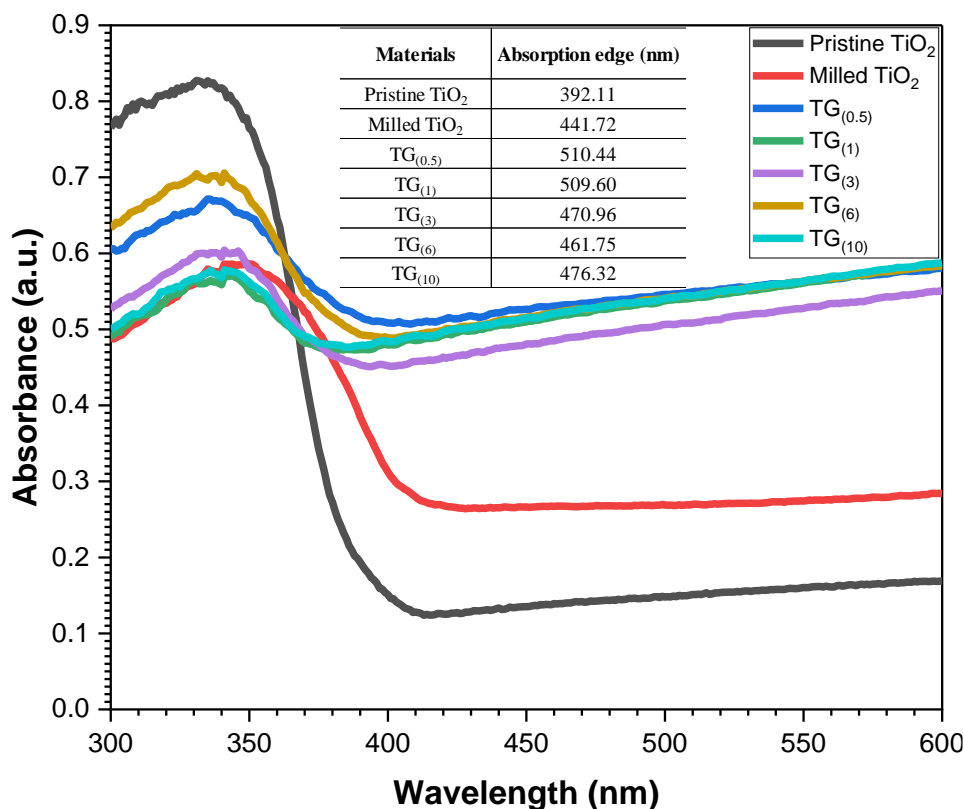


Fig. 5.11. UV-Vis absorption spectra of TiO₂ and TiO₂-GO nanostructures.

Then, after the incorporation of GOs, a further increase in absorption in the visible light region is observed, which could be due to the presence of the carbonaceous compounds [51, 52]. The increase in visible absorption observed in hybrid nanostructures indicates increased photon harvesting in this region [53], which is beneficial in advanced oxidation processes such as photocatalysis. Each spectrum showed a characteristic absorption in the UV region 200-400 nm associated with the O_{2p} → Ti_{3d} electron transition [54]. The absorption edge was further redshifted in the range of ≈461 and ≈510 nm, where the largest redshift was observed for the nanostructure with the lowest oxidized GO [TG_(0.5)].

5.5.2. Optical bandgap

The optical bandgap of the different materials was determined from the Kubelka-Munk functions vs the energy plot. As a result of the absorption edge shift in the different materials after mechanical milling, the resulting optical bandgap was reduced from ≈3.27 eV for pristine TiO₂ to ≈3.02 eV for milled TiO₂ (Fig. 5.12.a), which is in agreement with the reports of other

authors [55]. The nanostructures exhibited bandgaps in the range of ≈ 2.95 to 3.07 eV (Fig. 5.12.b.). This result suggests that mechanical milling modified the structure and properties of TiO_2 , significantly reducing its bandgap without the addition of GO. In this context, GO had no significant effect on the electronic structure of TiO_2 . It is therefore possible that the contribution of GO to the nanostructure is confined to the core-shell interface, as revealed by TEM, and does not significantly affect the optical properties of the core.

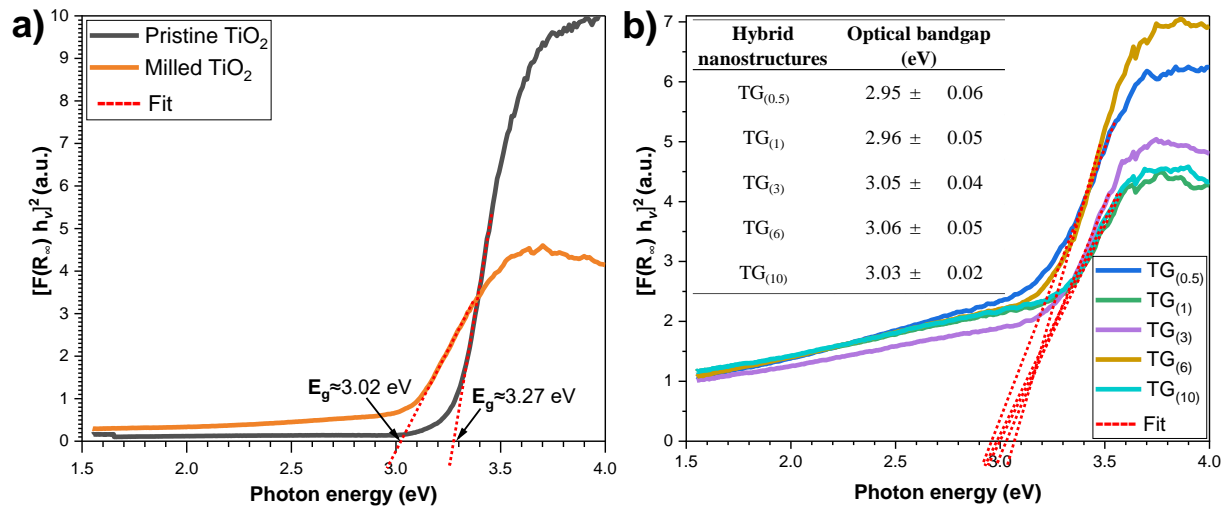


Fig. 5.12. Plots of $(\alpha h\nu)^2$ vs the energy of absorbed light of (a) TiO_2 and (b) TiO_2 -GO nanostructures.

5.6. Electrical conductivity

Fig. 5.13.a. shows the change in electrical conductivity as a function of frequency at room temperature for pristine and milled TiO_2 and hybrid nanostructures, respectively. The conductivity of all samples increased with increasing frequency. At low frequencies, charge carriers move a long distance within the material to change the direction of the electric field. In this case, the average distance crossed by the charge carriers is greater than the correlation length at frequencies below the critical frequency. At high frequencies, the electrical conductivity is realized as a hopping process of carriers between localized states, so an almost linear increase is observed in the plots [56]. Likewise, the materials showed the absence of a DC (direct current) plateau due to the interfacial polarization (Maxwell-Wagner-Sillars (MWS) polarization) caused by charge accumulation at the interface, as observed in other works [57–59]. However, the latent plateau of continuous conductivity (σ_{DC}) in systems with MWS polarization effects can be determined using the Jonscher model (eq.10) [60].

$$\sigma(\omega) = \sigma_{\text{DC}} + A\omega^n = \sigma_{\text{DC}} + \sigma_{\text{AC}} \quad (\text{eq. 10})$$

where $\sigma(\omega)$ is the total conductivity at frequency ω , σ_{DC} is the DC conductivity (direct current) σ_{AC} is the AC conductivity (alternating current) of the sample, n is the level of interaction of the mobile ions with the surrounding lattices and A is a constant whose value indicates the polarizability strength.

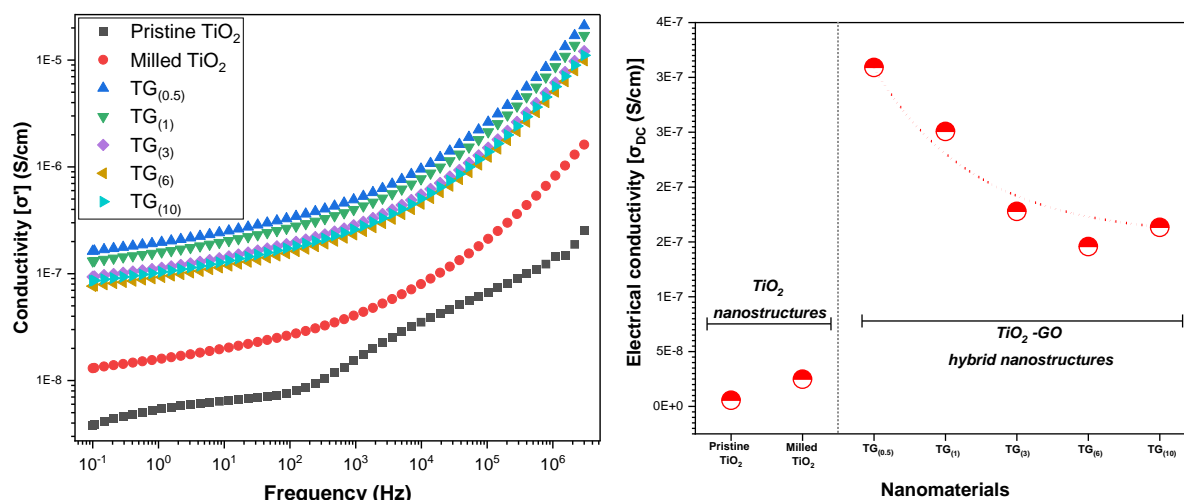


Fig. 5.13. Electrical conductivity at room temperature of TiO₂-GO nanostructures.

The calculated values show that the conductivity of pristine TiO₂ increased after the milling process, which can be attributed to the reduction in particle size and the increased number of defects in its crystal structure created by mechanical milling (Fig. 5.13.b.). These defects, such as vacancies or interstitials, facilitate electrical conduction [29]. TiO₂ is easily partially reduced, which can also contribute to its conductivity and can be further reduced with a less oxidized GO. After the incorporation of GO into the nanostructures, a slight increase in conductivity was observed. This may indicate that when GO is added to TiO₂, it can act as a 'glue' to bind the ground TiO₂ particles together, as shown by TEM (Fig. 5.10.). This creates a conductive network in the matrix, which improves dispersion and contact between the TiO₂ particles and improves conductivity by providing a pathway for electron flow. In this context, the interface between TiO₂ and GO is critical, allowing more efficient charge transfer, as evidenced by the increase in the exponent "n" in Table 5.2. Furthermore, the higher conductivity in the lower oxidation nanostructures [TG_(0.5) and TG₍₁₎] may be related to a higher specific surface area, which further facilitates charge transfer. This finding aligns with prior investigations conducted by Li X *et al* [61] and the BET calculated surface areas are shown in Fig. 5.5.

Table 5.2. The fitting parameters obtained from experimental data of the conductivity (σ_{DC}) as a function of frequency using Jonscher's power law

Materials	σ_{DC} (S/cm)	A	n	R ²
Pristine TiO ₂	5.590 x 10 ⁻⁹	6.803 x 10 ⁻¹⁰	0.386	0.984
Milled TiO ₂	2.485 x 10 ⁻⁸	9.379 x 10 ⁻¹¹	0.649	0.998
TG _(0.5)	3.090 x 10 ⁻⁷	1.059 x 10 ⁻⁹	0.662	0.999
TG ₍₁₎	2.507 x 10 ⁻⁷	8.593 x 10 ⁻¹⁰	0.661	0.999
TG ₍₃₎	1.778 x 10 ⁻⁷	6.095 x 10 ⁻¹⁰	0.662	0.998
TG ₍₆₎	1.457 x 10 ⁻⁷	4.996 x 10 ⁻¹⁰	0.663	0.999
TG ₍₁₀₎	1.632 x 10 ⁻⁷	5.595 x 10 ⁻¹⁰	0.662	0.998

5.7. Conclusion

Hybrid nanostructures based on TiO₂ and GO were successfully obtained by ball-milling.

- Microstructural analysis by XRD revealed a broadening and reduction in the intensity of the peaks corresponding to the anatase phase, as well as lower-quality diffractograms. This was attributed to the fracturing of the particles into smaller fragments, affecting the grain size distribution and crystalline orientation. The appearance of additional crystalline phases such as rutile and brookite was also observed and confirmed by Raman spectroscopy. These results suggest that the resulting hybrid nanostructures consist of a TiO₂ main matrix with a mixture of allotropic varieties with a high level of structural defects.
- Quantitative analysis by Raman spectroscopy has shown that high energy ball-milling generates a high concentration of structural defects and disorder in the GOs incorporated in the hybrid nanostructure, highlighting the predominant presence of “grain boundaries” in all cases. Furthermore, it was observed that the pronounced structural changes of the GOs concerning their oxidation degree, discussed in Chapter 4, lose a clear trend after the high energy ball-milling process, due to the aggressive nature of this method.
- The effect of high energy ball-milling was also evidenced by a significant increase in the specific surface area (SSA) of pristine TiO₂ from ≈ 8 m²/g to ≈ 12 m²/g. Subsequently, with the addition of GO, the SSA continued to increase to a maximum of ≈ 29 m²/g. However, when analyzing the behavior of different hybrid nanostructures, it was found that the SSA was higher in GOs with a lower oxidation degree compared to those with a higher oxidation, contrary to what was observed for the GOs of Chapter 4. This phenomenon was attributed to the fact that GOs with higher oxidation led to higher agglomeration. Because of there is a greater concentration of functional groups, as demonstrated by FTIR.
- SEM images confirmed the reduction of the TiO₂ particle size from ≈ 110 nm to particles with dimensions between ≈ 81 and ≈ 88 nm after the ball-milling process. On the other hand, TEM analysis revealed the formation of hybrid TiO₂-GO nanostructures, where irregular and agglomerated GO-coated TiO₂ particles were observed. FTIR analysis showed the formation of Ti-O-C bonds, which confirms the interaction and connection between the two investigated structures.
- The study of the electrical properties showed an improvement in the electrical conductivity of TiO₂ after milling from 5×10^{-9} to 2×10^{-8} S/cm. The optical bandgap was reduced from ≈ 3.27 eV to ≈ 3.02 eV. However, although the analysis of the GO hybrid nanostructures revealed a significant improvement in light absorption in the visible region, this was not reflected in the bandgap, which remained in the range of ≈ 2.95 -

3.03 eV. This behavior was also reflected in the electrical conductivity. These results suggest that although ball-milling improves the optical-electrical properties of TiO₂, the addition of GO does not cause a significant change in these properties, highlighting the need to explore other strategies to improve the properties of the hybrid material.

References

1. Kaupp, G.: Waste-free synthesis and production all across chemistry with the benefit of self-assembled crystal packings. *J Phys Org Chem.* 21, 630–643 (2008). <https://doi.org/10.1002/POC.1340>
2. Benjamin, J.S.: Mechanical alloying — A perspective. *Metal Powder Report.* 45, 122–127 (1990). [https://doi.org/10.1016/S0026-0657\(10\)80124-9](https://doi.org/10.1016/S0026-0657(10)80124-9)
3. Zhang, N., Mao, Y., Wu, S., Xu, W.: Effects of the Ball Milling Process on the Particle Size of Graphene Oxide and Its Application in Enhancing the Thermal Conductivity of Wood. *Forests* 2022, Vol. 13, Page 1325. 13, 1325 (2022). <https://doi.org/10.3390/F13081325>
4. Mondal, O., Mitra, S., Pal, M., Datta, A., Dhara, S., Chakravorty, D.: Reduced graphene oxide synthesis by high energy ball milling. *Mater Chem Phys.* 161, 123–129 (2015). <https://doi.org/10.1016/J.MATCHEMPHYS.2015.05.023>
5. Petridis, L. V., Kokkinos, N.C., Mitropoulos, A.C., Kyzas, G.Z.: Graphene aerogels for oil absorption. *Interface Science and Technology.* 30, 173–197 (2019). <https://doi.org/10.1016/B978-0-12-814178-6.00008-X>
6. Fajarin, R., Purwaningsih, H., Widyastuti, Susanti, D., Helmy, R.K.: Milling time and temperature dependence on Fe₂TiO₅ nanoparticles synthesized by mechanical alloying method. *AIP Conf Proc.* 1617, 63 (2015). <https://doi.org/10.1063/1.4897105>
7. Sánchez, L.C., Ortega, C., Espitia, M.J.: Estimation of mechanical milling characteristic parameters to explain the structural transformation of titanium dioxide. *J Phys Conf Ser.* 2046, 012055 (2021). <https://doi.org/10.1088/1742-6596/2046/1/012055>
8. Kim, B.R., Yun, K.S., Jung, H.J., Myung, S.T., Jung, S.C., Kang, W., Kim, S.J.: Electrochemical properties of the TiO₂(B) powders ball mill treated for lithium-ion battery application. *Chem Cent J.* 7, 1–5 (2013). <https://doi.org/10.1186/1752-153X-7-174>
9. Baláz, P., Achimovicová, M., Baláz, M., Billik, P., Zara, C.Z., Criado, J.M., Delogu, F., Dutková, E., Gaffet, E., Gotor, F.J., Kumar, R., Mitov, I., Rojac, T., Senna, M., Streletskii, A., Krystyna, W.C.: Hallmarks of mechanochemistry: from nanoparticles to technology. *Chem Soc Rev.* 42, 7571–7637 (2013). <https://doi.org/10.1039/C3CS35468G>
10. Tian, C.: Effects of Structural Factors of Hydrated TiO₂ on Rutile TiO₂ Pigment Preparation via Short Sulfate Process. *Scientific Reports* 2020 10:1. 10, 1–9 (2020). <https://doi.org/10.1038/s41598-020-64976-4>
11. Chalastara, K., Guo, F., Elouatik, S., Demopoulos, G.P.: Tunable Composition Aqueous-Synthesized Mixed-Phase TiO₂ Nanocrystals for Photo-Assisted Water Decontamination: Comparison of Anatase, Brookite and Rutile Photocatalysts. *Catalysts* 2020, Vol. 10, Page 407. 10, 407 (2020). <https://doi.org/10.3390/CATAL10040407>
12. Oppong, S.O.B., Opoku, F., Govender, P.P.: Remarkable Enhancement of Eu–TiO₂–GO Composite for Photodegradation of Indigo Carmine: A Design Method Based on Computational and Experimental Perspectives. *Catal Letters.* 151, (2021). <https://doi.org/10.1007/s10562-020-03386-7>
13. Orendorz, A., Brodyanski, A., Lösch, J., Bai, L.H., Chen, Z.H., Le, Y.K., Ziegler, C., Gnaser, H.: Phase transformation and particle growth in nanocrystalline anatase TiO₂ films analyzed by X-ray diffraction and Raman spectroscopy. *Surf Sci.* 601, 4390–4394 (2007). <https://doi.org/10.1016/J.SUSC.2007.04.127>
14. Chou, Y.Y., Cheng, C.L., Lin, H.Y., Chen, Y.F.: Giant enhancement of band edge emission based on ZnO/TiO₂ nanocomposites. *Optics Express*, Vol. 15, Issue 21, pp. 13832–13837. 15, 13832–13837 (2007). <https://doi.org/10.1364/OE.15.013832>
15. Thuy, N.M., Van, D.Q., Hai, L.T.H.: The visible light activity of the TiO₂ and TiO₂: V⁴⁺ photocatalyst. *Nanomaterials and Nanotechnology.* 2, (2012). <https://doi.org/10.5772/55318/ASSET/>
16. Mathpal, M.C., Tripathi, A.K., Singh, M.K., Gairola, S.P., Pandey, S.N., Agarwal, A.: Effect of annealing temperature on Raman spectra of TiO₂ nanoparticles. *Chem Phys Lett.* 555, 182–186 (2013). <https://doi.org/10.1016/J.CPLETT.2012.10.082>
17. Ekoi, E.J., Gowen, A., Dorrepaal, R., Dowling, D.P.: Characterisation of titanium oxide layers using Raman spectroscopy and optical profilometry: Influence of oxide properties. *Results Phys.* 12, 1574–1585 (2019). <https://doi.org/10.1016/J.RINP.2019.01.054>

18. Challagulla, S., Tarafder, K., Ganesan, R., Roy, S.: Structure sensitive photocatalytic reduction of nitroarenes over TiO₂. *Scientific Reports* 2017 7:1. 7, 1–11 (2017). <https://doi.org/10.1038/s41598-017-08599-2>
19. Cihlar, J., Navarro, L.K.T., Cihlar, J., Kasperek, V., Michalicka, J., Castkova, K., Lazar, I., Kastyl, J., Celko, L., Vesely, M., Dzik, P.: Influence of substituted acetic acids on “bridge” synthesis of highly photocatalytic active heterophase TiO₂ in hydrogen production. *J Solgel Sci Technol.* 105, 471–488 (2023). <https://doi.org/10.1007/S10971-022-06011-8/>
20. Ceballos-Chuc, M.C., Ramos-Castillo, C.M., Alvarado-Gil, J.J., Oskam, G., Rodríguez-Gattorno, G.: Influence of brookite impurities on the raman spectrum of TiO₂ anatase nanocrystals. *Journal of Physical Chemistry C.* 122, 19921–19930 (2018). <https://doi.org/10.1021/ACS.JPCC.8B04987>
21. Ellouzi, I., Oualid, H.A.: 3, 3; † Presented at the 1st International Online Conference on Nanomaterials. *Proc West Mark Ed Assoc Conf.* 1–15 (2019). https://doi.org/10.3390/IOCN_2018-1-05497
22. Rezaee, M., Mousavi Khoie, S.M., Liu, K.H.: The role of brookite in mechanical activation of anatase-to-rutile transformation of nanocrystalline TiO₂: An XRD and Raman spectroscopy investigation. *CrystEngComm.* 13, 5055–5061 (2011). <https://doi.org/10.1039/C1CE05185G>
23. Kanta, U.A., Thongpool, V., Sangkhun, W., Wongyao, N., Woothikanokkhan, J.: Preparations, characterizations, and a comparative study on photovoltaic performance of two different types of graphene/TiO₂ nanocomposites photoelectrodes. *J Nanomater.* 2017, (2017). <https://doi.org/10.1155/2017/2758294>
24. Sukumaran, S.S., Rekha, C.R., Resmi, A.N., Jinesh, K.B., Gopchandran, K.G.: Raman and scanning tunneling spectroscopic investigations on graphene-silver nanocomposites. *Journal of Science: Advanced Materials and Devices.* 3, 353–358 (2018). <https://doi.org/10.1016/J.JSAMD.2018.06.003>
25. Krishnamoorthy, K., Veerapandian, M., Yun, K., Kim, S.J.: The chemical and structural analysis of graphene oxide with different degrees of oxidation. *Carbon N Y.* 53, 38–49 (2013). <https://doi.org/10.1016/J.CARBON.2012.10.013>
26. Casallas Caicedo, F.M., Vera López, E., Agarwal, A., Drozd, V., Durygin, A., Franco Hernandez, A., Wang, C.: Synthesis of graphene oxide from graphite by ball milling. *Diam Relat Mater.* 109, 108064 (2020). <https://doi.org/10.1016/J.DIAMOND.2020.108064>
27. Pócsik, I., Hundhausen, M., Koós, M., Ley, L.: Origin of the D peak in the Raman spectrum of microcrystalline graphite. *J Non Cryst Solids.* 227–230, 1083–1086 (1998). [https://doi.org/10.1016/S0022-3093\(98\)00349-4](https://doi.org/10.1016/S0022-3093(98)00349-4)
28. Childres, I., Jauregui, L.A., Park, W., Cao, H., Chen, Y.P.: RAMAN SPECTROSCOPY OF GRAPHENE AND RELATED MATERIALS.
29. Calderón-Ayala, G., Cortez-Valadez, M., Mani-Gonzalez, P.G., Hurtado, R.B., Contreras-Rascón, J.I., Carrillo-Torres, R.C., Zayas, M.E., Castillo, S.J., Hernández-Martínez, A.R., Flores-Acosta, M.: Green synthesis of reduced graphene oxide using ball milling. *Carbon letters.* 21, 93–97 (2017). <https://doi.org/10.5714/CL.2017.21.093>
30. Zhang, N., Mao, Y., Wu, S., Xu, W.: Effects of the Ball Milling Process on the Particle Size of Graphene Oxide and Its Application in Enhancing the Thermal Conductivity of Wood. *Forests* 2022, Vol. 13, Page 1325. 13, 1325 (2022). <https://doi.org/10.3390/F13081325>
31. Mohanta, Z., Atreya, H.S., Srivastava, C.: Correlation between defect density in mechanically milled graphite and total oxygen content of graphene oxide produced from oxidizing the milled graphite. *Scientific Reports* 2018 8:1. 8, 1–6 (2018). <https://doi.org/10.1038/s41598-018-34109-z>
32. Calderón-Ayala, G., Cortez-Valadez, M., Mani-Gonzalez, P.G., Britto Hurtado, R., Contreras-Rascón, J.I., Carrillo-Torres, R.C., Zayas, M.E., Castillo, S.J., Hernández-Martínez, A.R., Flores-Acosta, M.: Green synthesis of reduced graphene oxide using ball milling. *Carbon Letters.* 21, 93–97 (2017). <https://doi.org/10.5714/CL.2017.21.093>
33. Ferrari, A., Robertson, J.: Interpretation of Raman spectra of disordered and amorphous carbon. *Phys Rev B.* 61, 14095 (2000). <https://doi.org/10.1103/PhysRevB.61.14095>
34. Xiu, Z., Ju, B., Duan, C., Fu, S., Zhang, N., Mei, Y., Liu, J., Feng, Y., Yang, W., Kang, P.: Study on the Evolution of Graphene Defects and the Mechanical and Thermal Properties of GNPs/Cu during CVD Repair Process. *Materials.* 15, (2022). <https://doi.org/10.3390/MA15010130>
35. Li, R., Zeng, S., Shen, K., Wang, G., Zhang, J.: Effects of mechanical grinding on the physicochemical properties of silica aerogels. *Front Mater.* 10, 1225481 (2023). <https://doi.org/10.3389/FMATS.2023.1225481/BIBTEX>
36. Stamboliadis, E., Pantelaki, O., Petrakis, E.: Surface area production during grinding. *Miner Eng.* 22, 587–592 (2009). <https://doi.org/10.1016/J.MINENG.2008.12.001>
37. Volfkovich, Y.M., Sosenkin, V.E., Rychagov, A.Y., Melezhik, A. V., Tkachev, A.G., Kabachkov, E.N., Korepanov, V.I., Khodos, I.I., Michtchenko, A., Shulga, Y.M.: Carbon material with high specific surface

- area and high pseudocapacitance: Possible application in supercapacitors. *Microporous and Mesoporous Materials*. 319, 111063 (2021). <https://doi.org/10.1016/J.MICROMESO.2021.111063>
38. Al-Oubidy, E.A., Kadhim, F.J.: Photocatalytic activity of anatase titanium dioxide nanostructures prepared by reactive magnetron sputtering technique. *Opt Quantum Electron*. 51, 1–11 (2019). <https://doi.org/10.1007/S11082-018-1738-Z>
 39. Janekbary, K.K., Gilani, N., Pirbazari, A.E.: One-step fabrication of Ag/RGO doped TiO₂ nanotubes during anodization process with high photocatalytic performance. *Journal of Porous Materials*. 27, 1809–1822 (2020). <https://doi.org/10.1007/s10934-020-00954-5>
 40. Hu, G., Yang, J., Zhao, D., Chen, Y., Cao, Y.: Research on Photocatalytic Properties of TiO₂-Graphene Composites with Different Morphologies. *J Mater Eng Perform*. 26, 3263–3270 (2017). <https://doi.org/10.1007/S11665-017-2776-6>
 41. Wang, S., Li, Y., Zhang, H., Lin, Y., Li, Z., Wang, W., Wu, Q., Qian, Y., Hong, H., Zhi, C.: Enhancement of thermal conductivity in water-based nanofluids employing TiO₂/reduced graphene oxide composites. *J Mater Sci*. 51, 10104–10115 (2016). <https://doi.org/10.1007/s10853-016-0239-3>
 42. Kim, H. il, Moon, G.H., Monllor-Satoca, D., Park, Y., Choi, W.: Solar photoconversion using graphene/TiO₂ composites: Nanographene shell on TiO₂ core versus TiO₂ nanoparticles on graphene sheet. *Journal of Physical Chemistry C*. 116, 1535–1543 (2012). <https://doi.org/10.1021/jp209035e>
 43. Kighuta, K., Kim, S.W., Hou, Y.L., Lee, K.P., Kim, W.J.: Facile and Simple Post Treatment Ball Milling Strategy for the Production of Low-Cost TiO₂ Composites with Enhanced Photocatalytic Performance and Applicability to Construction Materials. *Materials*. 16, 4931 (2023). <https://doi.org/10.3390/MA16144931/S1>
 44. Sengupta, I., Chakraborty, S., Talukdar, M., Pal, S.K., Chakraborty, S.: Thermal reduction of graphene oxide: How temperature influences purity. *J Mater Res*. 33, 4113–4122 (2018). <https://doi.org/10.1557/JMR.2018.338>
 45. Minitha, C.R., Anithaa, V.S., Subramaniam, V., Rajendra Kumar, R.T.: Impact of Oxygen Functional Groups on Reduced Graphene Oxide-Based Sensors for Ammonia and Toluene Detection at Room Temperature. *ACS Omega*. 3, 4105–4112 (2018). <https://doi.org/10.1021/ACSOMEGA.7B02085>
 46. Jeon, I.Y., Shin, Y.R., Sohn, G.J., Choi, H.J., Bae, S.Y., Mahmood, J., Jung, S.M., Seo, J.M., Kim, M.J., Chang, D.W., Dai, L., Baek, J.B.: Edge-carboxylated graphene nanosheets via ball milling. *Proc Natl Acad Sci U S A*. 109, 5588–5593 (2012). <https://doi.org/10.1073/PNAS.1116897109>
 47. Cano, F.J., Reyes-Vallejo, O., Ashok, A., Olvera, M.D.L.L., Velumani, S., Kassiba, A.: Mechanisms of dyes adsorption on titanium oxide– graphene oxide nanocomposites. *Ceram Int*. 49, (2023). <https://doi.org/10.1016/j.ceramint.2023.03.249>
 48. Jia, H., Zhang, Z., Qi, Z., Liu, G., Bian, X.: Formation of nanocrystalline TiC from titanium and different carbon sources by mechanical alloying. *J Alloys Compd*. 472, 97–103 (2009). <https://doi.org/10.1016/J.JALLCOM.2008.04.070>
 49. Saba, F., Kabiri, E., Khaki, J.V., Sabzevar, M.H.: Fabrication of nanocrystalline TiC coating on AISI D2 steel substrate via high-energy mechanical alloying of Ti and C. *Powder Technol*. 288, 76–86 (2016). <https://doi.org/10.1016/J.POWTEC.2015.10.030>
 50. Cao, S., Zhao, C., Han, T., Peng, L.: Oxalic acid assisted hydrothermal synthesis and optical absorption property of WO₃/TiO₂ nanocomposites. *Journal of Materials Science: Materials in Electronics*. 27, 5635–5639 (2016). <https://doi.org/10.1007/S10854-016-4471-Z>
 51. Zhang, L.W., Fu, H.B., Zhu, Y.F.: Efficient TiO₂ Photocatalysts from Surface Hybridization of TiO₂ Particles with Graphite-like Carbon. *Adv Funct Mater*. 18, 2180–2189 (2008). <https://doi.org/10.1002/ADFM.200701478>
 52. Zhang, X.Y., Li, H.P., Cui, X.L., Lin, Y.: Graphene/TiO₂ nanocomposites: synthesis, characterization and application in hydrogen evolution from water photocatalytic splitting. *J Mater Chem*. 20, 2801–2806 (2010). <https://doi.org/10.1039/B917240H>
 53. Athithya, S., Manikandan, V.S., Harish, S.K., Silambarasan, K., Gopalakrishnan, S., Ikeda, H., Navaneethan, M., Archana, J.: Plasmon Effect of Ag Nanoparticles on TiO₂/rGO Nanostructures for Enhanced Energy Harvesting and Environmental Remediation. *Nanomaterials*. 13, 65 (2023). <https://doi.org/10.3390/NANO13010065/S1>
 54. Linsebigler, A.L., Lu, G., Yates, J.T.: Photocatalysis on TiO₂ Surfaces: Principles, Mechanisms, and Selected Results. *Chem. Rev*. 95, 735–758 (1995)
 55. Ye, M., Pan, J., Guo, Z., Liu, X., Chen, Y.: Effect of ball milling process on the photocatalytic performance of CdS/TiO₂ composite. *Nanotechnol Rev*. 9, 558–567 (2020). <https://doi.org/10.1515/NTREV-2020-0045/MACHINEREADABLECITATION/RIS>
 56. Sinha, S., Chatterjee, S.K., Ghosh, J., Meikap, A.K.: Analysis of the Dielectric Relaxation and AC Conductivity Behavior of Polyvinyl Alcohol-Cadmium Selenide Nanocomposite Films. <https://doi.org/10.1002/pc.23586>

57. Walker, E., Akishige, Y., Cai, T., Roberts, J., Shepherd, N., Wu, S., Wang, Z., Neogi, A.: Maxwell-Wagner-Sillars Dynamics and Enhanced Radio-Frequency Elastomechanical Susceptibility in PNIPAm Hydrogel-KF-doped Barium Titanate Nanoparticle Composites. *Nanoscale Res Lett.* 14, 1–12 (2019). <https://doi.org/10.1186/S11671-019-3171-Z>
58. Füllbrandt, M., Von Klitzing, R., Schönhals, A.: The dielectric signature of poly(N-isopropylacrylamide) microgels at the volume phase transition: dependence on the crosslinking density. *Soft Matter.* 9, 4464–4471 (2013). <https://doi.org/10.1039/C3SM27762C>
59. Poplavko, Y.: Broadband dielectric spectroscopy. In: *Dielectric Spectroscopy of Electronic Materials* (2021)
60. Jonscher, A.K.: The ‘universal’ dielectric response. *Nature* 1977 267:5613. 267, 673–679 (1977). <https://doi.org/10.1038/267673a0>
61. Li, X., Jiang, L., Zhou, C., Liu, J., Zeng, H.: Integrating large specific surface area and high conductivity in hydrogenated NiCo₂O₄ double-shell hollow spheres to improve supercapacitors. *NPG Asia Materials* 2015 7:3. 7, e165–e165 (2015). <https://doi.org/10.1038/am.2015.11>

Chapter VI:

Photosonication: Engineering of hybrid nanostructures based on TiO₂ & GO

Sonochemistry is the study of the chemical reactions that occur when molecules are exposed to high-frequency ultrasound (between 20 kHz and 10 MHz) [1]. Sonochemistry is used to enhance chemical reactions such as synthesis and catalysis. This technique results in the formation of large-area nanostructures with limited agglomeration. When intense ultrasonic waves are coupled into liquids, very short-lived bubbles are created that grow and break immediately due to the phenomenon of acoustic cavitation. Ultrasonic cavitation enhances mass transfer between reactants, accelerates the reaction, and/or allows the chemical pathway to be altered [2]. During the formation and collapse of the formed bubbles, a high-stress region is created in the vicinity of the bubbles, which raises the local temperature and creates a high-pressure region of about 20 Mpa [3]. Sonochemical synthesis has gained interest in green chemistry because it is cost-effective and can reduce the use of additional reagents during synthesis. The use of sonochemical approaches offers several advantages, such as faster reaction times, larger surface area, uniform size distribution, and higher phase purity in nanomaterials synthesized using these strategies [2].

The application of ultrasound to TiO₂ is effective in reducing its particle size, producing greater sphericity and homogeneity compared to conventional methods [4]. In addition, the use of ultrasound can cause atomic rearrangements and the formation of defects in TiO₂, facilitating the activation of its surface [5]. This phenomenon is induced by cavitation bubbles, during the ultrasonication process, creating defects on the surface of nanoparticles [6]. For example, in a recent study on the ultrasonic treatment of TiO₂ by Bae *et al.* in 2022 [5], it was shown that the cavitation bubbles generated during this process led to the formation of Ti³⁺ defects on the surface of TiO₂ particles. In the case of GO, sonication plays a significant role in several properties. The sonication time during GO preparation affects the sheet dimension, point defects, surface morphology, oxidation degree, and interlayer spacing [7]. According to Mellado C. *et al.* 2019 [8], when direct sonication is applied to GO samples, interlayer deformation is generated, which increases the roughness and defects of the sheets. In a study by Ye S. *et al.* 2016 [9], the effect of sonication on the mechanical characteristics of GO was studied and it was found that soft and short sonication achieves complete delamination of GO flakes while maintaining a large lamella size. However, increasing the sonication time significantly reduced the size, resulting in a deterioration of the mechanical properties. Turner

P. *et al.* 2019 [10] pointed out that sonication is a method for in situ control of graphene flake size. Inertial cavitation drives exfoliation and provides a way to improve exfoliation rates. Other studies suggest that sonication plays a critical role in the reduction of GO to form reduced graphene oxide (rGO) [11]. Ručigaj A. *et al.* 2022 [12] demonstrated that ultrasonic cavitation not only leads to GO exfoliation but also causes cleavage of in-plane C-C covalent bonds, resulting in GO reduction. On the other hand, previous research has demonstrated the effectiveness of sonication in the formation of hybrid structures [13]. A study by Lee J. *et al.* in 2016 highlighted the achievement of SiO₂/TiO₂ core-shell structures, which were used in the degradation of methyl orange [14]. Similarly, Ghows N. *et al.* in 2012 [15] achieved CdS/TiO₂-based core-shell hybrid nanostructures by using sonication. These results highlight the potential of sonication in the synthesis of complex hybrid nanostructures.

Thus, the present chapter focuses on the analysis of hybrid nanostructures based on TiO₂ and GO prepared by photosonation. The discussion points out the influence of the oxidation degree of the incorporated GO on the structural, morphological, and chemical characteristics of the resulting hybrid nanostructures. The details of the fabrication have been described in detail in Chapter 2. The efficacy of the photosonation process for the formation of Ti³⁺ surface defects as paramagnetic species was demonstrated. The adsorption of GO induced the formation of Ti-O-C chemical bonds, limiting the concentration of Ti³⁺ surface defects. In addition, optical and electrical properties were evaluated to provide a complete picture of the potential applications of the fabricated nanostructures TiO₂-GO.

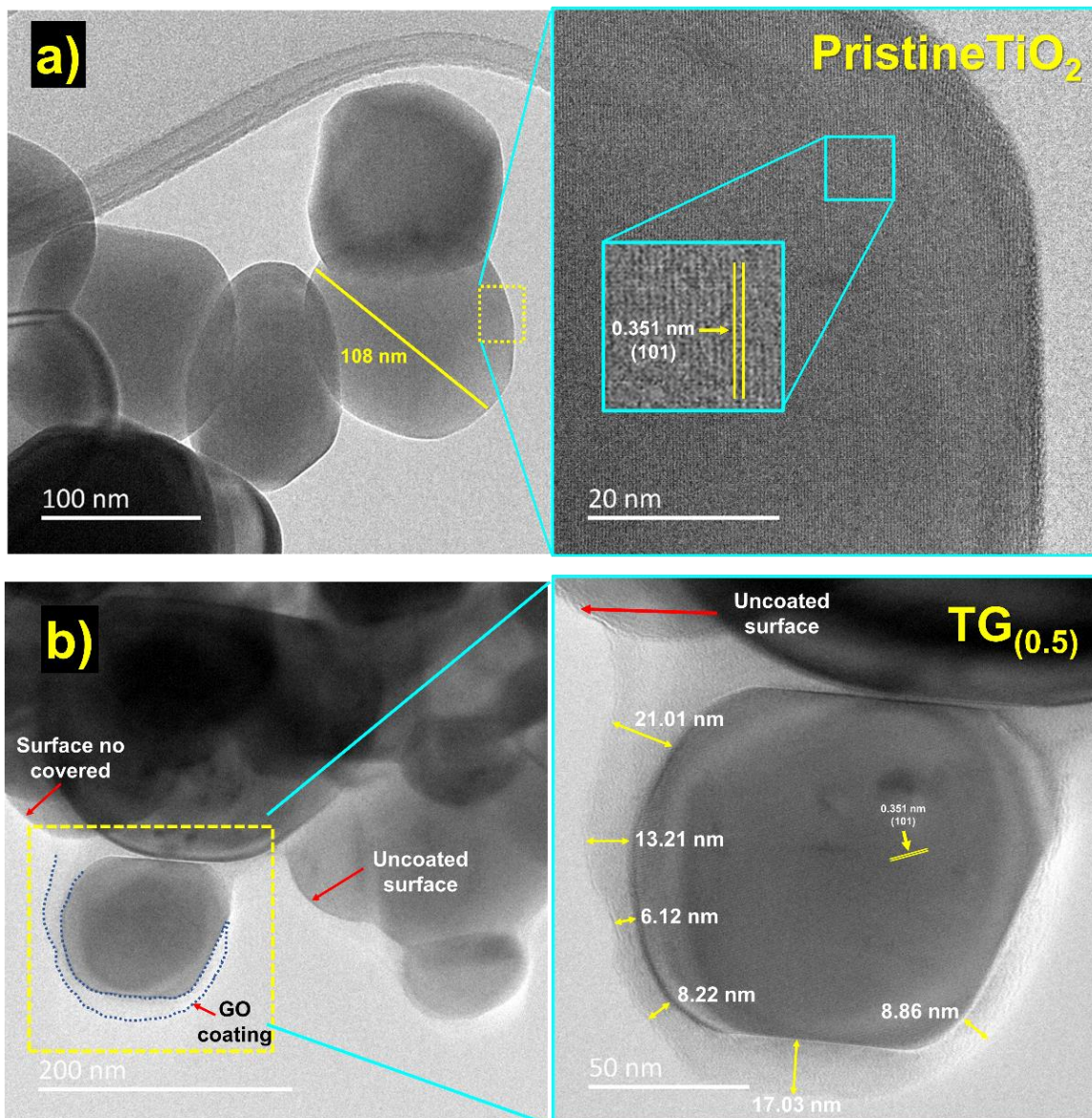
6.1. Structural and morphological analysis

The study of hybrid nanostructures based on TiO₂-GO by the photosonation process has been enriched by a detailed analysis of the structural and morphological properties of the resulting materials. The application of advanced techniques, such as SEM/TEM, has allowed direct observation at the nanometer scale, providing accurate visualization of the resulting morphology of the nanostructures. The use of X-ray diffraction allows the identification of the crystalline phases of TiO₂, while Raman spectroscopy sheds light on the characteristics of the graphite domain in the GOs after their incorporation into the nanostructures, as inferred from the changes in the D/G ratios. In addition, electron paramagnetic resonance (EPR) experiments were carried out to identify the active electronic defects present at the interfaces and to study their characteristics concerning GO oxidation and the effect of sonication of the TiO₂-GO nanostructures. The FTIR-ATR technique was used to elucidate the nature of the interface between the two structures, providing a deeper understanding of the interactions at the molecular level. This comprehensive set of analytical techniques has allowed a thorough investigation of the TiO₂-GO hybrid nanostructures, providing a solid basis for understanding their fundamental properties and emphasizing a suitable formation mechanism.

6.1.1. Morphology TiO₂-GO by TEM

Fig. 6.1.a. shows pristine TiO₂ particles, with an average size of ≈ 108 nm, while the hybrid nanostructures are mainly composed of TiO₂ particles coated with GO, forming a core-shell

type structure. These observations demonstrate the formation of a TiO₂-GO hybrid structure rather than a separate mixture of TiO₂ and GO. Fig. 6.1.b. presents the nanostructure with the lowest oxidation of GO [TG_(0.5)]. It is shown that TiO₂ particles are surrounded by an irregular GO shell with thicknesses between approximately 6 and 21 nm, as well as other uncoated areas. On the other hand, nanostructures with a higher oxidation degree as [TG₍₁₀₎], present a more homogeneous shell on the whole particle, albeit with less thickness (Fig. 6.1.c.). TEM images of the core-shell structures with intermediate oxidation degrees are shown in Fig. S.6.1. For TG₍₁₎, although it shows a coated particle, the outermost layer presents different thicknesses ranging between ≈10 and ≈3 nm while TG₍₃₎ and TG₍₆₎ show an improved homogeneity with average thicknesses of ≈5 and ≈4 nm, respectively. This organization is influenced by the morphology of the GO as a consequence of its oxidation degree described in Fig. 4.10. of Chapter 4. That is, the GO with lower oxidation presents larger carbon platelets, as well as greater stacking, compared to the GO with higher oxidation where there is a greater degree of flaking and wrinkling.



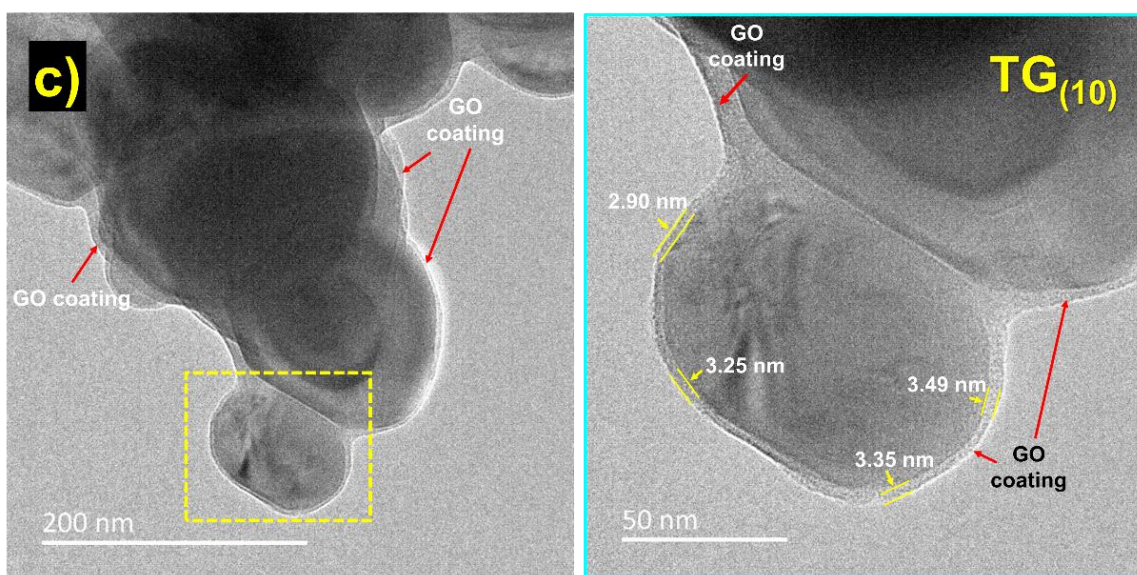


Fig. 6.1. TEM images of TiO₂-GO nanostructures by photosonification method (a) Pristine TiO₂ (b) TG_(0.5) nanostructure with lower oxidation (c) TG₍₁₀₎ nanostructure with higher oxidation (reprinted from our publisher work on Elsevier 2024 [16]).

6.1.2. X-ray diffraction analysis

Fig. 6.2. shows an overlay of the XRD patterns of pristine TiO₂ compared to those of the TiO₂-GO nanostructures. Pristine TiO₂ shows diffraction peaks from the planes (101), (004), (200), (211), and (105) at $2\theta \approx 25.24^\circ$, 37.75° , 47.99° , 53.85° , and 55.03° , respectively, all corresponding to the anatase phase of TiO₂ (JCPDS 21-1272). The XRD patterns of the nanostructures show a crystalline nature of TiO₂, and no peaks related to GO were observed, presumably due to their low concentration (2%) of GO compared to TiO₂.

The magnification of the TiO₂ XRD peak (101) in Fig. 6.2. shows a decrease in its intensity in the nanostructures compared to pristine TiO₂. This behavior reveals the reduction of the crystalline phase in TiO₂-GO nanostructures, which is attributed to two phenomena caused by the sonication process in a liquid medium. First, (i) the deagglomeration and delamination of the particles lead to smaller grains [17]. The reduction in particle size directly impacts the strength of the peaks. As the particle size drops, fewer lattice planes contribute to the diffraction pattern, resulting in a decrease in the intensity of the XRD peaks [18]. Second, (ii) the cavitation bubbles created in the solution when subjected to ultrasound facilitate the desorption and release of species that are typically adsorbed on the surface of the particles. This process leads to the reduction of surface titanium ions through the formation of Ti³⁺ [19–21] as discussed below in the EPR results section. Both phenomena (i) and (ii) actively contribute to the observed decrease in the peak intensity of TiO₂ in sonicated nanostructures.

Upon incorporation of GO under sonification, the Ti³⁺ ions generated on the surface of the particles were neutralized by forming bonds with the oxygen atoms in the surrounding GO. Thus, oxygen in GOs can act as an oxidizing agent and accept electrons to form bonds with reduced species, such as Ti³⁺ ions on the surface of sonicated TiO₂ particles. This may lead to

partial recovery of crystallinity in the region near the interface between TiO_2 and GOs, increasing the intensity of XRD peaks. Thus, the highest oxidized nanostructure $\text{TG}_{(10)}$ exhibits a higher intensity compared to the less oxidized $\text{TG}_{(0.5)}$. This behavior may also explain the modest displacement of the peak towards lower 2-theta angles. When Ti^{3+} is formed on the surface of TiO_2 particles, it generates a distortion in the arrangement of atoms in the crystalline planes near the surface [22, 23]. This distortion can lead to an increase in the spacing between the crystalline planes, resulting in a shift of the diffraction peak towards smaller angles. However, by incorporating GO, the partial recovery effect due to oxygenated groups will again shift the peak position to higher angles, and for this reason, the nanostructure with the most oxidized GO [$\text{TG}_{(10)}$] shows an XRD line position similar to pristine TiO_2 .

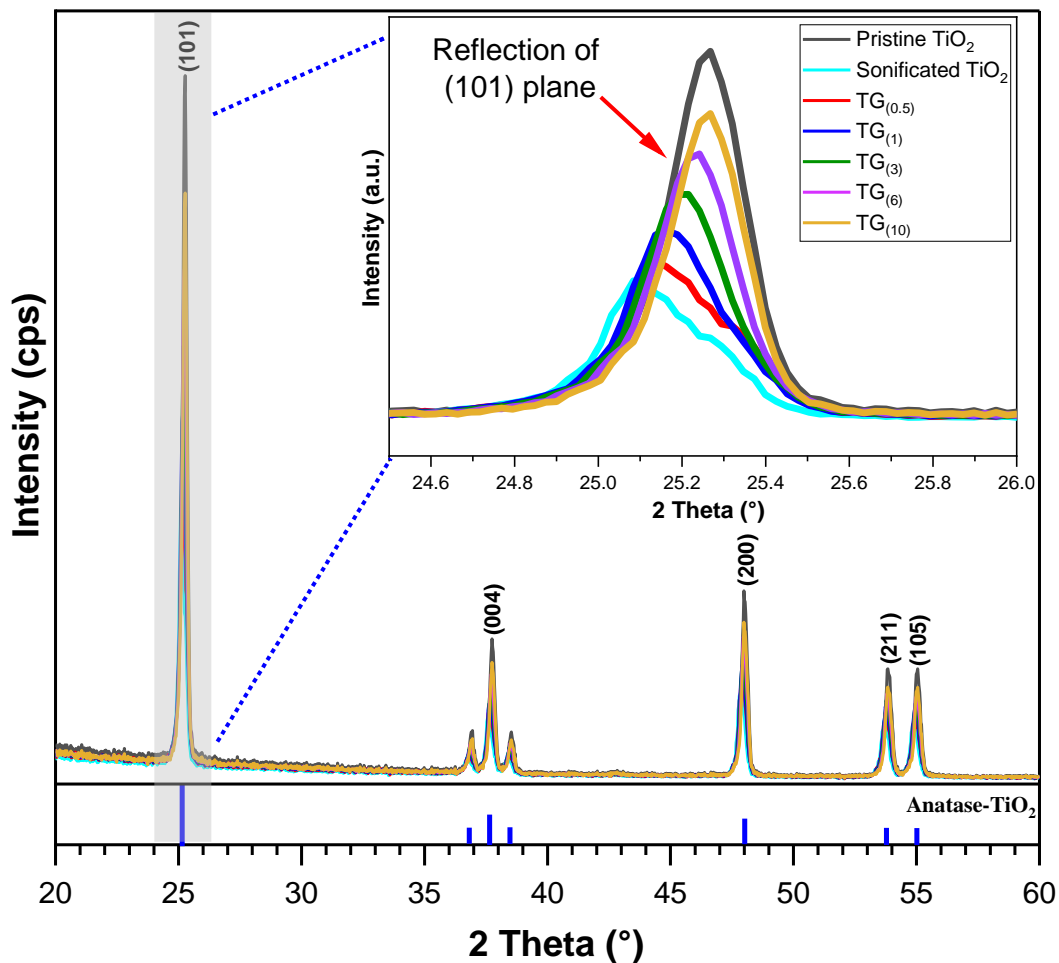


Fig. 6.2. XRD of pristine TiO_2 and TiO_2 -GO hybrid nanostructures by photosonication (reprinted from our published work on Elsevier 2024 [16]).

The Debye-Scherrer relation (Eq. 1) was used to evaluate the crystallite size (D) from the diffraction patterns. The average crystallite size calculated for the pristine TiO_2 was approximately 35 nm. In the $\text{TG}_{(10)}$ nanostructure, the D value is similar to pristine TiO_2 but decreases monotonically down to 27 nm for the $\text{TG}_{(0.5)}$ (Table 6.1.). The deformation (ϵ) and the dislocation density (δ) were calculated using eq. 3 and 4. The calculated ϵ and δ values show a similar evolution as a function of the GO oxidation degree (Table 6.1.). Moreover,

surface states play an important role in nanomaterials, particularly, when surface reactions are involved in phenomena such as adsorption or heterogeneous catalysis. The dislocation density (δ) and the average strain (ϵ) reduce the occurrence of surface defects resulting from the mechanical stress induced by the sound waves applied during the sonication process. The gradual increase of these parameters with the lowering of the GO oxidation degree demonstrated strong interactions at the nanostructure interfaces.

Table 6.1. Calculated values from the XRD pattern

Materials	Average crystallite size D (nm)	Dislocation density δ (nm⁻²)	Average Strain (ϵ)
Pristine TiO ₂	35.65	0.00079	0.00264
Sonicated TiO ₂	26.89	0.00138	0.00339
TG _(0.5)	27.21	0.00135	0.00336
TG ₍₁₎	30.10	0.00110	0.00305
TG ₍₃₎	32.25	0.00096	0.00287
TG ₍₆₎	33.90	0.00087	0.00270
TG ₍₁₀₎	35.58	0.00079	0.00260

In summary, the information in Table 6.1. shows a remarkable trend of TG₍₁₀₎ values converging to the behavior of pristine TiO₂. As mentioned above, the main reason can be due to the interaction of the oxygen in the GO with the Ti³⁺ defects created on the surface of the sonicated particles. Consequently, this interaction would partially contribute to restore the crystalline structure with a dislocation density (δ) comparable to that of pristine TiO₂. Similarly, such interaction would compensate for the deformations induced by Ti³⁺ defects. The interaction with the oxygen present in the GO would also attenuate the local deformations, resulting in an average deformation value similar to that of pristine TiO₂. These effects are more prominent at greater oxidation levels due to the increased oxygen concentration.

6.1.3. Raman spectroscopy analysis

The Raman spectra of the photosonicated hybridized nanostructures in the range of 100 to 800 cm⁻¹ are shown in Fig. 6.3. The identified Raman modes are consistent with the anatase phase (Fig. 5.2.-Chapter 5). The narrow and intense band at ≈ 142 cm⁻¹ is attributed to the Ti-O-C in nanostructures based on TiO₂ and GO [24], so the non-stoichiometry at the surface due to reduced Ti³⁺ ions strongly influence the intensity and signal width of the E_{g(1)} band.

The magnification of Fig. 6.3. shows an increase in E_{g(1)} signal intensity with increasing oxidation degree, together with a slight shift to a higher wavenumber position (Fig. 6.4.a.). The observed changes are attributed to the interactions between the adsorbed GO on the TiO₂ surfaces after the photosonation process, which modify the features of the interface. TiO₂

particles coated with GO fragments may create surface regions of higher or lower stress, which can alter the interaction of the interfaces. As shown in the TEM images for $TG_{(0.5)}$, an irregular GO shell occurs on TiO_2 surfaces, and this arrangement hardly changed the Raman fingerprint of TiO_2 . This behavior contrasts with the sample $TG_{(10)}$ where a more ordered GO shell is homogeneously realized as a thin layer on TiO_2 . In this case, the realization of layers with easy charge transport in the nanostructure can be expected. Therefore, the increase in Raman intensity of TiO_2 -GO nanoparticles could be related to the plasmonic effect originating from a large electronic density present within the shell layer. When GO interacts with light, it causes electronic oscillations that produce a locally amplified electric field. As a consequence, the detection of surface species is improved by intense Raman signals from the surface of TiO_2 core-shell nanoparticles [25, 26].

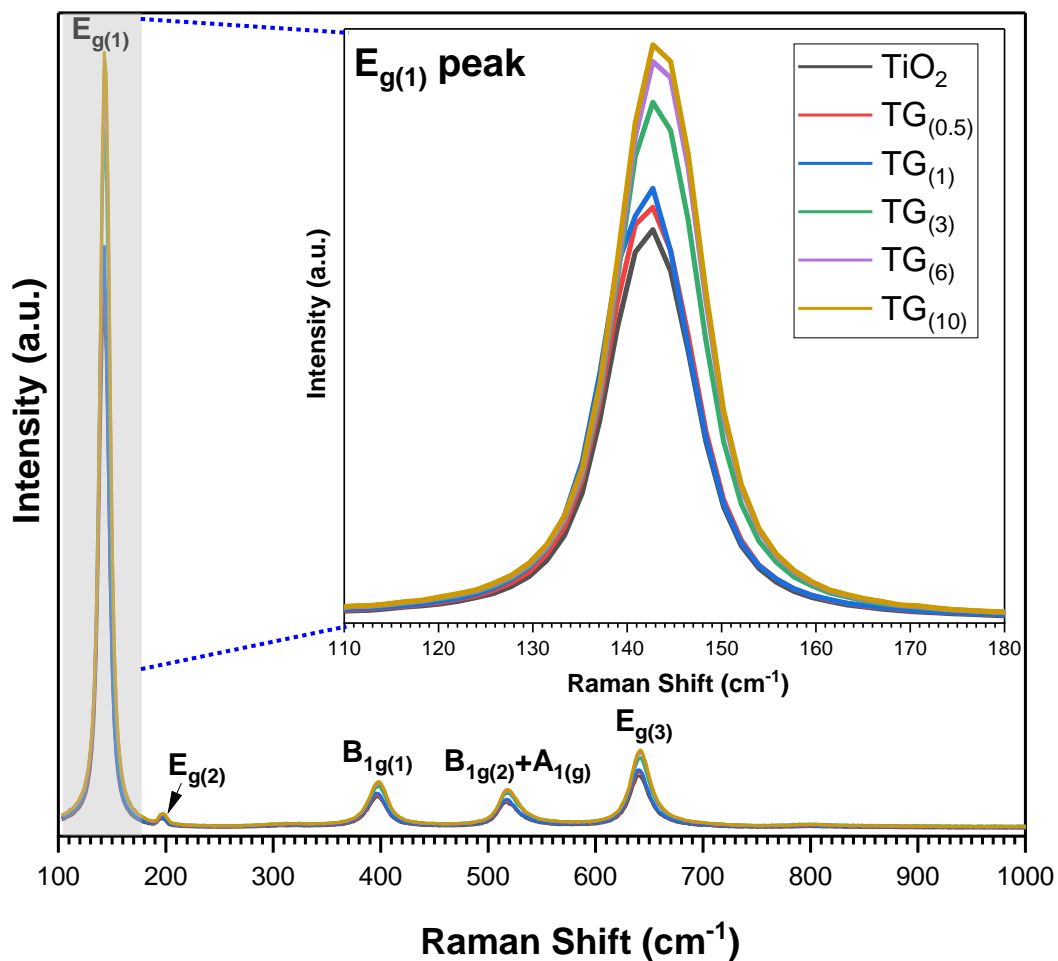


Fig. 6.3. Raman spectra of TiO_2 anatase and TiO_2 -GO nanostructures by photosonication (reprinted from our publisher work on Elsevier 2024 [16]).

Fig. 6.4.b. shows the decrease of FWHM with increasing crystallite size as determined by XRD. This phenomenon is attributed to the presence of a greater number of atoms with unsaturated coordination on the surface of smaller crystallites. This can result in a wider range of Ti-O bond lengths and increased disorder within the material.

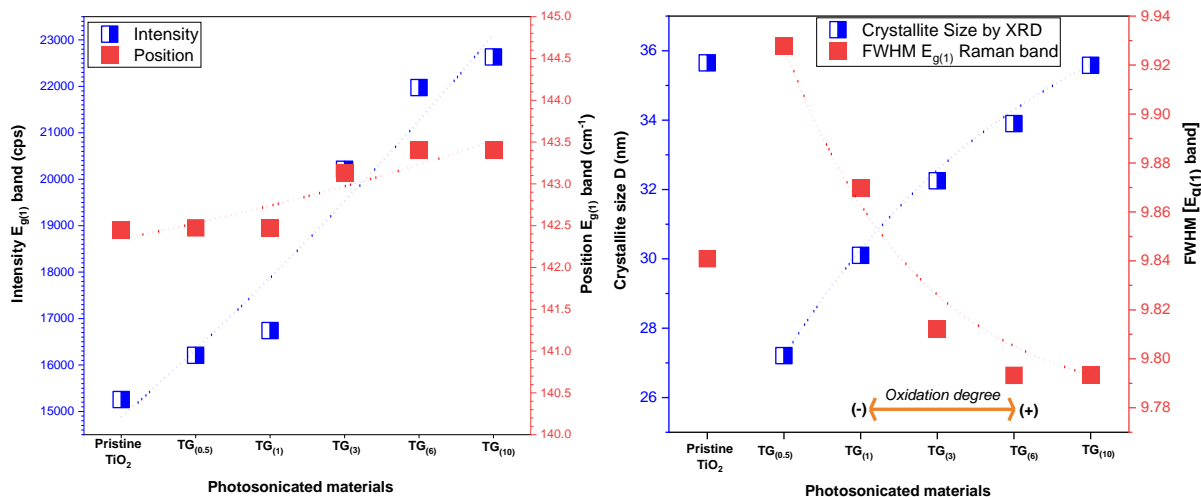


Fig. 6.4. Evolution of (a) intensity and $E_{g(1g)}$ position band and (b) changes in the amplitude [FWHM] of the $E_{g(1g)}$ band and the crystallite size.

Fig. 6.5 shows the Raman spectra of TiO₂-GO hybrid nanostructures in the range of 1000 to 2000 cm⁻¹. The presence of the D and G-bands are observed. The evolution of GO before and after its incorporation into TiO₂ nanostructures is discussed below.

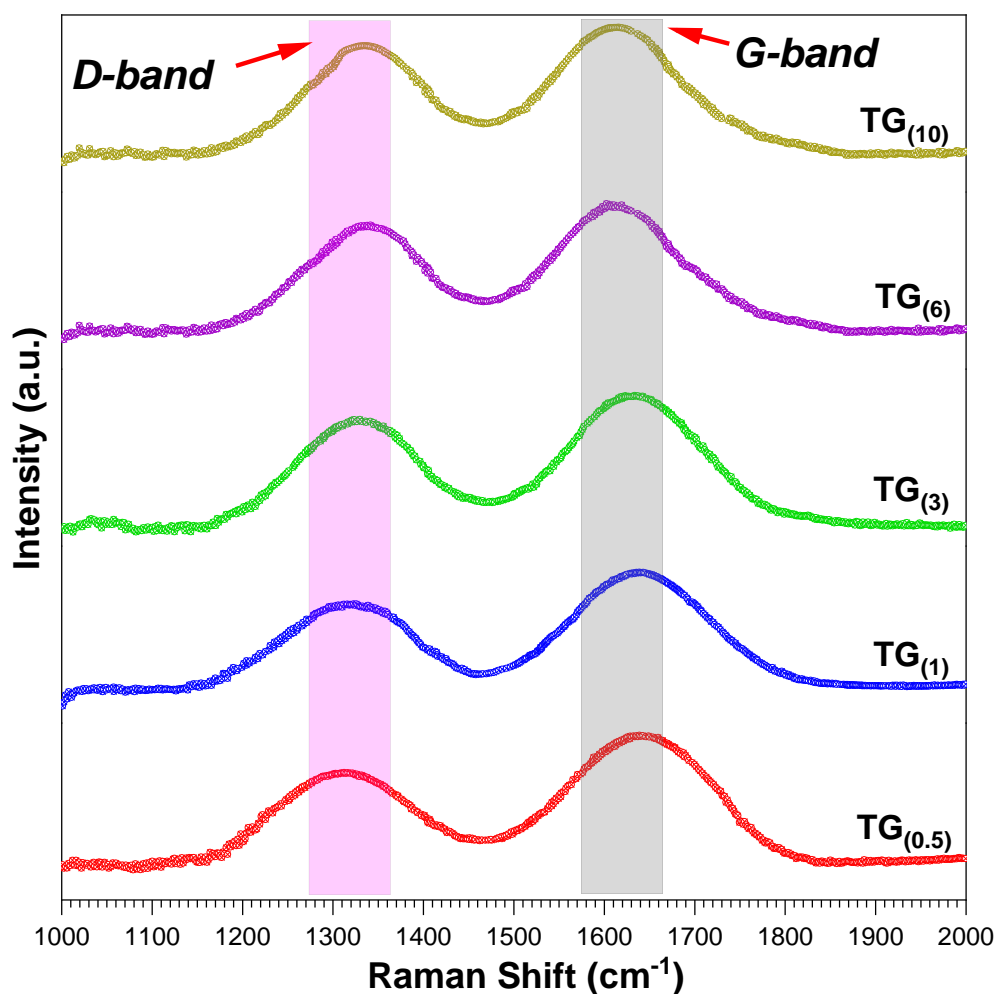


Fig. 6.5. Raman spectra of TiO₂-GO hybrid nanostructures (range 1000-2000 cm⁻¹)

6.1.3.1. Evolution of GO after incorporation into hybrid nanostructures

The spectra were deconvolved using the Lorentzian line shape to properly analyze the features of the D and G-bands of the GOs incorporated into the nanostructures. To evaluate the structural changes in the carbonaceous structure before and after its incorporation into the TiO₂ hybridized nanostructures, the spectra were deconvoluted using Lorentzian peaks to identify in detail the evolution of the identified bands D*, D, D'', G, and D'. The deconvolved spectra are shown in Fig. S.6.2. and the data obtained are given in Table 6.2.

Table 6.2. Values obtained from the Lorentzian deconvolutions of the Raman spectra.

Material	Parameters	D*	D	D''	G	D'
TG _(0.5)	Position	1182.16	1310.48	1582.49	1644.34	1705.98
	FWHM	20.39	129224.18	39383.65	91232.29	34218.68
	Area	6.38	158.60	95.48	114.55	86.21
TG ₍₁₎	Position	1182.63	1315.35	1589.15	1646.04	1700.77
	FWHM	21.55	140258.81	41110.04	92485.63	40996.71
	Area	5.82	153.59	89.57	119.22	125.44
TG ₍₃₎	Position	1182.71	1326.13	1584.42	1639.63	1697.97
	FWHM	20.00	238666.68	70546.17	153371.32	73043.35
	Area	6.00	143.41	82.93	113.91	121.96
TG ₍₆₎	Position	1182.77	1334.40	1568.83	1622.97	1682.39
	FWHM	28.15	291472.89	79104.20	168178.37	98611.15
	Area	6.69	142.29	81.43	104.25	153.35
TG ₍₁₀₎	Position	1182.08	1333.91	1570.65	1626.70	1676.04
	FWHM	21.25	285743.27	81915.79	163443.79	96310.37
	Area	2.45	138.75	84.20	106.45	168.42

6.1.3.1.1. D- and G-band positions

The results showed a shift towards lower positions of the D-band in the GOs after photosonication and incorporation into TiO₂ (Fig. 6.6.a.). This phenomenon indicates a decrease in structural defects and an improvement in the crystallinity of the material. A lower D-band position indicates a reduction in such defects, resulting in a more ordered structure. This shift is often observed during the reduction of GO to reduced graphene oxide (rGO), indicating an improvement in the quality of the material [27, 28].

In contrast, the shift of the G-band to a higher position, (Fig. 6.6.b.) indicates a reduction of oxygen-containing functional groups and an increase in the size of the sp^2 carbon domain of the material. This shift is commonly referred to as a "red shift" in Raman spectra. As discussed in Chapter 4, the G-band in the Raman spectrum of GO is associated with the sp^2 carbon domains, and a higher position indicates a decrease in oxygen-related functional groups and an increase in the average size of the sp^2 carbon domains, reflecting the restoration of the graphitic structure. Other researchers have shown that sonication is an effective method for GO reduction and graphitic structure restoration, resulting in the observed red shift in the G-band of Raman spectra [29, 30].

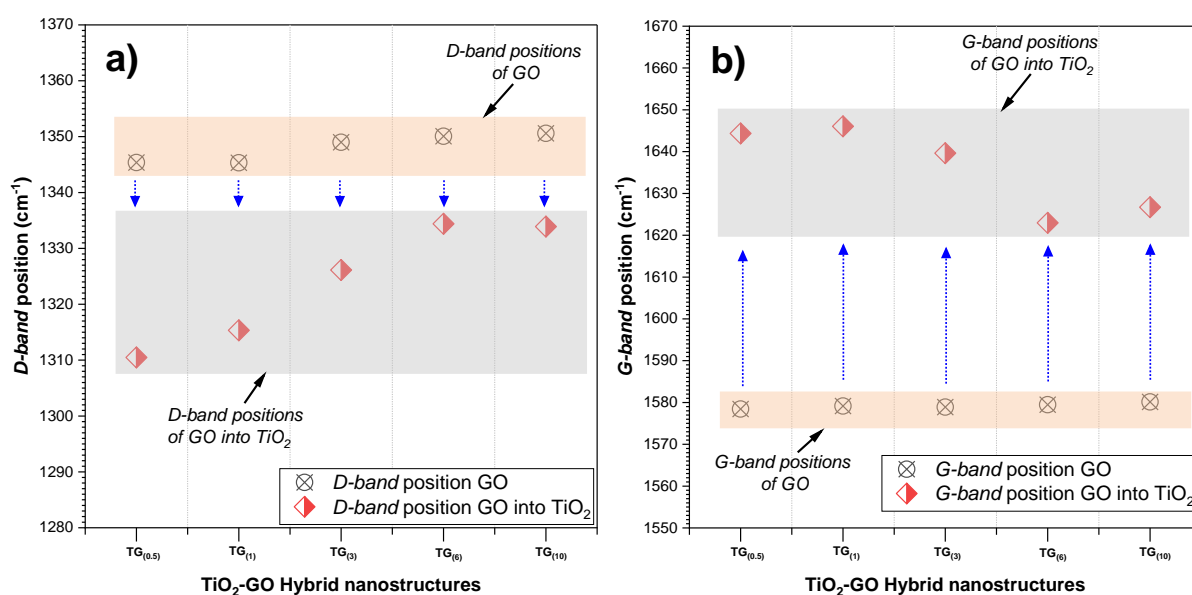


Fig. 6.6. Band position of GO before and after incorporation into TiO₂ nanostructures. (a) D-band position (b) G-band position

6.1.3.1.2. A_D/A_G ratio and graphitic crystallite size

The correlation between the D- and G-band areas (A_D/A_G) was evaluated as shown in Fig. 6.7.a. In all cases, a decrease in the A_D/A_G ratio of the GOs was observed after their incorporation into the nanostructures with TiO₂. This change is further reflected in the increased size of graphitic crystallites after photosonation (Fig. 6.7.b), which is associated to the reduction of structural defects and restoration of sp^2 carbon domains, thus improving crystallinity. Previous research has shown that sonication favors GO dispersion and stimulates the reduction of GO to rGO, which is associated with an increase in the average size of sp^2 carbon domains and crystallite size. These changes are manifested in the Raman spectra by a red shift of the G-band and a reduction of the D/G ratio [31, 32].

It was observed that the A_D/A_G ratio trend is maintained according to the initial oxidation degree of the GOs, *i.e.* as the oxidation increases, the A_D/A_G ratio increases. However, within the set of all GOs, the one with the lowest oxidation [TG_(0.5)] showed minimal changes after incorporation into TiO₂. In this context, the original low-oxidation GO presented larger

graphitic crystals without significant changes due to its initial oxidation. In addition, it showed a low presence of functional groups, suggesting a higher resistance to transformations during the sonication process. In contrast, the most oxidized GOs, being highly exfoliated and with a high concentration of oxygenated groups, experienced a more pronounced change in their structure during photosonification. This phenomenon involved, first of all, the removal of a greater concentration of functional groups, resulting in a more pronounced restoration of the graphitic domains. In conclusion, the GO oxidation degree exerts a significant influence on the resistance of its structure to photosonification-induced changes. The reduced presence of oxygenated groups in a low oxidation GO seems to give it a higher stability and a lower susceptibility to structural changes during the sonication process compared to highly oxidized GOs.

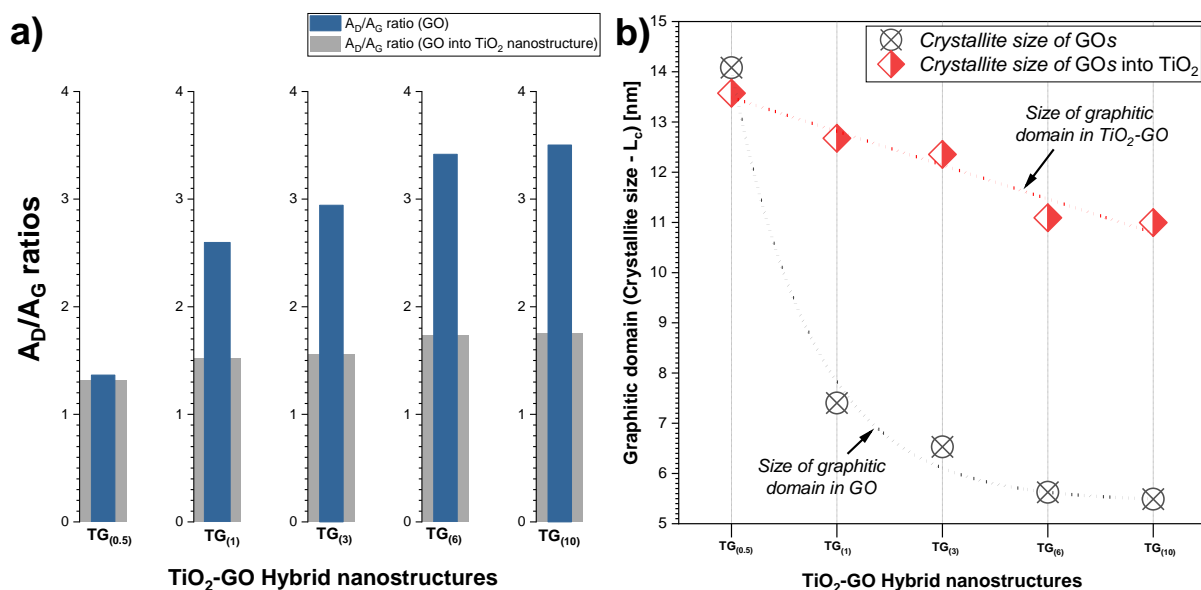


Fig. 6.7. Evolution of graphene oxide before and after incorporation into TiO₂ (a) A_D/A_G ratio and (b) GO graphitic domain size (L_c).

Analysis of the D' bands showed A_D/A_G values greater than ≈0.28 in all cases, consistent with boundary-type defects (discussion in Chapter 4). This is consistent with the nature of defects caused by the GOs sonication process [32]. Therefore, the research supports the idea that photosonification mainly promotes this type of defect.

6.1.4. Interface bonds analysis by FTIR-ATR

Fig. 6.8.a. shows the FTIR-ATR spectra of pristine TiO₂ and TiO₂-GO nanostructures. In pristine TiO₂, two bands corresponding to the Ti-O stretching vibration were observed at ≈731 and ≈445 cm⁻¹, while the band at ≈574 cm⁻¹ was attributed to Ti-O-Ti bonds in the lattice [33]. On the other hand, an additional band at ≈1063 cm⁻¹ corresponding to C-O stretching vibrations was identified in the nanostructures, which becomes more intense and defined with increasing GO oxidation degree (Fig. 6.8.b.). Thus, an increase in the intensity of the spectra in the range

of 400-900 cm^{-1} is also observed, which is associated with the formation of a higher concentration of Ti-O-C bonds [34].

To validate and fully elucidate the atomic interaction between the two structures at the interface, a Lorentzian deconvolution analysis of the spectra in the range of 400 to 900 cm^{-1} was performed (Fig. S.6.2.). This analysis identified a band at $\approx 800 \text{ cm}^{-1}$ that is attributed to the presence of Ti-O-C bonds. These bonds are related to the bonding between the free electrons on the TiO_2 surface and some unpaired π -electrons of the GO, resulting in a shift of the vibrational modes [35]. This finding evidences the formation of Ti-O-C bonds resulting from the neutralization of the Ti^{3+} surface defects of TiO_2 with oxygen from the GO functional groups. Furthermore, quantification of the area under the curve revealed a direct relationship between the GO oxidation degree and the formed amount of Ti-O-C bonds (Fig. 6.8.b.). This phenomenon is in agreement with the theoretical DFT study in Chapter 3 [42], where it was shown that after the geometrical relaxation of a hybrid structure based on TiO_2 and GO, both surfaces are connected by the oxygen atom from the GO, thus forming a Ti-O-C bond that bridges the two structures. The study also revealed the absence of bonds between the C and Ti atoms. Our results would then confirm the nature of the interaction between the two structures at the interface.

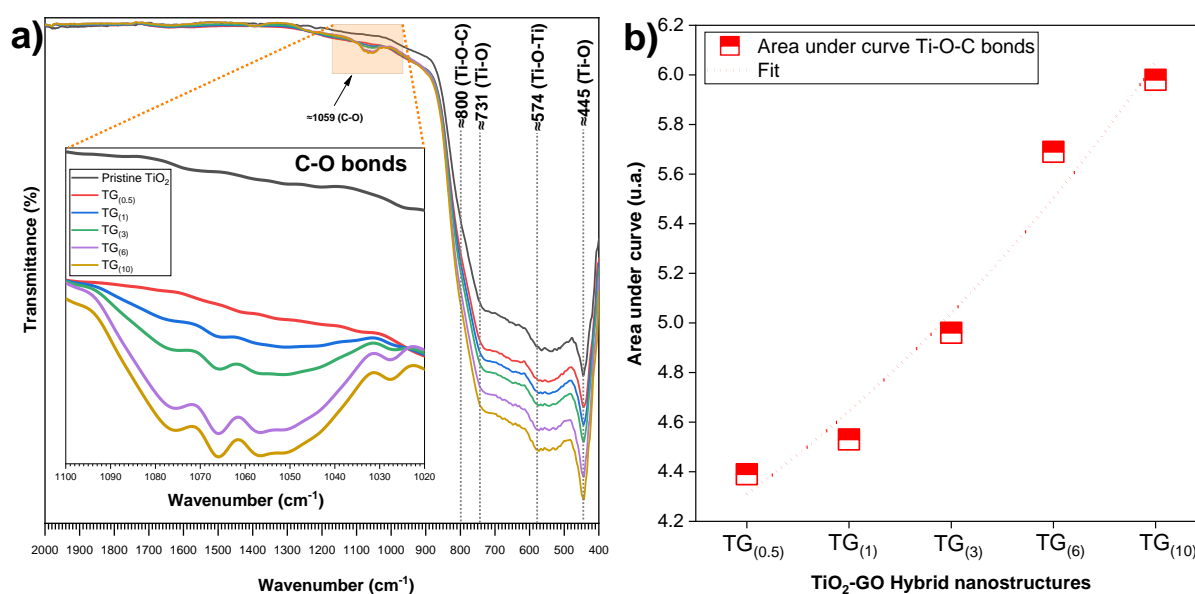


Fig. 6.8. (a) FTIR-ATR spectra range of 400-2000 cm^{-1} (b) Quantifying the area under the Ti-O-C bond curve (*reprinted from our published work on Elsevier 2024 [16]*).

6.2. EPR study

6.2.1. Ti^{3+} defects on TiO_2 by EPR

EPR spectroscopy is highly sensitive to paramagnetic species caused by defects such as vacancies, impurities, and valence changes due to oxidation or reduction. EPR has been used to elucidate the nature of electronic active defects that accompany the formation of TiO_2 -GO nanohybrid nanostructures during sonication treatment. Fig. 6.9. shows the EPR spectra of

TiO₂ at room temperature, before and after the photosonication process. In pristine TiO₂, Ti³⁺ ions exhibit a 3d¹ electronic configuration, generating a sharp EPR signal with the characteristics of dust spectra associated with d-unpaired (S=1/2) spin species in a local axial symmetry. The Ti³⁺ concentration is directly related to the signal intensity and the Landé \tilde{g} -tensor anisotropy which is traduced by different resonance lines in the EPR spectra is directly correlated with the local environment symmetry of Ti³⁺. In EPR spectroscopy, such symmetry is accounted theoretically by the anisotropic interaction between the applied magnetic field and the spin-related magnetic moment of the unpaired electron carried by Ti³⁺. In a general case, this interaction is represented by a spin Hamiltonian (\hat{H}) [36, 37] written as:

$$\hat{H} = \mu_B \cdot \vec{B} \cdot \tilde{g} \cdot \vec{S} \quad (\text{eq. 11})$$

Where μ_B represents the Bohr magnetron, \vec{B} is the magnetic field (vector), \tilde{g} is the Landé tensor and \vec{S} the electron spin operator (vectorial). From the observed form of the EPR spectrum composed of two well-resolved singularities, the parameters of the tensor in its orthonormal main frame (O_{XYZ}) are such that $g_z = g_{\parallel}$ and $g_x = g_y = g_{\perp}$.

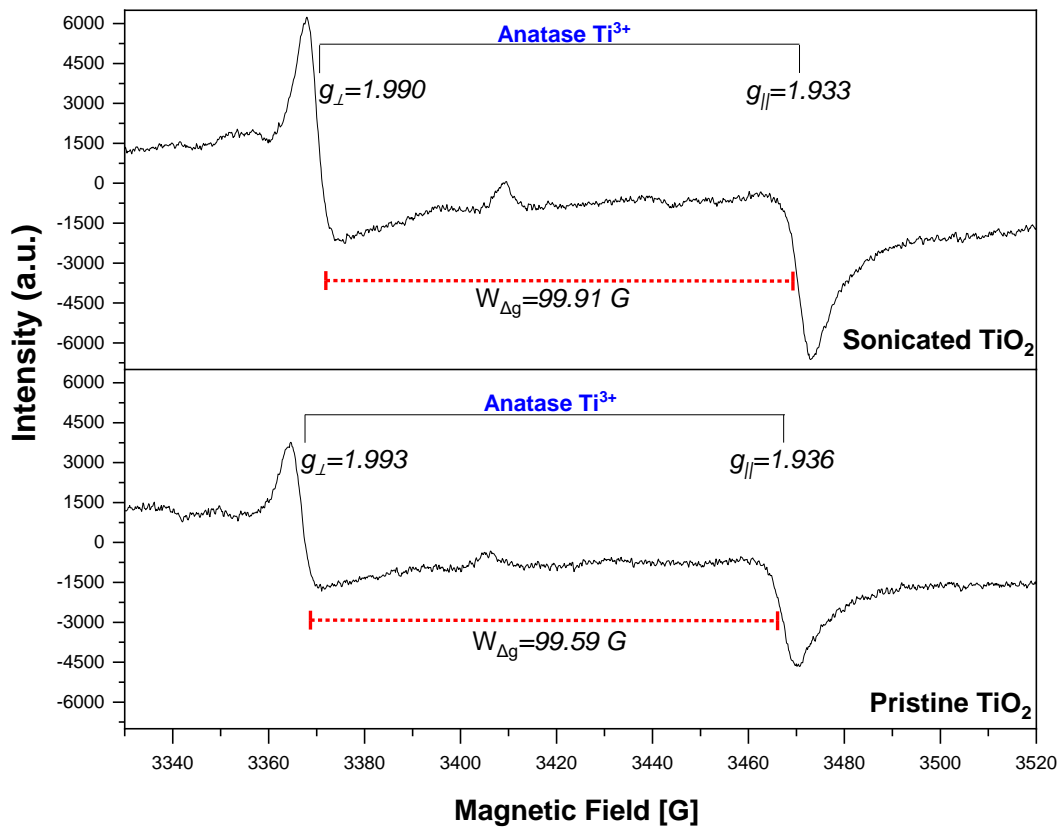


Fig. 6.9. EPR spectra of pristine and photosonicated TiO₂ at room temperature.

In this case, the positions of the analysis of the EPR line lead to the g -tensor values with $g_z = g_{\parallel} = 1.936$ and $g_x = g_y = g_{\perp} = 1.993$. These values describe the anisotropy of the host crystal site for Ti³⁺ as an octahedral or pyramidal environment with oxygen ligands on a square basis. After the TiO₂ sonication process and before incorporating GO, g -tensors at $g_z = g_{\parallel} = 1.933$ and

$g_x=g_y=g_z=1.990$ remain very close to those of pristine TiO_2 . The almost constant component values of the g -tensors suggest that the local structure of the hosting environment for Ti^{3+} is similar to that in which native defects are involved. Nevertheless, there is a noticeable rise in the strength of the EPR signal, indicating an increase in the concentration of Ti^{3+} caused by photosonication. Indeed, ultrasonic treatment of TiO_2 powders in solution influences the aggregation or dispersion of the particles and, at the same time, modifies the arrangement or distribution of the surface atoms. That is, if the TiO_2 particles were agglomerated before sonication, the process could have disorganized these environments, exposing a larger fraction of the surface area. This increase in surface area would confirm the increase in surface Ti^{3+} ion concentration. To summarize, the principal changes in the EPR spectra before and after photosonication confirm our XRD discussion and provide compelling proof that the procedure itself influences the rearrangement of atoms, resulting in defects on the TiO_2 surface.

6.2.2. Field splitting ($W_{\Delta g}$) and anisotropy after GO incorporation

Fig. 6.10. shows the EPR spectra of the sonicated TiO_2 after the incorporation of GOs with different oxidation degrees. Comparing the magnetic field splitting ($W_{\Delta g}$) due to the anisotropy of the g -tensor in the nanostructures with that of the photosonicated TiO_2 ($W_{\Delta g}=99.91$ G), we may notice a significant decrease in this value for all the nanostructures considered. The relative reduction of that factor, of the order of 18%, implies a significant effect of GO adsorption on the TiO_2 surfaces leading to the formation of core-shell-type structures, as demonstrated by the TEM observations discussed above. On one hand, GO is a material with excellent mechanical properties such as high tensile strength and stiffness [38]. The location of GO clusters on the TiO_2 surface leads to compressive forces that could influence the reduction of interatomic distances with a particular effect on surface bonding. Therefore, it is expected that the local environment of the reduced Ti^{3+} ions on the surface will change as it will be also the anisotropy of the associated EPR spectra. These experimental results support the theoretical findings presented in Chapter 3, where it was shown that the inclusion of GO on the TiO_2 surface resulted in a decrease in the distance between Ti-O atoms compared to the optimized TiO_2 structure.

On the other hand, analyzing the EPR line intensity of the nanostructures, it was first observed that the intensity of Ti^{3+} in the $\text{TG}_{(0.5)}$, $\text{TG}_{(1)}$, and $\text{TG}_{(3)}$ spectra gradually decreased with the adsorption of the GO layers. Within the GO shells formed, chemical oxygen bonding, and delocalized charges are involved and favor electronic interactions between the adsorbed GO and the TiO_2 surfaces. Surprisingly, despite the increase in the amount of oxygen contributed by the higher oxidizing GOs, $\text{TG}_{(6)}$ and $\text{TG}_{(10)}$ nanostructures again show an increase in the intensity of the Ti^{3+} EPR signals. While this observation contrasts with the straightforward interpretation, the clarity presented by the XRD data guides us toward a deeper explanation of the observed phenomena. The shift of the XRD peaks to higher angles provides a solid basis for developing the hypothesis about how the increased oxidation of GO contributes to defect neutralization. So, we would also expect it to decrease the intensity of the Ti^{3+} signals in the EPR spectra. However, the high density of functional groups present in highly oxidized GO would promote interaction with each other, which may lead to the formation of small

agglomerates or aggregates [39]. This agglomeration may result in more pronounced magnetic and electronic interactions in the material, which, in turn, may increase the intensity of the EPR signals.

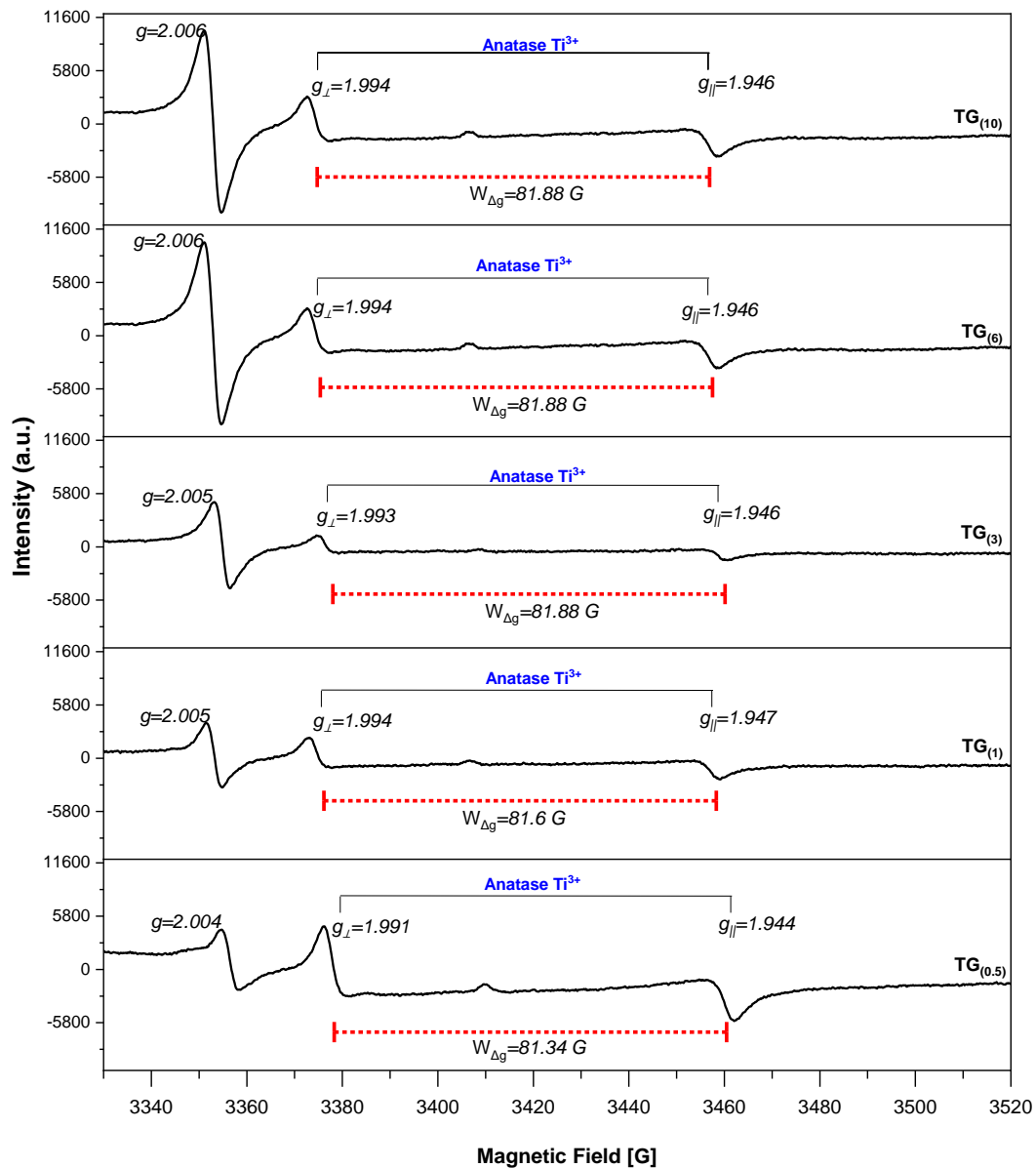


Fig. 6.10. EPR spectra of TiO_2 -GO hybrid nanostructures by photosonication (*Adapted from our published work on Elsevier 2024 [16]*).

6.2.3. Paramagnetic behavior of GO as a function of the oxidation degree

The room-temperature EPR signals of GO materials within the nanostructures were recorded. A single and sharp resonance line was observed with a Lorentzian shape located at $g \approx 2.004$. This value is characteristic of paramagnetic species involved in disordered carbon environments (sp^3) as dangling bonds. Nevertheless, the presence of conduction electrons is expected to affect the EPR signal, provided that the associated spin relaxation times are long enough to allow detection of the associated EPR signal. As will be discussed below, the

temperature evolution of the EPR signal is relevant to distinguish between localized spins in disordered environments and delocalized spins associated with conducting electrons or thermally activated spin species. For the room temperature EPR spectra, their analysis leads to the spectral parameters summarized in Fig. 6.11.

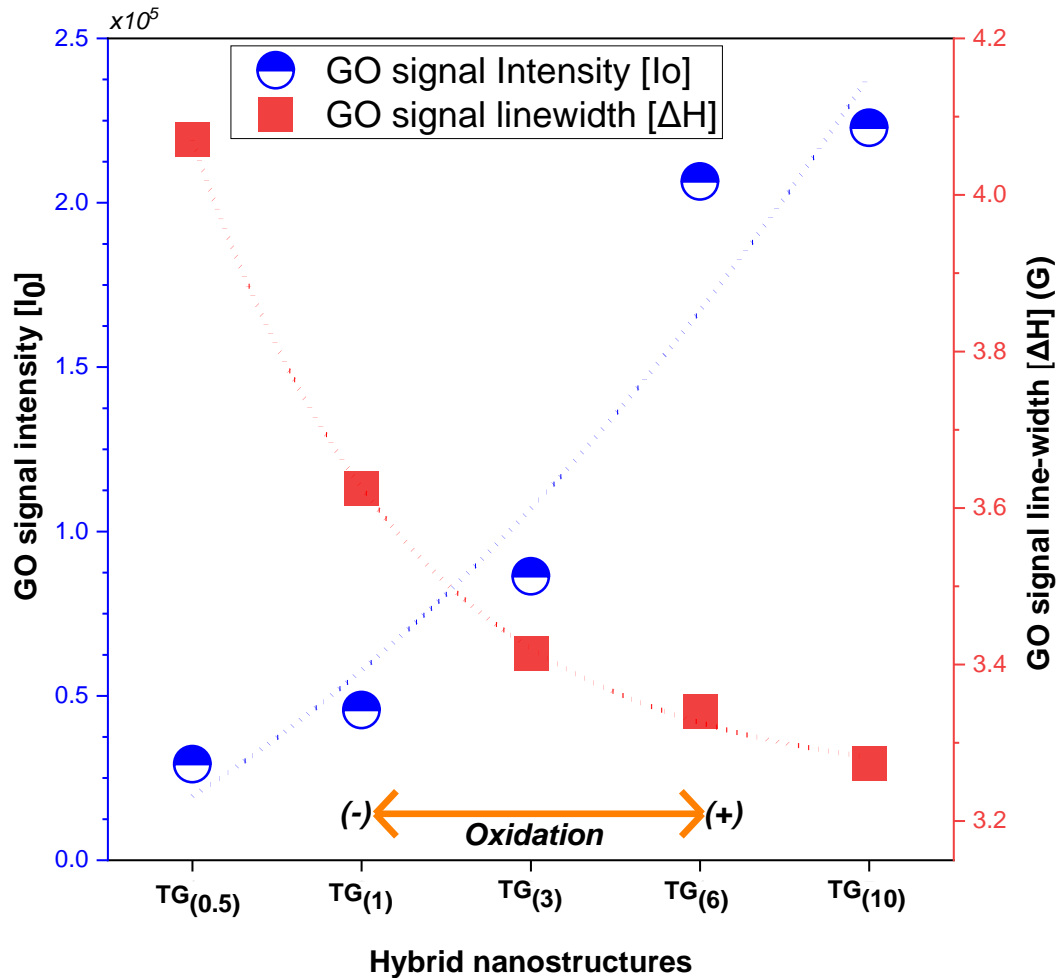


Fig. 6.11. EPR signal intensity and amplitude behavior of GO in TiO_2 -GO nanostructures (reprinted from our published work on Elsevier 2024 [16]).

The integrated intensity I_0 increases with increasing oxidation degree to reach the maximum for $\text{TG}_{(10)}$. This behavior is attributed to the presence of radical species formed with the incorporation of functional groups. An increase in the density of radicals and unpaired electrons in the sample can lead to more pronounced electron paramagnetic resonance (EPR) signals. Initially, the majority of the carbon rings are expected to remain intact, characterized by a low oxidation degree and consisting of three double bonds. However, as seen in Raman studies (D -band), the inherent disorder induces the formation of dangling bonds where sp^3 bonding and then accounts for the low radical concentration and then the low intensity of the EPR signal. With increasing the oxidation, a higher density of functional groups is created and with it an increased disorder. In parallel with the increase of the intensity, the line-width (ΔH) progressively decreased with increasing oxidation degree. The decrease of the linewidth can be understood by *exchange-narrowing* phenomena [40]. Indeed, oxidation increases the

concentration of unpaired spins, which stimulates interactions between nearby spins. These interactions average the EPR signal from the different EPR active sites and limit the dispersion of the resonance position. As a consequence, the narrowing of the EPR line occurs with more or less intensity depending on the strength of interactions between unpaired spin species.

6.2.4. Paramagnetic behavior of GO as a function of temperature

The magnetic properties of the embedded GO were studied using temperature-induced changes of the EPR spectra in the temperature range from 100 to 300 K. Fig. 6.12. presents temperature dependencies of the normalized EPR signals. Intensities were determined from the double integral of the EPR signal and fitted using the Curie-Weiss equation [$I_0=C/(T-\theta_C)$], where C is the Curie constant and θ_C is the Curie temperature. The result of the fit is shown as a dotted line superimposed on the experimental data.

The temperature-dependent magnetic susceptibility can inform the nature of interactions between paramagnetic species. Thus, a ferromagnetic interaction is shown for $TG_{(0.5)};(\theta_C=68.7>0)$ and for $TG_{(1)};(\theta_C=85.6>0)$ from the simulation of their temperature variation EPR signal intensity. No additional temperature constant spin susceptibility was observed. This excludes the existence of Pauli susceptibility which is associated with delocalized electrons. However, often structural defects, such as vacancies and edges, among other perturbations, are responsible for magnetic properties [41]. Therefore, the ferromagnetism observed in $TG_{(0.5)}$ and $TG_{(1)}$ would be attributed to local regions where defects can couple to each other [42, 43]. This can lead to spin interaction between magnetic moments located in defects or functional groups, resulting in preferential spin alignment, and promoting ferromagnetism [44]. Thus, for $TG_{(0.5)}$ and $TG_{(1)}$ the saturation of the intensity is observed below 130 K, indicating the manifestation of magnetic ordering at low temperatures.

In contrast, the negative Curie-Weiss temperature for $TG_{(3)}$ indicates the presence of antiferromagnetic interactions ($\theta_C=-28.2<0$). Although anti-ferromagnetism in GO has not been widely reported or definitively established, some studies have suggested such interactions in GO with the controlled introduction of defects. Ramakrishna *et al.* 2009 [45], revealed that in all prepared GO samples dominant ferromagnetic interactions coexist along with antiferromagnetic behavior similar to what occurs in disrupted or phase-separated systems. According to scientists, the magnetic properties of GOs are influenced by the number of layers and the area of the samples. In particular, lower values of both factors result in higher magnetism. Yazyev O *et al.* 2007 [46], determined that in graphitic materials with defects present with equal probability in both sublattices, the overall correlation of magnetic moments would be expected to be antiferromagnetic. They also found that both ferromagnetic and antiferromagnetic scenarios of magnetic interaction are possible, with the latter being more likely for truly disordered systems. Experimental evidence has shown that graphene with imperfections undergoes a transition from paramagnetic to antiferromagnetic when the temperature reaches a critical point. This behavior is caused by the appearance of numerous nucleations in the antiferromagnetic domains as a result of defect rearrangement with increasing temperature. Semenov Y., *et al.* 2011 [47] further add that since each domain is

characterized by partial compensatory magnetization of defects associated with different sublattices, the whole shows superparamagnetic behavior in the magnetic field.

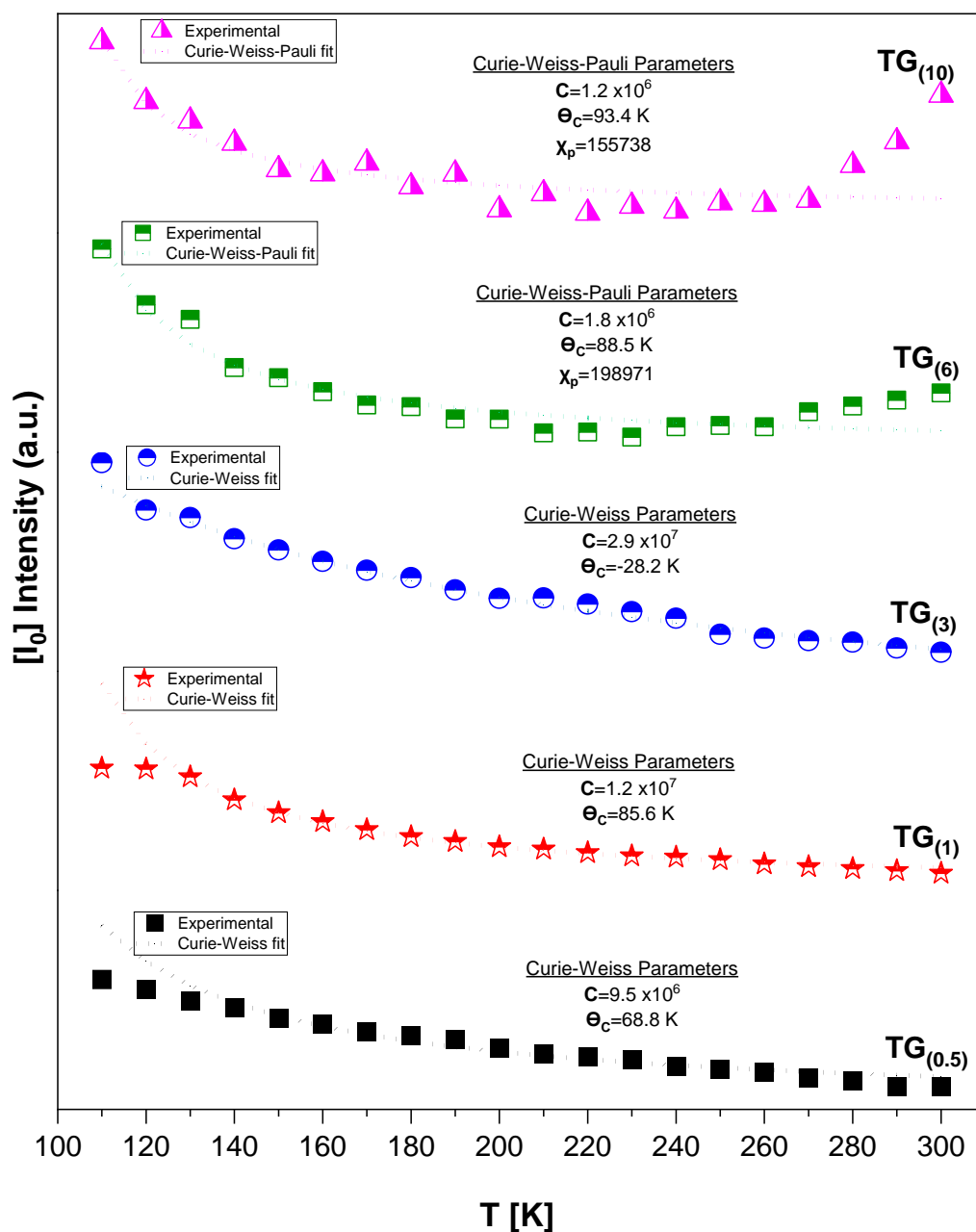


Fig. 6.12. Evolution of GO EPR signal intensity of TiO₂-GO nanostructures (Temperature range: 100-300K) (*reprinted from our published work on Elsevier 2024 [16]*).

Fig. 6.12 also shows an atypical spin susceptibility for the GOs with the highest oxidation degrees, namely TG₍₆₎ and TG₍₁₀₎. That is, with increasing temperature, the susceptibility decreases up to the inflection point around 270 K and then increases. The curves TG₍₆₎ and TG₍₁₀₎ were fitted using Curie and Pauli contributions [$I_0=C/(T-\theta_C)+\chi_p$], resulting in $\theta_C=88.5>0$ for TG₍₆₎ and $\theta_C=93.4>0$ for TG₍₁₀₎. Both fits indicate strong ferromagnetic interactions, similar to the behavior described for TG_(0.5) and TG₍₁₎. However, the fact that TG₍₆₎ and TG₍₁₀₎ again show an increase in intensity from 270 K suggests thermal activation and increased

concentration of paramagnetic species due to a rearrangement of the functional groups already present. In other words, the higher the oxidation, the greater the variety of functional groups and/or faults introduced into the material. The different characteristics of these functional groups and defects could lead to an inhomogeneous and more disordered distribution of spins in the material. Thus, some regions could have a higher concentration of spins, favoring a particular magnetic arrangement, while other regions could have a lower spin density and magnetic behaviors that can be thermally activated. The existence of Pauli spin susceptibility suggests the presence of free electrons within the GO networks. The possibility of the plasmonic effect suggested by the Raman spectra may be correlated with the involvement of free electrons at the interfaces of TiO₂-GO.

6.3. Relation between nanostructure formation by sonication and EPR active defects

From the results obtained and the analysis carried out, we can draw the following pictures for the TiO₂-GO nanostructures based on the features of the Ti³⁺ EPR active electronic defects. Fig. 6.13. shows the proposed mechanism for the formation of nanostructures by the photosonication method and the influence of the GO oxidation degree on the final structure of the material. Initially, during the first step of TiO₂ sonication in the aqueous medium (ethanol), an activated de-agglomeration of the primary powder particles occurs [48]. Subsequently, sonication produces a significant delamination effect by exposing a larger fraction of the surface area [49]. This would contribute to the increase in the surface concentration of Ti³⁺ ions, as confirmed by EPR (Fig. 6.13.a). Subsequently, when GO is introduced into the solution (Figs. 6.14.b-c), the positive charges present on the surface of TiO₂ (Ti³⁺) can attract the negative charges present on the oxygenated functional groups of GO. This electrostatic attraction between the opposite charges can contribute to the adhesion of GO to the TiO₂ surface, eventually leading to the formation of a core-shell-type structure. The concentration of Ti³⁺ decreases due to their neutralization with the GO shell. In this context, when a Ti³⁺ defect encounters any of the oxygen atoms present on the GO layers within the proposed scheme, a redox reaction occurs in which the Ti³⁺ defect is oxidized to Ti⁴⁺, and the oxygen atom of the GO as illustrated in Fig.6.13.a.

Previous works have mentioned that such covering features occur when one material has a lower surface energy than another. So, based on this rule, a GO with a calculated surface energy of 0.0621 J/m² [50], would be coating a TiO₂ with a calculated surface energy of 0.95 J/m² [51], which is in both cases consistent with the observed structural arrangement. The homogeneity of the GO shell is due to the structural arrangement shown in Fig. 6.13. That is, the less oxidized GOs show a marked tendency to present larger and less dispersed blocks in their configuration (Fig. 6.13.a). These blocks, which are essentially areas of less chemical modification, indicate the preservation of larger portions of the original graphite structure. The formation of core-shell structures with less oxidized GO would result in a thicker and less uniform shell (Fig. 6.13.b). In contrast, GOs with more oxidized have more dispersed, smaller, and exfoliated blocks in their structure (Fig. 6.13.b). This arrangement could promote a more uniform and effective interaction with the core particle, resulting in a more complete and

uniform adhesion to the TiO₂ surface, producing a core-shell structure with a homogeneous appearance and complete shell (Fig. 6.13.c).

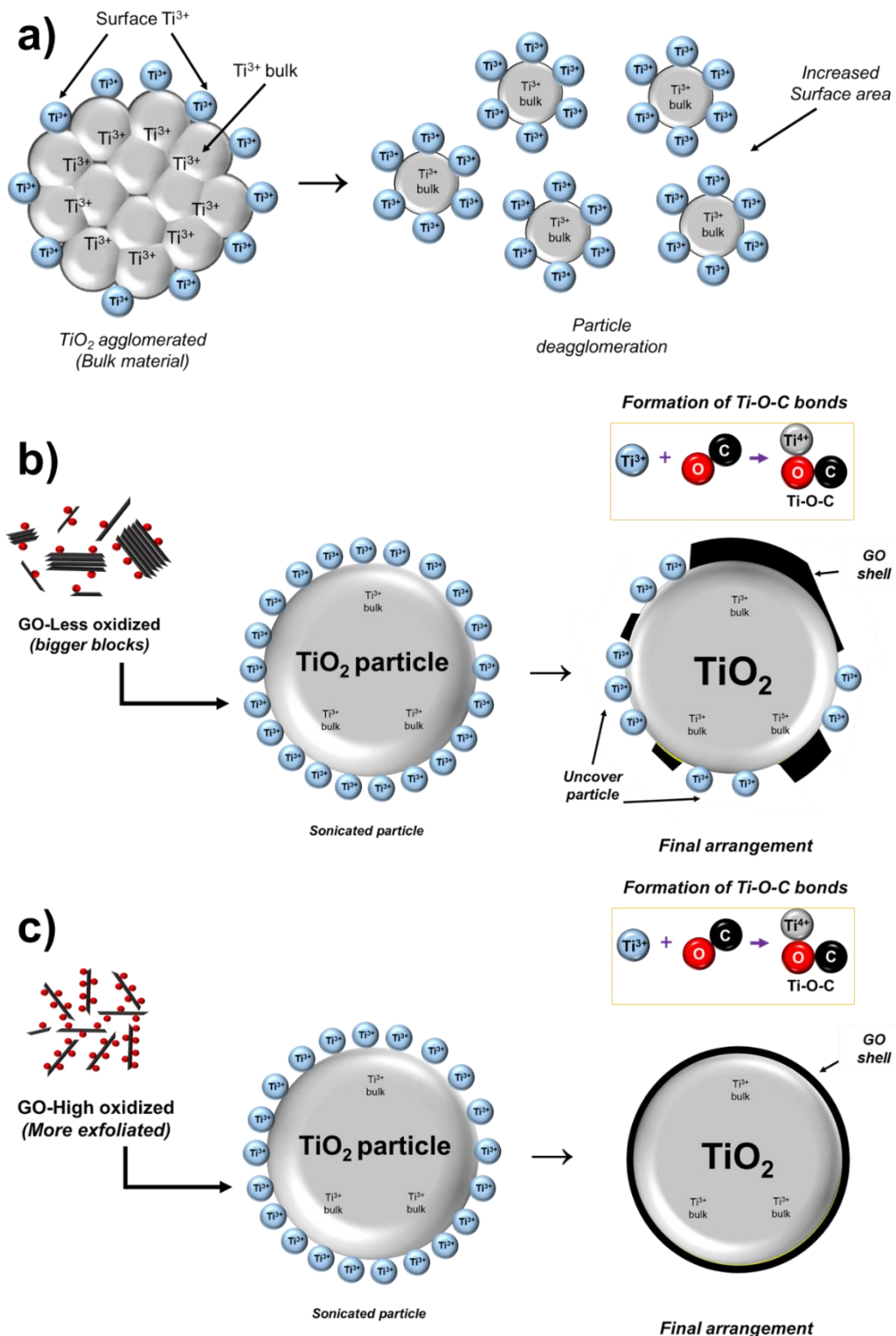


Fig. 6.13. Schematic progress of TiO₂-GO nanostructures formation by photosonification method (a) Deagglomeration of primary powder particles and reduction in particle size as a consequence of delamination and more formation of surface defects; (b) Incorporation of less oxidized GO (c) Incorporation of high oxidized GO (*reprinted from our publisher work on Elsevier 2024 [16]*).

6.4. Optical features

The diffuse optical reflectance spectra of pristine TiO_2 nanoparticles and TiO_2 -GO nanostructures are shown in Fig. 6.14.a. It can be seen from the spectra that the reflectance intensity of the nanostructures is lower than that of the pristine TiO_2 , which is related to the resulting structural arrangement at the surface. These modifications change the way how the light interacts with the surface of the nanostructures. Thus, when the TiO_2 particle is coated with GO, it absorbs some of the light that would originally have been reflected by the uncoated TiO_2 particle.

The reflectance values were converted to the absorption coefficient $F(R)$ using the Kubelka-Munk equation (eq. 6), and the optical bandgap was determined (eq. 7). The plots of Kubelka-Munk vs the energy of absorbed light can be seen in Fig. S.6.4. Fig. 6.14.b. shows a slight narrowing of the TiO_2 bandgap after the incorporation of GO. A trend was also observed as a function of the oxidation degree, with the lowest value being exhibited by the least oxidized nanostructure [$\text{TG}_{(0.5)}$]. Optical bandgap differences were not significant considering the uncertainty associated with their estimation, making it difficult to determine these values accurately. However, although the incorporation of GO significantly reduced the reflectance of the nanostructures, such changes in electronic structure and bandgap are attributed to localized effects occurring mainly at the interface between TiO_2 and GO. These effects may not extend far enough into the material to significantly alter the bandgap throughout the structure.

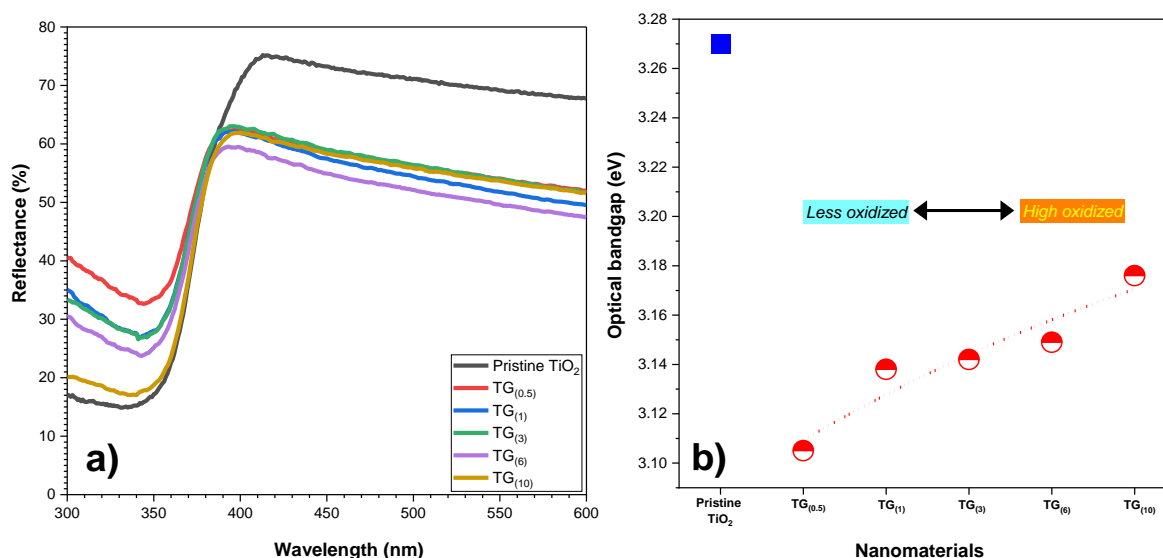


Fig. 6.14. (a) UV-diffuse reflectance spectra and (b) optical bandgap values of pristine TiO_2 and TiO_2 -GO hybrid nanostructures

6.5. Electrical Conductivity

Fig. 6.15. shows logarithmic scale curves of electrical conductivity vs. frequency for the different materials. It is shown that, as the frequency increases, the electrical conductivity

increases, while the incorporation of GO contributed to the increase in conductivity of the nanostructures compared to that of pristine TiO_2 . The graphs did not show a clear conductivity plateau, this is associated with the fact that in core-shell type nanostructures, the interface between the GO core and shell can have a significant influence on the electrical properties, since, if the interface is not perfect or if there are defects in it, the charge transfer and conduction processes can be affected. The absence of a DC (direct current) plateau is due to interfacial polarization (Max-Well-Wagner-Sillars (MWS) polarization) that is caused by bulk charge accumulation at the interface, which usually occurs in heterogeneous systems with components with different conductivities [52]. The MWS polarization of the nanostructures is observed in the frequency range from 10^{-1} to 10^2 Hz, which correlates with the structural results shown in Fig. 6.1. That is, a higher slope in the $\text{TG}_{(0.5)}$ nanostructure is related to the non-homogeneous shell shown in Fig. 6.1.b, while the lower slope is associated with the mostly homogeneous shell in Fig. 6.1.c [TG_{10}]. Still, the latent plateau of DC conductivity in systems with MWS polarization effects was determined using the Jonscher model shown in Chapter 5 (eq. 10).

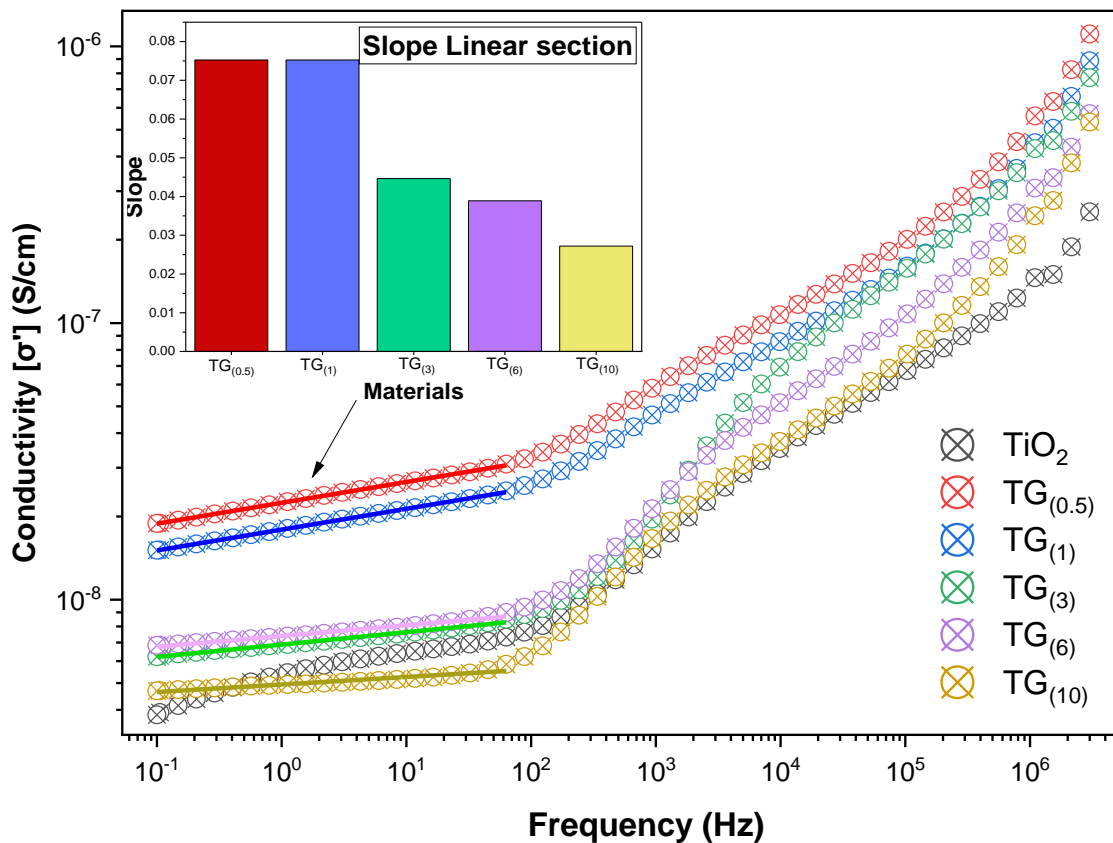


Fig. 6.15. Conductivity of TiO_2 -GO nanostructure vs. frequency at room temperature

The calculated parameters are shown in Table 6.3. At low frequencies, charge carriers move a large distance within the compound to change the direction of the electric field. In this case, the average distance traveled by charge carriers at frequencies lower than the critical frequency is greater than the correlation length. At high frequencies, electrical conductivity is realized by hopping charge carriers between localized states, so a nearly linear increase is observed in the plot [53]. Table 6.3. also reveals that the DC electrical conductivity (σ_{DC}) of TiO_2 experiences

an increase with the incorporation of GO, substantially improving the ability of the composite material to conduct electrical current. Furthermore, an additional trend can be observed in the data. As the GO oxidizes, the conductivity tends to decrease. This behavior could be related to changes in the structure and conduction properties of GO, *i.e.*, with little oxidation a highly conjugated π -bond structure is maintained, which allows for high electronic mobility and thus high conductivity. The introduction of oxygen groups disrupts this conjugated structure, leading to a dispersion of electronic states and reducing electron mobility through the material. As oxidation increases, more π -bonds are broken and the structure becomes less conductive, impacting the overall conductivity of the nanostructure. Additionally, an increase in the exponent " n " is seen, suggesting greater interaction between the charge carriers and the lattice.

Table 6.3. Fitting parameters obtained from experimental data of the conductivity (σ) as a function of frequency using Jonscher's power law

Materials	σ_{DC} (S/cm)	A	n	R ²
Pristine TiO ₂	5.6x10 ⁻⁹	6.8x10 ⁻¹⁰	3.9x10 ⁻¹	0.9849
TG _(0.5)	3.7x10 ⁻⁸	2.0x10 ⁻¹⁰	5.7x10 ⁻¹	0.9863
TG ₍₁₎	3.0x10 ⁻⁸	1.6x10 ⁻¹⁰	5.7x10 ⁻¹	0.9857
TG ₍₃₎	9.1x10 ⁻⁹	5.3x10 ⁻¹⁰	4.8x10 ⁻¹	0.9907
TG ₍₆₎	1.1x10 ⁻⁸	2.2x10 ⁻¹⁰	5.2x10 ⁻¹	0.9903
TG ₍₁₀₎	1.1x10 ⁻⁸	2.6x10 ⁻¹¹	6.6x10 ⁻¹	0.9841

6.5.1. Conductivity evolution with temperature changes

Using TG_(0.5) nanostructure, the dependence of the conductivity at different temperatures in the range of 173-473K was evaluated. The experimental conductivity spectra are shown in Fig. 6.16. and the results of the fit are summarized in Table S.6.4.

The internal image of Fig. 6.16 shows how the exponent " n " presents a dependent behavior, with three defined sections. The exponent " n " remains almost constant at low temperatures, indicating that the interaction between the mobile ions and the lattice of the material is relatively stable and constant. In such a case, the material may exhibit a certain degree of order or restricted mobility of the ions within the lattice. Subsequently, with increasing temperature (273-333K), the exponent " n " begins to increase slightly. This suggests that there could be a transition in the ion-lattice interaction, potentially due to the increase in thermal energy, whereby the ions could be gaining more mobility or overcoming certain barriers within the lattice. Finally, beyond 300 K, the exponent " n " begins to decrease rapidly with increasing temperature. This could indicate a change in the dominant conduction mechanism or a significant alteration in the interaction between the mobile ions and the lattice. The increase in thermal energy could result in increased ion mobility and a decrease in the degree of interaction. Additionally, due to the elevated temperatures, the ions could change from a more restricted

motion to a hopping-type motion, which could result in less interaction with the lattice. This change in the conduction mechanism could explain the observed rapid decrease in the exponent "n".

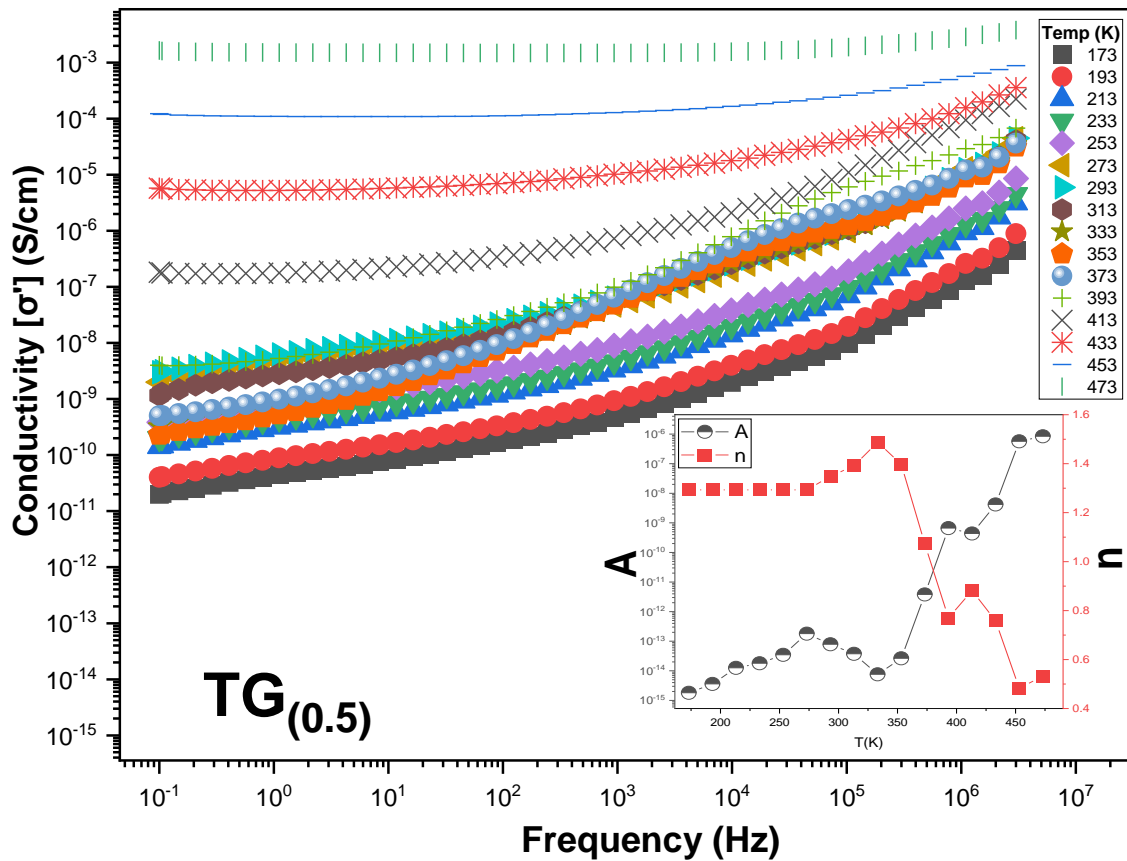


Fig. 6.16. Conductivity of TG_(0.5) nanostructure vs. frequency as a function of temperatures.

Fig. 6.17. shows the variation of DC conductivity (σ_{DC}) versus $1000/T$ used for the activation energy calculation. The plot clearly shows three sections where the conductivity increases, however, how this is achieved appears not to be constant. We fit each segment to the Arrhenius relation $\sigma_{DC} = \sigma_0 e^{\left(\frac{-E_g}{k_B T}\right)}$, where σ_0 is the pre-exponential factor corresponding to $1/T = 0$, k_B is the Boltzmann constant ($=8.617 \times 10^{-5} \text{ eV K}^{-1}$), E_g is the conduction activation energy and T is the absolute temperature. The different calculated energy values suggest that, at low temperatures, the increase in conductivity could indicate the onset of charge carrier mobility or a change in the conduction mechanism. Whereas, at high temperatures, thermal energy is more abundant, allowing charge carriers to access higher energy states. This higher thermal energy could allow the carriers to overcome higher energy barriers and contribute more effectively to conductivity. The higher activation energy required to initiate conduction may be indicative of the more energetic pathways that are activated at elevated temperatures.

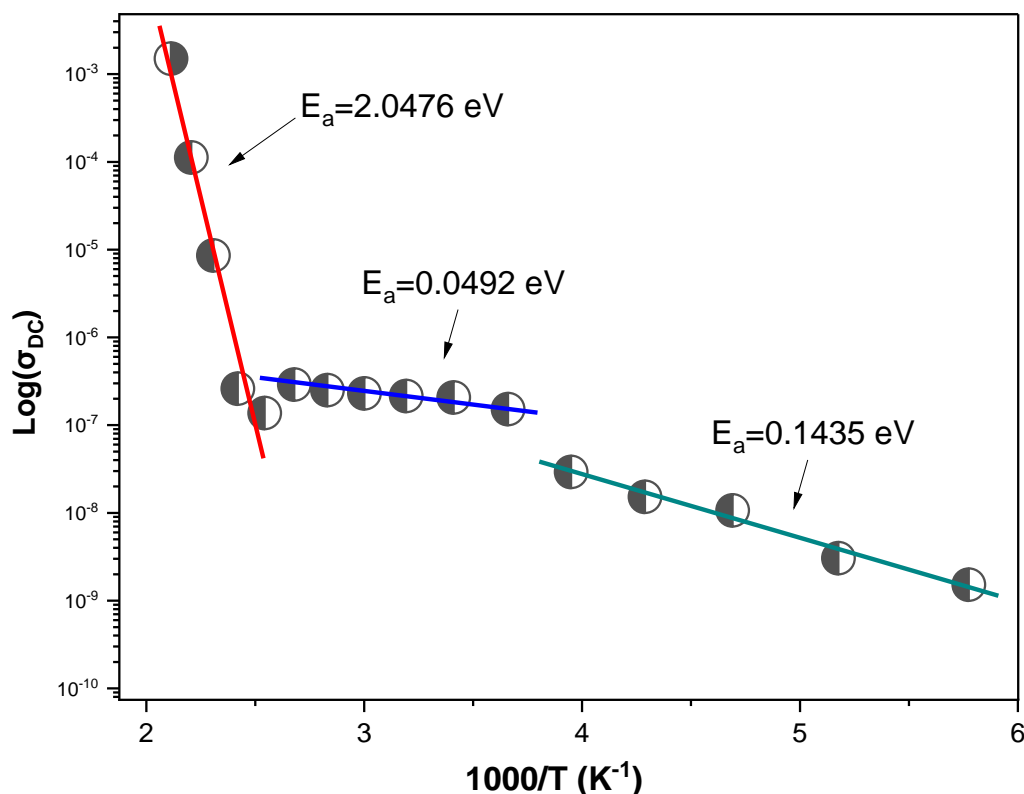


Fig. 6.17. Arrhenius plot of σ_{DC} conductivity for nanostructure TG_(0.5)

6.6. Conclusion

Photsonication proved to be an alternative and less aggressive method than ball-milling for obtaining hybrid nanostructures based on TiO₂ and GO.

- TEM revealed that the hybrid nanostructures are composed of TiO₂ particles coated by a GO layer, forming a core-shell structure. It was observed that the nanostructure with the GO of lower oxidation [TG_(0.5)] exhibited an irregular GO shell with varying thicknesses, ranging from approximately 6 to 21 nm, in addition to uncoated particle surfaces. Subsequently, as the GO oxidation increased, the shell became thinner, covering more of the particle surface. Consequently, the nanostructure with the highest GO oxidation [TG₍₁₀₎] showed a more uniform shell that completely envelops the particle, albeit with a reduced thickness. This organizational pattern is intrinsically linked to the morphology of the GO, being directly influenced by its oxidation degree as detailed in Chapter 4. That is, the GO with lower oxidation exhibits larger carbon platelets and greater stacking, in contrast to the more oxidized GO which presents a greater degree of flaking and wrinkling, with more dispersed lamellae.
- EPR analysis demonstrates the increased surface concentration of Ti³⁺ ions on TiO₂ as a result of sonication. Subsequently, when GO was incorporated, the positive charges present on the surface of TiO₂ (Ti³⁺) attracted the negative charges present on the oxygenated functional groups of GO. This electrostatic attraction between opposite

charges contributed to the adhesion of GO to the TiO₂ surface, ultimately leading to the formation of a core-shell structure. In this context, when a Ti³⁺ defect encounters any of the oxygen atoms present in the GO layers within the proposed scheme, a redox reaction occurs in which the Ti³⁺ defect is oxidized to Ti⁴⁺ which is an EPR silent ion. A formation mechanism was proposed that involves only the Ti³⁺ on the surface, not including the bulk. The mechanism was complemented with microstructural characterization by XRD and Raman spectroscopy.

- The incorporation of GO in the nanostructures has a noticeable impact on the interface properties between TiO₂ and GO particles. The formation of Ti-O-C bonds was demonstrated by FTIR. These surface interactions lead to modifications in the way light interacts with the surface of the nanostructures, where the GO shell on the TiO₂ particles leads to the absorption of part of the light that originally would have been reflected by the uncoated TiO₂ particles. The optical bandgap values of TiO₂ undergo a slight narrowing after GO incorporation, with the least oxidized nanostructure [TG_(0.5)] showing the lowest value of ≈3.11 eV. Analogous behavior is observed for the electrical properties of the nanostructures. Although the inclusion of GO significantly reduces the reflectance of the hybrid nanostructures, these changes are not reflected in the electrical conductivity or optical bandgap, suggesting that the effects are mainly localized at the interface between TiO₂ and GO, and do not extend far enough into the material to significantly alter its properties.
- The A_D/A_G ratio of the GO by Raman spectroscopy showed a decrease after incorporation, being related to the reduction of the GO. It was observed that the GO that presented the least changes concerning its original ratio was the one with the lowest oxidation [TG_(0.5)]. In this context, the low oxidation GO, already having a low presence of functional groups and a higher layer stacking, makes it more resistant to transformations during the sonication process. On the contrary, the more oxidized GOs, being highly exfoliated and with a high concentration of oxygenated groups, experienced a more pronounced change in their structure during sonication due to the removal of a higher concentration of functional groups.

References

1. Szabados, M., Sipos, P., Pálkó, I.: Application of sonochemical activation in synthetic organic chemistry. *Nontraditional Activation Methods in Green and Sustainable Applications*. 137–170 (2021). <https://doi.org/10.1016/B978-0-12-819009-8.00007-4>
2. Hinman, J.J., Kenneth, •, Suslick, S.: Nanostructured Materials Synthesis Using Ultrasound. 59–94 (2017). https://doi.org/10.1007/978-3-319-54271-3_3
3. Vijaya Kumar, R., Diamant, Y., Gedanken, A.: Sonochemical synthesis and characterization of nanometer-size transition metal oxides from metal acetates. *Chemistry of Materials*. 12, 2301–2305 (2000). <https://doi.org/10.1021/CM000166Z>
4. Tiple, A., Sinhar, P.S., Gogate, P.R.: Improved direct synthesis of TiO₂ catalyst using sonication and its application for the desulfurization of thiophene. *Ultrason Sonochem*. 73, 105547 (2021). <https://doi.org/10.1016/J.ULTSONCH.2021.105547>

5. Bae, J. hun, Do, S. bin, Cho, S. ho, Lee, K. min, Lee, S.E., Kim, T.O.: TiO₂ treatment using ultrasonication for bubble cavitation generation and efficiency assessment of a dye-sensitized solar cell. *Ultrason Sonochem.* 83, 105933 (2022). <https://doi.org/10.1016/J.ULTSONCH.2022.105933>
6. Giannakoudakis, D.A., Farahmand, N., Łomot, D., Sobczak, K., Bandosz, T.J., Colmenares, J.C.: Ultrasound-activated TiO₂/GO-based bifunctional photoreactive adsorbents for detoxification of chemical warfare agent surrogate vapors. *Chemical Engineering Journal.* 395, (2020). <https://doi.org/10.1016/J.CEJ.2020.125099>
7. Kumar, S., Garg, A., Chowdhuri, A.: Sonication effect on graphene oxide (GO) membranes for water purification applications. *Mater Res Express.* 6, 085620 (2019). <https://doi.org/10.1088/2053-1591/AB1FFD>
8. Mellado, C., Figueroa, T., Baez, R., Meléndrez, M., Fernández, K.: Effects of probe and bath ultrasonic treatments on graphene oxide structure. *Mater Today Chem.* 13, 1–7 (2019). <https://doi.org/10.1016/J.MTCHEM.2019.04.006>
9. Ye, S., Feng, J.: The effect of sonication treatment of graphene oxide on the mechanical properties of the assembled films. *RSC Adv.* 6, 39681–39687 (2016). <https://doi.org/10.1039/C6RA03996K>
10. Turner, P., Hodnett, M., Dorey, R., Carey, J.D.: Controlled Sonication as a Route to in-situ Graphene Flake Size Control. *Scientific Reports* 2019 9:1. 9, 1–8 (2019). <https://doi.org/10.1038/s41598-019-45059-5>
11. Le, G.T.T., Chanlek, N., Manyam, J., Opaprakasit, P., Grisdanurak, N., Sreearunothai, P.: Insight into the ultrasonication of graphene oxide with strong changes in its properties and performance for adsorption applications. *Chemical Engineering Journal.* 373, 1212–1222 (2019). <https://doi.org/10.1016/J.CEJ.2019.05.108>
12. Ručigaj, A., Connell, J.G., Dular, M., Genorio, B.: Influence of the ultrasound cavitation intensity on reduced graphene oxide functionalization. *Ultrason Sonochem.* 90, 106212 (2022). <https://doi.org/10.1016/J.ULTSONCH.2022.106212>
13. Huang, T., Xu, L., Wang, C., Yin, Z., Qiu, D.: Sonication-Aided Formation of Hollow Hybrid Nanoparticles as High-Efficiency Absorbents for Dissolved Toluene in Water. *Chem Asian J.* 11, 280–284 (2016). <https://doi.org/10.1002/ASIA.201501027>
14. Lee, J.W., Othman, M.R., Eom, Y., Lee, T.G., Kim, W.S., Kim, J.: The effects of sonification and TiO₂ deposition on the micro-characteristics of the thermally treated SiO₂/TiO₂ spherical core-shell particles for photo-catalysis of methyl orange. *Microporous and Mesoporous Materials.* 116, 561–568 (2008). <https://doi.org/10.1016/J.MICROMESO.2008.05.017>
15. Ghows, N., Entezari, M.H.: Sono-synthesis of core-shell nanocrystal (CdS/TiO₂) without surfactant. *Ultrason Sonochem.* 19, 1070–1078 (2012). <https://doi.org/10.1016/J.ULTSONCH.2012.01.009>
16. Cano, F.J., Coste, S., Reyes-Vallejo, O., Makowska-Janusik, M., Velumani, S., Olvera, M. de la L., Kassiba, A.: Influence of GO oxidation degrees on the organization and physical features of TiO₂-GO-based nanocomposites for water dye removal. *Surfaces and Interfaces.* 46, 104004 (2024). <https://doi.org/10.1016/J.SURFIN.2024.104004>
17. Seeharaj, P., Kongmun, P., Paipod, P., Prakobmit, S., Sriwong, C., Kim-Lohsoontorn, P., Vittayakorn, N.: Ultrasonically-assisted surface modified TiO₂/rGO/CeO₂ heterojunction photocatalysts for conversion of CO₂ to methanol and ethanol. *Ultrason Sonochem.* 58, (2019). <https://doi.org/10.1016/j.ultsonch.2019.104657>
18. Bhaskar, R., Li, J., Xu, L.: A comparative study of particle size dependency of IR and XRD methods for quartz analysis. *Am Ind Hyg Assoc J.* 55, (1994). <https://doi.org/10.1080/15428119491018682>
19. Bae, J. hun, Do, S. bin, Cho, S. ho, Lee, K. min, Lee, S.E., Kim, T.O.: TiO₂ treatment using ultrasonication for bubble cavitation generation and efficiency assessment of a dye-sensitized solar cell. *Ultrason Sonochem.* 83, (2022). <https://doi.org/10.1016/J.ULTSONCH.2022.105933>
20. Pan, X., Yang, M.Q., Fu, X., Zhang, N., Xu, Y.J.: Defective TiO₂ with oxygen vacancies: synthesis, properties and photocatalytic applications. *Nanoscale.* 5, 3601–3614 (2013). <https://doi.org/10.1039/C3NR00476G>
21. Çalışkan, B., Şayan, E.: A brief overview of the effects of ultrasound on the adsorption/desorption process: a review. *Int J Environ Anal Chem.* (2022). <https://doi.org/10.1080/03067319.2022.2093641>
22. Xiong, L. Bin, Li, J.L., Yang, B., Yu, Y.: Ti³⁺ in the surface of titanium dioxide: Generation, properties and photocatalytic application. *J Nanomater.* 2012, (2012). <https://doi.org/10.1155/2012/831524>
23. Xu, Y., Wu, S., Wan, P., Sun, J., Hood, Z.D.: Introducing Ti³⁺ defects based on lattice distortion for enhanced visible light photoreactivity in TiO₂ microspheres. *RSC Adv.* 7, 32461–32467 (2017). <https://doi.org/10.1039/C7RA04885H>
24. Oppong, S.O.B., Opoku, F., Govender, P.P.: Remarkable Enhancement of Eu-TiO₂-GO Composite for Photodegradation of Indigo Carmine: A Design Method Based on Computational and Experimental Perspectives. *Catal Letters.* 151, 1111–1126 (2021). <https://doi.org/10.1007/S10562-020-03386-7>

25. Zhang, M., Sun, H., Chen, X., Zhou, H., Xiong, L., Chen, W., Chen, Z., Bao, Z., Wu, Y.: The influences of graphene oxide (GO) and plasmonic Ag nanoparticles modification on the SERS sensing performance of TiO₂ nanosheet arrays. *J Alloys Compd.* 864, 158189 (2021). <https://doi.org/10.1016/J.JALLCOM.2020.158189>
26. Athithya, S., Manikandan, V.S., Harish, S.K., Silambarasan, K., Gopalakrishnan, S., Ikeda, H., Navaneethan, M., Archana, J.: Plasmon Effect of Ag Nanoparticles on TiO₂/rGO Nanostructures for Enhanced Energy Harvesting and Environmental Remediation. *Nanomaterials.* 13, 65 (2023). <https://doi.org/10.3390/NANO13010065/S1>
27. Bak, S.J., Kim, S.I., Lim, S.Y., Kim, T., Kwon, S.H., Lee, D.H.: Small reduced graphene oxides for highly efficient oxygen reduction catalysts. *Int J Mol Sci.* 22, (2021). <https://doi.org/10.3390/IJMS222212300/S1>
28. Kudin, K.N., Ozbas, B., Schniepp, H.C., Prud'homme, R.K., Aksay, I.A., Car, R.: Raman spectra of graphite oxide and functionalized graphene sheets. *Nano Lett.* 8, 36–41 (2008). <https://doi.org/10.1021/NL071822Y>
29. Young Lee, A., Ae Hwangbo, S., Seok Jeong, M., Geol Lee, T.: Eco-friendly sonochemical reduction of graphene oxide in water using TiO₂ photocatalyst activated by sonoluminescence. *Appl Surf Sci.* 605, 154820 (2022). <https://doi.org/10.1016/J.APSUSC.2022.154820>
30. Veluswamy, P., Sathiyamoorthy, S., Santhoshkumar, P., Karunakaran, G., Lee, C.W., Kuznetsov, D., Kadarkaraihangam, J., Ikeda, H.: Sono-synthesis approach of reduced graphene oxide for ammonia vapour detection at room temperature. *Ultrason Sonochem.* 48, 555–566 (2018). <https://doi.org/10.1016/J.ULTSONCH.2018.07.012>
31. Krishnamoorthy, K., Kim, G.S., Kim, S.J.: Graphene nanosheets: Ultrasound assisted synthesis and characterization. *Ultrason Sonochem.* 20, 644–649 (2013). <https://doi.org/10.1016/J.ULTSONCH.2012.09.007>
32. Zhang, R., Wang, Y., Ma, D., Ahmed, S., Qin, W., Liu, Y.: Effects of ultrasonication duration and graphene oxide and nano-zinc oxide contents on the properties of polyvinyl alcohol nanocomposites. *Ultrason Sonochem.* 59, 104731 (2019). <https://doi.org/10.1016/J.ULTSONCH.2019.104731>
33. Al-Oubidy, E.A., Kadhim, F.J.: Photocatalytic activity of anatase titanium dioxide nanostructures prepared by reactive magnetron sputtering technique. *Opt Quantum Electron.* 51, 1–11 (2019). <https://doi.org/10.1007/S11082-018-1738-Z>
34. Umrao, S., Abraham, S., Theil, F., Pandey, S., Ciobota, V., Shukla, P.K., Rupp, C.J., Chakraborty, S., Ahuja, R., Popp, J., Dietzek, B., Srivastava, A.: A possible mechanism for the emergence of an additional band gap due to a Ti–O–C bond in the TiO₂–graphene hybrid system for enhanced photodegradation of methylene blue under visible light. *RSC Adv.* 4, 59890–59901 (2014). <https://doi.org/10.1039/C4RA10572A>
35. Ojha, A., Thareja, P.: Graphene-based nanostructures for enhanced photocatalytic degradation of industrial dyes. *Emergent Mater.* 3, 169–180 (2020). <https://doi.org/10.1007/S42247-020-00081-6>
36. Kassiba, A., Hrabanski, R., Bonhomme, D., Hader, A.: Electron paramagnetic resonance investigations of MgSiF₆·6H₂O:Mn²⁺ single crystals. *Journal of Physics: Condensed Matter.* 7, 3339 (1995). <https://doi.org/10.1088/0953-8984/7/17/016>
37. Bertrand, P.: Electron Paramagnetic Resonance Spectroscopy: Fundamentals. *Electron Paramagnetic Resonance Spectroscopy: Fundamentals.* 1–422 (2020). <https://doi.org/10.1007/978-3-030-39663-3>
38. Eqra, R., Moghim, M.H., Eqra, N.: A study on the mechanical properties of graphene oxide/epoxy nanocomposites. *Polymers and Polymer Composites.* 29, S556–S564 (2021). <https://doi.org/10.1177/09673911211011150>
39. Zhou, S., Bongiorno, A.: Origin of the Chemical and Kinetic Stability of Graphene Oxide. *Scientific Reports* 2013 3:1. 3, 1–7 (2013). <https://doi.org/10.1038/srep02484>
40. Tenailleau, C., Kassiba, A., Lacorre, P.: EPR investigations of oxidation effects in (V_{1-x}Mo_x)₂-δO₃. *Journal of Physics and Chemistry of Solids.* 65, 1809–1815 (2004). <https://doi.org/10.1016/J.JPCS.2004.05.007>
41. Zhang, X., Li, G., Li, Q., Shaikh, M.S., Li, Z.: NC-ND license The pure paramagnetism in graphene oxide. *Physics (College Park Md).* 26, 104407 (2021). <https://doi.org/10.1016/j.rinp.2021.104407>
42. Sinha, A., Ali, A., Thakur, A.D.: Ferromagnetism in graphene oxide. *Mater Today Proc.* 46, 6230–6233 (2021). <https://doi.org/10.1016/J.MATPR.2020.04.771>
43. Liu, Y., Tang, N., Wan, X., Feng, Q., Li, M., Xu, Q., Liu, F., Du, Y.: Realization of ferromagnetic graphene oxide with high magnetization by doping graphene oxide with nitrogen. <https://doi.org/10.1038/srep02566>
44. Vozmediano, M.A.H., López-Sancho, M.P., Stauber, T., Guinea, F.: Local defects and ferromagnetism in graphene layers. *Phys Rev B Condens Matter Mater Phys.* 72, 155121 (2005). <https://doi.org/10.1103/PHYSREVB.72.155121>

45. Ramakrishna Matte, H.S.S., Subrahmanyam, K.S., Rao, C.N.R.: Novel magnetic properties of graphene: Presence of both ferromagnetic and antiferromagnetic features and other aspects. *Journal of Physical Chemistry C*. 113, (2009). <https://doi.org/10.1021/jp903397u>
46. Yazyev, O. V., Helm, L.: Defect-induced magnetism in graphene. *Phys Rev B Condens Matter Mater Phys*. 75, 125408 (2007). <https://doi.org/10.1103/PHYSREVB.75.125408>
47. Semenov, Y.G., Zavada, J.M., Kim, K.W.: Weak ferromagnetism of antiferromagnetic domains in graphene with defects. *Phys Rev B Condens Matter Mater Phys*. 84, 165435 (2011). <https://doi.org/10.1103/PHYSREVB.84.165435>
48. Sompech, S., Srion, A., Nuntiya, A.: The Effect of Ultrasonic Treatment on the Particle Size and Specific Surface Area of LaCoO₃. *Procedia Eng*. 32, 1012–1018 (2012). <https://doi.org/10.1016/J.PROENG.2012.02.047>
49. Franco, F., Pérez-Maqueda, L.A., Pérez-Rodríguez, J.L.: The effect of ultrasound on the particle size and structural disorder of a well-ordered kaolinite. *J Colloid Interface Sci*. 274, 107–117 (2004). <https://doi.org/10.1016/j.jcis.2003.12.003>
50. Wang, S., Zhang, Y., Abidi, N., Cabrales, L.: Wettability and surface free energy of graphene films. *Langmuir*. 25, 11078–11081 (2009). <https://doi.org/10.1021/LA901402F>
51. da Silva, A.L., Hotza, D., Castro, R.H.R.: Surface energy effects on the stability of anatase and rutile nanocrystals: A predictive diagram for Nb₂O₅-doped-TiO₂. *Appl Surf Sci*. 393, 103–109 (2017). <https://doi.org/10.1016/J.APSUSC.2016.09.126>
52. Poplavko, Y.: Broadband dielectric spectroscopy. In: *Dielectric Spectroscopy of Electronic Materials* (2021)
53. Sinha, S., Chatterjee, S.K., Ghosh, J., Meikap, A.K.: Analysis of the Dielectric Relaxation and AC Conductivity Behavior of Polyvinyl Alcohol-Cadmium Selenide Nanocomposite Films. <https://doi.org/10.1002/pc.23586>

Chapter VII:

Mechanisms of dye removal on titanium oxide– graphene oxide nanostructures

Methylene blue (MB) is an organic dye that has a wide range of applications, including cotton or wool dyeing, paper dyeing, temporary hair dyeing, and others [1]. Although not very toxic, MB can have some harmful effects on humans and animals [2]. It can irritate the gastrointestinal tract and cause nausea, vomiting, and diarrhea if ingested. It can also cause dyspnea, tachycardia, cyanosis, methemoglobinemia, and convulsions when inhaled [3]. MB is commonly used as a reference compound in the study of adsorption and photocatalytic processes due to its well-defined chemical structure, easy detection, and known behavior under various conditions. In adsorption studies, it is used to understand the interaction between adsorbent and adsorbate [4]. In photocatalysis, it serves as a model compound for the degradation of organic pollutants under light irradiation [5, 6]. The use of MB as a reference compound allows the comparison of different catalysts and adsorbents in terms of their efficiency in degrading or adsorbing organic compounds, providing valuable information on the performance of different materials in environmental remediation processes.

In this chapter, the hybrid nanostructures previously discussed in chapters 5 and 6 have been evaluated, focusing specifically on their ability to remove MB. To this end, the mechanisms of adsorption and photocatalysis as fundamental strategies in this process will be explored in detail. The removal efficiency of the pollutant is directly related to the intrinsic properties of these nanostructures, which have been discussed in detail above. Additionally, Raman spectroscopy provided an important qualitative analysis of the investigated dyes to demonstrate the removal of MB molecules from the liquid medium after the combined adsorption-photocatalysis processes. Through this experimental investigation, significant correlations between the properties of the hybrid nanostructures and their performance in the removal of MB could be established, thus providing a deeper understanding of the applicability of these technologies in the treatment of contaminated water.

7.1. MB removal by adsorption

7.1.1. Adsorption on TiO₂

Fig. 7.1. shows the effect of MB removal on pristine TiO₂ powder before and after mechanical milling and photosonation processes, respectively. It was observed that the adsorption

equilibrium was reached after 20 min. This indicates that there was an active adsorption process during the first 20 min, and then the amount of adsorbed MB stabilized and reached an equilibrium point. This behavior is common in adsorption processes where there is an initial rapid adsorption of solutes followed by a slower phase that eventually reaches saturation [7]. At the same time, an adsorption of $\approx 20.2\%$ was reached after 40 min. Similar behavior was observed for sonicated TiO_2 , which showed a removal of $\approx 22.2\%$ at the same time and conditions. The slight increase in the percentage removal suggests that sonication had a positive effect on the adsorption capacity of TiO_2 . This is attributed to the separation of agglomerates and the creation of smaller, more dispersed particles, resulting in a higher specific surface area and more active sites available for adsorption. However, the surface changes are not sufficient to produce a significant effect.

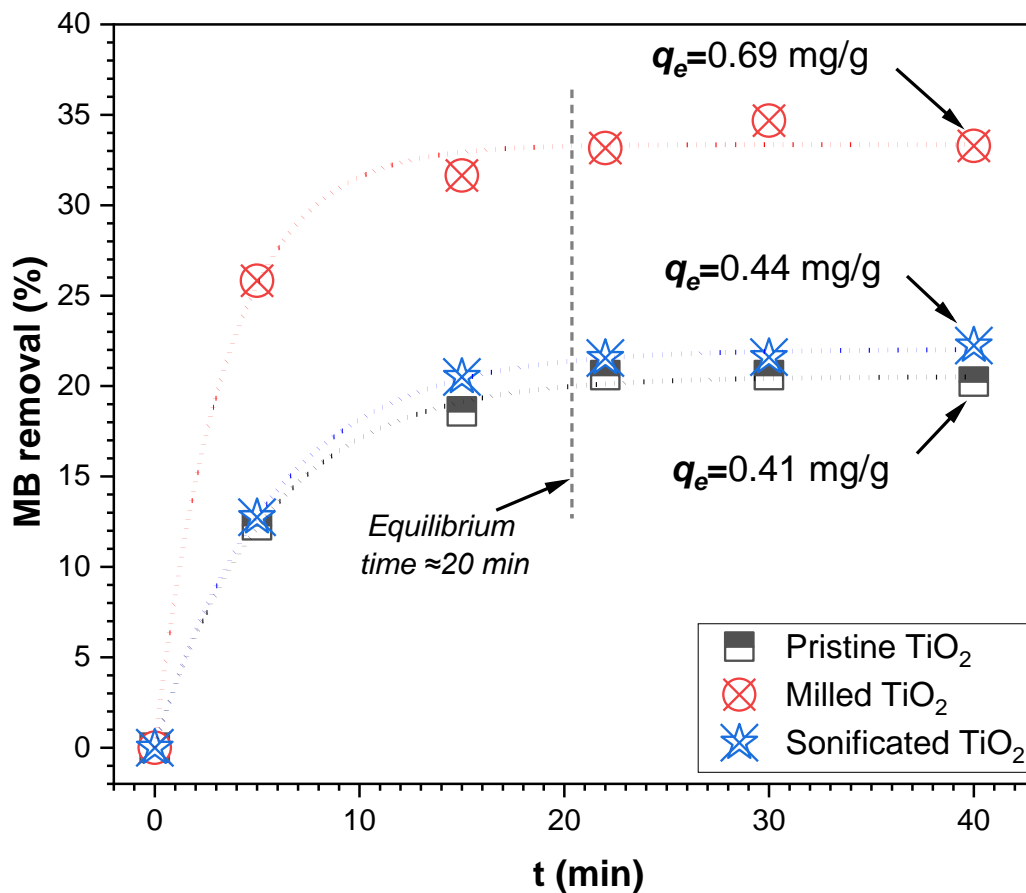


Fig. 7.1. MB adsorption of TiO_2 before and after ball-milling and photosonation processes

On the contrary, for milled TiO_2 , its adsorption is increased to $\approx 33.2\%$ after the same time, demonstrating that the process has a substantial influence on the material's ability to adsorb. The adsorption process is mainly controlled by the interactions between the adsorbate and the adsorbent surface. Previous studies on the adsorption capacity of TiO_2 nanoparticles have shown that the adsorption of MB dye depends on the importance and nature of the surfaces as well as the defects involved. Therefore, the improved adsorption efficiency of milled TiO_2 is attributed to the defects created on the surface, as well as the increased surface area demonstrated by BET in Chapter 5. Some authors have attributed the adsorption mechanism

of TiO₂ to its surface being positively charged so that the adsorption of MB molecules preferentially occurs by chemisorption through interactions between Ti-OH and MB molecules [8, 9]. However, there is no correlation between the type of interaction (electrostatic, Van der Waals, hydrophobic, π - π stacking, hydrogen bonding) and the adsorbent [10, 11].

7.1.2. Adsorption on TiO₂-GO mechano-synthesized nanostructures

7.1.2.1. Effect of contact time and oxidation degree

Fig. 7.2.a. shows the adsorption of MB over 40 minutes on the TiO₂-GO hybrid nanostructures fabricated by ball-milling. Adsorption equilibrium was reached after 9 min in all cases. It was found that, in general, the percentage removal was significantly higher compared to that achieved by pristine TiO₂ or even milled TiO₂. This indicates that the simple incorporation of GO significantly improves the adsorption capacity of the hybrid nanostructures. By comparing the efficiency between nanostructures, it was observed that the maximum removal of 100% was reached for TG_(0.5) and TG₍₁₎, while lower efficiencies of \approx 84%, \approx 81%, and \approx 67% were shown for TG₍₃₎, TG₍₆₎ and TG₍₁₀₎, respectively.

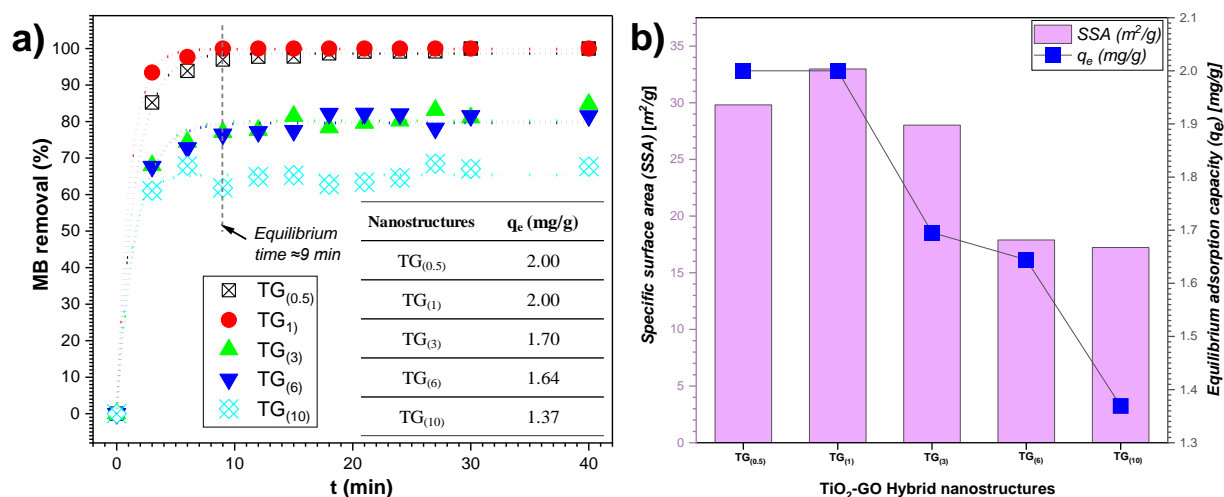


Fig. 7.2. (a) Effect of contact time of mechano-synthesized TiO₂-GO nanostructures (b) adsorption capacity and SSA

It was highlighted that the best removal results were obtained with nanostructures containing less oxidized GOs. This is in contrast to reports in the literature, where the adsorption efficiency of MB dyes is related to higher oxidation degrees [12]. In this context, the trend is mainly related to the specific surface area (SSA) discussed in Chapter 5. It was found that all GOs, regardless of the oxidation degree, underwent additional exfoliation and defect formation due to mechanical milling. However, the more oxidized GOs have a more negative surface charge due to the presence of more functional groups, which hinders their dispersion and favors agglomeration. Therefore, the more oxidized nanostructures have less surface area available for chemical adsorption. This is confirmed in Fig. 7.2.b. where a clear relationship between adsorption capacity (q_e) and surface area is observed. It is shown that the

higher the surface area (SSA), the higher the adsorption of MB [13, 14], which would explain why TG₍₁₎ reaches maximum removal in a shorter time (≈ 9 min) than TG_(0.5) (≈ 27 min).

7.1.2.2. Kinetic Study

The time evolution of the MB dye adsorption process did not follow a first-order kinetic law. Indeed, the plots of the logarithmic variation with time show dispersed curves and no valuable conclusion may be deduced on the adsorption process. Thus, an alternative model used in a chemisorption process is worthy of interest for the present kinetics and is discussed below. It consists of the pseudo-second-order model proposed by Ho *et al* [15] which can be used to analyze the kinetics of the process involved in chemisorption reactions and to estimate the equilibrium load and the characteristic time constants for the diffusion process. This model uses a linearized integral form in the following way:

$$\frac{t}{q_t} = \frac{1}{k_2 q_e^2} + \frac{1}{q_e} t \quad (\text{eq. 12})$$

Where k_2 and q_e were determined from the intersection and slope of the plot of $[t/q_t]$ vs t [16] as shown in Fig. 7.3.

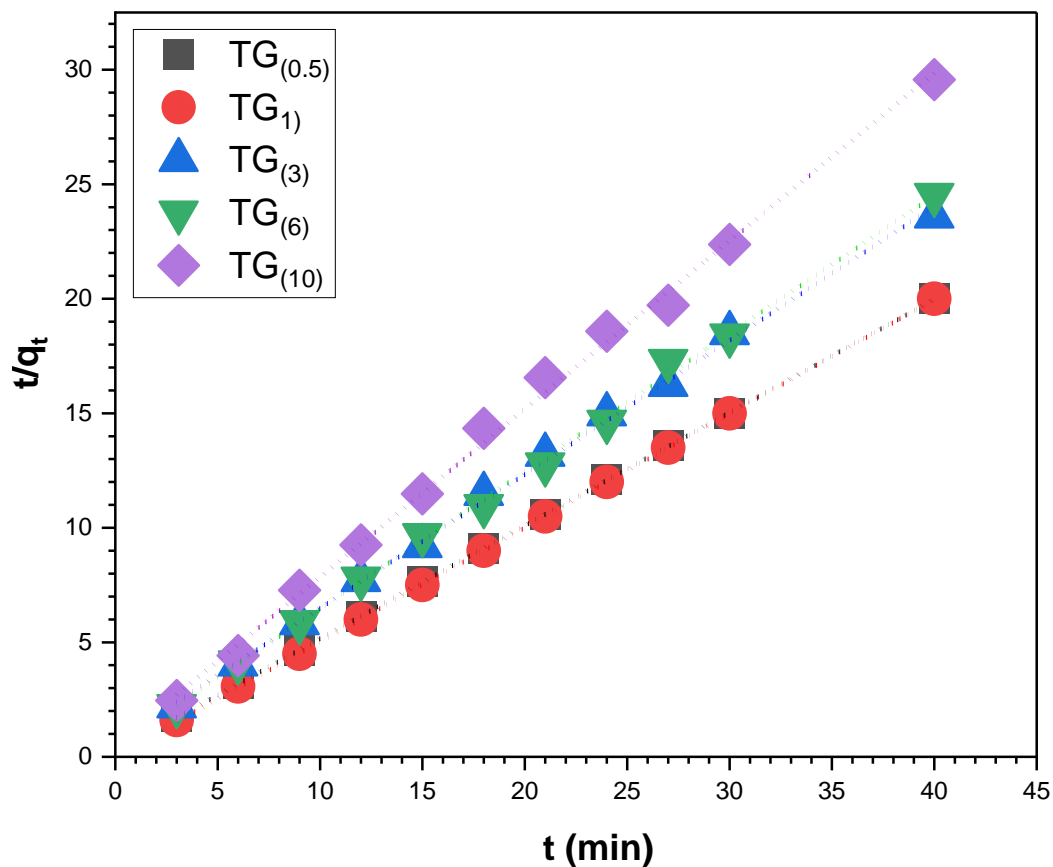


Fig. 7.3. Kinetic study of pseudo-second order of TiO₂-GO nanostructures by ball-milling.

Comparative estimation of q_e from experiments and fitting the curve makes us confident in the relevance and applicability of the second-order model for the kinetics of the MB adsorption process on TiO₂-GO nanostructures by ball-milling. Table 7.1. shows the kinetics calculated values. It was observed that the k_2 constant is higher for TG₍₁₎ compared to TG_(0.5). This would justify that although both materials have the same adsorption capacity, TG₍₁₎ reaches its maximum capacity in less time (≈ 9 min).

Table 7.1. The kinetic parameters for the adsorption by TiO₂-GO nanostructures by ball-milling

Nanostructures	q_e (mg/g) (experimental)	Adsorption Kinetics Pseudo-second order		
		k_2 (min ⁻¹)	q_e (mg/g) (calculated)	R^2
TG _(0.5)	2.0000	1.0289	2.0255	0.99997
TG ₍₁₎	2.0000	4.5685	2.0082	0.99997
TG ₍₃₎	1.6955	0.5292	1.7102	0.99839
TG ₍₆₎	1.6445	0.8233	1.6615	0.99847
TG ₍₁₀₎	1.3693	1.0499	1.3631	0.99728

7.1.2.3. A mechanistic model for dye diffusion

To identify the mechanisms behind the adsorption process, the time evolution curves of the adsorption of the dye in TiO₂-GOs hybrid nanostructures were analyzed using diffusion models based on the movement of adsorbate within the surrounding media. Two main processes are considered and consist of "film diffusion" and "intraparticle diffusion" processes. The first mechanism considers the MB dye diffusion from the solution phase to the outer particle surfaces of the adsorbent and disperses on it while in the second process, the dye molecules diffuse across the boundary layer and diffuse inside the open pores of the adsorbent material. Various models are presented below to analyze the processes of molecular diffusion and adsorption. These models are intended to provide insight into the problem of how MB dyes in solution are affected by the specific molar ratio of the nanostructures.

According to Lacin *et al* [17], the equation below was used to describe the intra-particle diffusion model:

$$q_t = k_{id}t^{1/2} + C \quad (\text{eq. 13})$$

Where k_{id} (mg/g.min^{1/2}) is the intra-particle diffusion rate constant obtained from the plot as also the constant C (mg/g) deduced from the intercept of the plotted graph q_t vs $t^{1/2}$. When the q_t graph passes through the origin (*i.e.*, $C = 0$), intra-particle diffusion is the rate-controlling step, and the diffusion in the film is negligible. However, if the straight line does not intersect the origin (*i.e.* $C \neq 0$), there is a discrepancy in the mass transfer rates between the initial and

final stages of adsorption. Both can be considered rate-controlling steps [18]. According to this model, the mechanism of dye adsorption is proposed in several stages. The first step consists of the diffusion of MB molecules (adsorbate) in the liquid film surrounding the adsorbent nanostructure particles (*film diffusion*). The second step consists of the diffusion of the adsorbate inside the particle pores or dispersed on the surface (*intra-particle diffusion*). The third step consists of the adsorption of MB adsorbate on the pore or the particle surfaces (*adsorption or surface reaction*) [19] (Fig. 7.4.).

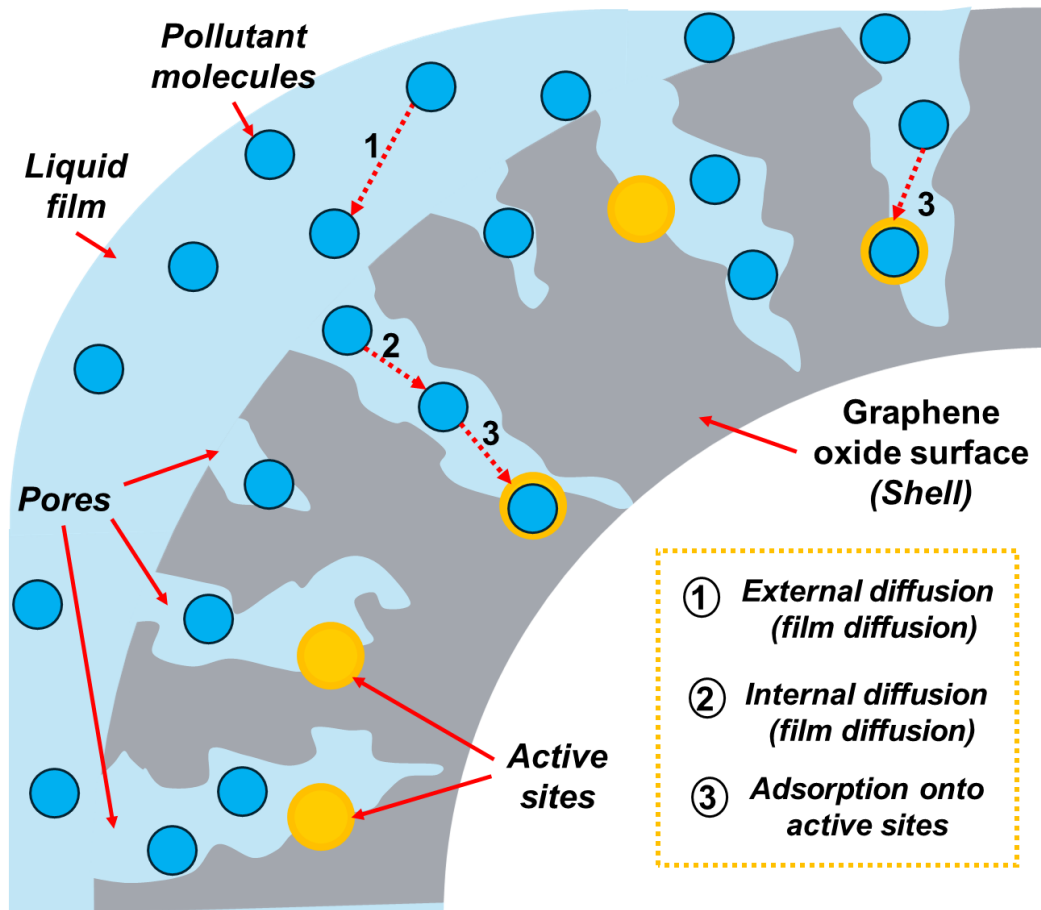


Fig. 7.4. Adsorption kinetics mass transfer processes.

The carried-out experiments account for $C=0$ and then the intra-diffusion mechanism proceeds through MB migration to the outer surface of the adsorbent followed by diffusion within the pore cavity [20]. Fig. 7.5. shows plots of q_t vs $t^{1/2}$ for the different TiO_2 -GOs nanostructures. The plots have a three-phase structure as three different slopes are required to accurately refine the data. Three behaviors may be pointed out for the adsorption process with the features of external diffusion, intra-particle diffusion, and adsorption equilibrium. A linearized form of the model was applied for each of the time evolution steps [21]. The first step with the large slope (k_{p1}) represents the rapid adsorption process of the dyes being transferred to the surface of the material [22] within the first period of about 3 minutes. The second stage of time variation with the characteristic slope k_{p2} is smoother and reflects the process by which MB molecules slowly diffuse and adsorb into the pores. The third stage characterized by the flat slope k_{p3} is attributed to the equilibrium adsorption process where the

adsorbate diffuses very slowly into the micropores because of the low concentration of dyes that remains in the solution [23].

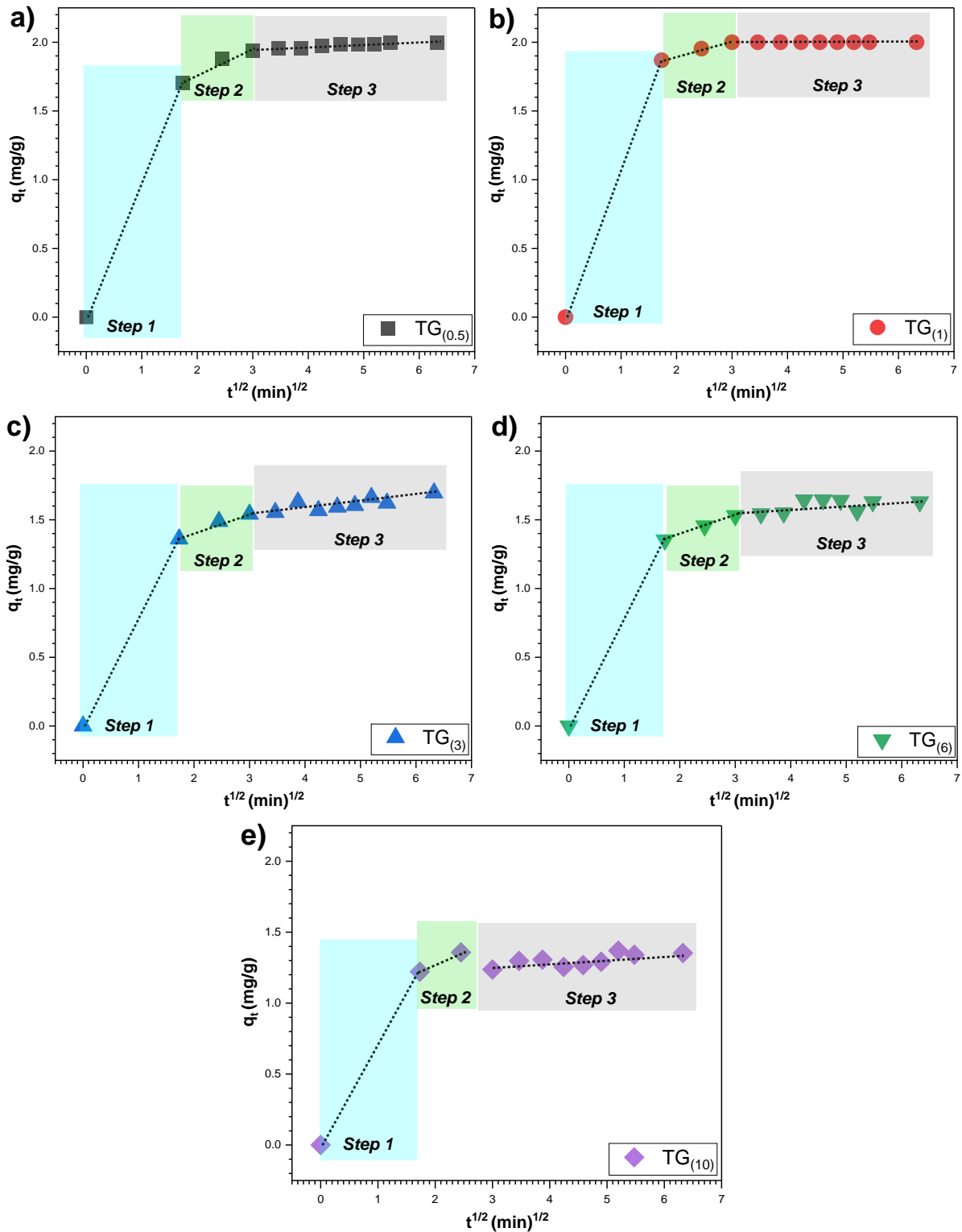


Fig. 7.5. Intraparticle diffusion kinetics of MB of TiO₂-GO nanostructures by ball-milling: (a) TG_(0.5), (b) TG₍₁₎, (c) TG₍₃₎, (d) TG₍₆₎, (e) TG₍₁₀₎.

Table 7.2. shows the fitted parameters in the frame of the intra-particle diffusion model during the different stages of the adsorption process. The values of K_{id} are higher in the external adsorption phase and decrease for the other two phases of adsorption ($k_{p1} > k_{p2} > k_{p3}$). The adsorption kinetics data of MB adsorption by the nanostructures fit quite well with the intraparticle diffusion model and then a relevant insight was obtained into the mechanisms behind the adsorption phenomenon [24].

Table 7.2. Intra-particle diffusion for the adsorption by TiO₂-GO nanostructures

Materials	Adsorption Kinetics					
	k_{p1} (mg/g.min ^{1/2})	R^2	k_{p2} (mg/g.min ^{1/2})	R^2	k_{p3} (mg/g.min ^{1/2})	R^2
TG _(0.5)	0.9841	1	0.6367	0.9743	0.3924	0.9708
TG ₍₁₎	1.0788	1	0.6561	0.9659	0.4071	0.9887
TG ₍₃₎	0.7854	1	0.5055	0.9738	0.3295	0.9744
TG ₍₆₎	0.7813	1	0.5001	0.9735	0.3276	0.9722
TG ₍₁₀₎	0.7051	1	0.4270	0.9564	0.2675	0.9740

7.1.2.4. Adsorption isotherms

Adsorption equilibrium occurs when the amount of solute adsorbed on the adsorbent is equal to the amount desorbed. The equilibrium adsorption isotherms were represented by the solid phase concentration (q_e) versus the liquid phase concentration (C_e) of the solute. Adsorption isotherms provide valuable information about the adsorption capacity of the adsorbent, the interactions between solute molecules and the extent to which the adsorbate accumulates on the surface of the adsorbent. In this study, two usual adsorption isotherm models, *i.e.*, Freundlich and Langmuir's equations were used to determine the equilibrium adsorption isotherm of MB dyes adsorbed on TiO₂-GO nanostructures. R^2 correlation coefficients are used to evaluate the applicability of the isotherm equation. The most important multi-site or multilayer adsorption isotherm for a heterogeneous surface is the Freundlich isotherm, where the heterogeneity factor $1/n$ defined by the equation [25]:

$$q_e = K_F C_e^{\frac{1}{n}} \quad (\text{eq. 14})$$

Where $1/n$ and K_F are the Freundlich constants for adsorption intensity and adsorption capacity, respectively. The values of K_F and n were calculated from the intercept and slope of the plots of $\log(q_e)$ versus $\log(C_e)$ (Fig. 7.6.). If the value of n is greater than one, this indicates good adsorption of MB on the adsorbent and for $1 < n < 10$, the sorption process is likely to be successful [26]. The values in Table 7.3. reveal that most of the considered TiO₂-GO composites lead to n values larger than one indicating then the good adsorption of dyes.

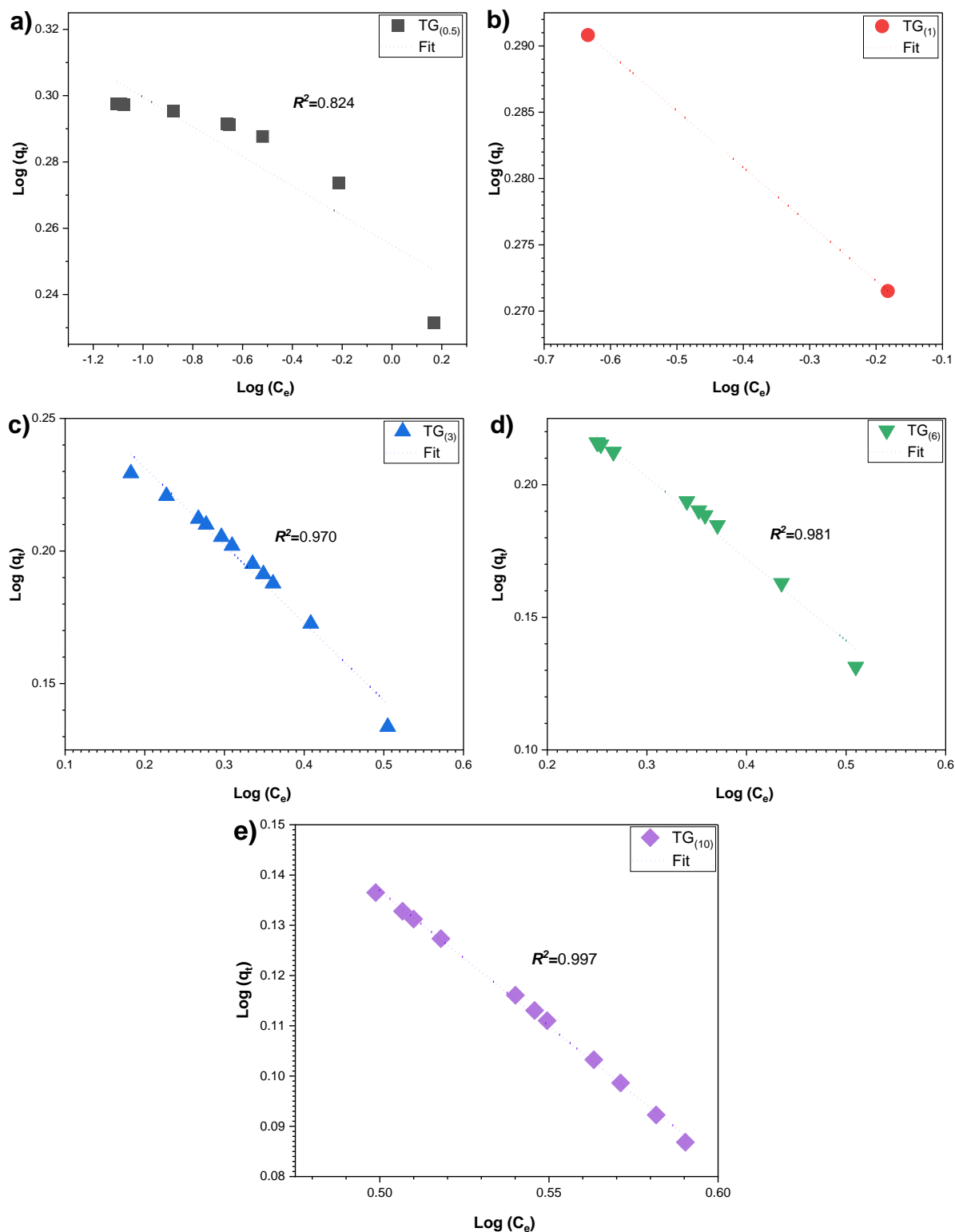


Fig. 7.6. Adsorption Freundlich isotherm study of TiO₂-GO nanostructures by ball-milling: (a) TG_(0.5), (b) TG₍₁₎, (c) TG₍₃₎, (d) TG₍₆₎, (e) TG₍₁₀₎.

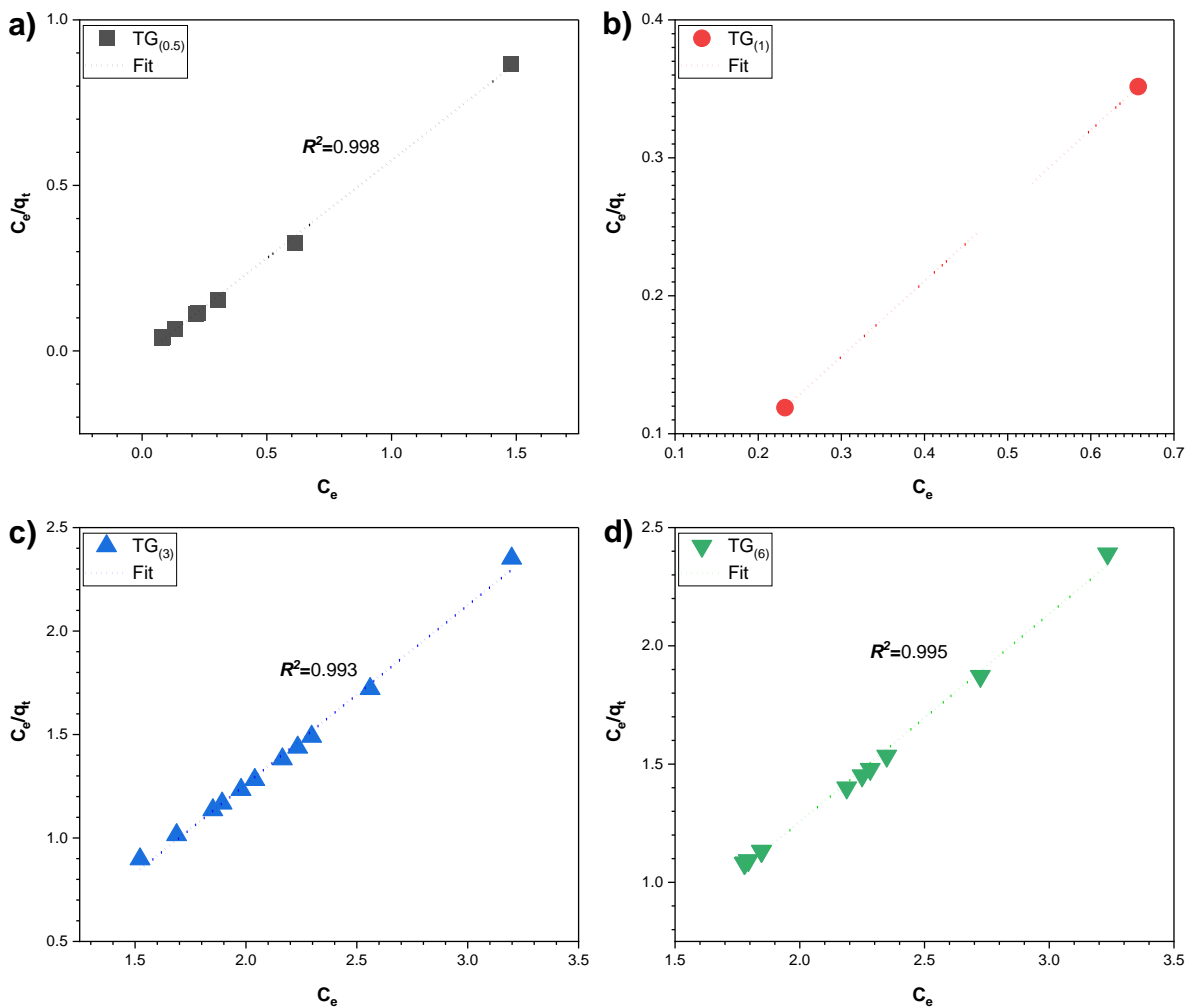
Alternatively, the Langmuir isotherm is a relevant model for adsorption in a monolayer on a completely homogeneous surface with a finite number of identical and specific adsorption sites and with negligible interaction between molecules. The Langmuir equation is presented in its linear form as [27]:

$$\frac{C_e}{q_e} = \frac{1}{q_m} C_e + \frac{1}{K_L q_m} \quad (\text{eq. 15})$$

Where q_e is the quantity of dyes that have been adsorbed at equilibrium (mg/g), C_e is the equilibrium concentration of the dyes in solution (mg/L), q_m is the maximum amount of adsorbate that can be adsorbed (mg/g). K_L refers to the Langmuir isotherm constants measured (L/mg). K_L and q_m can be determined from the slope and intercept of the graph between C_e/q_e and C_e [28]. The Langmuir isotherm is described in terms of the dimensionless constant (R_L), that is computed using the following equation:

$$R_L = \frac{1}{(1+q_m K_L)} \quad (\text{eq. 16})$$

According to the value of the separation factor, R_L of the Langmuir model, the adsorption process can be expressed as favorable ($0 < R_L < 1$), unfavorable ($R_L > 1$), linear ($R_L = 1$), and irreversible ($R_L = 0$) [29]. According to the experimental results in Fig. 7.7. and the data summary in Table 7.3., R_L indicates favorable adsorption for the TiO₂-GO nanostructures since the condition $0 < R_L < 1$ is satisfied.



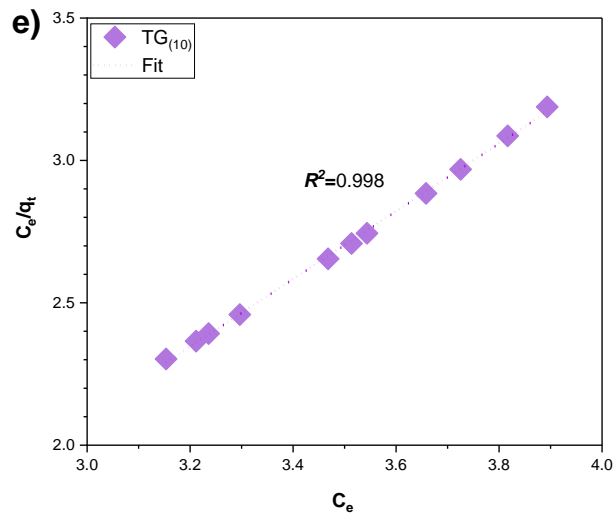


Fig. 7.7. Adsorption Langmuir isotherm study of TiO₂-GO nanostructures by ball-milling: (a) TG_(0.5), (b) TG₍₁₎, (c) TG₍₃₎, (d) TG₍₆₎, (e) TG₍₁₀₎.

A comparison of the R^2 values in Table 7.3. for the Freundlich and Langmuir models shows a marked similarity, although the values associated with the Langmuir isotherms tend to be closer to 1. The fact that the isotherms are closer to the Langmuir model than to the Freundlich model suggests that the adsorption process is more consistent with monolayer adsorption on a homogeneous surface. The Langmuir model postulates the formation of a single layer of adsorbate molecules on the adsorbent surface with no interactions between the adsorbed molecules [30, 31]. In contrast, the Freundlich model implies a heterogeneous surface with multilayer adsorption and adsorbate-adsorbate interactions. Thus, the predominance of the Langmuir isotherm suggests that the adsorption process is more uniform and fits a monolayer coverage model.

Table 7.3. Adsorption Isotherms for the adsorption of TiO₂-GO nanostructures by ball-milling

Materials	Adsorption Isotherms						
	Freundlich			Langmuir			
	K _F (mg/g)	n	R ²	q _{max} (mg/g)	K _L (L/mg)	R _L	R ²
TG _(0.5)	1.7985	22.4215	0.8249	1.7085	56.2788	0.0103	0.9990
TG ₍₁₎	1.8353	23.3645	1.0000	1.8755	1777.3333	0.0003	1.0000
TG ₍₃₎	1.9616	3.3322	0.9777	1.1477	1.8032	0.3258	0.9990
TG ₍₆₎	1.9756	3.2352	0.9837	1.1373	1.753	0.3341	0.9990
TG ₍₁₀₎	2.5504	1.8539	0.9980	0.8401	0.8135	0.5940	0.9990

7.1.3. MB adsorption on TiO₂-GO photo-sonicated nanostructures evaluation

7.1.3.1. Effect of the GO oxidation degree

Fig. 7.8. shows the effect of contact time on MB adsorption of photosonicated TiO₂-GO nanostructures during 40 min. The results showed that equilibrium was reached in about 15

min, and in all cases, the MB adsorption of the TiO₂-GO nanostructures exceeded that of pristine TiO₂. A comparison between the nanostructures consistently showed that those with higher oxidation exhibited superior adsorption capacity compared to the low oxidation variants. We attribute this relationship between oxidation and adsorption to the structural arrangement of the nanostructures and the oxidation degree of the GOs. Higher efficiency in nanostructures with higher oxidation supports the role of functional groups that increase the amount of available adsorption sites and improve the interactions between the target molecules and the surface. In addition, they exhibit a more homogeneous shell around the TiO₂ particles. While, for the less oxidized nanostructures, in addition to having GOs with fewer functional groups, the uncoated sections on the particles promote adverse effects that limit the opportunities for interaction and adsorption of the dye molecules. Sonification as a method of fabricating hybrid nanostructures, which is less aggressive and promotes fewer structural changes than ball milling, provides detailed insight into the effect of GO on MB adsorption, although total removal is not achieved.

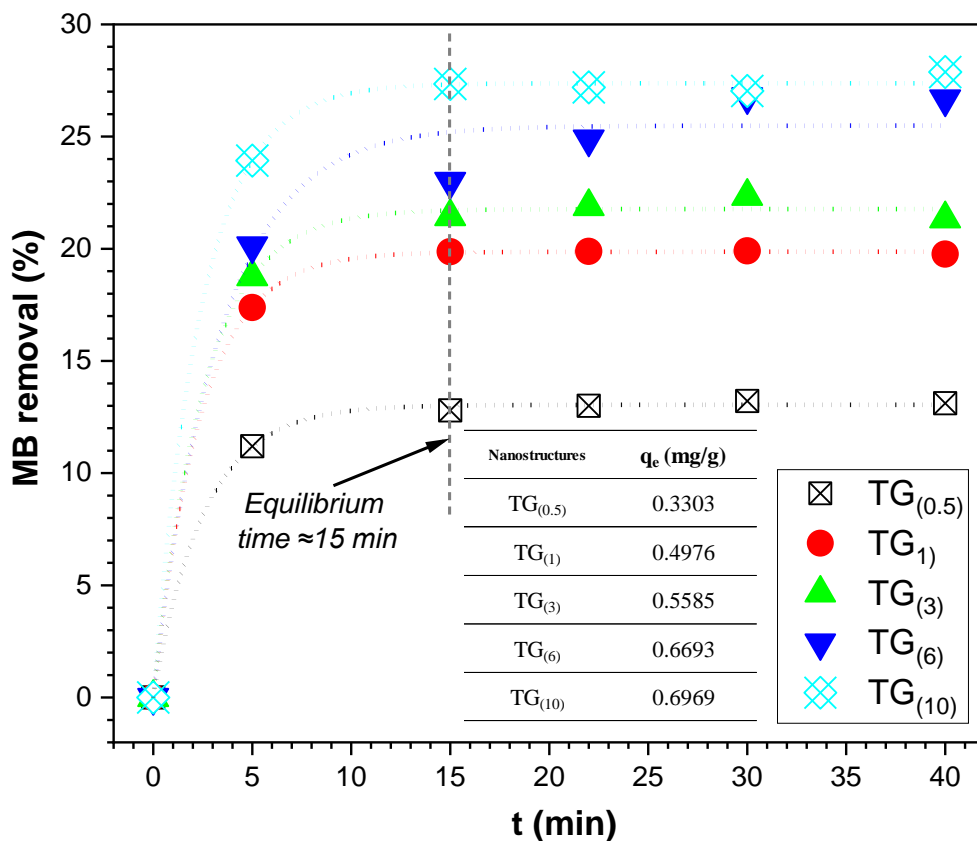


Fig. 7.8. Effect of contact time of photosonicated TiO₂-GO nanostructures.

Two fabrication methods of TiO₂-GO hybrid nanostructures by ball-milling and photosonication were investigated to evaluate their MB adsorption capacity. The results revealed significant findings, highlighting the advantage of the addition of carbonaceous materials as an effective strategy to significantly improve the adsorption capacity of TiO₂. The efficiency of the nanostructures obtained by ball milling is remarkable, achieving adsorption rates of 100%, especially in the case of TG₍₁₎, which reached this level in only ≈ 9 min. It is important to note that the influence of the oxidation degree in these nanostructures lost

relevance, attributing their high efficiency to the generation of a large surface area due to the milling process. The high adsorption capacity observed suggests that ball milling is an effective method to maximize the availability of active sites for adsorption, highlighting the importance of the surface structure in this process. Despite the high level of structural disorder associated with ball-milling, the adsorption efficiency overcomes the structural limitations. This dichotomy between enhanced adsorption capacity and more disordered structure highlights the need for a balanced approach when designing hybrid nanostructures for specific applications. In contrast, nanostructures fabricated by photosonation exhibited inferior adsorption capacity compared to those obtained by ball-milling. Although this method is less aggressive and allows for more ordered and organized structures, the adsorption capacity is affected. However, the direct relationship between the GO oxidation degrees and their efficiency in MB adsorption suggests that photosonation may offer advantages in applications where an ordered structure is critical.

7.1.3.2. Kinetic study

Fig. 7.9. shows the fits to the second-order model for the study of the adsorption kinetics of the photosonation nanostructures. The adsorption kinetics fitted a second-order model means that the adsorption rate is mainly controlled by chemical sorption or chemisorption, which is the interaction between the adsorbate and the adsorbent on the surface [7]. The pseudo-second-order kinetic model is founded on the assumption that the chemical sorption is the rate-determining step, and it reliably predicts the behavior of the adsorption process. Table 7.4. shows the kinetic parameters calculated using eq. 12 for the second-order model.

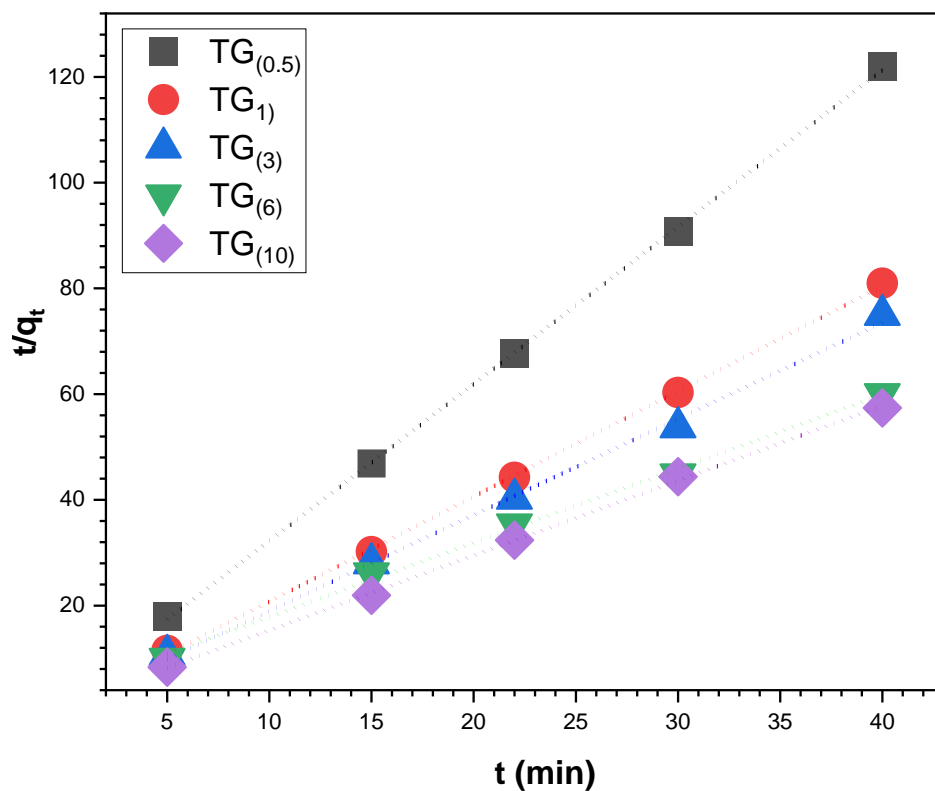


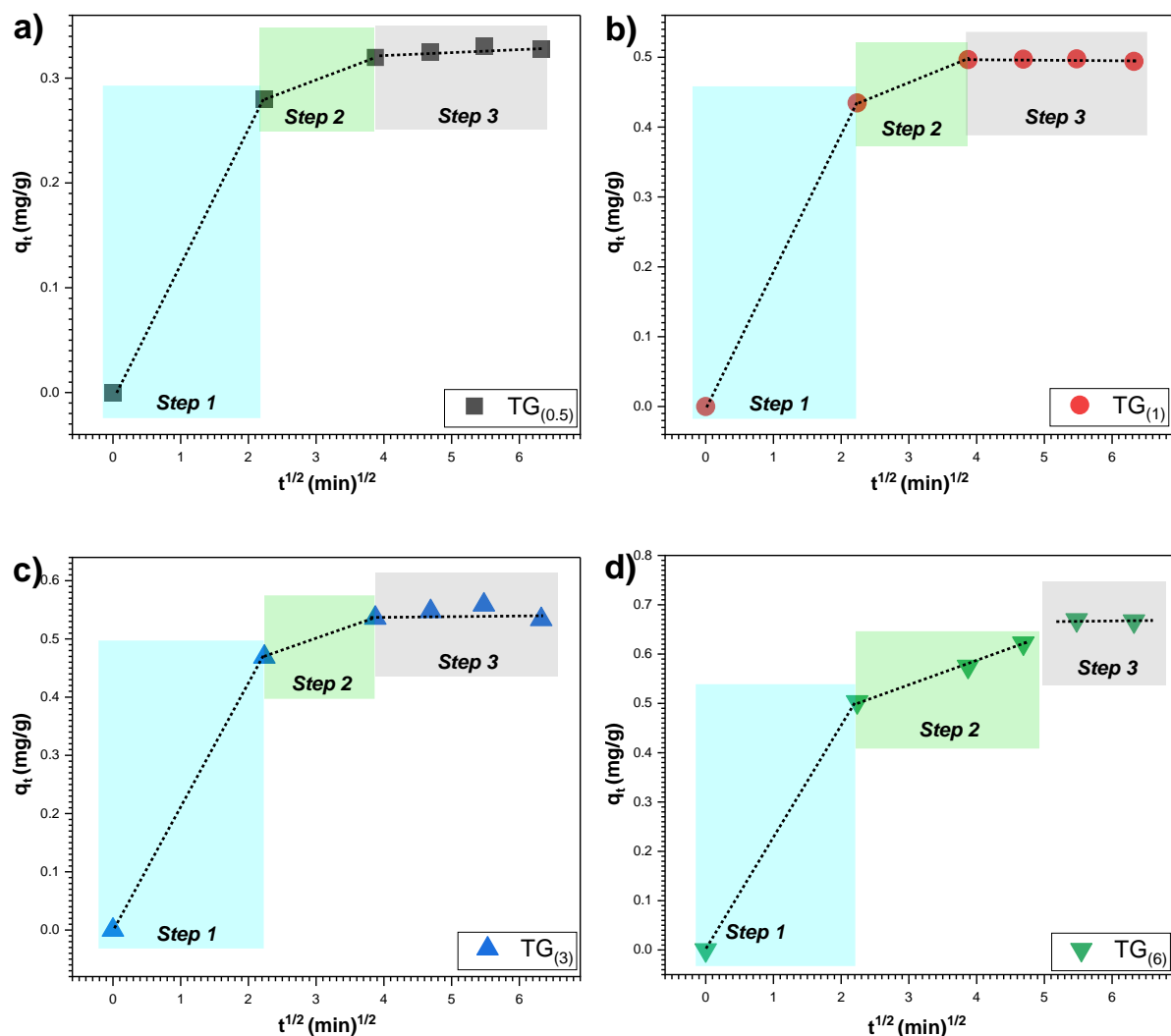
Fig. 7.9. Kinetic study of pseudo-second order of photosonicated TiO₂-GO nanostructures

Table 7.4. Second-order kinetic parameters for adsorption of photosonicated TiO₂-GO nanostructures

Material	q _e (mg/g) (experimental)	Pseudo-second order		
		k ₂ (min ⁻¹)	q _e (mg/g) (calculated)	R ²
TG _(0.5)	0.3303	3.4514	0.3368	0.9998
TG ₍₁₎	0.4976	4.3700	0.5029	0.9996
TG ₍₃₎	0.5585	4.3112	0.5498	0.9976
TG ₍₆₎	0.6693	0.5103	0.7136	0.9972
TG ₍₁₀₎	0.6969	1.7079	0.7062	0.9994

7.1.3.3. Mechanistic model for dye diffusion

Fig. 7.10 shows plots of q_t vs. $t^{1/2}$ for the different TiO₂-GOs nanostructures to evaluate the intraparticle diffusion.



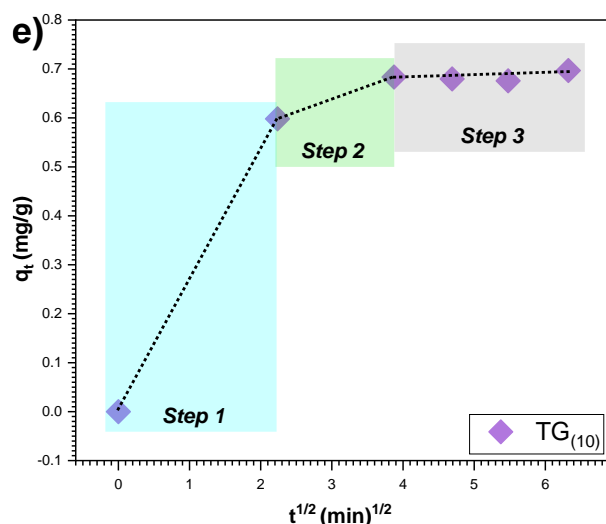


Fig. 7.10. Intraparticle diffusion of MB of TiO₂-GO nanostructures by photosonication: (a) TG_(0.5), (b) TG₍₁₎, (c) TG₍₃₎, (d) TG₍₆₎, (e) TG₍₁₀₎.

Table 7.5. shows the fitted parameters in the frame of the intra-particle diffusion model during the different stages of the adsorption process. The values of K_{id} are higher in the external adsorption phase and decrease for the other two phases of adsorption ($k_{p1} > k_{p2} > k_{p3}$). The three different slopes identified are characteristics of external diffusion, intraparticle diffusion, and adsorption equilibrium, similar to that discussed for nanostructures by ball-milling. The adsorption kinetics data of MB adsorption by the nanostructures fit quite well with the intraparticle diffusion model and then a relevant insight was obtained into the mechanisms behind the adsorption phenomenon.

Table 7.5. Intra-particle diffusion on TiO₂-GO photosonicated nanostructures

Materials	Stages of the adsorption process					
	k_{p1} (mg/g.min ^{1/2})	R^2	k_{p2} (mg/g.min ^{1/2})	R^2	k_{p3} (mg/g.min ^{1/2})	R^2
TG _(0.5)	0.1252	1	0.0932	1	0.0682	0.9438
TG ₍₁₎	0.1944	1	0.1448	1	0.1042	0.9657
TG ₍₃₎	0.2097	1	0.1562	1	0.1149	0.9673
TG ₍₆₎	0.2250	1	0.1676	1	0.1315	0.9753
TG ₍₁₀₎	0.2675	1	0.1993	1	0.1424	0.9708

7.1.3.4. Adsorption isotherms

The Freundlich isotherm model was calculated using eq. 14. Fig. 7.11. shows the values of K_F and n that were calculated from the intersection and slope of the plots of $\log(q_e)$ versus $\log(C_e)$.

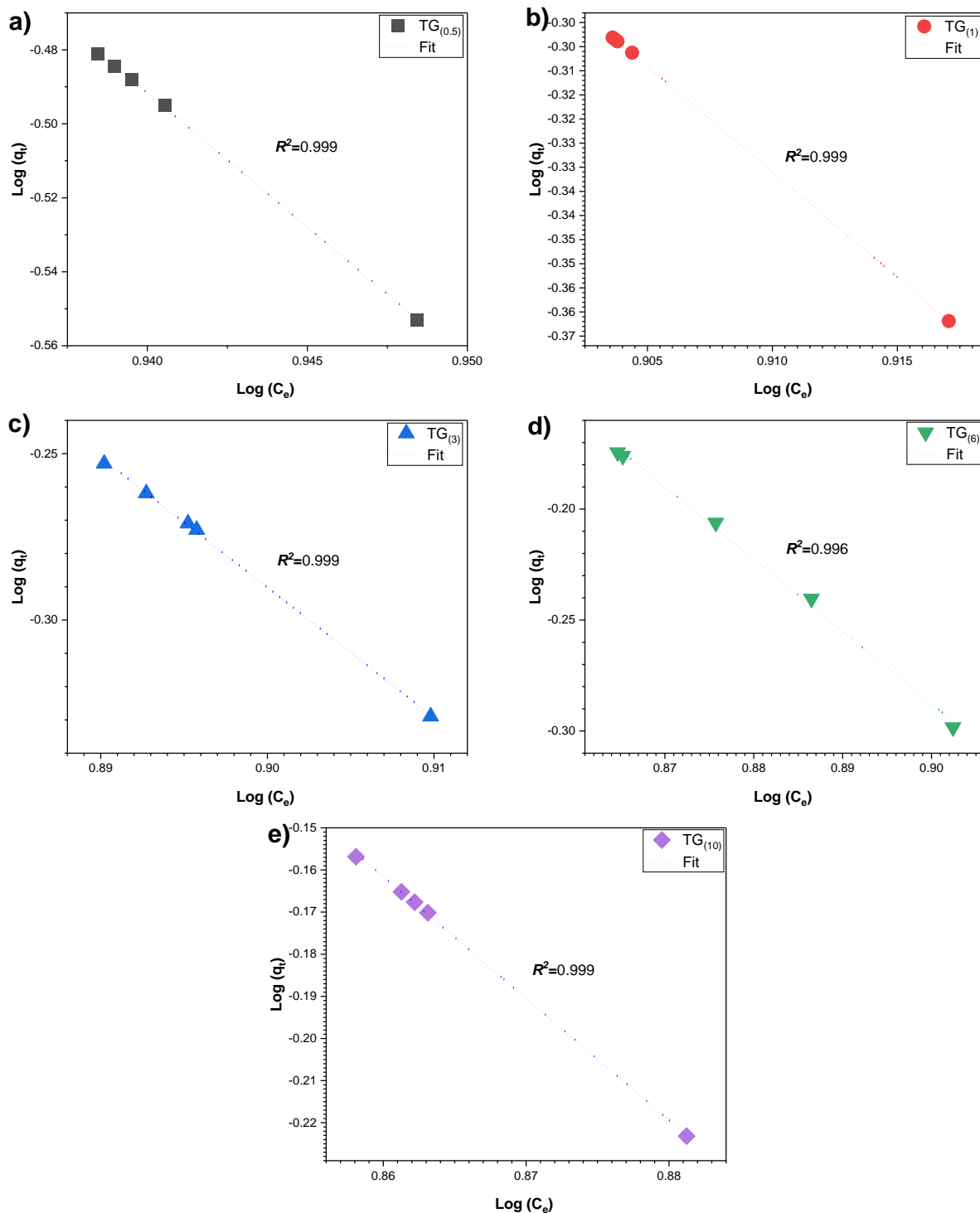


Fig. 7.11. Adsorption Freundlich isotherm of TiO₂-GO nanostructures by photosonication: (a) TG_(0.5), (b) TG₍₁₎, (c) TG₍₃₎, (d) TG₍₆₎, (e) TG₍₁₀₎.

Additionally, Fig. 7.12. shows the adsorption of Langmuir isotherms fitted using eq 15. According to the experimental results, R_L indicates favorable adsorption for the TiO₂-GO nanostructures since the condition $0 < R_L < 1$ is satisfied. Comparing the R^2 values of the Freundlich model and the Langmuir model (Table 7.6.), it may be concluded that the adsorption is quite well accounted for by both isotherms. If the isotherms fit both the Langmuir and Freundlich models, it indicates that the adsorption process involves both monolayer and

multilayer adsorption. The Langmuir model is based on the assumption of monolayer adsorption on a homogeneous surface, while the Freundlich model is based on multilayer adsorption on a heterogeneous surface. The coexistence of both models could suggest the presence of a heterogeneous surface.

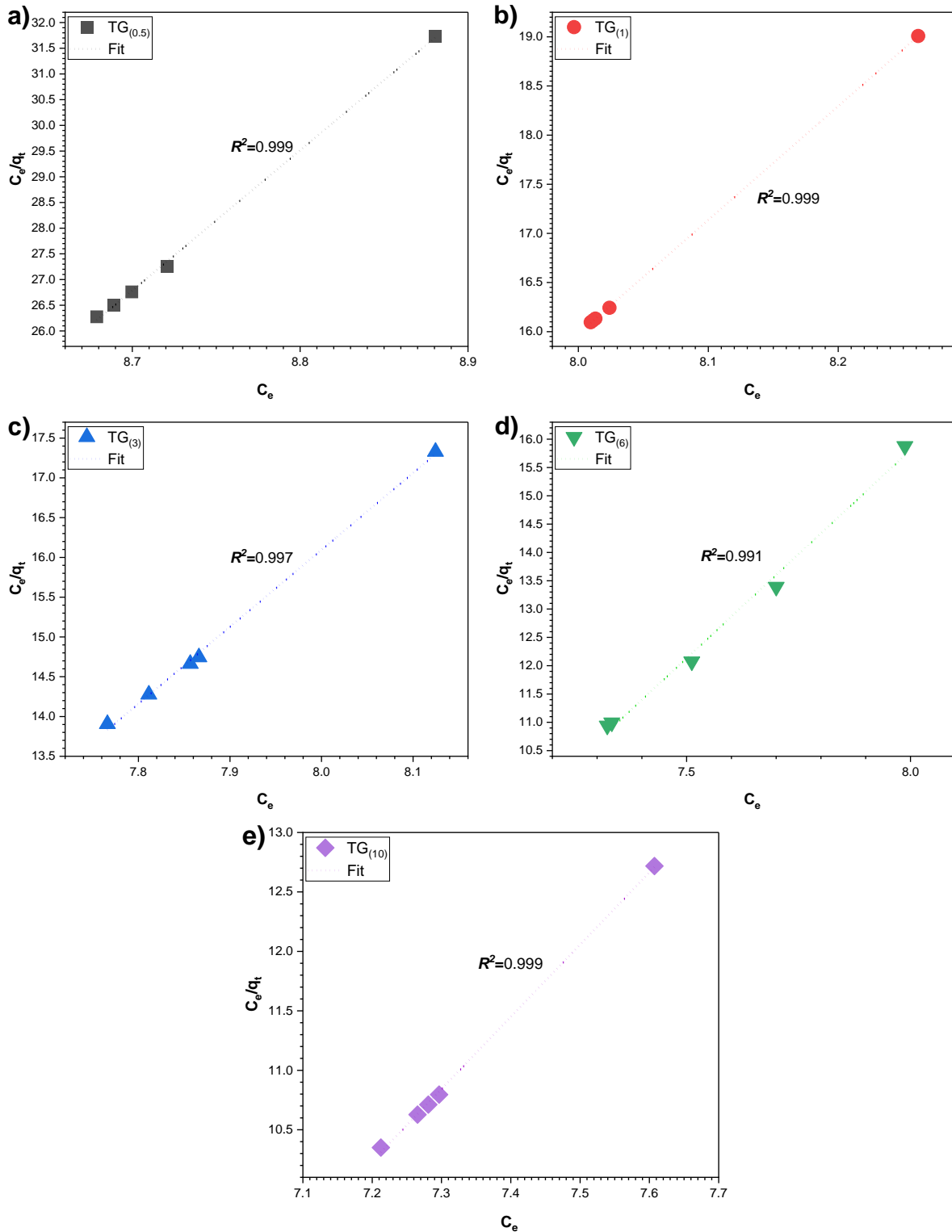


Fig. 7.12. Adsorption Langmuir isotherm of TiO₂-GO nanostructures by photosonication: (a) TG_(0.5), (b) TG₍₁₎, (c) TG₍₃₎, (d) TG₍₆₎, (e) TG₍₁₀₎.

Table 7.6. Adsorption Isotherms data TiO₂-GO nanostructures by photosonication

Materials	Adsorption Isotherms						
	Freundlich			Langmuir			
	K _F (mg/g)	n	R ²	Q _{max} (mg/g)	K _L (L/mg)	R _L	R ²
TG _(0.5)	57.9162	0.6690	0.9947	1.6042	0.2805	0.6900	0.9952
TG ₍₁₎	5.2783	2.5759	0.9964	2.5660	1.3597	0.2228	0.9989
TG ₍₃₎	3.2210	3.5842	0.9925	2.0316	2.1663	0.1851	0.9986
TG ₍₆₎	2.1822	12.8041	0.9967	2.1258	38.5573	0.0121	0.9943
TG ₍₁₀₎	1.79845	22.4215	0.9949	1.8341	139.7947	0.0039	0.9990

7.2. Degradation by photocatalysis

7.2.1. Degradation on TiO₂

Adsorption studies showed that equilibrium was reached between 15 and 30 minutes after the start of the experiment. Therefore, after a dark period of 30 minutes, the photocatalytic activity of the TiO₂ was studied. The initial time (t_0) was the percentage of removal determined by adsorption in section 7.1.1. Combining the adsorption and photocatalysis results, Fig. 7.13. shows an increase in the total percentage removal (%R) of MB with exposure to the light source for 150 min in all cases. When analyzing the %R of MB in the absence of the photocatalyst, it was observed that photolysis contributed minimally, representing a maximum of $\approx 2.2\%$ removal. This low incidence of photolysis suggests that its contribution is negligible compared to the total MB removal, allowing us to attribute the degradation process predominantly to the effect of the nanomaterials used as photocatalysts.

Table 7.7. shows the contribution of both processes to the total removal of MB on TiO₂. The results obtained in this study provide valuable insight into how different treatments affect the properties of TiO₂, specifically in terms of photocatalytic activity and adsorption capacity. Sonication was found to be effective in slightly improving the photocatalytic activity, presumably due to an increase in the concentration of Ti³⁺ surface defects. This observation is consistent with the existing literature, which highlights the importance of defects in improving the photocatalytic efficiency of semiconducting materials such as TiO₂ [33, 34]. On the other hand, although milled TiO₂ showed a significant increase in adsorption capacity, this does not seem to translate proportionally into a noticeable improvement in photocatalytic activity. The analysis of the optical and electronic properties in Chapter 5 showed that despite the reduction of the bandgap and the higher light absorption capacity in milled TiO₂, the electronic conductivity remains comparable to that of pristine TiO₂. The mechanical milling process would create a high amount of defects that can act as traps for photons, reducing the overall efficiency of electron-hole pair generation [35], but at the same time, the presence of phase mixing could influence not to further reduce the conductivity, keeping it at a similar level to

pristine TiO₂. In summary, it is important to note that defects can contribute to improved photocatalytic applications in certain cases, such as Ti³⁺ defects, while high defect concentrations can potentially reduce efficiency.

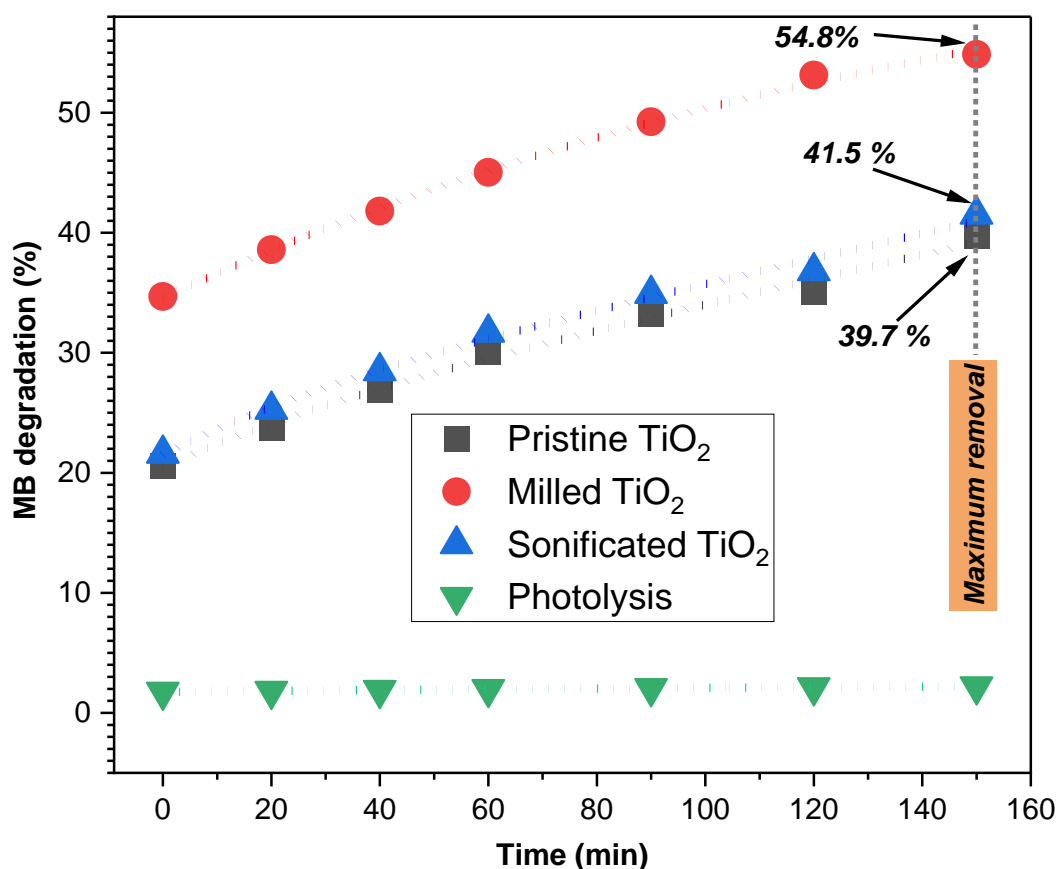


Fig. 7.13. Degradation of MB under visible irradiation of TiO₂.

Table 7.7. Distribution of removal mechanisms (%) on TiO₂

Removal mechanisms	Materials		
	Pristine TiO ₂	Milled TiO ₂	Sonificated TiO ₂
Adsorption (%) - 30 min	20.60%	34.68%	21.60%
Photocatalysis (%) - 150 min	19.10%	20.18%	19.92%
Total removal (%) - 180 min	39.71%	54.86%	41.52%

7.2.2. Degradation on TiO₂-GO mechano-synthesized nanostructures

Unlike TiO₂ and nanostructures fabricated by photosonation, nanostructures fabricated by ball-milling exhibited remarkable adsorptive removal capacity in a short time. Specifically, TG_(0.5) and TG₍₁₎ removed 100% of the dye, indicating that no additional treatments are required

to improve the removal efficiency. While TG₍₃₎, TG₍₆₎, and TG₍₁₀₎ were able to remove between 60-80% of the dye, suggesting that photocatalysis could be beneficial to complete the total removal. However, to properly evaluate the photocatalytic activity of all mechano-synthesized nanostructures, pellet fabrication was chosen. Fig. 7.14. shows the % degradation of MB in 150 min under visible light irradiation.

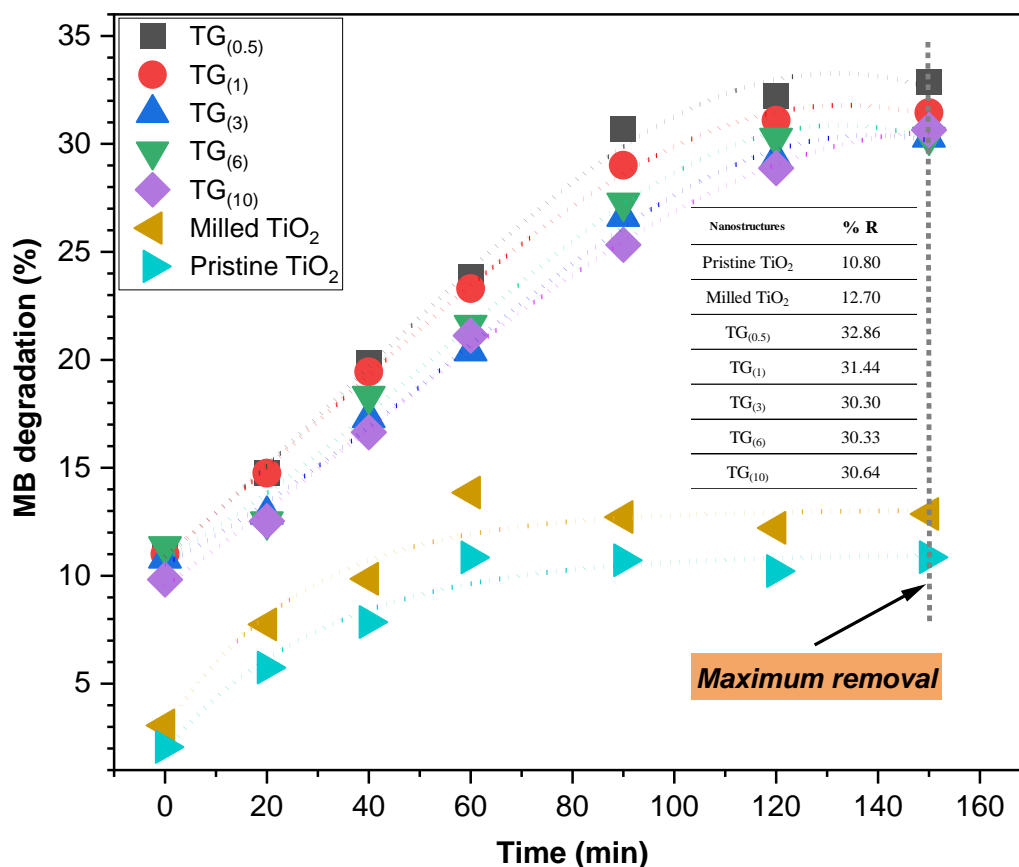


Fig. 7.14. Degradation of MB under visible irradiation of mechano-synthesized nanostructures (Pellets)

Initially, the adsorption after 30 min showed similarities in all cases (between 9 and 11%), which is attributed to the fact that the pellets did not accurately reflect crucial surface features such as the specific surface area (SSA). In this context, the uniformity of adsorption could be due to the limitation of the pellets to provide a detailed representation of the SSA, which was essential for understanding the adsorption dynamics at depth. Photocatalytic degradation, on the other hand, did not show significant differences in terms of oxidation levels (between 30 and 32%). This finding is in significant agreement with the similarities previously described in the optical and electrical properties in Chapter 5. The results suggest that the ball-milling process largely eliminates the influence of the oxidation level of the GOs on their properties and efficiency. Nevertheless, photocatalytic activity was demonstrated in all cases under visible light irradiation, supporting the feasibility of achieving total MB removal by complementing the adsorption process.

7.2.2.1. Kinetic study

The kinetics of photocatalytic degradation of MB were investigated using the pseudo-second-order kinetics model. The integrated form of the pseudo-second-order model is given by eq. 17 [30]:

$$\frac{1}{C_t} = \frac{1}{C_0} + k_2 t \quad (\text{eq. 17})$$

Where C_0 is the concentration at the start of the experiment, C_t is the concentration measured at time t (min) and k_2 is the apparent kinetic constant (min^{-1}), determined from the slope of the linear fit. Fig. 7.15. shows the linear transform of the kinetic curves and calculated values in Table 7.8.

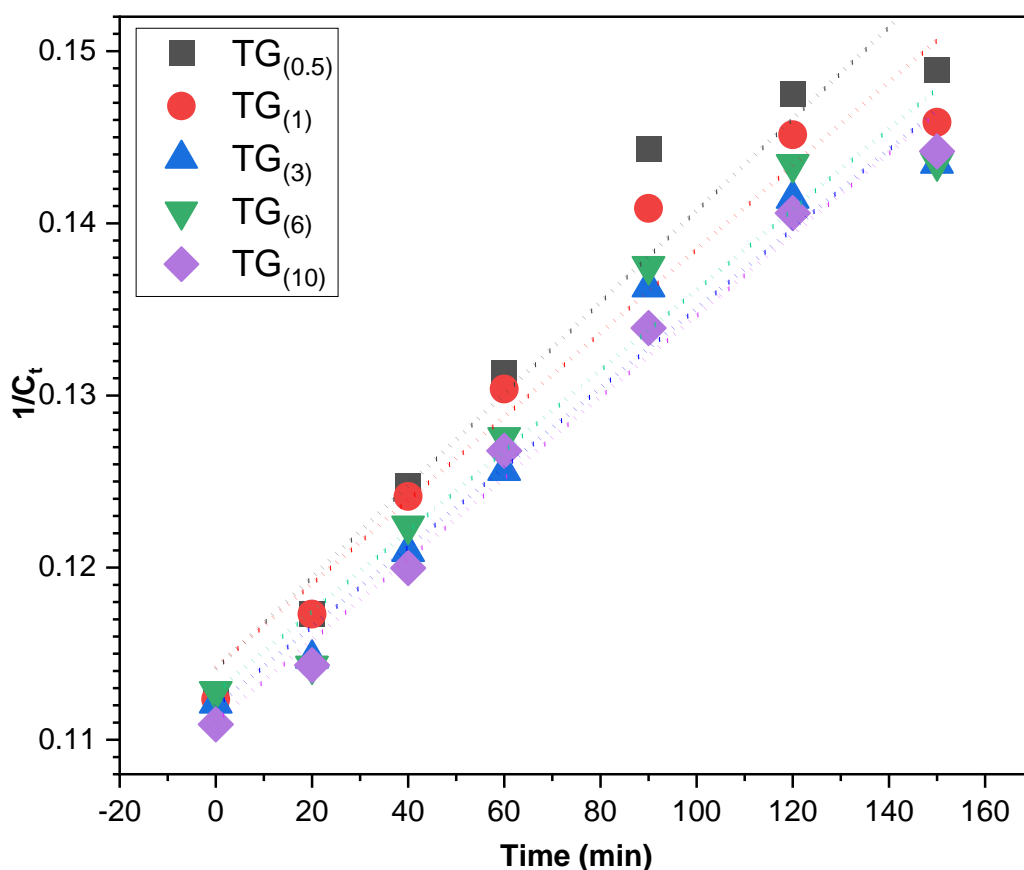


Fig. 7.15. Second-order model kinetics of TiO₂-GO nanostructures fabricated by ball-milling

The fact that the kinetics of the photocatalytic degradation of MB conforms more to pseudo-second-order kinetics implies that the rate of MB degradation depends on the square of its concentration. The similarity of the k_2 constants might suggest that the rate of the reaction is relatively constant and does not depend significantly on initial conditions such as oxidation degrees.

Table 7.8. Pseudo-second order kinetic data of degradation of photosonicated nanostructures

Materials	Pseudo-second order parameters	
	k_2 (min^{-1})	R^2
TG _(0.5)	0.0003	0.9426
TG ₍₁₎	0.0002	0.9471
TG ₍₃₎	0.0002	0.9702
TG ₍₆₎	0.0002	0.9511
TG ₍₁₀₎	0.0002	0.9858

7.2.3. Degradation on TiO₂-GO photosonicated nanostructures

Fig. 7.16. shows that the photodegradation of MB by the TiO₂-GO nanostructure was significantly improved compared to that by pristine TiO₂. In particular, excellent results were observed for the lowest oxidation nanostructure, TG_(0.5), where a maximum removal rate of $\approx 82.20\%$ was achieved after 150 min, reaching 100% after 210 min. However, for the discussion and comparison of the degradation between the different nanostructures, it was chosen to consider the percentage of removal achieved in the 150-minute interval.

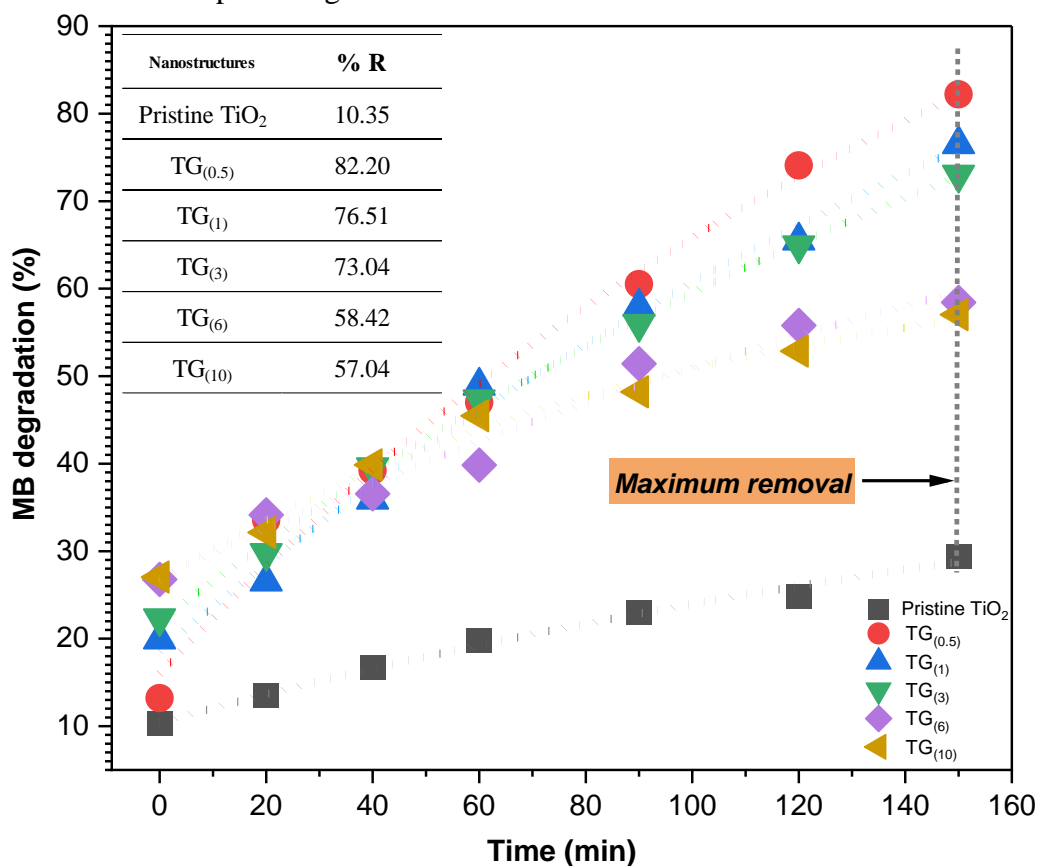


Fig. 7.16. Degradation of MB under visible irradiation on photosonicated nanostructures

The evaluation of dye removal revealed a relationship between the photocatalytic activity and the GO oxidation degree. The core-shell arrangement also had an important influence in photocatalytic activity. The presence of uncoated areas in TiO₂ particles creates synergy with coated areas, further enhancing photocatalytic efficiency. Ti³⁺ ions on uncoated surfaces act as active centers that introduce additional energy levels into the TiO₂ energy bandgap, facilitating the formation and charge transfer.

For the GO shell in low-oxidation-degree samples, this favors higher electronic mobility and better separation of e^-/h^+ pairs generated during excitation by the light source. This may promote efficient charge transfer on the surface of GO, resulting in increased generation of reactive oxygen species (ROS) such as superoxide (O_2^-). However, the combined effect becomes less noticeable as the level of oxidation increases. The shell becomes more homogeneous and the nanolayers are formed by a GO with a higher density of oxygenated groups that disrupt the electronic mobility. Thus, oxygenated functional groups could increase the adsorption capacity of more oxidized nanostructures, resulting in the accumulation of contaminants on the surface and reducing the availability of active sites for photocatalysis. In summary, the distribution of the total dye removal in the nanostructure is an interesting aspect that provides valuable information about the mechanisms underlying the removal process. Table 7.9. shows the contribution of both processes to the total removal of dye.

Table 7.9. Distribution of removal mechanisms (%) of photosonicated nanostructures

Removal Mechanisms	Materials				
	TG _(0.5)	TG ₍₁₎	TG ₍₃₎	TG ₍₆₎	TG ₍₁₀₎
Adsorption (%) - 30 min	13.21%	19.90%	22.34%	26.77%	27.03%
Photocatalysis (%) - 150 min	68.99%	56.61%	50.70%	31.65%	30.00%
Total removal (%) - 180 min	82.20%	76.51%	73.04%	58.42%	57.04%

The observation confirms the dependence of the GO oxidation degree on the percentage of contribution of each mechanism to the total removal. Thus, low oxidation favors mainly removal by photocatalysis, and this is reduced with a gradual increase in oxidation, to the extent that an almost balanced distribution between adsorption and photocatalysis is observed in TG₍₆₎ and TG₍₁₀₎. The combination of adsorption and photodegradation in total removal demonstrates an effective synergy between these two processes. The initial adsorption of dye molecules may facilitate the proximity of the molecules to the nanostructure surface, increasing the probability of interaction with the reactive species generated during photocatalysis. This interaction can accelerate the degradation and improve the overall efficiency of the removal process.

7.2.3.1. Kinetic study

The kinetics of photocatalytic degradation of MB were investigated using the pseudo-first-order kinetics model. The integrated form of the pseudo-first-order model is given by eq. 18 [36]:

$$\ln\left(\frac{C_t}{C_0}\right) = k_1 t \quad (\text{eq. 18})$$

Where C_0 is the concentration at the start of the experiment, C_t is the concentration measured at time t (min) and k_1 is the apparent kinetic constant (min^{-1}), determined from the slope of the linear fit. Fig. 7.17. shows the linear transform of the kinetic curves and calculated values in Table 7.10.

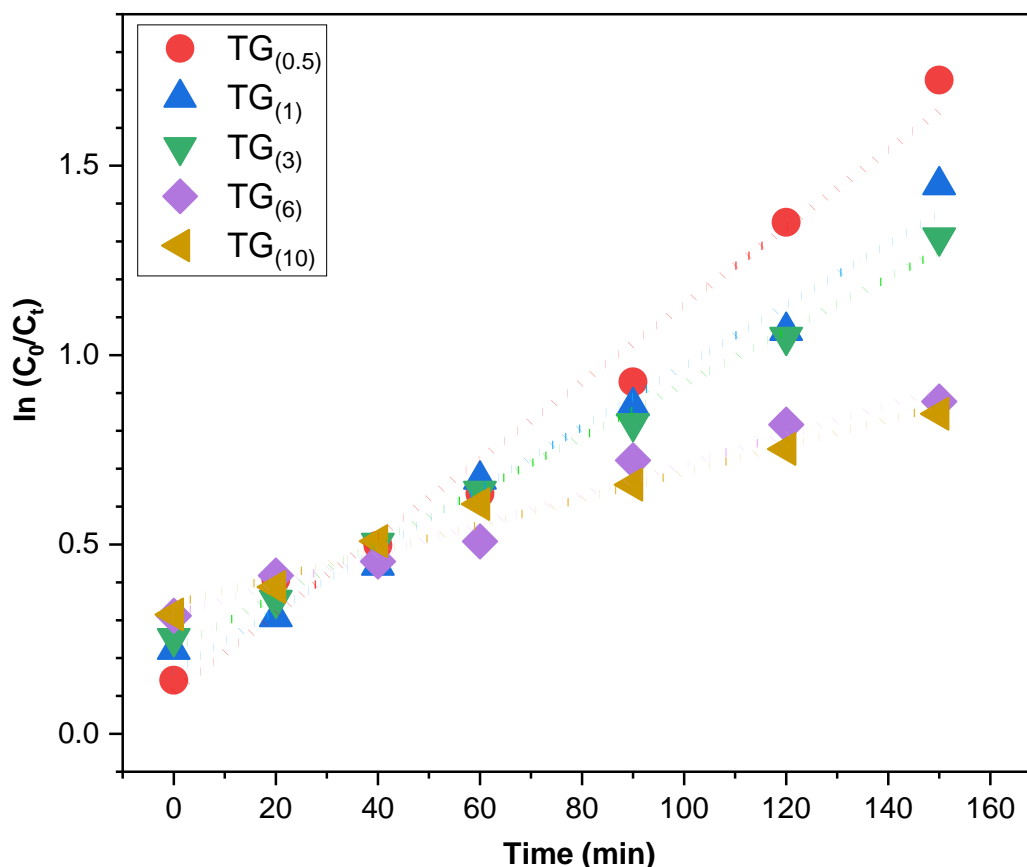


Fig. 7.17. Plots of $\ln(C_0/C_t)$ versus irradiation time with $\text{TiO}_2\text{-GO}$ nanostructures fabricated by photosonication

The fact that the kinetics of the photocatalytic degradation of MB conforms more to pseudo-first-order kinetics implies that the rate of MB degradation depends mainly on the concentration of the MB itself, and not on the square of its concentration, which would be the case for a second-order kinetic model.

Table 7.10. Kinetic data degradation of the photosonicated nanostructures

Materials	Pseudo-first order parameters	
	k_1 (min^{-1})	R^2
TG _(0.5)	0.0102	0.9753
TG ₍₁₎	0.0081	0.9856
TG ₍₃₎	0.0070	0.9958
TG ₍₆₎	0.0040	0.9749
TG ₍₁₀₎	0.0035	0.9746

7.2.3.2. Degradation mechanisms

Our observations are consistent with other reports of enhanced MB degradation with the formation of hybrid nanostructures [37, 38]. Considering all the above facts, we can say that several factors play an important role in achieving better efficiency of nanostructures in the removal of MB by joint adsorption-photocatalysis processes. Some of these factors are as follows:

- *Adsorption*: Adsorption plays an important role in the complete removal of MB by photocatalysis. The method works by concentrating, trapping and holding the MB molecules in close proximity to the reactive species generated during photocatalysis. This synergy between adsorption and photocatalysis enhances the overall efficiency of the process and plays a key role in the effective removal of contaminants such as MB.
- *GO shell*: Because of the formation of Ti-O-C bonds at the TiO₂ particles and GO interface's, the formation of a GO shell on the surface of TiO₂ particles is favored. The formation of Ti-O-C bonds can extend the optical absorption range of nanostructures and enhance photogenerated charges. This is in broad agreement with that mentioned by Cigarroa-Mayorga, O. E. (2022), who attributed the enhancement of photocatalytic activity in ZnO-Fe₂O₃ heterostructures to the interfacial charge transfer mechanism [39].

7.2.3.3. Photocatalytic reactions and charge transfer mechanism

Based on the results described above, the possible mechanism can be explained as follows. During photocatalytic activity, the GO-adhered material acts as a material that can absorb light that is not absorbed by pristine TiO₂. When TiO₂-GO hybrid nanostructures are irradiated with light of a wavelength corresponding to the bandgap of the GO shell, electrons in the C_B of GO are excited and can migrate into the C_B of TiO₂. The combination of two materials with different bandgaps allows the vectorial transfer of electrons and photogenerated holes through the π - π conjugation and vice-versa. The electron cloud in the TiO₂ C_B and on the GO, surface

promotes the formation of superoxides ($O_2^{\bullet-}$) on the uncoated surfaces of the TiO_2 by reaction with oxygen absorbed on the particle surface. These highly reactive ions trigger a series of reactions, which are the most powerful tool for decomposing the MB dye in CO_2 and H_2O .

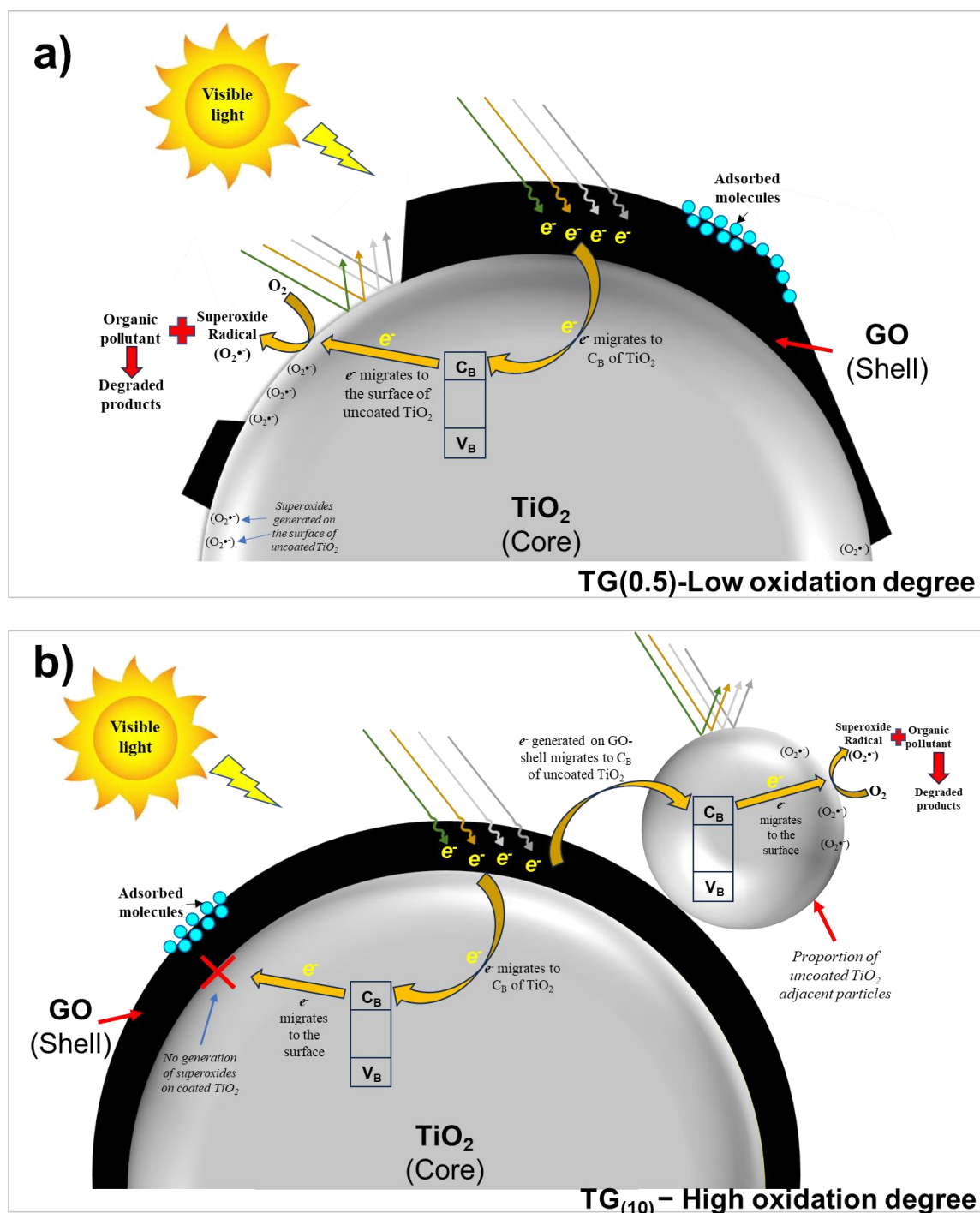


Fig. 7.18. Schematic illustration of the charge transfer process between photo-excited GO and TiO_2 (a) GO low oxidation degree and (b) GO high oxidation degree.

In this context, the morphology is a crucial factor for the photocatalytic efficiency. An inhomogeneous GO shell at $TG_{(0.5)}$ indicates the presence of significant regions of the uncoated particle, which leads to a higher generation of reactive oxygen species (ROS) (Fig. 7.18.a).

While increasing particle coverage at higher oxidation degrees, the GO shell acts as a barrier, preventing the contact of migrating electrons from the C_B of TiO_2 with O_2 molecules on the surface of the surrounding medium, which is necessary for the formation of superoxides. As a result, fully coated TiO_2 particles are limited in their ability to generate reducing species. However, the photocatalytic activity exhibited by these structures may be due to some electrons generated in the GO shell migrating to the surface of neighboring uncoated TiO_2 particles, where pollutant degradation would take place (Fig. 7.18.b).

Additionally, the electrical conductivity of the GOs determined in Chapter 4 plays an important role as it can have a significant effect on the π - π conjugation. The electrical conductivity of GO, which is influenced by its oxidation degree, is a determining factor in the electron transport within hybrid TiO_2 -GO nanostructures. A high oxidation degree introduces numerous oxygenated functional groups, which disrupt the sp^2 carbon network, increasing the electrical resistance and decreasing the conductivity of GO. In contrast, a low oxidation degree maintains a more intact sp^2 carbon network, allowing better electrical conductivity and more efficient electron transport to reach the TiO_2 surface. This balance is critical for improving charge separation and transfer in photocatalytic processes, as higher GO conductivity reduces the rate of e^-/h^+ pair recombination, thereby optimizing photocatalytic activity. Therefore, optimizing the GO oxidation degree is essential to maximize the synergistic effects in TiO_2 -GO hybrid nanostructures and significantly improve their performance.

7.2.4. MB molecular analysis after degradation by Raman spectroscopy

In the course of this chapter, we have conducted studies that have yielded significant results regarding the decolorization of MB solution in the presence of TiO_2 -GO hybrid nanostructures. Photocatalytic degradation experiments based on MB decolorization are commonly found in the literature [40, 41]. In such processes, the decolorization of the molecule is due to the destruction of the chromophore groups of the dyes. Consequently, water discoloration can be monitored by visible absorption but does not certify complete mineralization in CO_2 and H_2O . Therefore, UV-visible absorption characterization is a powerful technique to follow the disappearance of an absorbing group but does not give any confirmation of mineralization. In this regard, and in an attempt to look for the possible formation of by-products, we performed a comprehensive analysis of the chemical bonds present in the MB solution before and after subjecting it to photocatalysis by Raman spectroscopy. The analysis was performed on the degraded solution with the $TG_{(0.5)}$ nanostructure, which showed a 100% complete decolorization after 210 min of exposure.

Fig. 7.19. shows the comparison of the Raman spectra of MB solutions before and after total removal by photocatalysis. Fig. 7.19.a shows the spectrum of the MB solution with a concentration of 100 ppm, as described in the methodology section of Chapter 2. In this spectrum, the bands associated with the MB dye are identified, along with some bands corresponding to water (Fig. 7.19.d). The MB-specific bands are listed in Table 7.11. [42]. Upon dilution of the solution to 10 ppm, as shown in Fig. 7.19.b, an increase in the intensity of the water bands is observed, while the dye bands decrease; however, the latter are still

sufficiently defined to distinguish them from water and compare them after photocatalysis process.

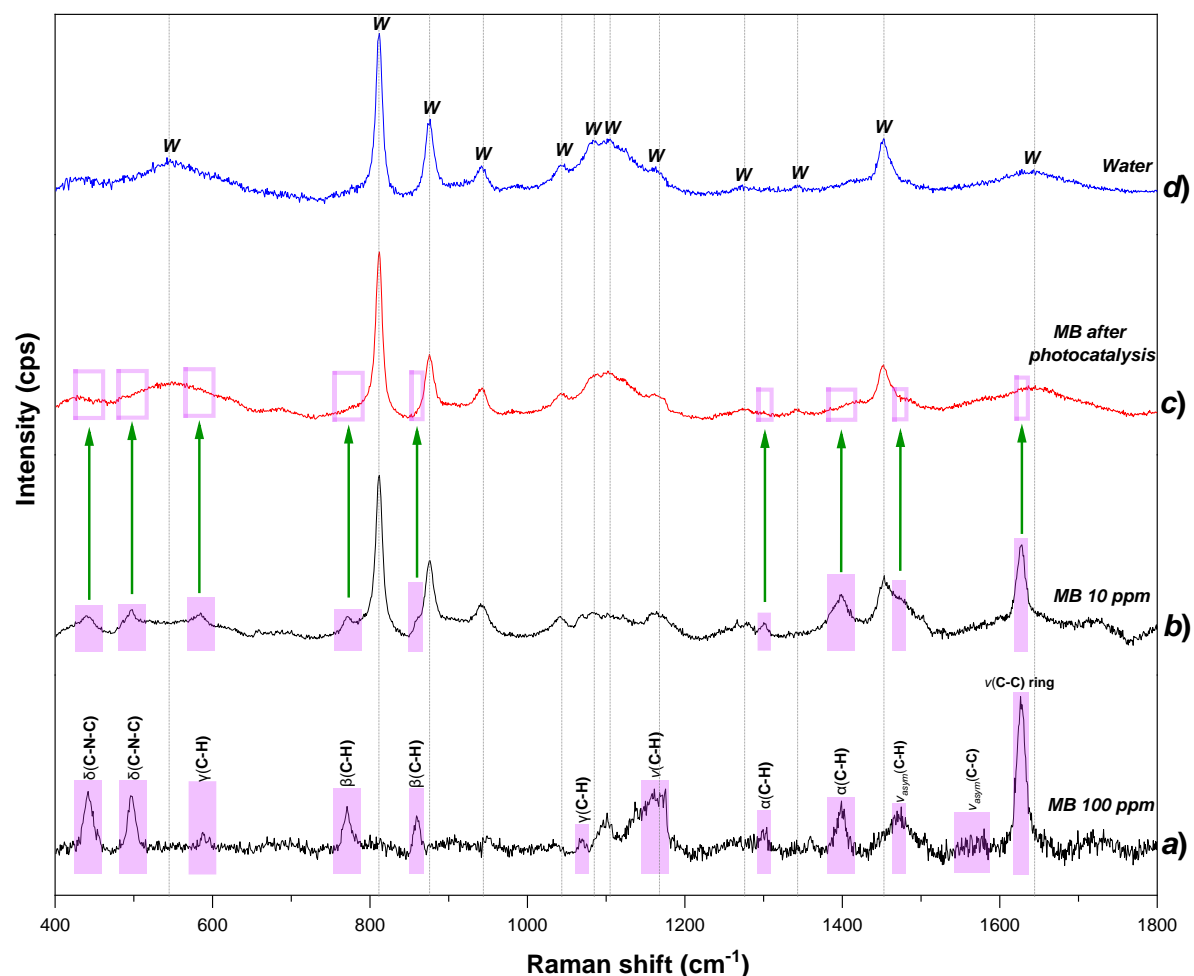


Fig. 7.19. Raman spectrum of solutions (a) MB 100 ppm, (b) MB 10 ppm, (c) MB solution 10 ppm after photocatalysis, and (d) deionized water (*w*-signals associated with water)

Subsequently, after 210 min of exposure to the light source in the presence of the photocatalyst [TG_(0.5)], the solution showed 100% decolorization, as confirmed by UV-vis spectroscopy. Analysis of the corresponding Raman spectrum (Fig. 7.19.c) shows that the bands associated with the dye are no longer visible (pink boxes indicated by green arrows). This observation confirms the hypothesis of degradation of MB molecules during photocatalysis with TiO₂-GO. The interaction of electron-hole pairs generated by the activation of the photocatalyst with the dye led to the breaking of bonds and degradation of the molecules, resulting in simpler and less colored compounds. This degradation explains the decolorization, as the final products formed are less absorbent in the visible range of the electromagnetic spectrum. The absence of the Raman bands associated with MB confirms that the specific vibrational characteristics of the molecules have changed or disappeared due to photocatalysis.

Table 7.11. The Raman shifts peaks associated with MB dye [42–44]

MB solution 100 ppm <i>Position (cm⁻¹)</i>	MB solution 10 ppm <i>Position (cm⁻¹)</i>	After photocatalysis <i>(status)</i>	Band assignments
1618	1618 (<i>s</i>)	<i>Not detected</i>	$\nu(\text{C-C})$ ring
1544	<i>Not detected</i>	<i>Not detected</i>	$\nu_{\text{asym}}(\text{C-C})$
1441	1441 (<i>w</i>)	<i>Not detected</i>	$\nu_{\text{asym}}(\text{C-N})$
1396	1396 (<i>m</i>)	<i>Not detected</i>	$\alpha(\text{C-H})$
1272	1272 (<i>w</i>)	<i>Not detected</i>	$\alpha(\text{C-H})$
1161	<i>Not detected</i>	<i>Not detected</i>	$\nu(\text{C-N})$
1067	<i>Not detected</i>	<i>Not detected</i>	$\gamma(\text{C-H})$
858	858 (<i>w</i>)	<i>Not detected</i>	$\beta(\text{C-H})$
768	768 (<i>w</i>)	<i>Not detected</i>	$\beta(\text{C-H})$
677	677 (<i>w</i>)	<i>Not detected</i>	$\gamma(\text{C-H})$
497	497 (<i>w</i>)	<i>Not detected</i>	$\delta(\text{C-N-C})$
445	445 (<i>s</i>)	<i>Not detected</i>	$\delta(\text{C-N-C})$

Abbreviations include ν (stretching), α (in-plane ring deformation), β (in-plane bending), γ (out-of-plane bending), and δ (skeletal deformation).

7.3. Conclusion

- The MB dye adsorption capacity of TiO₂ powder was extensively explored. The results revealed significant variations in the adsorption capacity of TiO₂ depending on its pretreatment. The pristine TiO₂ exhibited an initial adsorption capacity of 0.41 mg/g ($\approx 20.2\%$), which increased marginally to 0.44 mg/g ($\approx 22.2\%$) after sonification. However, ball-milling treatment led to a remarkable improvement, raising the adsorption capacity to 0.69 mg/g ($\approx 33.2\%$). These findings indicate the direct influence of the modification processes on the adsorptive properties of TiO₂. Furthermore, it was observed that the time required to reach adsorption equilibrium was consistent in all cases, with an equilibrium point reached at 20 minutes.
- The incorporation of GO into TiO₂ by ball-milling results in a remarkable enhancement of MB adsorption capacity in both pristine and milled TiO₂. It has been observed that

the TG_(0.5) and TG₍₁₎ nanostructures exhibit a maximum removal of 100%, significantly exceeding the efficiency of nanostructures with a higher oxidation degree. This phenomenon, contrary to what has been reported in the literature, suggests that less oxidized GOs favor higher adsorption due to a higher specific surface area (SSA), facilitated by additional exfoliation and defect formation during ball-milling. In addition, it has been shown that more oxidized GOs have a more negative surface charge, which hinders their dispersion and favors agglomeration, thus reducing the surface availability for chemical reactions. Therefore, the direct relationship between surface area and adsorption efficiency was confirmed, which explains the differential behavior in MB removal times between the studied nanostructures.

- It has been shown that the incorporation of GO on TiO₂ by the photosonication method results in a significant improvement in the adsorption capacity of pristine TiO₂. Although this adsorption capacity is lower compared to the ball-milling method, the importance of photosonication as a less aggressive process for the crystalline structure of the material has been highlighted. This approach has allowed us to systematically investigate the effects of the oxidation degree on the adsorption behavior of MB, revealing a direct relationship between increasing the GO oxidation and the adsorption capacity of the dye.
- Kinetic analyses of the MB adsorption process on TiO₂-GOs hybrid nanostructures fabricated by both methods indicated that the adsorption mechanism follows a pseudo-second-order model, suggesting that adsorption is predominantly by chemisorption. Furthermore, the fit of the experimental data to the Langmuir isotherms supports the idea of a more uniform adsorption process consistent with a monolayer coverage model. To further investigate the mechanisms underlying the adsorption process, detailed analyses of the adsorption time evolution curves were performed using diffusion models that take into account diffusion into the surrounding liquid film, intraparticle diffusion, and surface adsorption. These analyses revealed that the adsorption process of MB on hybrid TiO₂-GOs nanostructures involves several sequential stages, from the initial diffusion of MB molecules into the liquid film to their adsorption onto the pores or surface of the particles.
- The degradation results provide detailed insight into the photocatalytic efficiency of TiO₂-GO nanostructures in the degradation of dyes using visible light. Initially, pristine TiO₂ exhibited modest degradation capability, which was slightly enhanced by sonification and ball-milling, respectively. However, it was evident that the degradation capacity is still limited, despite the significant improvement in adsorption capacity. Subsequently, the incorporation of GO in both methodologies improved the photocatalytic efficiency, mainly due to the enhanced light absorption promoted by GO. In particular, in the nanostructures obtained by mechanical milling, the photocatalytic removal efficiency varied between $\approx 30.6\%$ and $\approx 32.8\%$, without showing a clear trend depending on the oxidation degree of the GO. On the other hand, in the nanostructures

obtained by photosonation, the photocatalytic activity was noticeably affected by the oxidation of the GO, this being attributed to the structural characteristics of the GO discussed in Chapter 4.

- In summary, this study has shown that TiO₂-GO hybrid nanostructures fabricated by ball-milling exhibit outstanding MB removal capacity through the adsorption mechanism, albeit with limited photocatalytic activity. On the other hand, nanostructures obtained by photosonation showed an initially limited adsorption capacity but allowed investigation of the influence of the oxidation degree and presented a considerably improved photocatalytic efficiency. The combination of adsorption and photocatalysis on these nanostructures has shown an effective synergy in MB removal. The initial adsorption of the dye molecules facilitates their proximity to the nanostructure surface, which increases the probability of interaction with the reactive species generated during photocatalysis. This interaction results in an acceleration of the degradation and an improvement in the overall efficiency of the removal process. In conclusion, this research highlighted the importance of considering the synergy between adsorption and photocatalysis, as well as the importance of considering both the TiO₂ modification methodology and the GO oxidation degree to optimize the efficiency of organic pollutant removal in water.

References

1. Rafatullah, M., Sulaiman, O., Hashim, R., Ahmad, A.: Adsorption of methylene blue on low-cost adsorbents: A review. *J Hazard Mater.* 177, 70–80 (2010). <https://doi.org/10.1016/J.JHAZMAT.2009.12.047>
2. Sheng, J., Xie, Y., Zhou, Y.: Adsorption of methylene blue from aqueous solution on pyrophyllite. *Appl Clay Sci.* 46, 422–424 (2009). <https://doi.org/10.1016/J.CLAY.2009.10.006>
3. Senthilkumaar, S., Varadarajan, P.R., Porkodi, K., Subbhuraam, C. V.: Adsorption of methylene blue onto jute fiber carbon: kinetics and equilibrium studies. *J Colloid Interface Sci.* 284, 78–82 (2005). <https://doi.org/10.1016/J.JCIS.2004.09.027>
4. Duran, F., Diaz-Uribe, C., Vallejo, W., Muñoz-Acevedo, A., Schott, E., Zarate, X.: Adsorption and Photocatalytic Degradation of Methylene Blue on TiO₂ Thin Films Impregnated with Anderson-Evans Al-Polyoxometalates: Experimental and DFT Study. *ACS Omega.* 8, 27284–27292 (2023). <https://doi.org/10.1021/ACSOMEGA.3C02657>
5. Vasiljevic, Z.Z., Dojcinovic, M.P., Vujancevic, J.D., Jankovic-Castvan, I., Ognjanovic, M., Tadic, N.B., Stojadinovic, S., Brankovic, G.O., Nikolic, M. V.: Photocatalytic degradation of methylene blue under natural sunlight using iron titanate nanoparticles prepared by a modified sol–gel method. *R Soc Open Sci.* 7, (2020). <https://doi.org/10.1098/RSOS.200708>
6. Ulfa, M., Al Afif, H., Saraswati, T.E., Bahruji, H.: Fast Removal of Methylene Blue via Adsorption-Photodegradation on TiO₂/SBA-15 Synthesized by Slow Calcination. *Materials.* 15, (2022). <https://doi.org/10.3390/MA15165471>
7. Saleh, T.A.: Kinetic models and thermodynamics of adsorption processes: classification. *Interface Science and Technology.* 34, 65–97 (2022). <https://doi.org/10.1016/B978-0-12-849876-7.00003-8>
8. Pan, X., Zhang, M., Liu, H., Ouyang, S., Ding, N., Zhang, P.: Adsorption behavior and mechanism of acid orange 7 and methylene blue on self-assembled three-dimensional MgAl layered double hydroxide: Experimental and DFT investigation. *Appl Surf Sci.* 522, 146370 (2020). <https://doi.org/10.1016/J.APSUSC.2020.146370>
9. Hamidi, S. El, Khnifira, M., Machrouhi, A., Mahsoun, A., Boumya, W., Tounsadi, H., Zahra Mahjoubi, F., Sadiq, M., Barka, N., Abdennouri, M., Abdennouri, M.: Theoretical and experimental study of the adsorption characteristics of Methylene Blue on titanium dioxide surface using DFT and Monte Carlo dynamic simulation. email, (2020). <https://doi.org/10.5004/dwt.2020.25737>

10. Tang, H., Zhao, Y., Shan, S., Yang, X., Liu, D., Cui, F., Xing, B.: Theoretical insight into the adsorption of aromatic compounds on graphene oxide. *Environ Sci Nano*. 5, 2357–2367 (2018). <https://doi.org/10.1039/C8EN00384J>
11. Bai, Y., Sui, H., Liu, X., He, L., Li, X., Thormann, E.: Effects of the N, O, and S heteroatoms on the adsorption and desorption of asphaltenes on silica surface: A molecular dynamics simulation. *Fuel*. 240, 252–261 (2019). <https://doi.org/10.1016/J.FUEL.2018.11.135>
12. Yan, H., Tao, X., Yang, Z., Li, K., Yang, H., Li, A., Cheng, R.: Effects of the oxidation degree of graphene oxide on the adsorption of methylene blue. *J Hazard Mater*. 268, 191–198 (2014). <https://doi.org/10.1016/J.JHAZMAT.2014.01.015>
13. Gao, H., Cao, R., Xu, X., Xue, J., Zhang, S., Hayat, T., Alharbi, N.S., Li, J.: Surface Area- and Structure-Dependent Effects of LDH for Highly Efficient Dye Removal. *ACS Sustain Chem Eng*. 7, 905–915 (2019). <https://doi.org/10.1021/acssuschemeng.8b04476>
14. Özsin, G., Kılıç, M., Apaydın-Varol, E., Pütün, A.E.: Chemically activated carbon production from agricultural waste of chickpea and its application for heavy metal adsorption: equilibrium, kinetic, and thermodynamic studies. *Appl Water Sci*. 9, 1–14 (2019). <https://doi.org/10.1007/S13201-019-0942-8>
15. Ho, Y.S.: Review of second-order models for adsorption systems. *J Hazard Mater*. 136, 681–689 (2006). <https://doi.org/10.1016/J.JHAZMAT.2005.12.043>
16. Husein, D.Z., Hassanien, R., Al-Hakkani, M.F.: Green-synthesized copper nano-adsorbent for the removal of pharmaceutical pollutants from real wastewater samples. *Heliyon*. 5, e02339 (2019). <https://doi.org/10.1016/J.HELIYON.2019.E02339>
17. Lacin, D., Aroguz, A.Z.: Kinetic studies on adsorption behavior of methyl orange using modified halloysite, as an eco-friendly adsorbent. *SN Appl Sci*. 2, 1–12 (2020). <https://doi.org/10.1007/S42452-020-03799-4>
18. Amadi, O.K., Odidiozor, C., Okoro, I., Okpara, M.: Sorption Kinetic and Intraparticle Diffusivities of As³⁺ and Hg²⁺ Detoxification from Aqueous Solution Using Cellulosic Biosorbent Derived from Okra (*Abelmoschus esculentus*) Stems. *International Journal of Engineering and Information Systems*. 1, 72–85 (2017)
19. Yao, C., Chen, T.: A film-diffusion-based adsorption kinetic equation and its application. *Chemical Engineering Research and Design*. 119, 87–92 (2017). <https://doi.org/10.1016/J.CHERD.2017.01.004>
20. Gusain, R., Kumar, N., Ray, S.S.: Recent advances in carbon nanomaterial-based adsorbents for water purification. *Coord Chem Rev*. 405, 213111 (2020). <https://doi.org/10.1016/J.CCR.2019.213111>
21. Tran, H.N., You, S.J., Hosseini-Bandegharaei, A., Chao, H.P.: Mistakes and inconsistencies regarding adsorption of contaminants from aqueous solutions: A critical review. *Water Res*. 120, 88–116 (2017). <https://doi.org/10.1016/J.WATRES.2017.04.014>
22. Albayati, T.M., Sabri, A.A., Abed, D.B.: Functionalized SBA-15 by amine group for removal of Ni(II) heavy metal ion in the batch adsorption system. (2020). <https://doi.org/10.5004/dwt.2020.24845>
23. Boparai, H.K., Joseph, M., O'Carroll, D.M.: Kinetics and thermodynamics of cadmium ion removal by adsorption onto nano zerovalent iron particles. *J Hazard Mater*. 186, 458–465 (2011). <https://doi.org/10.1016/J.JHAZMAT.2010.11.029>
24. Asuquo, E., Martin, A., Nzerem, P., Siperstein, F., Fan, X.: Adsorption of Cd(II) and Pb(II) ions from aqueous solutions using mesoporous activated carbon adsorbent: Equilibrium, kinetics and characterisation studies. *J Environ Chem Eng*. 5, 679–698 (2017). <https://doi.org/10.1016/J.JECE.2016.12.043>
25. Yagub, M.T., Sen, T.K., Afroze, S., Ang, H.M.: Dye and its removal from aqueous solution by adsorption: A review. *Adv Colloid Interface Sci*. 209, 172–184 (2014). <https://doi.org/10.1016/J.CIS.2014.04.002>
26. Goldberg, S.: Equations and Models Describing Adsorption Processes in Soils. *Chemical Processes in Soils*. 489–517 (2018). <https://doi.org/10.2136/SSSABOOKSER8.C10>
27. Jaman, H., Chakraborty, D., Saha, P.: A Study of the Thermodynamics and Kinetics of Copper Adsorption Using Chemically Modified Rice Husk. *Clean (Weinh)*. 37, 704–711 (2009). <https://doi.org/10.1002/CLEN.200900138>
28. Yagub, M.T., Sen, T.K., Ang, H.M.: Equilibrium, kinetics, and thermodynamics of methylene blue adsorption by pine tree leaves. *Water Air Soil Pollut*. 223, 5267–5282 (2012). <https://doi.org/10.1007/S11270-012-1277-3>
29. Memon, S.Q., Memon, N., Shah, S.W., Khuhawar, M.Y., Bhangar, M.I.: Sawdust—A green and economical sorbent for the removal of cadmium (II) ions. *J Hazard Mater*. 139, 116–121 (2007). <https://doi.org/10.1016/J.JHAZMAT.2006.06.013>
30. Liu, Y., Shen, L.: From Langmuir kinetics to first- and second-order rate equations for adsorption. *Langmuir*. 24, 11625–11630 (2008). <https://doi.org/10.1021/LA801839B>

31. Zhao, X., Zhang, H., Li, W., Li, X., Fan, W., Zhang, Y.: Langmuir-diffusion model: Its modification and further application to glutinous rice flour particles. *J Food Process Eng.* 43, e13470 (2020). <https://doi.org/10.1111/JFPE.13470>
32. Cheng, R., Shen, L.J., Zhang, Y.Y., Dai, D.Y., Zheng, X., Liao, L.W., Wang, L., Shi, L.: Enhanced Phosphate Removal from Water by Honeycomb-Like Microporous Lanthanum-Chitosan Magnetic Spheres. *Water* 2018, Vol. 10, Page 1659. 10, 1659 (2018). <https://doi.org/10.3390/W10111659>
33. Xu, Y., Wu, S., Wan, P., Sun, J., Hood, Z.D.: Introducing Ti^{3+} defects based on lattice distortion for enhanced visible light photoreactivity in TiO_2 microspheres. *RSC Adv.* 7, 32461–32467 (2017). <https://doi.org/10.1039/C7RA04885H>
34. Zhang, Y., Li, Y., Yu, H., Yu, K., Yu, H.: Interfacial defective Ti^{3+} on Ti/TiO_2 as visible-light responsive sites with promoted charge transfer and photocatalytic performance. *J Mater Sci Technol.* 106, 139–146 (2022). <https://doi.org/10.1016/J.JMST.2021.06.081>
35. Zafar, Z., Yi, S., Li, J., Li, C., Zhu, Y., Zada, A., Yao, W., Liu, Z., Yue, X.: Recent Development in Defects Engineered Photocatalysts: An Overview of the Experimental and Theoretical Strategies. *Energy & Environmental Materials.* 5, 68–114 (2022). <https://doi.org/10.1002/EEM2.12171>
36. Youssef, N.A., Shaban, S.A., Ibrahim, F.A., Mahmoud, A.S.: Degradation of methyl orange using Fenton catalytic reaction. *Egyptian Journal of Petroleum.* 25, 317–321 (2016). <https://doi.org/10.1016/J.EJPE.2015.07.017>
37. Saldivar-Ayala, D., Ashok, A., Cigarroa-Mayorga, O.E., Hernández-Rodríguez, Y.M.: Tuning the plasmon resonance of Au-Ag core-shell nanoparticles: The influence on the visible light emission for inorganic fluorophores application. *Colloids Surf A Physicochem Eng Asp.* 677, 132359 (2023). <https://doi.org/10.1016/J.COLSURFA.2023.132359>
38. Ramos-Álvarez, D., Hernández-Rodríguez, Y.M., Vega-Gómez, J., Cigarroa-Mayorga, O.E.: Influence of copper support on the charge transfer enhancement of zinc oxide nanoflakes. *Mater Lett.* 349, 134875 (2023). <https://doi.org/10.1016/J.MATLET.2023.134875>
39. Cigarroa-Mayorga, O.E.: Enhancement of photocatalytic activity in ZnO NWs array due to Fe_2O_3 NPs electrodeposited on the nanowires surface: The role of $ZnO-Fe_2O_3$ interface. *Mater Today Commun.* 33, 104879 (2022). <https://doi.org/10.1016/J.MTCOMM.2022.104879>
40. Sánchez-Albores, R., Cano, F.J., Sebastian, P.J., Reyes-Vallejo, O.: Microwave-assisted biosynthesis of $ZnO-GO$ particles using orange peel extract for photocatalytic degradation of methylene blue. *J Environ Chem Eng.* 10, 108924 (2022). <https://doi.org/10.1016/J.JECE.2022.108924>
41. Drisya, K.T., Edely, M., Solís-López, M., Jantrania, A., Auguste, S., Rousseau, A., Casteneda, H., Velumani, S., Kassiba, A.: Structural features and morphology of titanium dioxide–bismuth vanadate heterojunctions. *CrystEngComm.* 23, 7679–7690 (2021). <https://doi.org/10.1039/D1CE00982F>
42. Xiao, G.N., Man, S.Q.: Surface-enhanced Raman scattering of methylene blue adsorbed on cap-shaped silver nanoparticles. *Chem Phys Lett.* 447, 305–309 (2007). <https://doi.org/10.1016/J.CPLETT.2007.09.045>
43. Naujok, R.R., Duevel, R. V., Corn, R.M.: Fluorescence and Fourier Transform Surface-Enhanced Raman Scattering Measurements of Methylene Blue Adsorbed onto a Sulfur-Modified Gold Electrode. *Langmuir.* 9, 1771–1774 (1993). <https://doi.org/10.1021/LA00031A026>
44. Ruan, C., Wang, W., Gu, B.: Single-molecule detection of thionine on aggregated gold nanoparticles by surface enhanced Raman scattering. *Journal of Raman Spectroscopy.* 38, 568–573 (2007). <https://doi.org/10.1002/JRS.1691>

Chapter VIII:

Study on microalgal photocatalytic destruction

Microalgae are unicellular microorganisms that contain *chlorophyll a*, and other photosynthetic pigments and are capable of oxygenic photosynthesis [1]. They are found in colonies as well as single cells [2]. Microalgae combine characteristics typical of higher plants, such as efficient oxygenic photosynthesis, simple nutritional requirements, and rapid growth, with the ability to accumulate or secrete primary and secondary metabolites, similar to microorganisms [3]. While microalgal growth can occur naturally, driven by environmental factors such as temperature, light, and nutrient availability, it is important to note that its frequency and intensity increase with the eutrophication of water bodies. Eutrophication is a process by which water quality deteriorates due to the accumulation of nutrients, mainly nitrogen and phosphorus [4, 5]. This phenomenon usually occurs naturally and is a gradual and slow process. However, climate change, coupled with abiotic and biotic conditions caused by human activities, contributes to excessive N and P concentrations, which trigger excessive algal growth [6]. This proliferation reduces dissolved oxygen levels in the water, making it difficult for other aquatic species to survive. Ultimately, this leads to accelerated eutrophication of aquatic systems (artificial or cultural eutrophication), resulting in ecological imbalance.

The use of photocatalytic nanomaterials represents an attractive alternative to effectively treat water bodies contaminated with microalgae. When working with microalgae and photoactive material, light plays a dual role: its purpose is to produce reactive oxygen species (ROS) and facilitate the process of photosynthesis. While light has a good effect on the former activity, the latter activity is not always affected by an abundance of photons and may instead increase the internal risk of oxidation. In this second scenario, the toxicity of nanoparticles interacting with surrounding microalgae is related to damage to cellular functions leading to cell death [7]. In this context, hybrid TiO₂-GO nanostructures fabricated by photosonation were used in the study of the destruction of microalgae, specifically the one with the lowest oxidation degree was used, due to its outstanding photocatalytic activity demonstrated in Chapter 7. The details of the procedure and conditions are shown in Chapter 2.

This chapter is intended as an important step toward practical applications to address challenges such as cell death in microalgae and degradation of the byproducts they produce. By expanding research beyond traditional contaminant removal to encompass the complex interactions of aquatic ecosystems, this work lays the groundwork for specific solutions to

mitigate the adverse effects of microalgal blooms. This interdisciplinary approach highlights the relevance and potential impact of the findings, opening avenues for addressing environmental problems with nanomaterials and innovative methodologies.

8.1. Measurements of *chlorophyll fluorescence*

Prior to measurement, the sample was exposed to low-intensity far-red light (FR-L) with a wavelength of 720 nm and an intensity of $13 \mu\text{mol photons/m}^2\cdot\text{s}$ for 20 min in order to inhibit the electron transport chain while in darkness. Upon deactivating FR-L, the sample underwent irradiation with a low-intensity modulated light (FML, with a maximum wavelength of 620 nm, a frequency of 800 Hz, and an intensity of less than $15 \mu\text{mol photons/m}^2\cdot\text{s}$) for 1 min. The measured fluorescence level was denoted as F_0 . The FR-L was reactivated to promote PSI activities. Subsequently, a high-intensity white light pulse (L-P) with a duration of 800 ms and an intensity exceeding $1500 \mu\text{mol photons/m}^2\cdot\text{s}$ was applied to the sample. F_M was used to identify the measured fluorescence level. The sample was subsequently illuminated by L-ACT at various intervals.

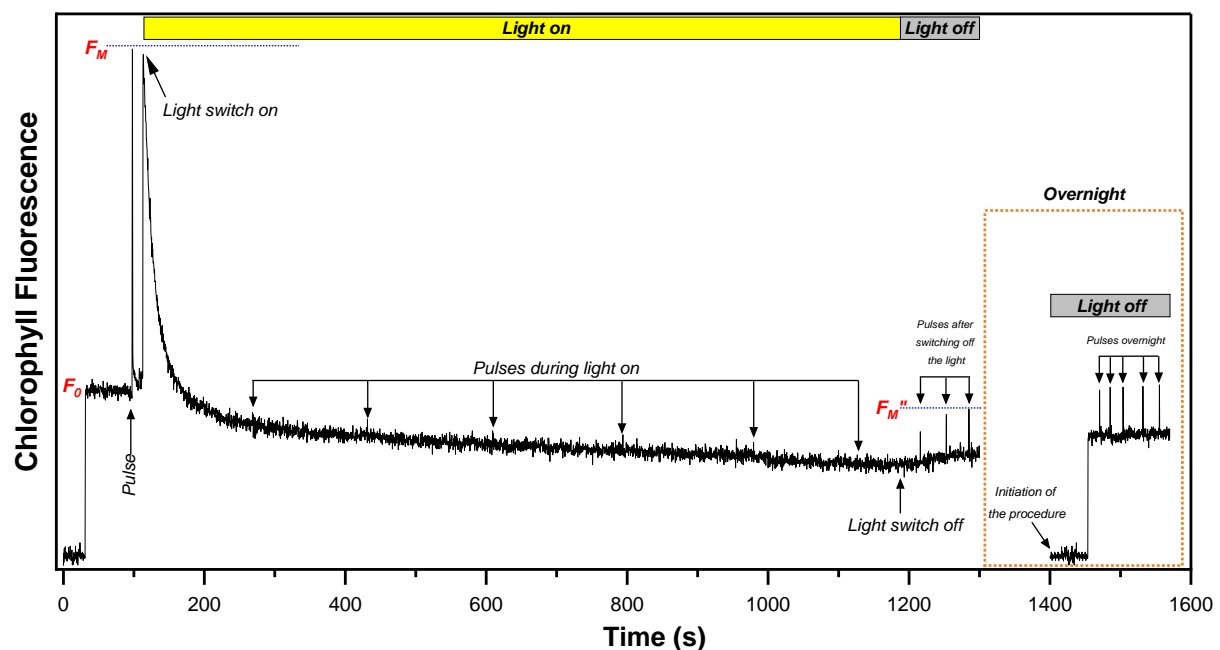


Fig. 8.1. Data illustrating the fluctuations in the intensity of chlorophyll fluorescence.

During the process of illumination, the fluorescence intensity attained a stable and unchanging level, which is referred to as F_s . Throughout this time frame, the sample had consistent exposure to intense light pulses (L-P), resulting in a temporary rise in fluorescence known as F_M . At the conclusion of the L-ACT time, L-ACT was deactivated whereas FR, FML, and L-P remained active for a duration of 20 min. The subsequent lighting ultimately caused a temporary rise in the fluorescence intensity, referred to as F''_M . After the 20-minute period, the sample remained on the bench overnight, exposed to the surrounding light. The levels of F_0 , F_M , and F''_M were subsequently recorded. The fundamental chlorophyll fluorescence yields were used to construct parameters that characterize the photosynthetic activity and the

management of absorbed light energy. Fig. 8.1. shows a representative picture of variations in *chlorophyll fluorescence* intensity.

8.2. Chlorophyll fluorescence under visible light

Fig. 8.2 illustrates the contrast in fluorescence kinetics of *chlorophyll* when measured without photolysis and with the inclusion of the photocatalytic film. In both cases a good-quality signal is observed, suggesting the use of a dense culture. Initially, a disparity in F_0 levels is observed between the two curves. In the absence of the photocatalyst, the F_0 level was ≈ 0.018 , whereas, in the presence of the photocatalyst, this level was slightly lower at ≈ 0.013 . The difference in F_0 levels before light source activation suggests that the presence of the photocatalyst generates a significant effect on the fluorescence level from the start. This effect could be related to the adsorption of molecules on the surface during the resting time before irradiation with light.

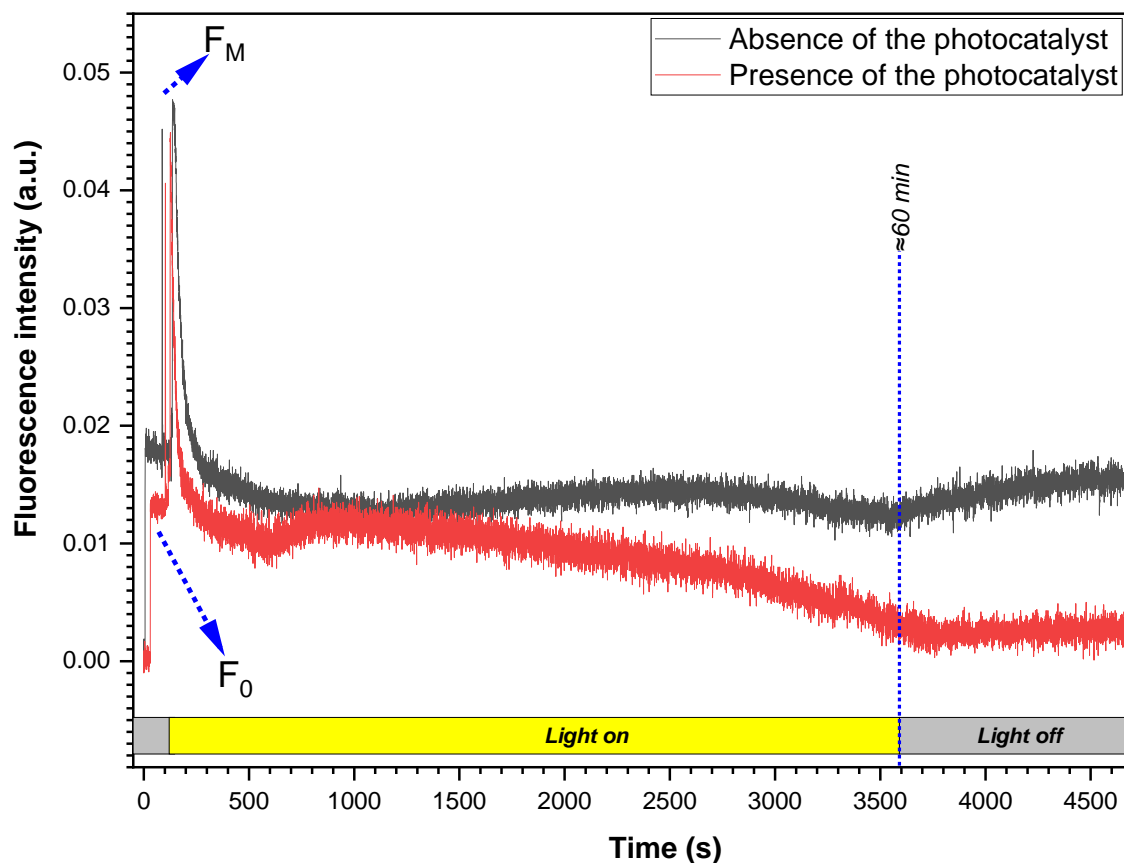


Fig. 8.2. Chlorophyll fluorescence curves recorded with continuous actinic light illumination for ≈ 1 h, in the presence and absence of the photocatalyst.

Subsequently, after starting the illumination and reaching a maximum level (F_M), in both cases, it is observed that the fluorescence yield of chlorophyll decreases to a minimum level during illumination, although with evident qualitative differences in the curves. On the one hand, in the absence of the photocatalyst, a slight increase in fluorescence is observed from \approx the 1600s onwards, which decreases again from \approx the 3300s onwards. The changes during the illumination period are not significant, so it could be considered that a steady state is maintained

until the end of the illumination. On the other hand, during illumination in the presence of the photocatalyst, a slight increase in fluorescence is observed starting at ≈ 600 s, reaching a maximum level at ≈ 1100 s. This subtle but evident change could be related to an acclimatization effect of the microalgae during continuous exposure to light. Subsequently, the fluorescence level starts to decrease suddenly until it reaches a minimum stationary level (F_s) at ≈ 2600 s. This behavior remains constant after switching off the light at ≈ 3600 s.

Immediately after the cessation of continuous illumination, in the absence of the photocatalyst, fluorescence appears to increase slowly and transiently. This indicates the adaptation process occurring as the Calvin cycle becomes more efficient in utilizing the products of the light phase, namely ATP and NADPH [8]. Whereas, in the presence of the photocatalyst, the level remained stationary. Under photocatalytic circumstances, the quenching of chlorophyll fluorescence is heightened. In addition, a color change in the solution was observed with the naked eye as shown in Fig. 8.3.

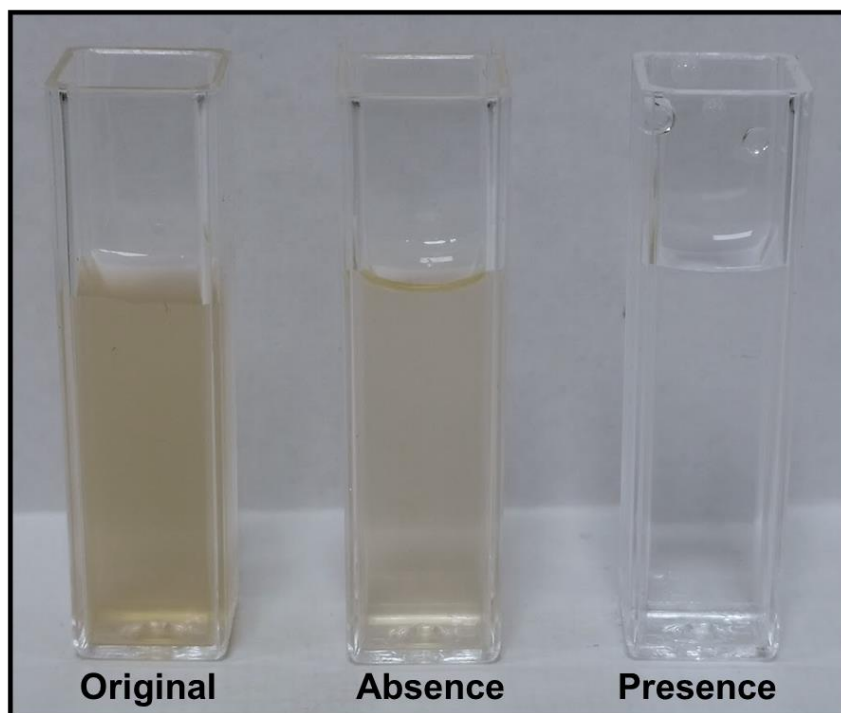


Fig. 8.3. Solution with microalgae after photolysis and photocatalysis after 1 h.

8.3. Chlorophyll fluorescence after overnight

From a qualitative point of view, 1 h of continuous illumination seems to show clear changes in the fluorescence curves in the absence and presence of the photocatalytic material, as shown by the color changes in Fig. 8.3. However, to be sure of the changes recorded, the fluorescence levels of the illuminated samples were measured again after overnight storage at room temperature and light. For comparison, these solutions were compared with the fluorescence curve of the unilluminated cells, *i.e.*, the original solution. Measurements were made in the absence of light and only for a total time of 450 s, as shown in Fig. 8.4.

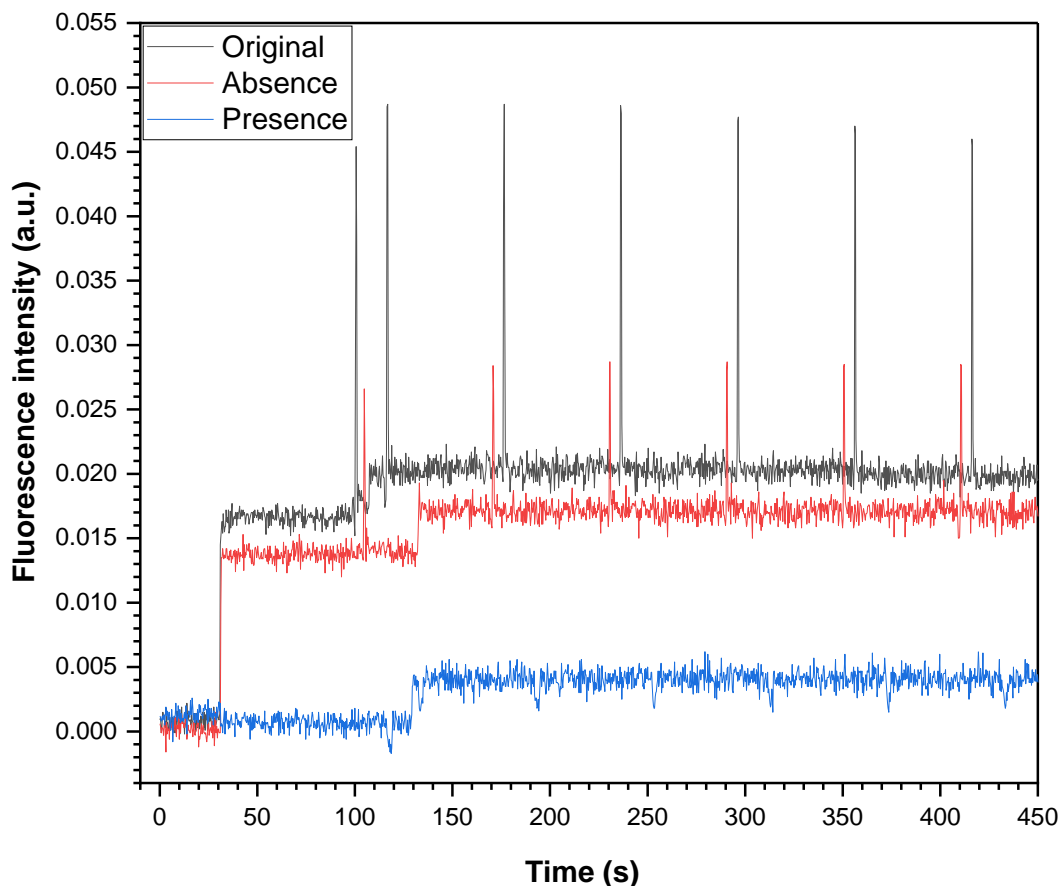


Fig. 8.4. Graph of *chlorophyll* peaks obtained from an overnight incubation test conducted in the dark: Original solution without illumination (—black line), absence of photocatalyst - photolysis- (—red line) and presence of photocatalyst -photocatalysis- (—blue line)

The analysis of the initial solution (—) revealed prominent peaks indicating a high concentration of *chlorophyll*, indicating the vitality of the unilluminated microalgae, while the solution in the absence of the photocatalyst (—) showed similar peaks, although at a lower intensity. This would show that both the irradiation time and the irradiation condition themselves affected the destruction of the *chlorophyll* pigment, although it was not sufficient to eliminate it, so that after the overnight incubation period the cells had enough time to recover, although not to the *chlorophyll* levels of the original solution (—). Finally, the solution in the presence of the photocatalyst (—) showed no peaks associated with *chlorophyll*, with levels close to zero, demonstrating the destruction or elimination of the *chlorophyll* pigment. This suggests that after 1 hour of continuous illumination in the presence of the photocatalyst, it is an effective treatment to kill diatoms.

8.4. Microalgae absorption spectra

Chlorophylls and carotenoids are essential pigments in photosynthesis, where they play complementary roles in light-harvesting. *Chlorophylls* have a closed, fully conjugated tetrapyrrole, forming an aromatic structure with electron density delocalization in the π -orbitals

[9]. This type of structure produces electronic transitions from the higher molecular orbitals to the lower unoccupied molecular orbitals, providing absorption of light in the blue (*Soret bands*) and red (*Q bands*) to the near-infrared region [10]. In a typical absorption spectrum, the intense Soret bands are observed in the ≈ 400 - 500 nm region, while the lower intensity Q bands are observed in the ≈ 500 - 700 nm region [11–13]. The light absorption patterns of the microalgae in the different experiments are shown in Fig. 8.5. The wavelength was scanned in the range of 400-800 nm. In the absorption spectrum of unilluminated cells (—), narrow bands with absorption maxima at ≈ 681.39 and ≈ 639.14 nm were observed, corresponding to *chlorophylls a* and *b*, respectively [14]. Carotenoids have broad absorptions with shoulders in the blue spectral region between 400 and 500 nm [15].

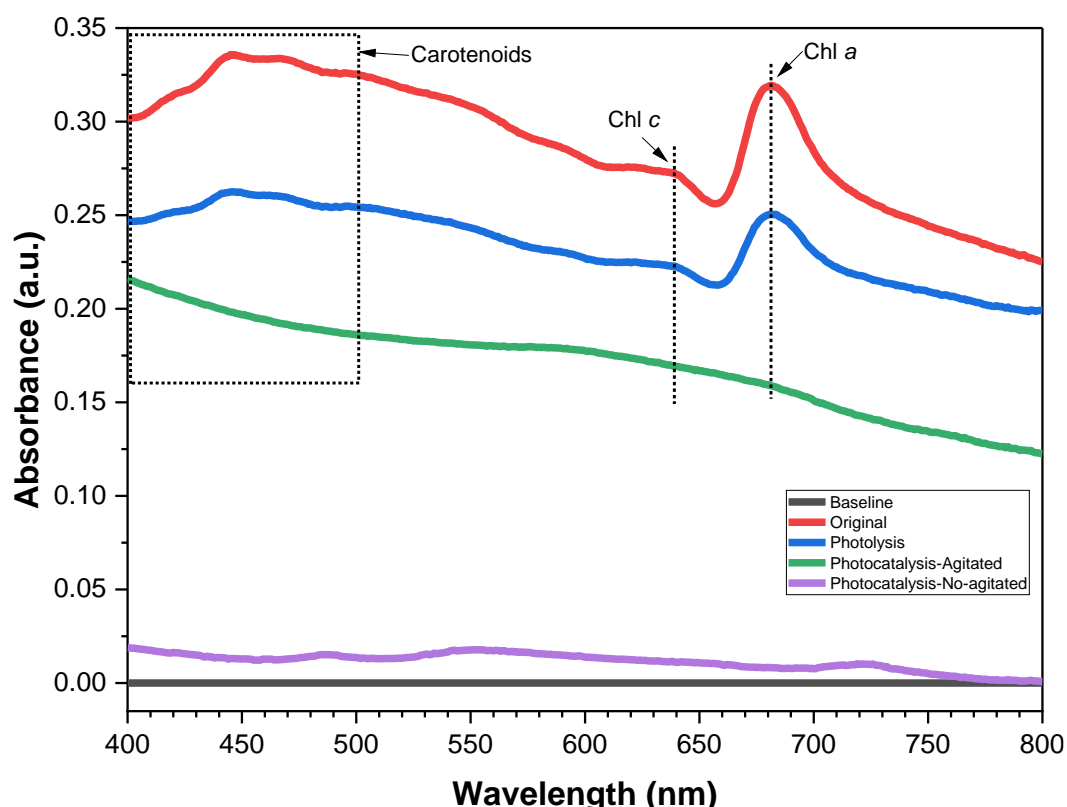


Fig. 8.5. Absorption spectra of *Phaeodactylum tricornerutum* cells without prior illumination (—), and cells after continuous illumination for 1 h: in the absence of the photocatalyst (—*photolysis*) and the presence of the photocatalyst (—*agitated* and —*no-agitated*).

After illumination and in the absence of the photocatalyst (—), it is possible to observe the same peaks as in the original cells, but with a decrease in absorbance intensity. Quantitative analysis of the intensity showed a decrease of 21.67% for *chlorophyll a* (≈ 681.39 nm), 18.26% for *chlorophyll c* (≈ 639.14 nm), and 22.09% for the *carotenoid* intensity at ≈ 444.69 nm. These values, which are close to each other, would indicate damage or stress in microalgae and would confirm the effect of light itself on photosynthetic processes and pigment integrity in cells. Finally, the absorbance of the solution in the presence of the photocatalyst was measured in two ways. The first measurement was made after the solution had been left to stand overnight without stirring. Under these conditions, a completely transparent solution was observed, as

shown in Figure 7.7 (photocatalysis), but with sediment at the bottom of the measuring cuvette. The absorbance under these conditions (—) showed intensities close to zero, very similar to the baseline (H₂O). The second measurement was carried out in the presence of stirring to homogenize the solution with the sediment. In this case, the absorbance intensity was increased (—), showing a turbid solution with no coloration. It is worth noting that in both measurements the peaks corresponding to *chlorophylls* and *carotenoids* disappeared, confirming the destruction of the pigments. The higher absorbance intensity in the turbid solution (—) may be related to the presence of suspended cells that scatter the light [16] and contribute to the total absorbance. Subsequent sedimentation may result in a decrease in turbidity and thus a decrease in intensity (—). This difference was seen in the light microscopy images. The photographs in Fig. 8.6. provided visual confirmation that the algal cells in the samples were of the *fusiform* type shown in Fig. 2.10. of Chapter 2. The solution in absence showed no apparent difference from the original solution (8.6.a and b), while Fig. 8.6.c, in contrast to the turbid sample in Fig. 8.6.d, showed little suspended cell content, confirming the light absorption patterns of the microalgae described.

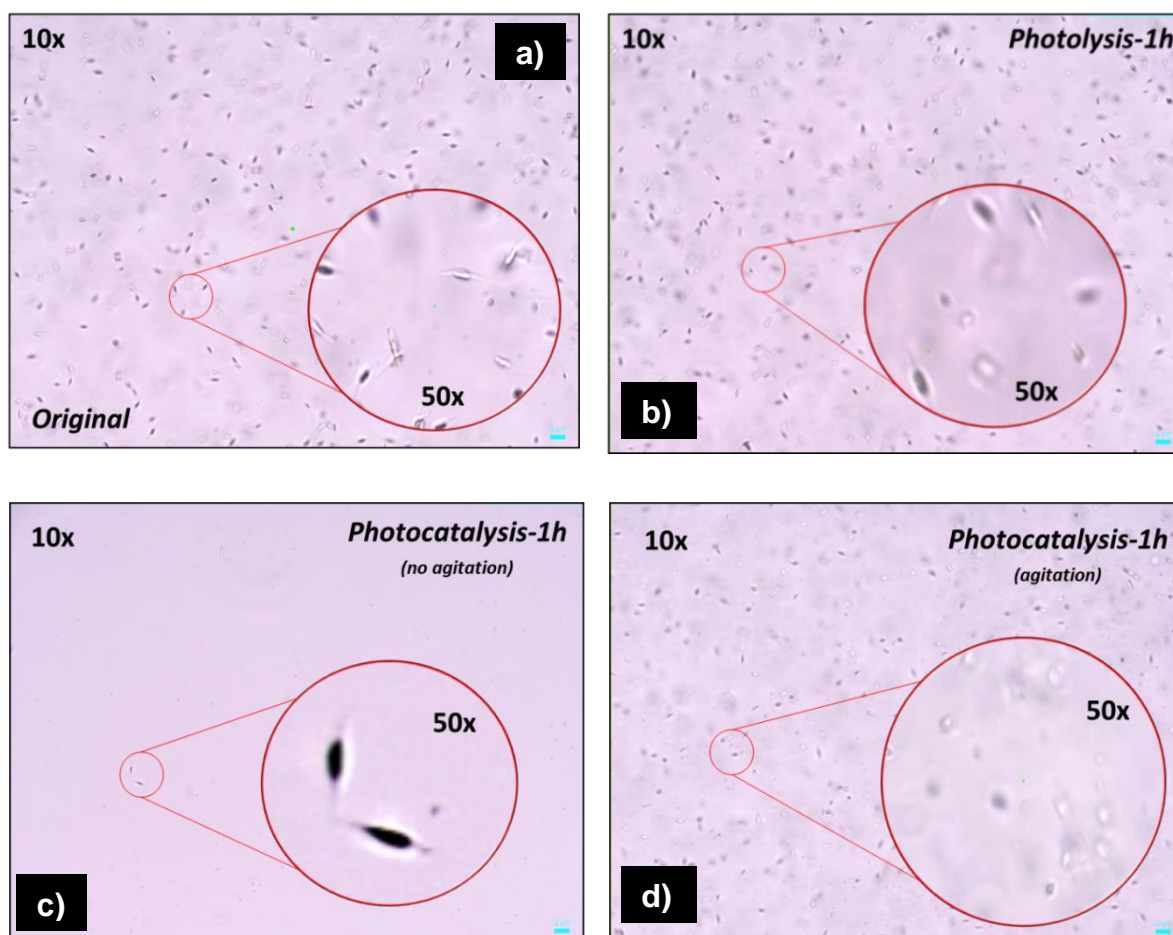


Fig. 8.6. Optical microscopic observation of diatoms: (a) without prior illumination, (b) cells after continuous illumination for 1 h in the absence of the photocatalyst, and (c) in the presence of the photocatalyst agitated, and (d) in the presence of the photocatalyst agitated.

8.5. Quantification of cell concentration

Quantification of *Phaeodactylum tricornerutum* cells concentration was performed by flow cytometry. Flow cytometry is a technique used to detect and measure the physical and chemical characteristics of a population of cells or particles. In flow cytometry, cells or particles are suspended in a fluid and passed through a laser beam, where the scattered light is characteristic of the cells and their components. Cells are often labeled with fluorescent markers, and the emitted fluorescence is measured to analyze multiple parameters of the cells [17]. The results showed a decrease in the concentration of live cells emitting fluorescence, as demonstrated in Fig. 8.7. After illumination in the absence of the photocatalyst, the concentration decreased by $\approx 34.04\%$, while in presence the concentration decreased by $\approx 99\%$.

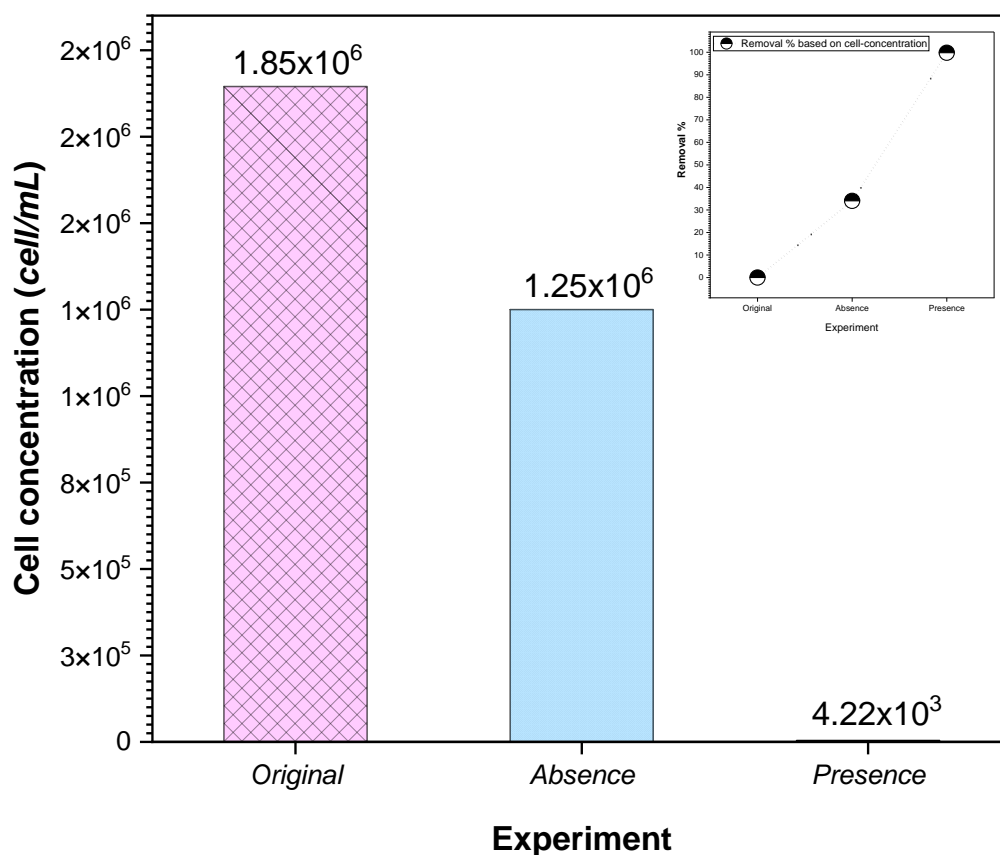


Fig. 8.7. Quantification of *Phaeodactylum tricornerutum* cells concentration by flow cytometry

8.6. Molecular analysis after degradation by Raman spectroscopy

In an attempt to look for possible by-product formation, we performed a comprehensive analysis of the chemical bonds present in the microalgae solution by Raman spectroscopy before and after illumination in the presence and absence of the photocatalyst. Fig. 8.8. illustrate the comparison of the Raman spectra.

The spectrum of the original solution with microalgae shows defined bands associated with proteins, carotenoids, and lipids. After illumination in the absence of the photocatalyst, a

reduction in the intensity of the bands is observed, demonstrating an effect caused by the light itself. Subsequently, analysis of the Raman spectrum of the illuminated sample in the presence of the photocatalyst shows that the bands associated with the dye are no longer visible. The absence of the associated Raman bands confirms that the specific vibrational characteristics of the associated products have changed or disappeared due to photocatalysis. The interaction of the e^-/h^+ pairs generated by the activation of the photocatalyst with the solution led to the breaking of bonds and the degradation of the molecules, giving rise to simpler and less colored compounds as confirmed by Uv-Vis. This degradation explains the discoloration, as the final products formed are less absorbent in the visible range of the electromagnetic spectrum.

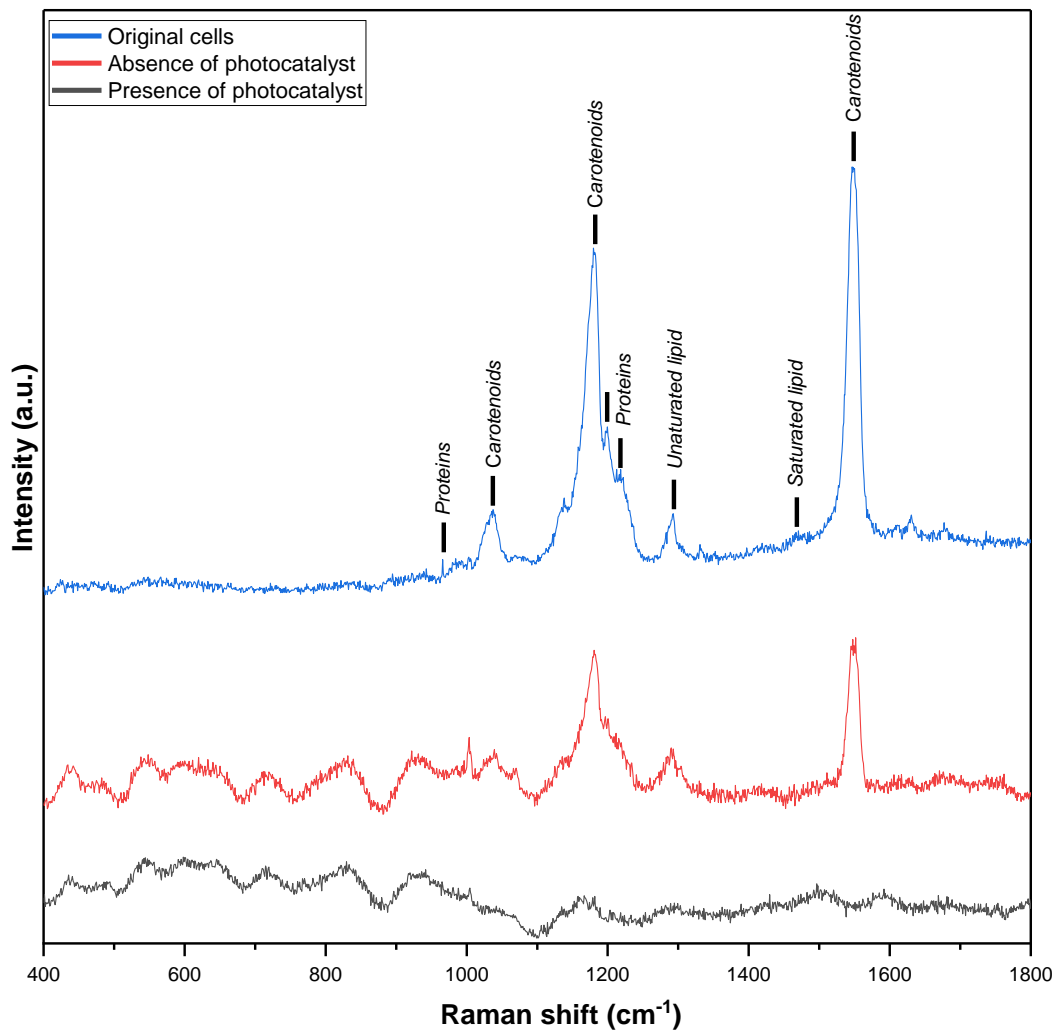


Fig. 8.8. Raman spectrum of solutions with *Phaeodactylum tricornutum* cells in the absence and presence of photocatalyst.

8.7. Conclusion

This chapter is a major step towards translating research into tangible solutions for environmental challenges. The performed study concerns microalgae cell death and the degradation of associated by-products such as chlorophylls and carotenoids. Through extensive concentration measurements, it has been shown that the introduction of photocatalysts leads to

99% microalgae cell death after 1 hour of visible illumination. The findings presented in this chapter not only contribute to the academic understanding of microalgal dynamics but also provide practical insights that can serve as a basis for the design and implementation of real-world solutions. By bridging the gap between theory and application, this research paves the way for the effective use of TiO₂-GO-based nanomaterials in mitigating environmental degradation, thus fostering sustainable practices for the preservation of aquatic ecosystems.

References

1. Hu, Q.: Environmental Effects on Cell Composition. Handbook of Microalgal Culture: Applied Phycology and Biotechnology: Second Edition. 114–122 (2013). <https://doi.org/10.1002/9781118567166.CH7>
2. Williams, P.J.L.B., Laurens, L.M.L.: Microalgae as biodiesel & biomass feedstocks: Review & analysis of the biochemistry, energetics & economics. Energy Environ Sci. 3, 554–590 (2010). <https://doi.org/10.1039/B924978H>
3. Guedes, A.C., Amaro, H.M., Malcata, F.X.: Microalgae as Sources of Carotenoids. Marine Drugs 2011, Vol. 9, Pages 625–644. 9, 625–644 (2011). <https://doi.org/10.3390/MD9040625>
4. Chislock, M., Doster, E.: Eutrophication: Causes, Consequences, and Controls in Aquatic Ecosystems. Nature Education (2013)
5. Schindler, D.W.: Recent advances in the understanding and management of eutrophication. Limnol Oceanogr. 51, 356–363 (2006). https://doi.org/10.4319/LO.2006.51.1_part_2.0356
6. Olguín, E.J.: Phycoremediation: key issues for cost-effective nutrient removal processes. Biotechnol Adv. 22, 81–91 (2003). [https://doi.org/10.1016/S0734-9750\(03\)00130-7](https://doi.org/10.1016/S0734-9750(03)00130-7)
7. Chen, F., Xiao, Z., Yue, L., Wang, J., Feng, Y., Zhu, X., Wang, Z., Xing, B.: Algae response to engineered nanoparticles: current understanding, mechanisms and implications. Environ Sci Nano. 6, 1026–1042 (2019). <https://doi.org/10.1039/C8EN01368C>
8. Fratamico, A., Tocquin, P., Franck, F.: The chlorophyll a fluorescence induction curve in the green microalga *Haematococcus pluvialis*: further insight into the nature of the P–S–M fluctuation and its relationship with the “low-wave” phenomenon at steady-state. Photosynth Res. 128, 271–285 (2016). <https://doi.org/10.1007/S11120-016-0241-2>
9. Chlorophyll - American Chemical Society, <https://www.acs.org/molecule-of-the-week/archive/c/chlorophyll.html>
10. Torres, M.A., Ritchie, R.J., Lilley, R.M.C., Grillet, C., Larkum, A.W.D.: Measurement of photosynthesis and photosynthetic efficiency in two diatoms. N Z J Bot. 52, 6–27 (2014). <https://doi.org/10.1080/0028825X.2013.831917>
11. Gross, J.: Pigments In Vegetables - Chlorophylls And Carotenoids. (1991)
12. Almomani, F.A., Örmeci, B.: Monitoring and measurement of microalgae using the first derivative of absorbance and comparison with chlorophyll extraction method. Environ Monit Assess. 190, 1–19 (2018). <https://doi.org/10.1007/S10661-018-6468-Y>
13. Akimoto, S., Teshigahara, A., Yokono, M., Mimuro, M., Nagao, R., Tomo, T.: Excitation relaxation dynamics and energy transfer in fucoxanthin–chlorophyll a/c-protein complexes, probed by time-resolved fluorescence. Biochimica et Biophysica Acta (BBA) - Bioenergetics. 1837, 1514–1521 (2014). <https://doi.org/10.1016/J.BBABIO.2014.02.002>
14. Oka, K., Ueno, Y., Yokono, M., Makio, S., Shen, J.-R., Nagao, R., Akimoto, S.: Adaptation of light-harvesting and energy-transfer processes of a diatom *Phaeodactylum tricorutum* to different light qualities. Photosynth Res. 146, 227–234 (2020). <https://doi.org/10.1007/s11120-020-00714-1>
15. Fabrowska, J., Messyasz, B., Szyling, J., Walkowiak, J., Łęska, B.: Isolation of chlorophylls and carotenoids from freshwater algae using different extraction methods. Phycological Res. 66, 52–57 (2018). <https://doi.org/10.1111/PRE.12191>
16. Popek, E.: Practical Approach to Sampling. Sampling and Analysis of Environmental Chemical Pollutants. 145–225 (2018). <https://doi.org/10.1016/B978-0-12-803202-2.00004-5>
17. Ormerod, M.G., Imrie, P.R.: Flow Cytometry. Animal Cell Culture. 543–558. <https://doi.org/10.1385/0-89603-150-0:543>

General conclusions

In this research, GOs with different oxidation degrees have been synthesized, achieving this variability by gradual manipulation of KMnO_4 . Subsequently, the GOs were incorporated into hybrid nanostructures with TiO_2 . The fabrication of these nanostructures was carried out by two different methods: ball-milling and photosonication, respectively. Despite using the same materials and concentrations in both methods, significant differences in the morphologies and characteristics of the resulting nanostructures were observed, highlighting the crucial importance of the fabrication method in modulating essential properties that contribute to the improvement of processes such as adsorption and/or photocatalysis.

1. Initially, theoretical studies using Density Functional Theory (DFT) revealed the relationship between bandgap variations and epoxide functional groups in GO. A gradual increase in bandgap was observed as the O/C ratio varies, due to the alteration of the hexagonal structure of graphene. Also, the potential for connectivity and interface in TiO_2 -GO systems was highlighted, where the integration of GO reduces the bandgap of TiO_2 . These findings emphasize the importance of DFT simulations to understand and optimize the atomic interactions that occur in both materials when studied experimentally.
2. The successful preparation of GO by the Tour method has been demonstrated, with precise control of the oxidation degree achieved by adjusting the KMnO_4 concentrations during the synthesis. Through a thorough analysis of the physicochemical properties of the obtained GOs, important insights into the structural, morphological, and chemical characteristics have been obtained. X-ray diffraction confirmed the presence and evolution of the characteristic (001) planes of GO, with a marked increase in crystallite size and interplanar spacing corresponding to higher KMnO_4 concentrations. Raman spectroscopy provided further insight, revealing a transition in structural defects and carbon ordering, from sp^3 hybridizations to vacancies and grain boundary defects, along with a reduction in the size of the graphite domains. SEM imaging corroborated these findings, showing changes in morphology indicative of increased exfoliation and disorder. Chemical composition analysis by FTIR and XPS revealed the presence and distribution of oxygenated functional groups, demonstrating a clear evolution in response to the controlled oxidation conditions.
3. The synthesis of hybrid nanostructures based on TiO_2 and GO by ball-milling has provided significant information on their microstructural, morphological, and electrical properties. Microstructural analysis revealed a complex interplay between phase composition and crystallinity, with the formation of a main TiO_2 matrix accompanied by additional phases such as rutile and brookite, indicative of structural defects and *grain boundary* formation.

Furthermore, the incorporation of GO led to a marked increase in specific surface area, accompanied by reductions in TiO₂ particle size and improvements in electrical conductivity. However, while ball-milling was effective in modifying the TiO₂ properties, the impact of the GO oxidation was less pronounced, due to the aggressiveness of the method on the material.

4. The use of photosonation emerged as a promising method to fabricate hybrid nanostructures composed of TiO₂ and GO, offering a less aggressive alternative to the conventional ball-milling technique. Through comprehensive characterization techniques including transmission electron microscopy (TEM), electron paramagnetic resonance (EPR) analysis, Fourier transform infrared spectroscopy (FTIR), and Raman spectroscopy, several key findings have been elucidated. First, TEM images revealed the core-shell morphology of the nanostructures, in which the TiO₂ particles are covered by a GO layer. This arrangement is closely related to the degree of GO oxidation: at lower oxidation, the layers are thicker and more irregular, while at higher oxidation, the layers are thinner and more uniform. Secondly, EPR analysis provided information on the increased surface concentration of Ti³⁺ ions on TiO₂ after sonication, which facilitates electrostatic attraction between the Ti³⁺ defects and the oxygenated functional groups of the GO, ultimately promoting the formation of Ti-O-C bonds at the interface. Thirdly, FTIR spectroscopy confirmed the formation of Ti-O-C bonds and revealed alterations in the optical properties, as the incorporation of GO led to a reduction of the optical bandgap values and changes in the light absorption behavior. Finally, Raman spectroscopy revealed the reduction of GO after incorporation into TiO₂.
5. The study of dye removal from MB has provided valuable insights that highlight the strong influence of the fabrication method of the hybrid nanostructures on their adsorption-photocatalysis properties. The incorporation of GO, either by ball milling or photosonation, showed a synergistic effect, improving both the adsorption and photocatalytic degradation capacity. It was shown that TiO₂-GO hybrid nanostructures fabricated by ball milling exhibit excellent MB removal capacity through the adsorption mechanism, albeit with limited photocatalytic activity. On the other hand, nanostructures obtained by photosonation showed an initially limited adsorption capacity but allowed investigation of the influence of the oxidation degree and presented a considerably improved photocatalytic efficiency. The combination of adsorption and photocatalysis on these nanostructures has shown an effective synergy in MB removal. The initial adsorption of the dye molecules facilitates their proximity to the nanostructure surface, which increases the probability of interaction with the reactive species generated during photocatalysis. This interaction results in an acceleration of the degradation and an improvement of the overall efficiency of the removal process. In conclusion, this research highlighted the importance of considering the synergy between adsorption and photocatalysis, as well as the importance of considering both the TiO₂ modification methodology and the GO oxidation to optimize the efficiency of organic pollutant removal in water.

Future potential directions

Based on the conclusions drawn from the research, several potential directions for future studies can be proposed:

1. Immobilization in films: In this research, powders of various hybrid nanostructures based on TiO₂-GO have been used. However, exploring the possibility of immobilizing these powders on substrates to create films could represent a viable alternative to allow direct application of the nanomaterials. Methods such as sol-gel or RF sputtering could be a highly recommended alternative, as they offer unique advantages, ranging from precise control of thickness and composition to flexibility in structure and compatibility with a variety of substrates, as well as high purity and homogeneity. The use of films instead of powders would offer many significant advantages in a variety of applications.

2. Reduction of graphene oxide: This research has demonstrated the significant impact of GO oxidation on the properties of hybrid nanostructures. Future studies could focus on fine-tuning the oxidation process to achieve specific structural and functional characteristics in GO. One of them could be the creation of reduced graphene oxide (rGO), which could combine structural features of high oxidation such as high exfoliation, nanometer size, and higher dispersion, with the outstanding properties of low oxidation such as electrical conductivity and chemical stability due to its more planar and less defective structure.

3. Variation of the GO concentration. Although the results obtained with 2% GO have been outstanding, increasing the GO concentration could offer new perspectives and possibilities in terms of the properties of the resulting material. Investigating how different GO concentrations affect the optical, electrical, and even mechanical properties of the TiO₂-GO matrix could provide valuable information to optimize its performance.

4. Scalability and practical applications: The scalability and practical feasibility of the fabrication methods used in this study need to be further investigated to facilitate the translation of laboratory findings to real-world applications. Large-scale synthesis of hybrid TiO₂-GO nanostructures and their evaluation under realistic environmental conditions could provide valuable data to assess their potential for water purification and remediation.

5. Other contaminants: In the context of the previous paragraph, possible future directions of this research could focus on the exploration of hybrid nanostructures in the removal of other pollutants, such as FPAS, and pharmaceuticals, as well as in the eradication of living organisms, including viruses, bacteria, and invasive aquatic plants. These additional aspects

represent important challenges in preserving the health of aquatic ecosystems and protecting native species. Investigating the effectiveness of hybrid nanostructures in removing these pollutants and undesirable organisms could provide innovative and sustainable solutions to address critical environmental problems.

6. Exploration of multifunctional nanostructures: In addition to TiO₂-GO hybrid nanostructures, the synthesis of multifunctional nanostructures incorporating other nanomaterials or functional additives could be explored. Combining TiO₂-GO with materials such as metal nanoparticles or carbon nanotubes can produce synergistic effects that enhance adsorption and photocatalytic properties for the elimination of a broad spectrum of organic contaminants from water.

Supplementary information

Fig. S.2.1. Equipment used for characterization of the materials manufactured in this research. (a) Bruker D2 PHASER diffractometer, (b) Bragg-Brentano PANalytical Empyrean Bragg-Brentano diffractometer; (c) X'Plora Raman Spectrometer; (d) Vertex 60V Spectrometer ; (e) Scanning Electron Microscope (JEOL, JSM 6510 LV); (f) Microscope JEOL JEM 2100 HR -IMMM; (g) UV-Vis Spectrophotometer, Agilent Cary ; (h) Ocean Optics ISP-REF integrating sphere; (i) Electron paramagnetic resonance spectrometer; (j) Novocontrol Broadband Dielectric Spectrometer (Alpha-A High-Performance Frequency Analyzer); (k) Dual-beam spectrophotometer (Perkin Elmer) with Dual PAM-100.



Fig. S.4.1. Raman spectra's Lorentzian deconvolutions of GO nanostructures with different oxidation degrees.

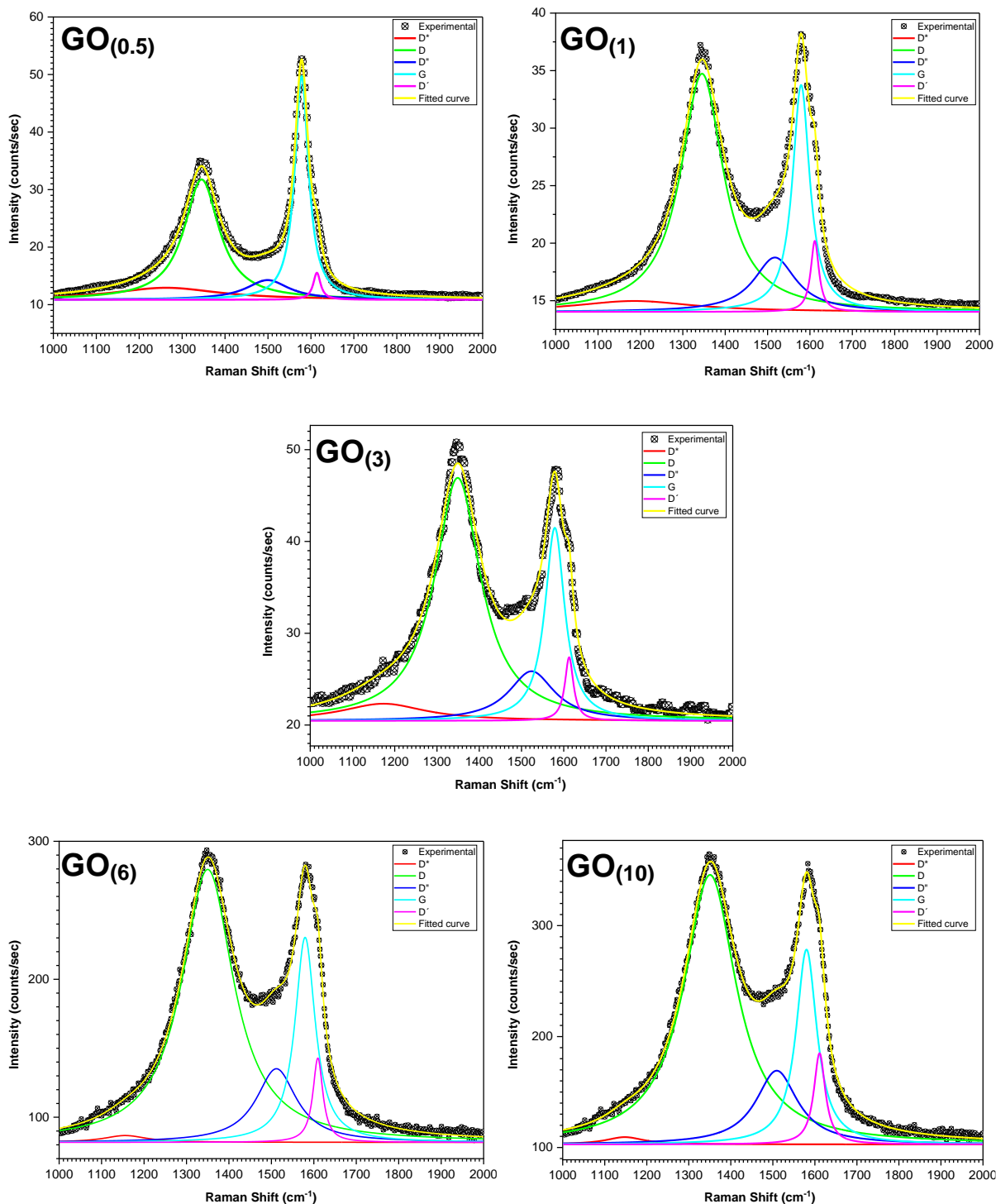


Table S.5.1. Hybrid TiO₂-based structures fabricated by ball-milling

Hybrid nanostructures	Applications	Ref.
CdS/TiO ₂	Photocatalysis	[1]
TiO ₂ /CaCO ₃	Photocatalysis	[2]
TiO ₂ -carbon nanotubes	Photocatalysis	[3]
TiO ₂ /ZnO	UV-protection	[4]
TiO ₂ /ZnO	Photovoltaic applications	[5]
TiO ₂ /Fe ₂ O ₃	Arsenic adsorption	[6]
TiO ₂ /GO	MB degradation	[7]
WO ₃ /TiO ₂	Photocatalysis	[8]
Fe/TiO ₂	Photocatalysis	[9]
TiO ₂ /CuPc	Solar cells	[10]
SnO ₂ /TiO ₂	Photocatalysis	[11]

Fig. S.5.1. Raman spectra's Lorentzian deconvolutions of TiO₂-GO hybrid nanostructures by ball-milling.

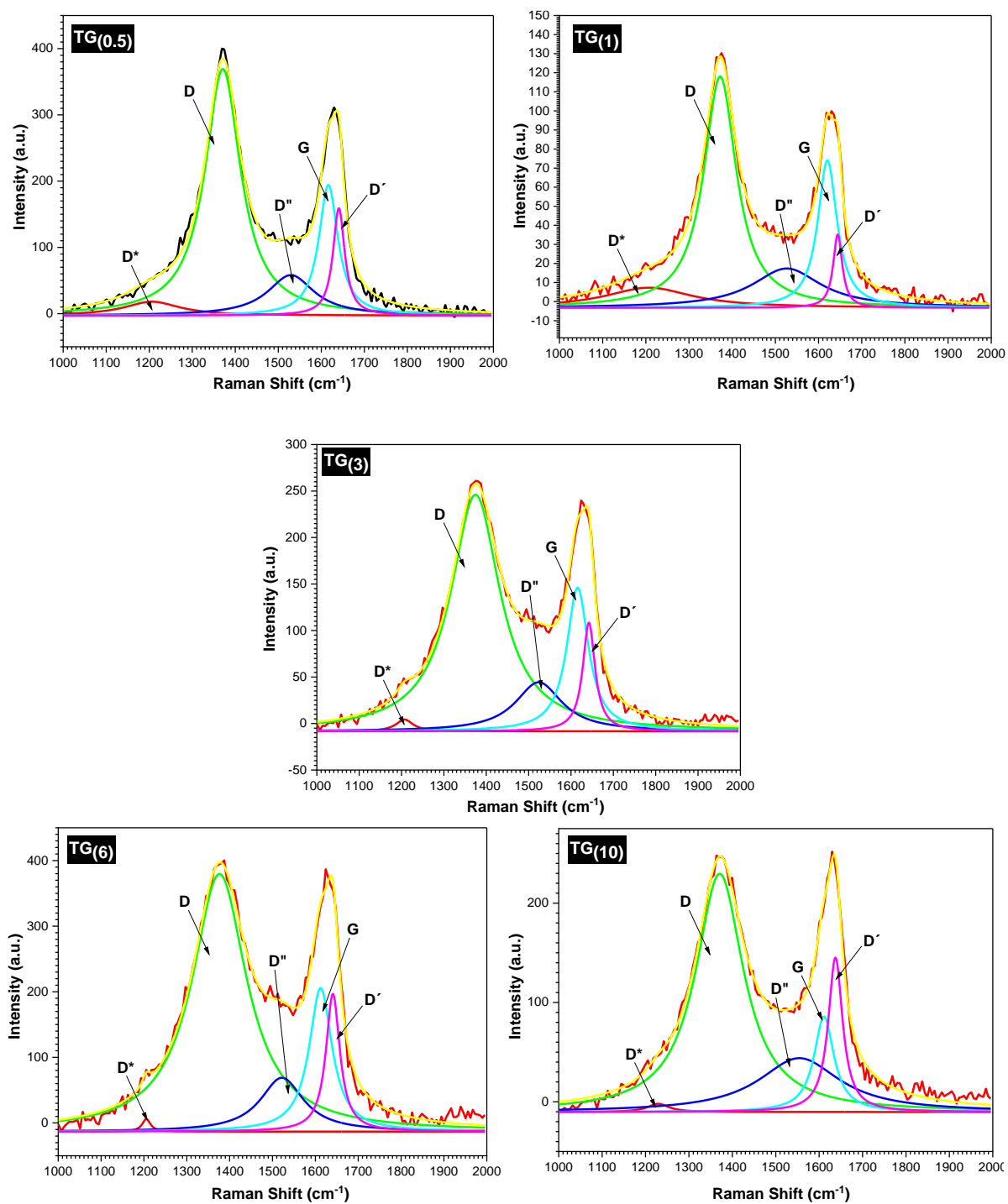


Fig. S.5.2. FT-IR spectra Lorentzian deconvolutions of TiO₂-GO hybrid nanostructures fabricated by ball-milling.

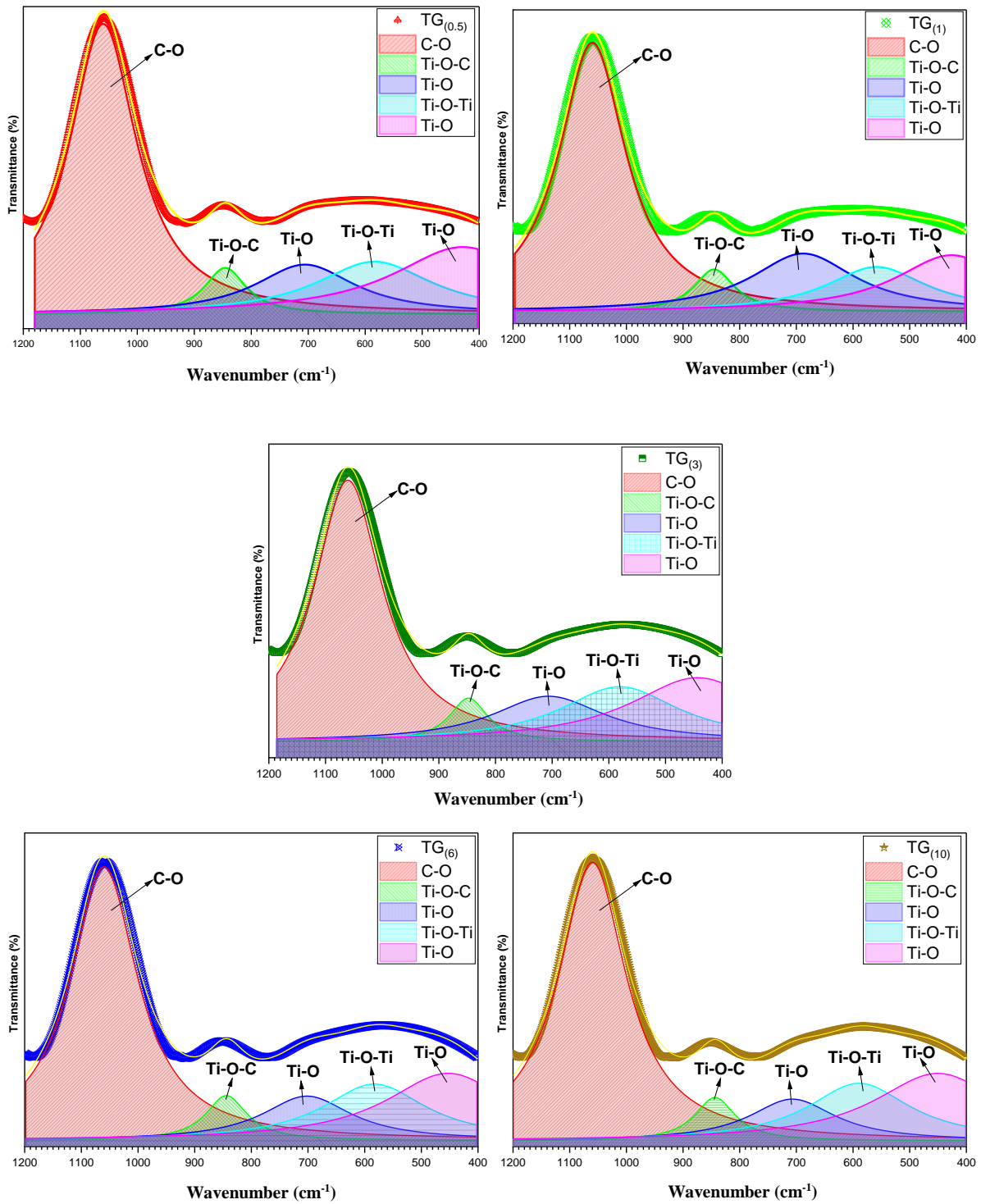


Fig. S.6.1. SEM/ TEM images of hybrid core-shell nanostructures TiO₂-GO fabricated by photosonification

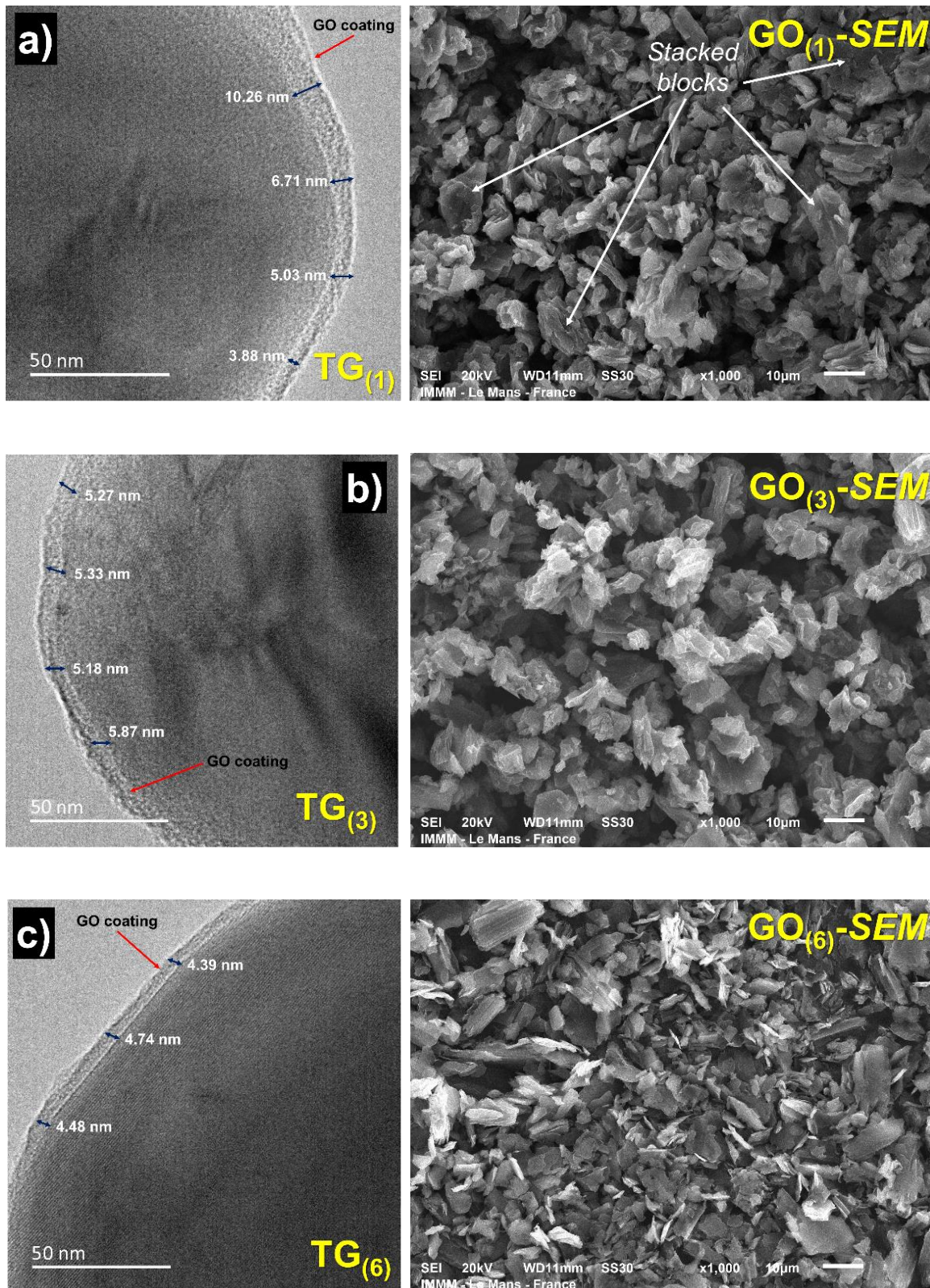


Fig. S.6.2. Lorentzian deconvolution of the Raman spectra of TiO₂-GO nanostructures fabricated by photosonification (a) TG_(0.5), (b) TG₍₁₎ and (c) TG₍₃₎, (d) TG₍₆₎, (e) TG₍₁₀₎

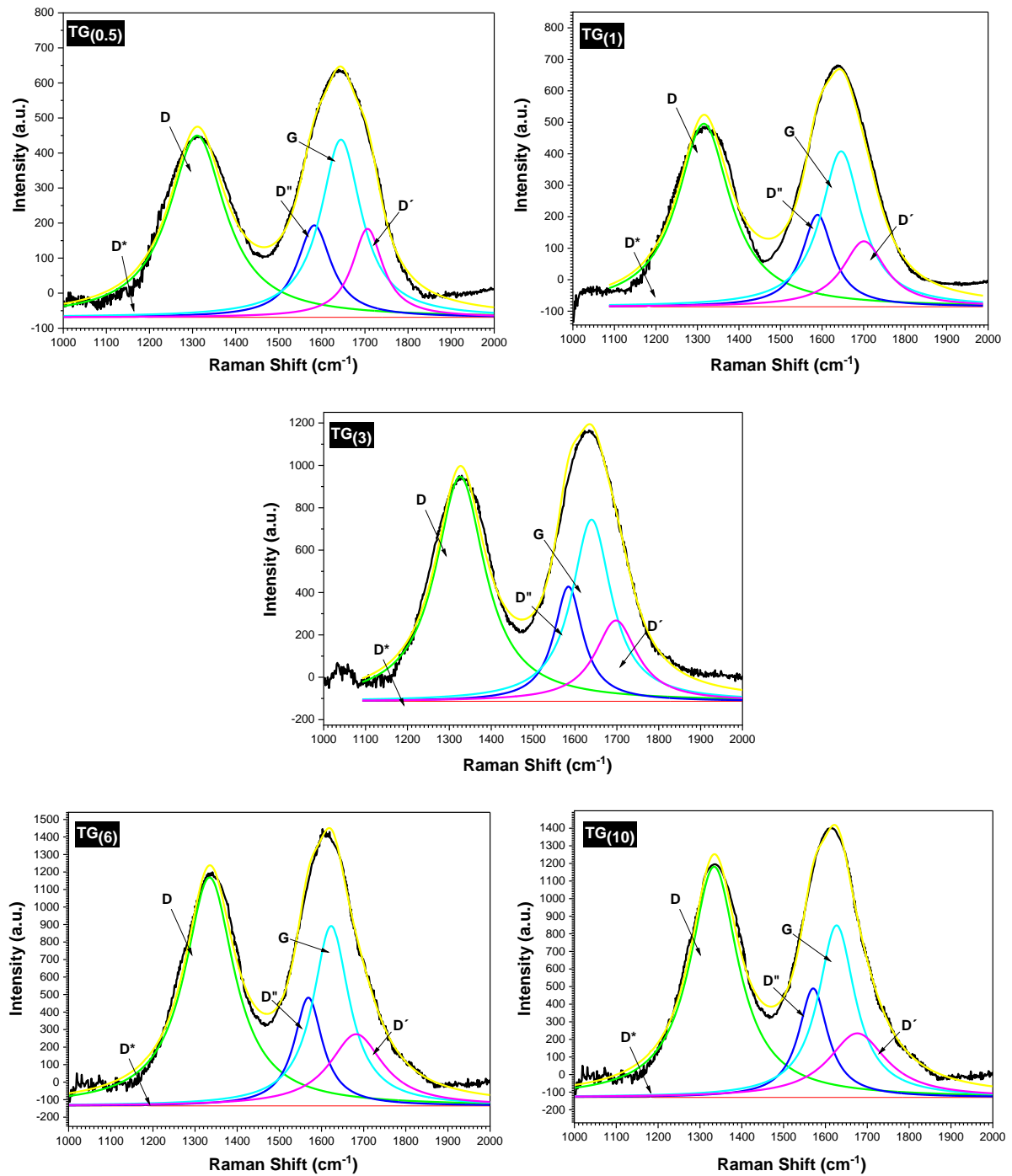


Fig. S.6.3. Lorentzian deconvolution of the FTIR spectra in the range of 400 to 900 cm^{-1} , of TiO_2 -GO nanostructures fabricated by photsonification (a) $\text{TG}_{(0.5)}$, (b) $\text{TG}_{(1)}$ and (c) $\text{TG}_{(3)}$, (d) $\text{TG}_{(6)}$, (e) $\text{TG}_{(10)}$

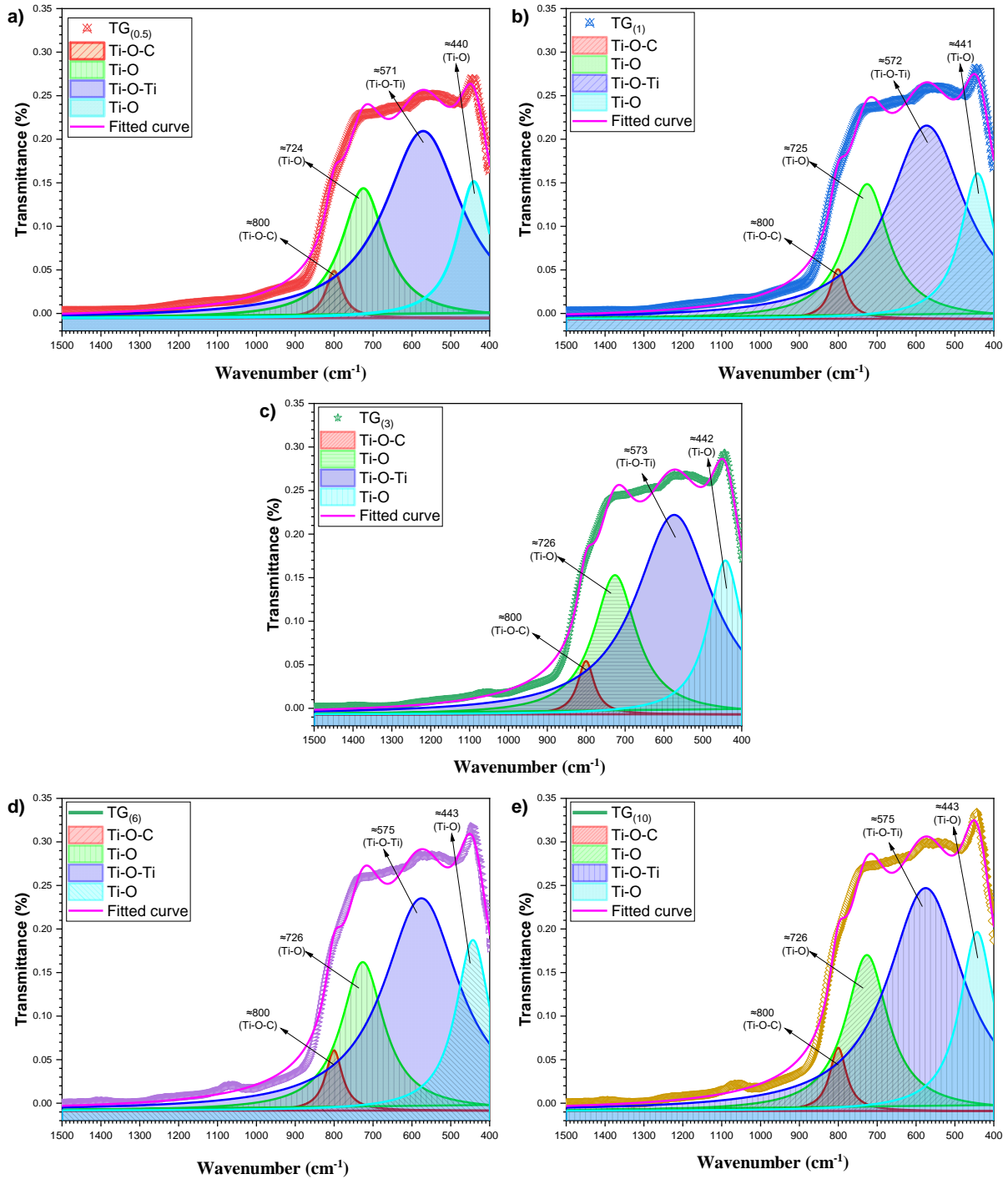


Fig. S.6.4. Plots of Kubelka-Munk vs the energy of absorbed light to determine the optical bandgap of hybrid nanostructures fabricated by photosonification.

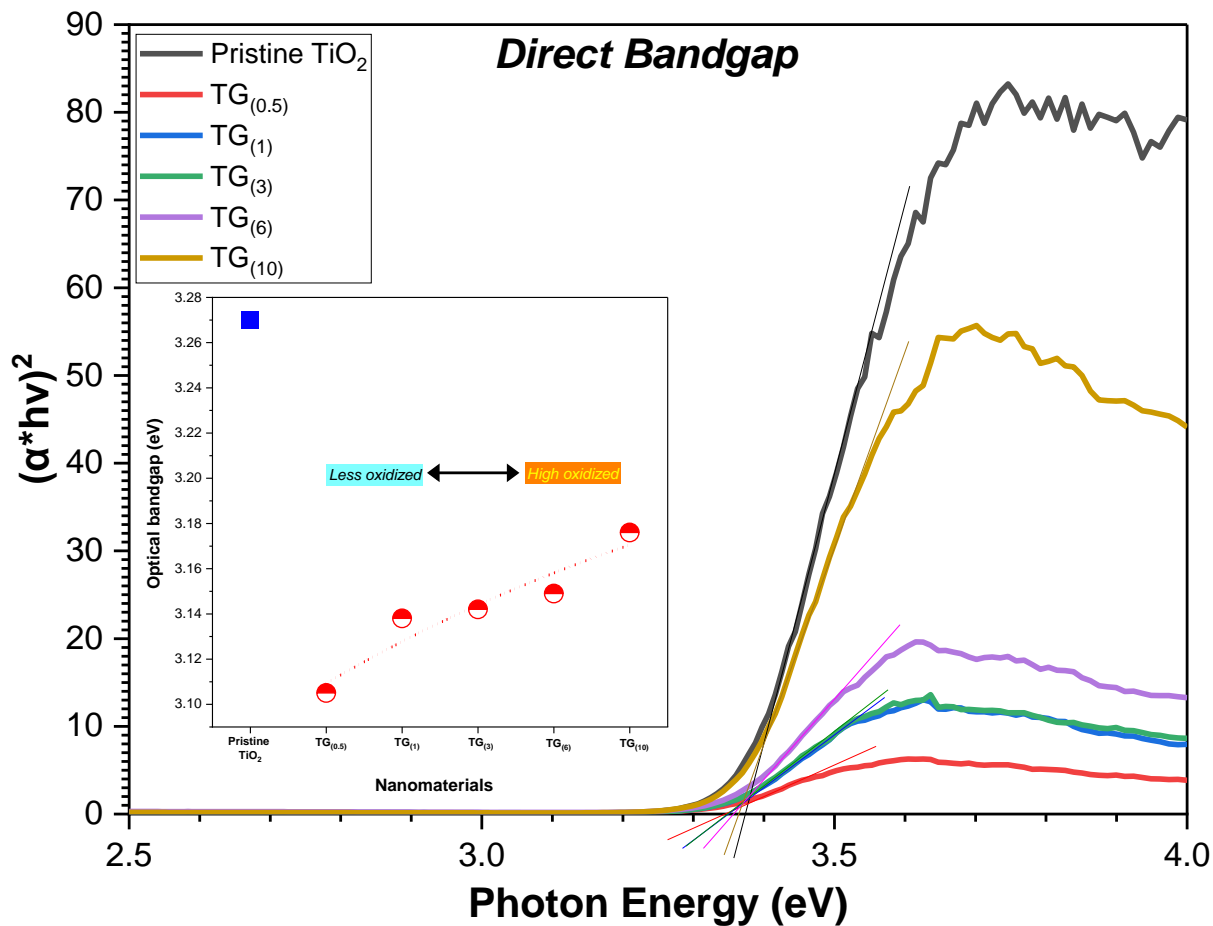


Table S.6.4. The fitting parameters obtained from experimental data of the conductivity (σ) as a function of Temperatures using Jonscher's power law

T(K)	σ_{DC} (S/cm)	A	n
173	1.52×10^{-9}	1.80×10^{-15}	1.29323
193	3.04×10^{-9}	3.59×10^{-15}	1.29323
213	1.06×10^{-8}	1.26×10^{-14}	1.29323
233	1.52×10^{-8}	1.80×10^{-14}	1.29323
253	2.92×10^{-8}	3.45×10^{-14}	1.29323
273	1.52×10^{-7}	1.80×10^{-13}	1.29322
293	2.06×10^{-7}	7.86×10^{-14}	1.34862
313	2.14×10^{-7}	3.75×10^{-14}	1.39157
333	2.29×10^{-7}	7.57×10^{-15}	1.48815
353	2.50×10^{-7}	2.64×10^{-14}	1.39703
373	2.90×10^{-7}	3.80×10^{-12}	1.07262
393	1.37×10^{-7}	6.62×10^{-10}	0.76948
413	2.60×10^{-7}	4.35×10^{-10}	0.88194
433	8.57×10^{-6}	4.16×10^{-9}	0.7579
453	1.12×10^{-4}	5.67×10^{-7}	0.48275
473	1.50×10^{-3}	8.39×10^{-7}	0.53236

References:

1. Ye, M., Pan, J., Guo, Z., Liu, X., Chen, Y.: Effect of ball milling process on the photocatalytic performance of CdS/TiO₂ composite. *Nanotechnol Rev.* 9, 558–567 (2020). <https://doi.org/10.1515/ntrev-2020-0045>
2. Kighuta, K., Kim, S.W., Hou, Y.L., Lee, K.P., Kim, W.J.: Facile and Simple Post Treatment Ball Milling Strategy for the Production of Low-Cost TiO₂ Composites with Enhanced Photocatalytic Performance and Applicability to Construction Materials. *Materials.* 16, 4931 (2023). <https://doi.org/10.3390/MA16144931/S1>
3. Orge, C.A., Soares, O.S.G.P., Faria, J.L., Pereira, M.F.R.: Synthesis of TiO₂-Carbon Nanotubes through ball-milling method for mineralization of oxamic acid (OMA) by photocatalytic ozonation. *J Environ Chem Eng.* 5, 5599–5607 (2017). <https://doi.org/10.1016/J.JECE.2017.10.030>
4. Yang, P., Wang, H., Chen, Y., Li, Y., Zhang, J., Zhang, C., Lin, B., Wei, X.: Ball-milling of titanium dioxide and zinc oxide for enhanced UV protection. *Front Mater.* 10, 1273659 (2023). <https://doi.org/10.3389/fmats.2023.1273659>
5. Malevu, T.D.: Ball Milling synthesis and characterization of highly crystalline TiO₂-ZnO hybrids for photovoltaic applications. *Physica B Condens Matter.* 621, 413291 (2021). <https://doi.org/10.1016/J.PHYSB.2021.413291>
6. Babudurai, M., Nwakanma, O., Romero-Nuñez, A., Manisekaran, R., Subramaniam, V., Castaneda, H., Jantrania, A.: Mechanical activation of TiO₂/Fe₂O₃ nanocomposite for arsenic adsorption: effect of ball-to-powder ratio and milling time. *J Nanostructure Chem.* 11, 619–632 (2021). <https://doi.org/10.1007/S40097-021-00388-8>
7. Ahmad, J., Sofi, F.A., Mehraj, O., Majid, K.: Fabrication of highly photocatalytic active anatase TiO₂-graphene oxide heterostructures via solid phase ball milling for environmental remediation. *Surfaces and Interfaces.* 13, 186–195 (2018). <https://doi.org/10.1016/J.SURFIN.2018.09.010>
8. Shifu, C., Lei, C., Shen, G., Gengyu, C.: The preparation of coupled WO₃/TiO₂ photocatalyst by ball milling. *Powder Technol.* 160, 198–202 (2005). <https://doi.org/10.1016/J.POWTEC.2005.08.012>
9. Rodrigues, A.E., Paluch, A.S., Taghipour, S., Yeung, K.-L., Ataie-Ashtiani, B.: Efficiency of Mechanochemical Ball Milling Technique in the Preparation of Fe/TiO₂ Photocatalysts. *ChemEngineering* 2022, Vol. 6, Page 77. 6, 77 (2022). <https://doi.org/10.3390/CHEMENGINEERING6050077>
10. Mekprasart, W., Jarernboon, W., Pecharapa, W.: TiO₂/CuPc hybrid nanocomposites prepared by low-energy ball milling for dye-sensitized solar cell application. *Materials Science and Engineering: B.* 172, 231–236 (2010). <https://doi.org/10.1016/J.MSEB.2010.05.022>
11. Shifu, C., Lei, C., Shen, G., Gengyu, C.: The preparation of coupled SnO₂/TiO₂ photocatalyst by ball milling. *Mater Chem Phys.* 98, 116–120 (2006). <https://doi.org/10.1016/J.MATCHEMPHYS.2005.08.073>

Contributions

i. Peer-reviewed articles in SCOPUS-indexed journals

Cano, F. J., Coste, S., Reyes-Vallejo, O., Velumani, S., Iouri Koudriavtsev, & Kassiba, A. (2024). A mini-review of the influence of GO integration with TiO₂ in hybrid nanostructures: A water remediation perspective (Review and editing process)

Cano, F. J., Coste, S., Reyes-Vallejo, O., Velumani, S., Iouri Koudriavtsev, & Kassiba, A. (2024). Effect of GO concentration on the morphology of TiO₂-GO hybrids and its influence on adsorption-photocatalysis processes. *Materials Letters*.

Cano, F. J., Coste, S., Reyes-Vallejo, O., Makowska-Janusik, M., Velumani, S., de la Luz Olvera, M., & Kassiba, A. (2024). Influence of GO oxidation degrees on the organization and physical features of TiO₂-GO-based nanocomposites for water dye removal. *Surfaces and Interfaces*, 46, 104004. <https://doi.org/10.1016/j.surfin.2024.104004>

Cano, F. J., Romero-Núñez, A., Liu, H., Reyes-Vallejo, O., Ashok, A., Velumani, S., & Kassiba, A. (2023). Variation in the bandgap by gradual reduction of GOs with different oxidation degrees: A DFT analysis. *Diamond and Related Materials*, 139, 110382. <https://doi.org/10.1016/j.diamond.2023.110382>

Cano, F. J., Reyes-Vallejo, O., Ashok, A., Olvera, M. D. L. L., Velumani, S., & Kassiba, A. (2023). Mechanisms of dye adsorption on titanium oxide-graphene oxide nanocomposites. *Ceramics International*, 49(13), 21185-21205. <https://doi.org/10.1016/j.ceramint.2023.03.249>

ii. Peer-reviewed proceedings indexed in SCOPUS

Cano, F. J., Korolevych, O., Makowska-Janusik, M., Coste, S., Ashok, A., Velumani, S., & Kassiba, A. (2023, October). G and GO interaction into TiO₂(010) anatase and its influence on the bandgap: DFT Study. *20th International Conference on Electrical Engineering, Computing Science and Automatic Control (CCE)* (pp. 1-5). IEEE. <https://doi.org/10.1109/CCE60043.2023.10332908>

Cano, F. J., Reyes-Vallejo, O., Romero-Núñez, A., García, J. C., García-Sotelo, A., Velumani, S., & Kassiba, A. (2022, November). MB adsorption by TiO₂/GO nanocomposites: A comparison of the synthesis method. *19th International Conference on Electrical Engineering, Computing Science and Automatic Control (CCE)* (pp. 1-6). IEEE. <https://doi.org/10.1109/CCE56709.2022.9975906>

Cano, F. J., Reyes-Vallejo, O., Díaz, J. J., Velumani, S., & Kassiba, A. (2022, November). Effect of the oxidation degree on the bandgap of graphene oxides by Tour method. *19th International Conference on Electrical Engineering, Computing Science and Automatic Control (CCE)* (pp. 1-6). IEEE. <https://doi.org/10.1109/CCE56709.2022.9975930>

Cano, F. J., Romero-Núñez, A., Jantrania, A., Liu, H., Kassiba, A., & Velumani, S. (2021, November). Bandgap dependence on facet and size engineering of TiO₂: A DFT Study. *18th International Conference*

on Electrical Engineering, Computing Science and Automatic Control (CCE) (pp. 1-5). IEEE. <https://doi.org/10.1109/CCE53527.2021.9632880>

iii. Divulgation publications

Cano, F. J., Reyes-Vallejo, O., Velumani, S., & Kassiba, A. (2024). Remediación del agua con nanomateriales híbridos adsorbentes. *Avance y perspectiva (Cinvestav)*. avancey perspectiva.cinvestav.mx/remediacion-del-agua-con-nanomateriales/

Cano, F. J., Coste, S., Reyes-Vallejo, O., Makowska-Janusik, M., Velumani, S., & Kassiba, A. (2024). Ingeniería de nanomateriales híbridos GO/TiO₂: *Avance y perspectiva (Cinvestav)*.

iv. International Congresses & Conferences

Cano, F. J., Coste, S., Velumani, S., & Kassiba, A. (2021). "Influence of GO Incorporation Into TiO₂ on Water Remediation by Photocatalytic Processes". Symposium F2 (Oral presentation), *XXVIII International Materials Research Congress* in Cancún, México, August 13-18, 2023.

Cano, F. J., Korolevych, O., Makowska-Janusik, M., Coste, S., Ashok, A., Velumani, S., & Kassiba, A. (2023). "G and GO interaction into TiO₂(010) anatase and its influence on the bandgap: DFT Study", Symposium Nanotechnology, Materials and Applications (Oral presentation), *20th International Conference on Electrical Engineering, Computing Science and Automatic Control (CCE)*. IEEE. Mexico city, Mexico, October 25-27, 2023

Cano, F. J., Coste, S., Reyes-Vallejo, O., Velumani, S., & Kassiba, A. (2023). "Influence of GO incorporation into TiO₂ on water remediation by adsorption process", (Poster), *RSCPoster*, 28 February 2023

Cano, F. J., Reyes-Vallejo, O., Velumani, S., & Kassiba, A. (2022). "Influence of the degree of oxidation of graphene oxides in TiO₂-GO composites on dye removal". Symposium 13. Nanostructured materials (Oral presentation), *XX International Congress on Metallurgy and Materials* in Mar del Plata, Argentina, May 2-6, 2022

Cano, F. J., Romero-Núñez, A., Reyes-Vallejo, O., Velumani, S., & Kassiba, A. (2022). "TiO₂/GO composites for Methylene Blue removal: Influence of the Oxidation degree of GO". Symposium D4 (Oral presentation), *XXX International Materials Research Congress (IMRC2022) and International Conference on Advanced Materials (ICAM2021)* in Cancún, México, August 14-19, 2022

Cano, F. J., Reyes-Vallejo, O., Romero-Núñez, A., García, J. C., García-Sotelo, A., Velumani, S., & Kassiba, A. (2022), "MB adsorption by TiO₂/GO nanocomposites: A comparison of the synthesis method", Symposium Nanotechnology, Materials and Applications (Oral presentation), *19th International Conference on Electrical Engineering, Computing Science and Automatic Control (CCE)*. IEEE. Mexico City, Mexico, November 9-11, 2022.

Cano, F. J., Reyes-Vallejo, O., Díaz, J. J., Velumani, S., & Kassiba, A. (2022). "Effect of the oxidation degree on the bandgap of graphene oxides by Tour method", Symposium Nanotechnology, Materials and Applications (Oral presentation) *19th International Conference on Electrical Engineering, Computing Science and Automatic Control (CCE)*. IEEE. Mexico City, Mexico, November 9-11, 2022.

Cano, F. J., Romero-Núñez, A., Liu, H., Velumani, S., & Kassiba, A. (2021). "Tuning the electronic properties of graphene oxide by incorporating functional groups: a DFT simulation". Symposium A6 (Oral presentation), *XXVIII International Materials Research Congress* in Cancún, México, August 16-20, 2021.

Cano, F. J., Romero-Núñez, A., Jantrania, A., Liu, H., Kassiba, A., & Velumani, S. (2021). "Bandgap dependence on facet and size engineering of TiO₂: A DFT Study". Symposium Nanotechnology, Materials and Applications (Oral presentation) *18th International Conference on Electrical Engineering, Computing Science and Automatic Control (CCE)*. IEEE. Mexico City, Mexico, November 10-12, 2022.

Copyright permissions

Copyright permissions can be found at the following link:

https://drive.google.com/file/d/1aEVnsFDoT1yo0KFor9yir265eA-5jd0C/view?usp=drive_link

Titre : Influence de l'oxyde de Graphene (GO) sur les nanostructures TiO₂-GO appliquées à la dépollution de l'eau

Mots clés : Dioxyde de titane, Oxyde de graphène, Nanostructures hybrides, Dépollution de l'eau

Résumé : Les préoccupations croissantes en matière de préservation de l'environnement ont orienté les efforts de la recherche vers le développement de nanomatériaux adaptés aux applications de la dépollution de l'eau. Dans ce contexte, des oxydes de graphène (GO) et leurs nanostructures hybrides associant des nanoparticules de TiO₂ ont été synthétisés en vue d'exploiter des processus tels que l'adsorption et la photocatalyse pour l'élimination des polluants organiques dans l'eau. Les travaux menés ont permis d'étudier l'influence des propriétés physicochimiques des GO et en particulier leurs degrés d'oxydation sur les propriétés structurales, électronique et de photoactivité des nanocomposites hybrides TiO₂-GO. La fabrication de nanostructures hybrides à base de TiO₂ et de GO par broyage à haute énergie et par photosonication a été mise en œuvre ainsi que des techniques de caractérisations complémentaires telles que la diffraction de RX, la spectrométrie Raman, la microscopie électronique SEM/TEM, la spectroscopie FT-IR, XPS et de résonance paramagnétique électronique RPE. L'analyse approfondie des résultats obtenus sur une variante de nanocomposites TiO₂-GO a mis en évidence l'évolution des

propriétés physico-chimiques et morphologiques des nanostructures en fonction des conditions d'oxydation contrôlées du GO. En complément, des études théoriques par DFT ont révélé la corrélation entre les variations de la bande électronique interdite et la concentration des groupes fonctionnels dans le matériau GO. Les phénomènes d'adsorption et de photocatalyse des différentes compositions TiO₂-GO ont été étudiés à travers l'élimination du bleu de méthylène (MB) avec des efficacités remarquables. La même approche expérimentale qui a été ensuite explorée sur des organismes biologiques tels que des microalgues à travers la dégradation de sous-produits associés, souligne le caractère interdisciplinaire de ces travaux. Ainsi, en explorant systématiquement les degrés d'oxydation du GO et les techniques de fabrication des nanocomposites, les études effectuées contribuent à la compréhension et l'optimisation des propriétés et caractéristiques des nanostructures hybrides à base de TiO₂ et de GO pour une meilleure efficacité de leur utilisation pour la dépollution de l'eau.

Title: Influence of graphene oxide (GO) on TiO₂-GO nanostructures applied to water pollution control

Keywords: Titanium dioxide, Graphene oxide, Hybrid nanostructures, Water remediation

Abstract: Growing environmental concerns have focused research efforts on the development of nanomaterials suitable for water pollution control applications. In this context, graphene oxides (GOs) and their hybrid nanostructures combining TiO₂ nanoparticles have been synthesized to exploit processes such as adsorption and photocatalysis to remove organic pollutants from water. The work carried out has made it possible to study the influence of the physicochemical properties of GOs and in particular their oxidation degrees, on the structural, electronic, and photoactivity properties of TiO₂-GO hybrid nanocomposites. Hybrid nanostructures based on TiO₂ and GO were prepared by high-energy milling and photosonication, and complementary characterization techniques such as X-ray diffraction, Raman spectrometry, SEM/TEM electron microscopy, FT-IR, XPS, and EPR electron paramagnetic resonance spectroscopy were used. An in-depth analysis of the results obtained on a variant of TiO₂-GO nanocomposites highlighted the evolution of the physicochemical and morphological properties of the

nanostructures as a function of the controlled GO oxidation conditions. In addition, theoretical studies using DFT revealed the correlation between variations in the electronic bandgap and the concentration of functional groups in the GO material. The adsorption and photocatalysis phenomena of the different TiO₂-GO compositions were studied by eliminating methylene blue (MB) with remarkable efficiency. The same experimental approach, which was then studied on biological organisms such as microalgae through the degradation of associated by-products, underlines the interdisciplinary nature of this work. Thus, by systematically studying the oxidation levels of GO and the techniques used to produce nanocomposites, the studies carried out are helping to understand and optimize the properties and characteristics of hybrid nanostructures based on TiO₂ and GO, so that they can be used more effectively for water purification.